

Matthew R. Betney

Magdalen College

Supervisors

Ronald A. Roy, Yiannis Ventikos

COMPUTATIONAL AND EXPERIMENTAL STUDY OF INTENSE SHOCK-CAVITY INTERACTIONS

A thesis submitted for the degree of Doctor of Philosophy

Michaelmas Term, 2015

For my mother.

A thesis submitted for the degree of Doctor of Philosophy.

Computational and experimental study of intense shock-cavity interactions

By Matthew R. Betney, Magdalen College.

Submitted Michaelmas Term, 2015.

Abstract

This thesis presents a numerical and experimental study of the interaction of shock waves with air-filled cavities in a liquid. At the incident shock pressures studied, this process leads to the formation of high-speed jets which propagate across the cavities, causing them to collapse. This phenomenon is modelled numerically using a front-tracking approach, which enables explicit tracking of the gas-liquid interface. In arrays of multiple cavities, this method is used to show that inter-cavity effects can lead to intensification of the collapse process under certain conditions. A number of different arrangements are presented, demonstrating that in all cases the separation distance between the cavities and the relative radius of the cavities are of key importance. This result is highlighted with the study of an array of three cavities, in which it is shown that pressures over five times higher than the maximum pressure observed in the single cavity case may be achieved.

Experimentally, a single stage light-gas gun is utilised to create strong shock waves in hydrogel blocks, into which spherical cavities are cast. With this setup, high-speed imaging and optical diagnostics are used to show that cavities collapse as predicted numerically, and that light is emitted upon collapse. In the single cavity case, this light is formed initially at the position at which the high-speed jet strikes the far cavity wall, propagating out subsequently into a torus. The spectral intensity of the light emission increases consistently with increased incident shock pressure. In multiple cavity arrangements, the complex inter-cavity effects seen numerically are found to be substantiated by experimental results. The spectral intensity of the light emission is seen to vary significantly with the separation distance between the cavities, with order of magnitude increases observed for particular cases.

Statement of Originality

I hereby declare that this submission is my own work and to the best of my knowledge it contains no materials previously published or written by another person, or substantial proportions of material which have been accepted for the award of any other degree or diploma at the University of Oxford or any other educational institution, except where due acknowledgement is made in the thesis.

Any contribution made to the research by others, with whom I have worked at the University of Oxford or elsewhere, is explicitly acknowledged in the thesis.

I also declare that the intellectual content of this thesis is the product of my own work, except to the extent that assistance from others in the project's design and conception or in style, presentation and linguistic expression is acknowledged.

Matthew Robert Betney.
29th October 2015

Acknowledgements

This thesis is the culmination of four and a half years of work. I would like to thank my supervisors Professors Yiannis Ventikos and Ron Roy; Yiannis for inspiring me with the confidence to pursue my own course, and Ron for the many 9am breakfast meetings that actually got this thesis written.

My research has greatly benefited from the endeavours of fellow researchers undertaking complementary work. My particular thanks go to Brett Tully, for his expert help in writing the code used in this work, and Phil Anderson, for turning our vague ideas into a high-quality experimental setup. For this, and the many times they have dropped whatever they were doing to help me out, I am deeply grateful. It is a great privilege to view both of these individuals as friends as well as colleagues.

I must express particular gratitude to Nick Hawker for introducing me to this fascinating topic five years ago, and for his continued encouragement and support ever since. Thanks also go to Hugo Doyle, for his great help both in the modelling of air spectra and in the running of experiments, and James Cook, for his advice on numerical methods and simulations. Away from research, Stephen Brindle and David Bryon greatly simplified my time working on this project.

The experiments in this work were conducted in the Impact Engineering Laboratory at the University of Oxford, and I would like to thank Professor Nik Petrinic for his generosity in allowing us to use this fantastic facility. I would also like to thank Stuart Carter for his help and many useful ideas, as well as Graham Hillsdon and Jeffrey Fullerton. I thank Professor Robert Carlisle for the use of his UV spectrometer, and Professor Constantin Coussios for persuading me to study for a DPhil (against my better judgement).

Finally, I must express my appreciation for my wonderful friends and family. In particular, I would like to thank Emma, whose dependable editing and unfailing encouragement over the years has been a happy constant. My brother Daniel's work ethic and competitive spirit continue to be sources of inspiration. My mother, Judith, has provided much needed advice and affirmation during difficult moments, without which I would not be where I am today. Above all, this thesis is my gift to her.

I kindly acknowledge First Light Fusion Ltd. for its financial support during this project, and The Institute of Mechanical Engineers for its award of a graduate scholarship.

Dissemination

Peer-Reviewed Journal Papers

M.R. Betney, N.A. Hawker, B. Tully *et al.* Computational modelling of the interaction of shock waves with multiple gas bubbles in a liquid. Physics of Fluids, 27(3):036101, 2015

Peer-Reviewed Conference Proceedings

M.R. Betney, P.A Anderson, H. Doyle *et al.* Numerical and experimental study of shock-driven cavity collapse. 9th International Symposium on Cavitation CAV, Lausanne Switzerland, 2015 (To be published)

Conference Presentations and Posters

M.R. Betney, P.A. Anderson, B. Tully *et al.* Experimental and numerical study of shock-driven collapse of multiple cavity arrays. Presentation, 56th Annual Meeting of the APS Division of Plasma Physics, New Orleans USA, 2014

CONTENTS

Contents vii

Acronyms ix

1 Introduction 1
- 1.1 Scope of this work . . . 2

2 Literature Review 4
- 2.1 Introduction . . . 4
- 2.2 Acoustically-driven cavity collapse . . . 5
- 2.3 Cavity collapse in the vicinity of a wall . . . 11
- 2.4 Shock wave driven cavity collapse . . . 14

3 Numerical Methods 33
- 3.1 Introduction . . . 33
- 3.2 The front-tracking approach . . . 34
- 3.3 Equations of state . . . 46
- 3.4 Improvements to the user interface . . . 49
- 3.5 Post processing methods . . . 50

4 Numerical modelling of multi-cavity collapse 52
- 4.1 Introduction . . . 52
- 4.2 Grid independence and validation . . . 53
- 4.3 Two cavities . . . 60
- 4.4 Focusing triangular array . . . 75
- 4.5 Concluding remarks . . . 84

5 Experimental Methods 85
- 5.1 Introduction . . . 85
- 5.2 Shock generation system . . . 87
- 5.3 Triggering system . . . 95
- 5.4 Target design and manufacture . . . 96
- 5.5 Image capture . . . 100
- 5.6 Light detection . . . 111
- 5.7 Pressure measurement . . . 121

5.8 Comparisons between simulated and experimental results . . . 126
5.9 Summary . . . 133

6 Shock wave characterisation 134
6.1 Introduction . . . 134
6.2 Results . . . 135
6.3 Discussion . . . 141

7 Experimental study of single cavity collapse 142
7.1 Introduction . . . 142
7.2 Comparison between spherical and cylindrical cavities . . . 143
7.3 Collapse of a single spherical cavity . . . 146
7.4 Discussion . . . 168

8 Experimental study of multi-cavity collapse 170
8.1 Introduction . . . 170
8.2 Collapse of a two-cavity array . . . 171
8.3 Three cavities . . . 195
8.4 Six cavities . . . 201
8.5 Discussion . . . 204

9 Conclusions 205
9.1 Executive summary . . . 205
9.2 Conclusions . . . 210
9.3 Suggestions for future work . . . 211

References 213

A Experimental information 224
A.1 Contact trigger . . . 224
A.2 Photo-multiplier tube circuits . . . 225

B Radiation from hot air 228
B.1 Radiation transport and processes . . . 229
B.2 Radiation from air literature review . . . 233
B.3 PrismSPECT . . . 234
B.4 Calculated spectra and the validity of a black-body approach . . . 238

ACRONYMS

2D	Two dimensional
3D	Three dimensional
ALE	Arbitrary Lagrangian Eulerian method
APD	Avalanche photo-detector
$AUSM^+ - up$	Advection upstream method plus scheme
CFL	Courant-Friedrichs-Lewy criterion
EOS	Equation of state
FLM	Free-Lagrange method
FOPH	Fibre optic probe hydrophone
HLLC	Harten-Lax-van Leer approximate Riemann solver
LCA	Light curtain array
LTE	Local thermal equilibrium
MBSL	Multiple bubble sonoluminescence
MPI	Message Passing Interface
MUSCL	Monotonic upstream-centred scheme for conservation laws
PIV	Particle image velocimetry
PMMA	Polymethyl methacrylate
PMT	Photomultiplier tube
ppr	Points per cavity radius
RT instability	Rayleigh-Taylor instability
SBSL	Single bubble sonoluminescence
SNR	Signal to noise ratio
SWL	Shock wave lithotripsy
TC-SPC	Time-correlated single-photon counting
VTK	Visualization ToolKit
WENO	Weighted essentially non-oscillating
WLSP	Weighted least squares polynomial fitting



CHAPTER 1

INTRODUCTION

The premise for this thesis begins with the work of Hawker and Ventikos[1,2], and their numerical study of the interaction of a shock wave with a single gas cavity in a liquid medium. When a shock wave of sufficient pressure strikes a gas cavity, the cavity does not collapse spherically, as is seen for example in sonoluminescence. Instead, a high-speed jet is formed, which propagates across the cavity, striking the far wall. This effect has been seen both numerically[3] and experimentally,[4] and is well known. Through high fidelity simulations of this problem, Hawker and Ventikos predicted that high temperatures and densities would be reached in the cavity through this process. This prediction was supported by older experimental results,[5] which showed that cavities emit light when collapsed by a planar shock wave. Additionally, and importantly, it was predicted that the conditions in the cavity would continue to intensify as the pressure of the incident shock wave was increased, and that the collapse process would stay fundamentally the same. Through the use of a deliberately aspherical process, some of the major difficulties of driving the collapse of cavities spherically, in particular the formation of Rayleigh-Taylor type instabilities, could potentially be overcome.

The study of Hawker and Ventikos omitted some important physics, for example radiation transport, and utilised simple equations of state. However, the idea was deemed sufficiently promising that a number of patents were filed, and a small start-up company 'Oxyntix Ltd.' (now known as 'First Light Fusion Ltd.') was formed. The original goal of the company was to assess whether conditions sufficient to achieve nuclear fusion could be reached using such an approach, in conjunction with the University of Oxford. As part of this research effort but without looking at the problem in the context of fusion, the study as presented in this thesis sought to better understand the conditions reached at more modest conditions, and how they might be intensified.

Away from the goals of First Light Fusion, the fundamental process at work, whereby energy is focussed using the collapse of a cavity, has wide applicability. Perhaps the most famous example of this is sonoluminescence, where cavities are driven under the influence of a periodic acoustic wave to collapse and emit light. More useful examples include the intensification of explosives, the driving of chemical processes or biomedical applications such as shock wave lithotripsy. An extensive review of these applications is given in chapter 2.

1.1 SCOPE OF THIS WORK

There are two major, interrelated aspects to this work. In the first part, the numerical study of the interaction of a shock wave with a single gas cavity is expanded to multiple cavity arrangements. This investigation, recently published in the journal 'Physics of Fluids', is given in chapter 4. The same numerical methods are used as in the work of Hawker and Ventikos[1], and are summarised in chapter 3. As will be seen, the expansion of the problem to include multiple cavities leads to a rich new level of detail and complexity. Inter-cavity effects significantly change the process, intensifying it under certain circumstances. The problem is addressed through the detailed study of a number of spe-

cific arrangements. These include a two-cavity array, where the second cavity is placed at a variable separation distance behind the first relative to the incident shock wave, and where the relative size of the cavities is varied. The final arrangement studied is a triangular array of three cavities, where the third cavity is placed behind the first two and is of a much smaller size. With this arrangement, significant amplification of pressures is demonstrated.

The second major part of this thesis is the experimental study of shock driven cavity collapse. Both single and multiple cavity arrangements are investigated, primarily to assess whether results predicted numerically are borne out in reality. As in previous experimental work on the subject,[4] a single stage light gas gun is used to form shock waves within a hydrogel block, in which air cavities are cast. This method allows tight control over the size and spacing of the cavities, with the hydrogel acting in a manner very similar to water when shocked. The experimental setup designed and built in order to conduct these experiments is described in chapter 5. Diagnostic tools employed include both high speed optical imagery and light detection diagnostics, enabling quantitative measurement of any light emission produced by collapsing cavities. The shock waves which are formed in the hydrogel block by this experimental setup are analysed in chapter 6, while the collapse of single and multiple cavity arrangements are presented in chapters 7 and 8 respectively. As will be shown, many of the processes seen in the numerical study of shock-driven cavity collapse are also seen experimentally. In the case of multiple cavity arrangements, it will be shown that intensification of the collapse process may be achieved under certain conditions, although as seen in numerical studies, the addition of multiple cavities greatly increases the complexity of the problem.



CHAPTER 2

LITERATURE REVIEW

In this chapter, previous work on the subject is summarised. Cavity collapse is broken down into three main areas: acoustical (spherical) collapse, cavity collapse in proximity to a wall, and shock-driven cavity collapse. Acoustical cavity collapse in general consists of repeating events, varying with the frequency of the sound wave. The most interesting aspect of this is sonoluminescence, where the cavity is seen to emit light. Cavity collapse close to a wall is a single event, and is a major damage mechanism for ship propellers. This process is driven primarily by the formation of a jet in the cavity. This jet formation is also seen in the interaction of a shock wave with a cavity, the main focus of this thesis. Previous research on this subject is summarised, including a detailed description of the collapse of a single cavity.

2.1 INTRODUCTION

The subject of this thesis is the collapse of gas cavities, situated within a denser medium such as water. These cavities may come in the form of naturally occurring bubbles, or can be artificial cavities, cut out of or placed in the medium. Either way, when a pressure differential is applied across the cavity wall these cavities can collapse, the walls imploding in, compressing the cavity contents. This process leads to a significant focussing of energy; a result that is widely exploited in science, industry and in nature. A more specific example is the collapse of cavities when struck by shock waves. Under these conditions,

cavities can collapse in complex and interesting ways, and it is this specific subject that is the focus of this work. Much work has been done looking at this problem over the years, and a comprehensive summary is given in this chapter. However, to provide an impression of the greater significance of this field, the larger area of research, that of acoustically driven cavity collapse, will first be briefly summarised.

2.2 Acoustically-driven cavity collapse

Whilst in many ways a very different process to the subject of the present work, acoustically driven cavity collapse, and in particular sonoluminescence, is the subject of one of the largest bodies of research in this area. As such, it is the natural starting point for this review. Rather than being a single event, the processes discussed in this section are driven by continuous, relatively low amplitude acoustic waves, and are repetitive processes.

2.2.1 Sonoluminescence

Sonoluminescence is the process whereby a bubble, or multiple bubbles, collapse so strongly that light is emitted. This phenomenon has been achieved using a number of methods, for example utilising cavitation from a converging flow in a Venturi tube,[6] the impact of a shock wave on a bubble,[7] or the cavitation of bubbles in a water hammer tube.[8] However, the term is most commonly applied to the more specific case, where a single bubble (Single Bubble Sonoluminescence, SBSL), or cloud of bubbles (Multiple Bubble Sonoluminescence, MBSL) are grown and collapsed under the influence of a driving ultrasonic pressure field. This latter case is the subject of this section.

Sonoluminescence was first observed in clouds of cavitation bubbles[10–14] as a diffuse glowing, that was only visible with long exposure photography. Although hints of the process in a single bubble were seen earlier in ultrasonically driven fields,[15] the phenomenon

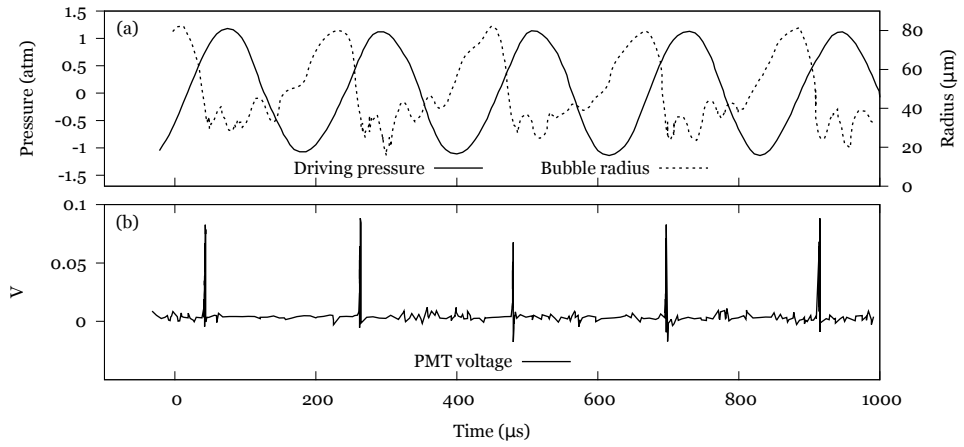

Figure 2.1: Variation in the driving pressure and radius of a sonoluminescing bubble over time (a), and the measured light emission (b). Data taken from Gaitan *et al.*[9].

of *stable* single bubble luminescence was first isolated by Gaitan.[9,16] It was found that in a flask of degassed water driven under ultrasound injected bubble clouds would coalesce as a single bubble present at the antinode of the sound field. This bubble was seen to oscillate stably, collapsing in a spherical manner, almost to a singularity, before rebounding. A clear light was emitted with every oscillation that was visible to the naked eye. Measuring the change in radius of the bubble using laser scattering techniques and capturing the light emission using a photomultiplier tube (PMT), Gaitan was able to show that the bubble collapsed quantitatively in the same way as predicted by classical bubble dynamics,[17,18] and that the light was emitted at the point of minimum volume with every oscillation (figure 2.1).

Since the discovery of Gaitan there has been a very large body of work on the subject. The use of time-correlated single-photon counting (TC-SPC)[19,20] and streak cameras[21] has shown that the width of the light pulse is at least 100 ps, whilst analysis of PMT results has shown that the intensity of light varies smoothly with no spectral peaks, increasing towards the ultraviolet.[22–24] This very short light pulse (too short to be related directly to the dynamics of the bubble collapse) has been supported by a number of numerical simulations,[25–27] which suggest that a strong spherical shock wave forms in the gas ahead of

the imploding bubble walls, thus strongly compressing the gas in the centre of the bubble. Subsequent experimental work has concluded that the bubble walls move at Mach 4 immediately prior to minimum volume, reinforcing this argument.[28–30]

The stable oscillation of bubbles as in the case of SBSL is an extremely complex process, and is highly dependent on a number of experimental parameters. Particularly important are the composition of the liquid,[16,31] the temperature of the liquid,[24,32] the equilibrium radius of the bubble and the driving pressure. It has been found that small deviations in these parameters can lead to wild bubble oscillations and even chaotic behaviour.[33–35] Below a threshold driving pressure, bubbles will oscillate quasi-statically, without actually collapsing.[36] As the pressure is increased, instabilities affect the range in which repeating, stable collapses can occur. Brenner *et al.*[36] cite three major causes of instability that must be avoided for SBSL: (i) the bubble must not change shape over time, (ii) the number of gas molecules in the bubble must not change from cycle to cycle (diffusive stability), and (iii) the bubble must stay in the acoustic trap (Bjerknes instability). Diffusive stability dictates the limit on the dissolved gas concentration in the liquid, while shape instabilities place a limit on the size that a bubble can reach for a particular forcing pressure.[37,38] There is thus a relatively narrow band of relative gas concentrations and forcing pressure amplitudes within which the process can occur.

Experiments have shown[39] that with air bubbles nitrogen and oxygen must be removed from the bubble before light emission is observed. This happens through the process of noble gas rectification, whereby these molecules dissociate due to the high temperatures, causing them to react with the water vapour in the bubble and dissolve into the liquid.[40–44] Water vapour concentration is also thought to act to limit temperatures reached,[45] due to its higher polytropic exponent and the endothermic splitting of the water vapour into H and OH molecules, which absorbs a substantial amount of energy.

The choice of liquid in SBSL is critical for the success of the process. Whilst numerous

studies have attempted to achieve SBSL in other liquids,[16,31] the best liquid has generally been found to be water.[30] This has proven to be very sensitive: Ashokkumar *et al.*[46] found that only small amounts of alcohol added to water were sufficient to quench luminescence. Didenko *et al.*[47] studied various liquids for use in SBSL, and concluded that for the process to work the liquid had to have a very low vapour pressure (in order to minimise the amount of vapour that the bubble absorbs as it expands), and to contain a high content of heteroatoms, such as oxygen or nitrogen (to react with the gas to form species that dissolve into or react with the surrounding liquid and are thus removed from the bubble). They found that with both these conditions met, bubble collapse with high levels of sonoluminescence could be induced, although these bubbles could not be made to sit on the pressure antinode, but rather oscillated around it. In recent experiments, light emission has been achieved in non-volatile liquids such as concentrated sulphuric acid[48–50] and phosphoric acid.[8] In sulphuric acid, collapse was found to be much slower than in water, but light emission 1000 times brighter was seen. Light emissions that stretched over microseconds were observed from bubble collapse in a water hammer shock tube containing phosphoric acid.[8]

While the hydrodynamic and chemical processes that drive SBSL have become reasonably well understood, there is still some discrepancy as to the processes that occur inside the bubble and, critically, the processes that cause emission of light. Various numerical studies of the process have either predicted the formation of an imploding shock wave in the gas,[25–27] or suggested that this does not play a significant role.[51,52] Unless a method is found to view the processes occurring inside the bubble experimentally, this is unlikely to be resolved.

Numerous theories have been proposed for the emission of the light in sonoluminescence, from the more exotic, such as the quantum-electrodynamical Casimir effect,[53] to simple thermal heating of the gas due to the level of compression.[54,55] However, it is gen-

erally assumed that light emission comes from a combination of multiple processes, including plasma processes such as bremsstrahlung* and pressure-broadened discrete electronic transitions.[56,57] Recent studies have suggested that that the bubble collapse leads to the formation of a plasma, which emits photons that can be detected and analysed. This plasma compresses down to a hot, opaque core at the point of maximum compression, at which point light is only emitted from the surface, in the form of smooth blackbody radiation with no peaks[58]. It is speculated that temperatures in the centre of the bubble at this point, which cannot be measured, could exceed 10^5 K.[49,59] In experiments involving SBSL with argon in concentrated sulphuric acid, emissions from specific entities in the spectra have been detected, in particular from argon atoms and O^{2+} ions providing direct evidence of plasma formation inside the bubble.[48] Analysis of these results suggests effective peak temperatures and pressures in MBSL reach 5000 K and 300 bar, while conditions can exceed 16,000 K and 1000 bar in SBSL, with corresponding electron densities of 10^{21} cm^{-3}.[56]

Once the bubble reaches minimum volume, one of the key processes absorbing energy is the formation of a strong spherical shock in the liquid, which propagates rapidly away from the bubble.[60–63] Pecha *et al.*[62] were able to measure the amplitude of the pressure wave within 50 μm of the bubble, and compared the results to those from a streak camera used to visualise the shock. They found that the shock velocity in the vicinity of the bubble reached 4000 m/s, with pressures reaching 4 to 6 GPa.

2.2.2 Sonofusion

While the remarkable focussing of energy demonstrated by SBSL has led many to speculate on the ultimate potential of the process,[64,65] to date the only claim of a successful measurement of fusion from acoustically driven bubble collapse ('sonofusion') was made

*From the German: *Bremse* (brake) and *Strahlung* (radiation). The electromagnetic radiation released when an electron is deflected when passing another charged particle. See section B.1.2 for more details.

by the group of Rusi Taleyarkhan.[66] In this work, degassed deuterated acetone was held under a strong acoustic field of amplitude ±15 bar. Acetone was used instead of water to prevent cavitation at these elevated pressures. A neutron source was then used to nucleate cavitation activity in the acetone, and a scintillator and photo-multiplier tube used to detect neutron emission and light emission respectively. Using this setup, Taleyarkhan claimed to have conclusively demonstrated sonofusion.

When the work of Taleyarkhan was published, it was met by a substantial amount of criticism from members of the scientific community,[67,68] who questioned the validity of the results based on the poor quality of the experimental technique. Additionally, several attempts to repeat the work by other groups[69–71] met with negative results. Further work to substantiate the original claims by the Taleyarkhan group through further experimental work,[72–75] and detailed numerical studies[76] have again been met with scepticism.[77] In part this is due to an inquiry by Purdue University on scientific malpractice,[78] that criticised (among other things) the heavy involvement of Taleyarkhan in the work of Xu and Butt,[74], which had been claimed as independent research. Beyond the work of Taleyarkhan, further work on achieving sonofusion has been conducted along different lines, principally by the company Impulse Devices,[79,80] but with no reported successes.

2.2.3 Sonochemistry

One notable application of acoustically driven bubble collapse is sonochemistry, where cavity collapse is used to enhance or drive chemical reactions. Due to the very high temperatures, pressures and heating/cooling rates possible, sonochemistry can provide a means to generate products not normally accessible by other methods.[56,81] Additionally, liquid motion in the vicinity of bubbles can lead to very large shear and strain gradients in the solvent. This is due to the rapid streaming of molecules around the oscillating bubbles, and the strong shock waves emitted on bubble collapse.[82] Near solid surfaces, as-

pherical bubble collapse leading to jet formation can be used to damage or fragment the surface of brittle materials, which can improve reactivity.[82,83]

Sonochemistry has a number of applications. The remarkable cooling rates present in bubble collapse, up to 10^{10} K/s,[82] have been harnessed in the formation of amorphous iron.[84] Other examples include enhancement of superconductor properties in superconductor slurries,[85] the treatment of pollutants in water,[86] or the preparation of nanoparticles.[87,88] In the esterification of biodiesels, cavitation can be used to promote mixing of the otherwise immiscible reactants, intensifying the process.[89]

2.2.4 Examples from nature

Bubble collapse is also utilised in nature. A good example is the case of the snapping shrimp (*Alpheus heterochaelis*). This animal has an over-enlarged front claw, which it closes rapidly, creating a shock wave which stuns or kills its prey. Rather than the claw itself causing the damage, the rapid closure leads to the formation of a high velocity water jet. The jet velocity is sufficiently high that the corresponding pressure drops below the vapour pressure of the water, leading to the formation of cavitation bubbles. Peak pressures measured in situ correlate with the collapse of these bubbles[90], the collapse being so intense that sonoluminescence occurs,[91] a phenomenon that has been coined 'shrimpoluminescence'.[91] The relative amplitude of the sound waves produced by this process have been recorded at 190 dB,[92] and the crackling produced by large numbers of these animals is the dominant source of ambient noise in tropical waters.

2.3 Cavity collapse in the vicinity of a wall

Some of the earliest studies of bubble collapse centred around cavitation erosion, in large part due to the damage that can be caused to ship propellers or hydraulic machinery. This

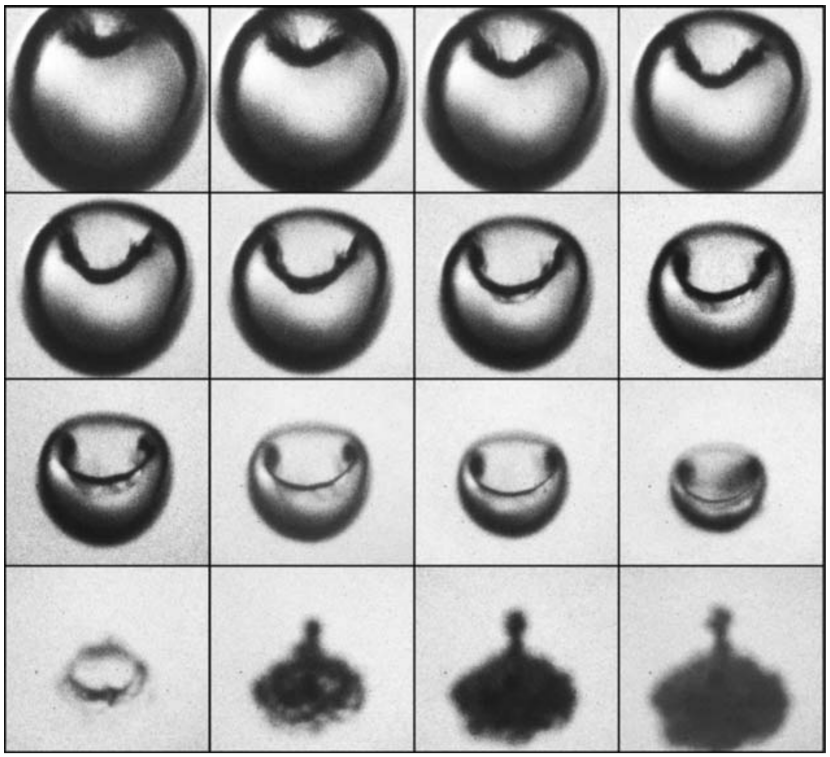

Figure 2.2: Jet development in a cavitated bubble in proximity to a boundary. The centre of the cavity, of maximum radius R_{max} = 1.5 mm, was initially positioned a distance 2.6 R_{max} from the boundary. Inter-frame time 1 µs. Images taken from Lindau and Lauterborn.[93]

process is in essence the collapse of a cavity in close proximity to a boundary. Much like in shock-driven cavity collapse (to be discussed in section 2.4), a jet is formed in the cavity, which propagates through,[94] producing a water hammer shock on impact on the far side of the cavity. However, in this case no incident shock is involved, the process instead being caused by the presence of the boundary. A good example of this process, taken from the work of Lindau *et al.*[93], is shown in figure 2.2. This figure shows the collapse of a laser-cavitated, vapour-filled cavity of maximum radius R_{max} = 1.5 mm, initially positioned a distance 2.6 R_{max} from a ground glass boundary. A very clear jet is seen to form, which propagates across the cavity in the direction of the boundary.

Although the pressure waves produced by a collapsing spherical bubble were first analysed by Lord Rayleigh,[17] the identification of 'erosion by water hammer' during cavitation as the principal cause of damage is generally attributed to Cook[95]. Experimental

and numerical verification of this non-spherical collapse mechanism was conducted by Benjamin *et al.*[96], and Plesset *et al.*[97] respectively.

Subsequent studies have generally looked at cavities generated using lasers[98–101] or sparks,[102] with similar results. The dynamics of the collapse are heavily dependent on the normalised distance from the boundary and the boundary impedance. But, at least for the case of a rigid boundary, certain key processes are generally seen. When a cavity is formed it initially grows in size. As the size of the cavity increases the pressure outside the cavity becomes much larger than the pressure inside. As a result, the sides of the cavity begin to move inwards spherically. However, when the cavity is close to a solid boundary, the inward flow on the solid boundary side is inhibited by the presence of the boundary, and its motion is reduced. The acceleration of the cavity wall is thus greater away from the boundary, and the pressure becomes higher on the side away from the boundary for the entirety of the collapse. The cavity therefore experiences a force towards the boundary.[103] By this method, cavities that were initially created a distance from the solid boundary may come into contact with it by the point of collapse.[101]

The asymmetric collapse of the cavity is inherently unstable (it can be thought of as a form of Rayleigh-Taylor (RT) instability). As a result, at the point of maximum acceleration, which occurs at the point furthest from the boundary, a jet forms in the cavity wall towards the boundary. This jet propagates across the cavity to strike the near cavity wall, protruding through to strike the boundary. The remainder of the cavity is left as a toroid. The combination of the continued flow through the centre of the toroid and the flow towards the remainder of the cavity cause it to develop into a vortex ring. This ring continues to collapse and expand until it decays into a series of micro-bubbles.[101]

Numerous studies have suggested that only cavities in direct contact with a surface lead to damage,[94,101,104] although the movement of a cavity towards the wall during collapse can bring a cavity that was initially spaced from the wall into direct contact later

on in the collapse process. From analysis of the shock waves formed and the damage to surfaces, which can be seen to form a circular pattern, it is now generally supposed that collapse of the remaining vortex ring is the principal cause of damage.[105] This is particularly prevalent at close proximities when the cavity is in direct contact with the wall from the start, where 'splashing' can lead to pressures on the surface several orders of magnitude higher than those caused by the jet impact.[106]

One interesting aspect of cavitation collapse that long remained a mystery was the formation of a 'counter jet' away from the wall.[98,100] While there has been some speculation as to the cause of this jet, it is now believed to be a large number of small cavitated bubbles, possibly caused by overlapping rarefactions that follow the shocks formed by the first collapse of the cavity.[93]

2.4 SHOCK WAVE DRIVEN CAVITY COLLAPSE

This section discusses the principal area of research in this study - the collapse of cavities or bubbles under the influence of a shock wave. While this process can influence all areas of research discussed to this point in some capacity, not least through inter-cavity effects, this section presents an overview of the direct applications of this process. Also discussed are the numerous works conducted in which the phenomenon has been isolated and studied away from any application, as is the case in the present work.

2.4.1 Explosive ignition

A significant application of shock-driven cavity collapse is the sensitisation of explosives. Bowden *et al.*[107] identified that the collapse of cavities present within an explosive matrix could act as a local source of ignition, leading to local hot spots that were of sufficiently high temperature to ignite the medium. This process was modelled by Mader[108], who

demonstrated that cavities collapse to form a jet, which leads to local regions of high temperature. Bowden *et al.*[109] suggested that the formation of these jets could facilitate the initiation of burning by dispersing the explosive within the heated gas. Coley *et al.*[110] conducted high speed photographic studies of the growth of explosions in thin films, and found that the transition from deflagration to detonation was dependent on the production and collapse of cavities ahead of the reaction front. They outlined four methods through which cavity collapse could enhance explosive ignition: (i) adiabatic collapse of the cavities by compression waves from the deflagration front, giving rise to hot-spots in the explosive; (ii) the presentation of a larger surface area to the deflagration front as it enters the cavitated zone; (iii) the formation of jets during the collapse of the cavities (referred to as 'micro-Munroe' jets), leading to the dispersion of explosive droplets in the heated cavity, or production of high temperatures by impact; and (iv) the action of the water hammer shock formed on collapse on neighbouring cavities.

Other studies have looked more closely at individual cavities in explosive ignition. Chaudhri *et al.*[111] studied the collapse of bubbles on explosive crystals. It was concluded that the main effect leading to explosive detonation was the adiabatic heating of gas inside the bubbles rather than the impact of expanding shock waves, as bubbles had to be placed directly on the crystal for detonation to occur. Bourne and Field[5,112,113] studied explosive ignition with single and multiple cavities in an explosive emulsion, using a two dimensional method (to be discussed in more detail in section 2.4.5) whereby thin sheets of material, containing cavities, were sandwiched between PMMA blocks and struck with a shock wave produced by an explosive. They concluded that reaction was caused by the ignition of vapour within the cavity at the final moments prior to jet impact and in the material immediately adjacent to this heated gas at the downstream cavity wall. From studying arrays of cavities, they concluded that significant inter cavity effects were present, with the primary point of ignition in each cavity being the point of jet impact on the leeward

cavity wall. They also observed that the vortices produced by cavity collapse favour the continuation of the reaction through improved mixing. Bourne *et al.*[114] compared this work to simulations of the same process. They concluded that water hammer shock formation coincided with the main light emission from the explosive, indicating this as the main point of ignition. They concluded that although luminescence was seen in the remaining lobes of the cavity, compression of the gas likely did not play a substantial role in the process.

2.4.2 Shockwave lithotripsy

Another important application of bubble collapse is in shock wave lithotripsy (SWL), where pressure waves from outside the body are used to non-invasively break down stones within the body. Although shock wave lithotripsy has been used for some time to treat kidney stones effectively, it was not until long after the method became established that it was suggested that the action of bubbles cavitating in the vicinity of the stone could be important.[115]

Although the direct action of shock waves on the stone undoubtedly plays a significant role,[116–118] it is now well understood that cavitation is a vital aspect of the process. Zhu *et al.*[118] suggest that while the breakup of stones into large sections is primarily due to the influence of shock waves through mechanisms such as spalling, cavitation action leads to fine surface erosion of the stone, breaking it up into sufficiently small fragments that they may be passed out of the body. It has also been suggested that expansion of gas in cracks could enhance the breakup of the stone.[119] The importance of cavitation in the process has been emphasised in numerous other studies.[117,120]

There have been a number of attempts to model cavitation action and the pressure waves produced in shock wave lithotripsy.[122–124] One such study is the work of Church[122], in which a lithotripsy pressure pulse was applied to the Gilmore-Akulichev model of

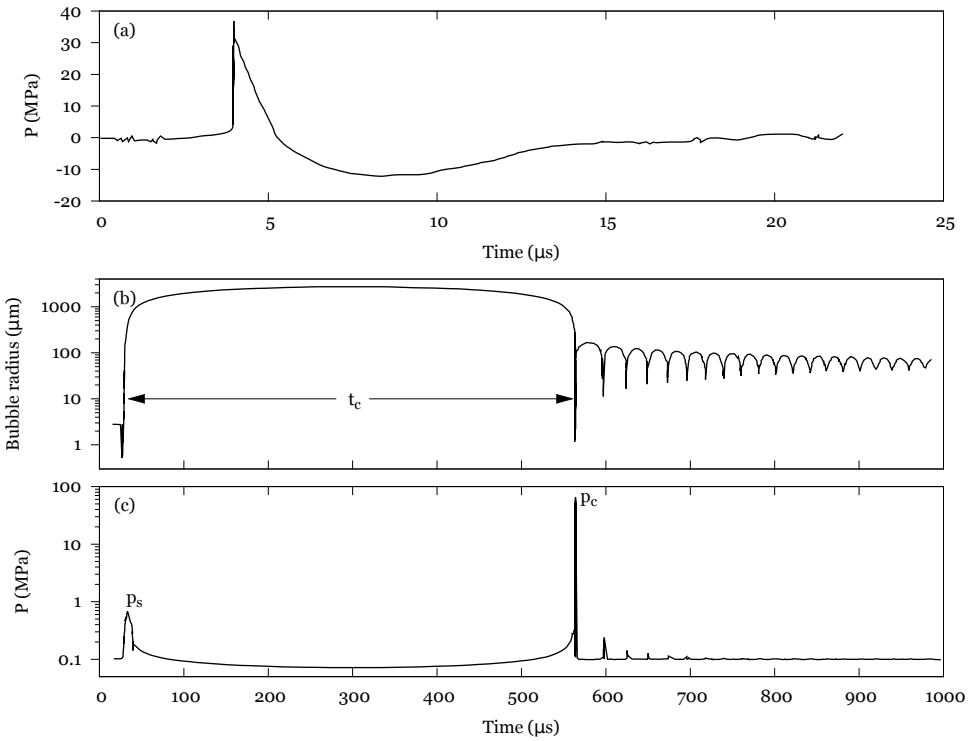

Figure 2.3: Predicted bubble dynamics under the influence of a lithotripsy pulse, taken from Cleveland *et al.*[121] (a) driving pressure wave, (b) calculated radius vs time curve for a 3 μm radius bubble, (c) calculated radiated pressure 10 mm from the bubble.

spherical bubble collapse,[125] an example of which is shown in figure 2.3. This study predicts a pressure wave p_s to be released on first interaction of the high pressure region of the pulse with the bubble. A long period of no emission is then predicted of time t_c, in which the bubble expands under the negative tail of the pulse. At the end of this period, long after the pressure has returned to ambient conditions, the bubble collapses, releasing a second pressure wave of magnitude p_c. This peak pressure is expected to be at least an order of magnitude stronger than the first pulse. Although there are a number of assumptions in this study which are unlikely to be accurate (for example spherical collapse or the exclusion of inter-bubble effects), numerous experimental studies have shown that the pressure pulses released correlate well with those predicted in this study, both *in vitro* and *in vivo*.[117,121,126–129] For example, Coleman *et al.*[130] used a hydrophone and a photo-multiplier tube to measure pressure pulses and light emission from water

when cavitated by a lithotripter. Bubble clouds created were shown to luminesce, and the timings of the light emission and pressure waves correlated well with those predicted by Church. Philipp *et al.*[126] demonstrated that this correlation also held for asymmetrical jet formation, with far field pressures detected corresponding well with the (spherical collapse based) Gilmore model. Other studies looking at the interaction of shock waves with pre-existing bubbles on surfaces show substantial damage to the surface when the shock wave strikes the bubble, causing it to involute to form a jet towards the wall.[131]

One key additional aspect of SWL is the influence of inter-cavity effects on the dynamics of cavity collapse. Pishchalnikov *et al.*[132] used high-speed photography to study the formation and collapse of cavitation bubbles on artificial and real kidney stones, *in vitro*. They found that cavitated bubbles initially formed as individual entities, but then gradually coalesced into larger bubble clouds. These bubble clouds were then seen to collectively collapse. This process was modelled by Hamilton *et al.*[133] and Zabolotskaya *et al.*[134] using a Rayleigh-Plesset type approximation of spherical growth and collapse, with qualitatively similar results.

Cavitation in SWL is also thought to be one of the principal causes of tissue damage in the process.[127,135,136] The work of Zhong *et al.*[129] [137,138] suggests that *in vivo* bubble expansion in SWL is substantially reduced compared to *in vitro* studies. They attribute this to tissue constraints on the bubble, and suggest that this could be one of the causes of damage to small capillaries, with repetitive dilation of vessels leading to rupture. Through the *ex vivo* study of bubble growth and collapse within vessels, Chen *et al.*[139,140] observed both expansion and compression of vessels due to the action of micro-bubbles. In some circumstances, they also observed jet formation within bubbles, directed away from the vessel wall. From the observation of dye leakage in their experiments, they concluded that micro-bubbles can rupture vessels of diameter less than 20 μm.

2.4.3 Description of single cavity collapse

Having outlined a number of the applications of the process, the studies in which shock-cavity interaction has been isolated will now be discussed. However, before covering the full extent of research in this area, a brief overview of the work of Hawker and Ventikos[1,2] on the collapse of a single cavity is presented here. This work is the original basis of the present study, and utilises the same numerical methods to analyse the problem.

2.4.3.1 Single cavity collapse by a 1 GPa incident shock wave

Figures 2.4 and 2.5 show a time sequence of the collapse of a single cavity of diameter 1 mm, struck by a 1 GPa incident shock wave, taken from the work of Hawker *et al.*[1]. This simulation is modelled in planar 2D using a front tracking approach (see chapter 3), the gas is modelled as air using an ideal gas equation of state (EOS), and the liquid is modelled as water using a stiffened polytropic EOS. Following this time sequence, on impact of the incident shock on the upstream wall of the cavity a transmitted shock is formed in the gas, and, because the acoustic impedance of the air is less than that of the water, a reflected rarefaction is formed in the liquid (figure 2.4 (a)). As can be seen in figure 2.4 (a), as the incident shock propagates around the sides of the cavity, the reflected rarefaction behind breaks away from the cavity and moves along the incident shock, weakening it and causing it to bend. Additionally, the reflected rarefaction reduces the pressure above the cavity, causing the flow to accelerate. Due to its curvature, this acceleration is fastest at the top of the cavity, causing the top of the cavity to involute and form a jet, labelled here as 'the main transverse jet' (figure 2.4 (b)). As this jet moves downwards, a bow shock is formed, which propagates ahead of the jet. When this bow shock reaches the far cavity wall, a transmitted shock forms in the liquid, and a reflected shock forms in the gas (see for example figure 2.4 (c)). This reflected shock may then also be reflected from the main transverse jet, and possibly re-reflected several times more. This is a major source

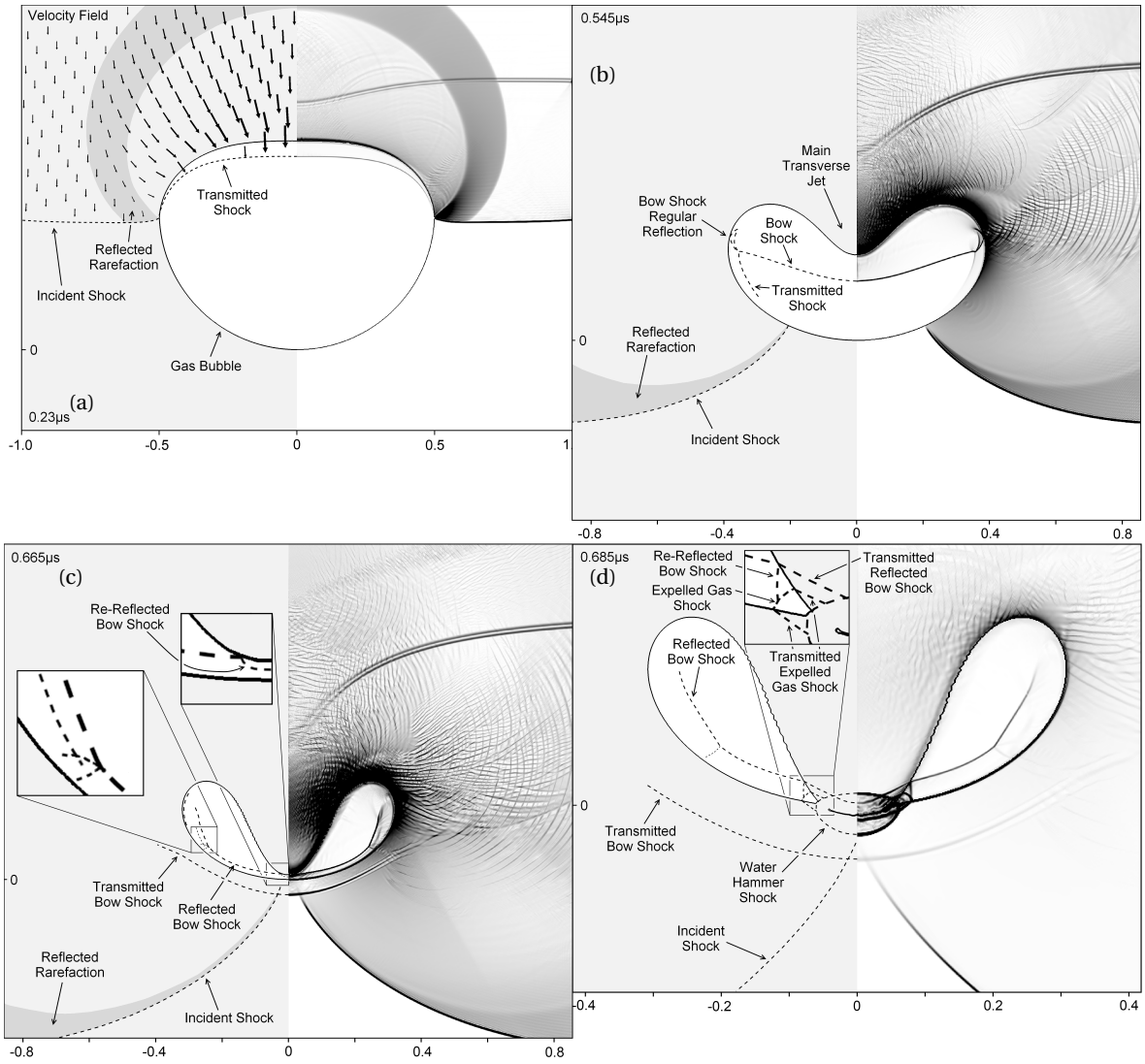

Figure 2.4: Time sequence showing the first phase of the collapse of a single cavity struck by a 1 GPa shock wave. Images taken from the work of Hawker *et al.*[1]. Right half of images show the magnitude of the gradient of the density, left half a simplified representation of the key processes at work. Displayed times relative to the time of first contact of the shock wave on the cavity. Distances in mm.

of heating in the gas prior to jet strike.

When the main transverse jet strikes the far cavity wall, a pocket of gas is compressed under the tip of the jet. This section of gas breaks away (visible in all frames of figure 2.5), with the temperatures and pressures within reaching some of the highest values seen at this stage of the process. The remains of the cavity form two 'lobes', with a sharp cusp at

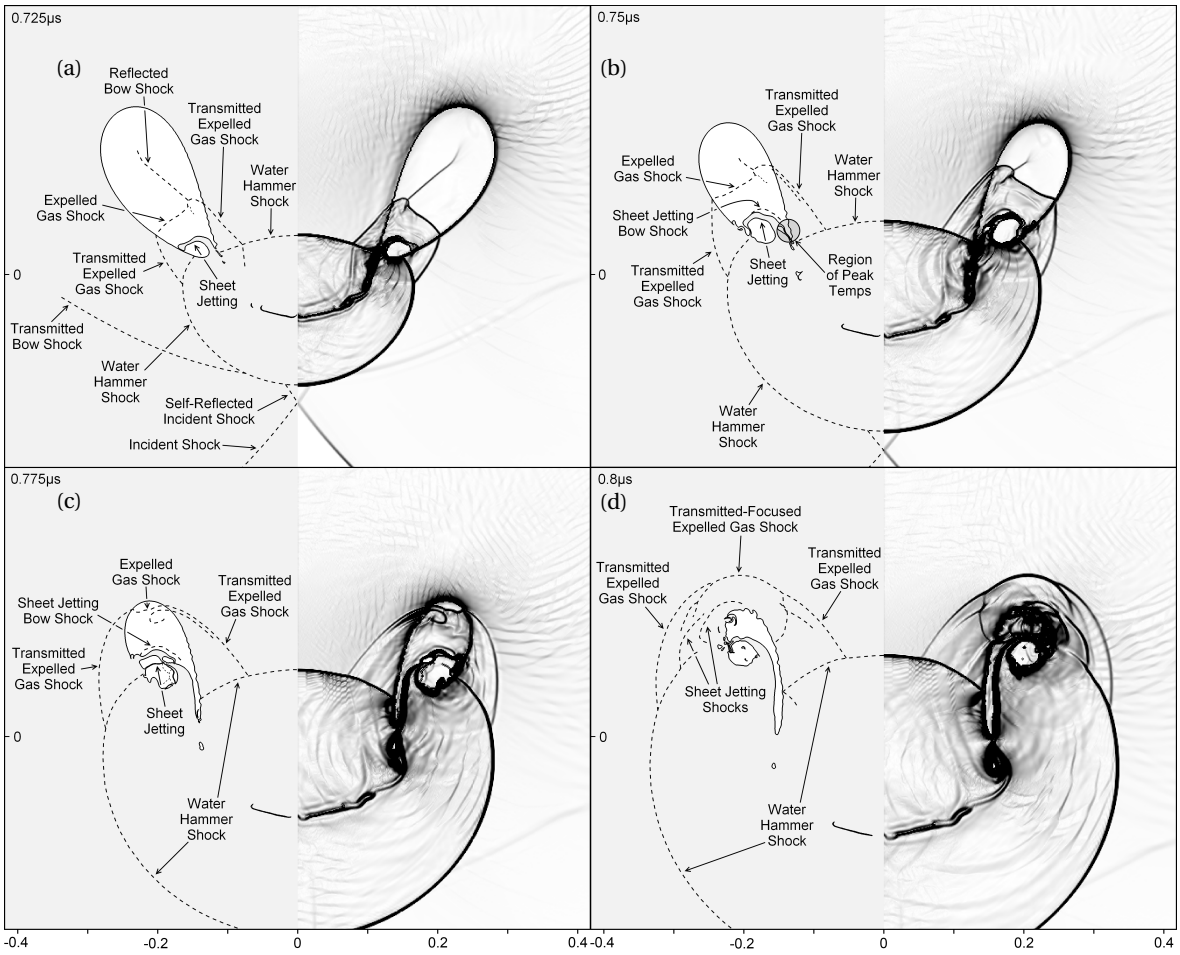

Figure 2.5: Time sequence showing the second phase of the collapse of a single cavity struck by a 1 GPa shock wave. Images as in figure 2.4, taken from the work of Hawker *et al.* [1]

the point of interaction with the main transverse jet as it continues to move through the cavity. In the case of a spherical cavity, these lobes would form a torus. As gas is forced out from underneath the jet, expelled gas shocks are formed in the lobes, which propagate in the gas away from the point of impact (figure 2.5 (a)).

In addition to the shock waves which form in the gas, on impact of the jet a strong water hammer shock is formed in the liquid (figure 2.4 (d), also described as the 'blast wave' in other literature[3,141]). This shock propagates out from the point of impact, and on formation the pressures seen can be up to 10 times higher than in the incident shock. This is therefore a major damage mechanism, and is of key significance when consider-

ing multiple-cavity interactions. Peak pressures in this shock occur on the cusp of the remains of the cavity as it continues to be compressed by the main transverse jet. As can be seen in figure 2.5, these high pressures drive liquid into the gas lobes, forming 'sheet jetting' which travels rapidly into the remains of the collapsing cavity. As this sheet jetting propagates, it drives a high pressure bow shock ahead of itself, and traps and compresses a thin region of gas between itself and the main transverse jet (labelled as 'Region of Peak Temps' in figure 2.5 (b)). This process leads to the highest temperatures seen anywhere in the collapse process.

Once the expelled gas shocks and sheet jetting reach the top of the lobes, a series of high-pressure 'secondary shocks' are emitted into the liquid (labelled as the 'transmitted focussed expelled gas shocks' and 'sheet jetting shocks' in figure 2.5 (d)). As these shocks propagate outwards from the top of the lobes (figure 2.5 (d)), they overlap on the line of symmetry, leading to momentary spikes in pressure that are the highest seen in the collapse process. Beyond this point, the water hammer shock and these overlapping shocks spread outwards away from the cavity, weakening as they spread. The action of the main transverse jet leads to the formation of a vortex ring, in which the remainder of the cavity moves slowly downwards.

2.4.3.2 Cylindrical vs spherical effects

In shock-driven collapse of a spherical cavity, the flow is focussed on to a single point during jet formation, as compared to a line for a 2D cylinder. This extra degree of focussing leads to an increase in the intensity of collapse. Hawker *et al.*[1] found that this difference translates into jet speeds that are approximately 20% faster, and water hammer shock pressures that are approximately 40% higher for the spherical case. However, they also found that as the water hammer shock spreads spherically, pressures are not sustained for as long, dropping off much more quickly compared to the cylindrical case.

Comparison was also made between a three dimensional and axisymmetric model of shock-driven spherical cavity collapse. Comparing the two, Hawker and Ventikos showed conclusively that three dimensional effects do not play a significant role in the process, with jet speeds at impact modelled to within 1% and water hammer shock pressures modelled to within 4% using axisymmetric coordinates.

2.4.3.3 Effect of incident shock pressure

As part of their study, Hawker *et al.*[1] conducted a parametric study into the effects of incident shock pressure on the dynamics of collapse. The incident shock pressure was varied logarithmically from 100 MPa to 100 GPa, for cylindrical cavity collapse. They found that in all cases cavity collapse was driven by the superposition of two competing factors - a spherical component driven by the step change in pressure, similar to the processes seen in SBSL, and an aspherical component driven by shock-impact on the cavity, leading to jet formation. At very low incident shock pressures, they found that the aspherical process took much longer to develop, and the spherical component significantly affected the process. As the shock strength was increased, jet formation began to dominate, such that at very high driving pressures the tip of the jet reached the far side of the cavity well before the incident shock.

Figure 2.6 shows the effect of incident shock pressure on the pressures seen in the collapse process. As can be seen, pressures are predicted to increase monotonically with incident shock pressure, even at extreme values. Although there are a number of caveats in this result, most notably around equations of state, this is a particularly interesting result given the difficulties in intensifying cavity collapse encountered in SBSL research discussed in section 2.2.1. While pressures are predicted to increase monotonically, Hawker and Ventikos found that the ratio of the water hammer shock pressure to the incident shock pressure was higher at lower incident shock pressures, with the ratio decreasing

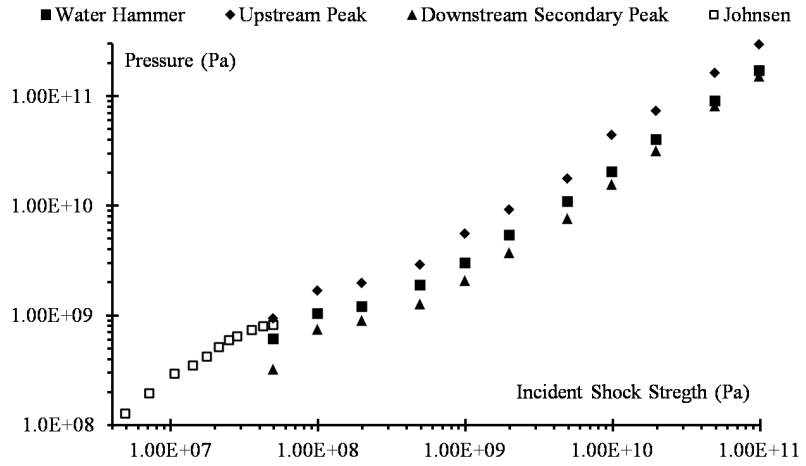

Figure 2.6: Effect of incident shock strength on pressures seen in shock-cavity interactions, taken from Hawker and Ventikos[1]. Results are compared to the work of Johnsen and Colonius.[142]

from approximately 10 at 100 MPa to a value of roughly 1.7 at very high shock strengths. Somewhat counter-intuitively, peak gas densities were found to actually decrease with increased incident shock pressure. This result was attributed by the authors to a reduced number of reflections of the bow shock ahead of the jet, prior to jet strike. With a single shock, there is a limit to which a fluid may be compressed, with the density ratio asymptotically approaching $(\gamma+1)/(\gamma-1)$ as defined by the principal Hugoniot, where γ is the heat capacity ratio. However, with a reflecting shock the fluid may be re-shocked multiple times, and higher levels of compression may be reached.

2.4.4 Numerical studies

With the work of Hawker and Ventikos outlined, useful comparison may now be made to other studies conducted on the subject. The history of the subject begins with the one dimensional models of spherical collapse first studied by Rayleigh,[17] work that has subsequently been built upon by numerous authors.[18,125,143] However, whilst these solutions model bubble collapse during SBSL astonishingly accurately, the collapse of a cavity by a shock wave is a fundamentally asymmetric process. As a result, though some attempts have been made to quantify the process analytically,[144] numerical methods have

formed the basis of the modelling of shock-cavity interactions. The presence of discontinuities in the flow, both due to shock waves and interfaces between media, substantially increases the complexity of the problem. While the first stage of the collapse process can be modelled using the potential-flow-based Boundary Integral Method,[97,123,145] the basic assumption of an incompressible liquid makes the method invalid after the jet impacts the far cavity wall.

Compressible methods have demonstrated better results. Ding *et al.*[146] analysed the interaction of a spherical gas cavity with both weak (20 - 30 MPa) and strong (500 MPa - 2 GPa) shock waves using an Arbitrary Lagrangian Eulerian code (ALE).[147] While the resolution of this work was comparatively low, they found that for a weak shock wave the cavity collapses almost spherically, with comparisons to the Gilmore model showing qualitative agreement. For strong shock waves they observed jet formation in the cavity, leading to the development of a water hammer shock on impact with the far wall. Another method that utilises a Lagrangian approach is the free-Lagrange method (FLM).[3,124,148–150] In this method, the working fluid is divided into discrete packages, between which no mass transfer can take place. The flow variables are stored for the centre of each package, and the Euler equations solved to propagate the packages and calculate updated states. In this way, areas of high resolution naturally build up in areas of high density, where it is required, and discrete capturing of interfaces is handled automatically since each package is made up of one medium or the other. A downside of this method is that the interfaces develop small irregularities at the scale of the mesh size, which can lead to Richtmyer-Meshkov instabilities. As a result, artificial smoothing routines need to be applied. Johnsen and Colonius[141,142,151] used a Weighted Essentially Non-Oscillating (WENO) Eulerian scheme with the Harten-Lax-van Leer (HLLC) approximate Riemann solver to capture the salient features of the flow. This method effectively prevents numerical oscillations across shock wave and interfaces, but without explicit tracking inter-

faces are spread over several grid cells, blurring some detail. More sophisticated methods that capture, rather than track, shocks and interfaces include the work of Chang and Liou,[152] who used a modified version of the Advection Upstream Method Plus scheme ($AUSM^+ - up$), with some success.

Many studies, including the present work, have attempted to track the positions of interfaces explicitly. One popular method that achieves this is the level set method.[153] This method has been used successfully in a number of studies of the problem, including the implementation of a ghost cell method to account for cells on the other side of the interface.[154,155] Other examples include the work of Nourgaliev *et al.*[156] [157,158], who combined the level set approach with an adaptive mesh refinement algorithm to improve computational accuracy at key points in the flow. Prior to the work of Hawker and Ventikos,[1,2] other studies have also utilised the front tracking approach to model this problem.[159,160]

A natural extension to the study of the interaction of a shock wave with a gas cavity in a liquid is shock-cavity interaction in proximity to a rigid wall. This has been the topic of interest for a number of studies, in particular in relation to shock wave lithotripsy. Johnsen and Colonius[141,142] found that in the regime studied (cavity radius approx. 50 μm) cavities collapse principally due to the initial positive pressure pulse, and that the proximity of the wall intensifies collapse, as the shock waves reflected from the wall re-contact cavities on the leeward side, accelerating the collapse process. As a result, it was found that the peak pressures on the wall were inversely proportional to the separation distance. It was also found that the width of the lithotripsy pulse had a significant effect on the collapse, with longer pulses leading to more intense collapses.[†] Smaller cavities were seen to produce more intense shocks than larger cavities, as the positive portion of the pulse was stronger for more of the collapse. These results are also supported by the work of Jamaluddin[149], who studied the influence of nearby walls on cavity collapse as part of a larger study, in-

[†]In this study pulse width was defined as the distance between the initial rise in the lithotripsy pulse, and the point at which the pressure became positive after the long negative tail.

cluding analysis of the shock waves seen in the far field.[124] Jamaluddin also found that the collapse time of cavities decreased as the distance to the wall was reduced.

While the analysis of shock waves interacting with solitary cavities provides important information as to the fundamentals of the process, almost inevitably bubbles form in clouds in nature. Hence it is also inevitable that inter-bubble effects and interactions will take place. Although some attempts have been made to analyse shock waves interacting with bubble clouds on a macroscopic basis,[161] there have been very few numerical studies of resolved multiple bubble collapse. Hankin[162] modelled the interaction of a shock wave with two cavities as an example of the use of a gas-liquid equation of state, an arrangement that was recreated by Hu *et al.*[163] as part of the validation of their level-set based scheme. Notable studies that analysed multiple cavity processes in more detail include the work of Sushchikh *et al.*[164], who analysed the interaction of a converging cylindrical shock with multiple cavities; Leighton *et al.*[150], who studied the interaction of a lithotripsy pulse with multiple cavities; and Lauer *et al.*[165], who performed a detailed study of a shock wave interacting with multiple cavities in a line perpendicular and parallel to the shock front, using the methodology of Hu *et al.* In the perpendicular case, it was found that all cavities bar the first were collapsed by the water hammer shock produced by the collapse of the preceding cavity. The intensity of collapse was seen to slowly increase from cavity to cavity in the line, although the authors note that this intensification would not hold for an infinite line of cavities. In the parallel case, it was found that the formation of low pressure regions in between the cavities caused the jets of the outer cavities to point in towards the centre of the array. This effect was reversed in the presence of free surfaces beyond the outer cavities, as the incident shock reflected from the free surfaces as rarefactions, which slowed the collapse of the outer cavities.

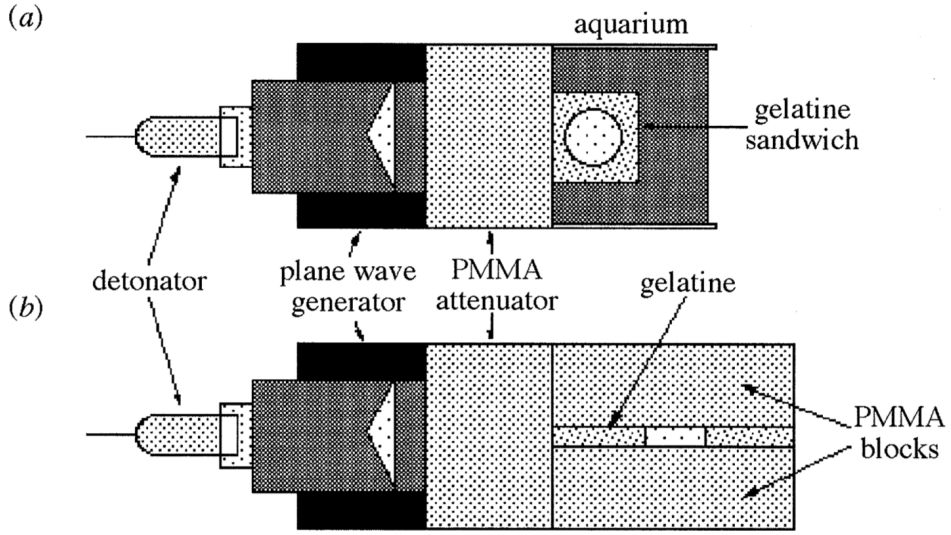

Figure 2.7: Commonly used setup for the experimental investigation of cavity collapse. Cylindrical cavities are cast in thin sheets, and collapsed by shock waves from explosive charges or the impact of flyer plates. (a) the cavity containing sheet is held between other gel sheets, and placed in an aquarium. (b) an alternative setup whereby the gel sheet is held between PMMA blocks. Image taken from Bourne and Field.[5]

2.4.5 Experimental studies

In addition to the numerical studies outlined in the previous section, there has been a concerted effort to analyse the process of shock-cavity interaction experimentally. Some of the most insightful studies have used a pseudo two-dimensional technique, whereby thin sheets of gelatin containing cylindrical air-filled cavities are compressed between glass or PMMA blocks.[4,166] An example of this type of setup is shown in figure 2.7. Using this arrangement eliminates the difficulties of viewing the inside of cavities inherent to spherical cavities. To produce a shock wave, the gelatin is struck by a projectile from a gas gun to form low magnitude shocks (approx. 0.3 GPa), or an explosive is detonated next to the setup, with a separating spacer, to generate high magnitude shocks (approx. 3 GPa). Once the shock wave strikes the gelatin, the forces on the matrix are easily sufficient to overcome bonding and it behaves in a manner very similar to water. The process is observed using high speed Schlieren photography, though Swantek *et al.*[166] supplemented this with particle image velocimetry (PIV) to study the velocities in the flow. For the ex-

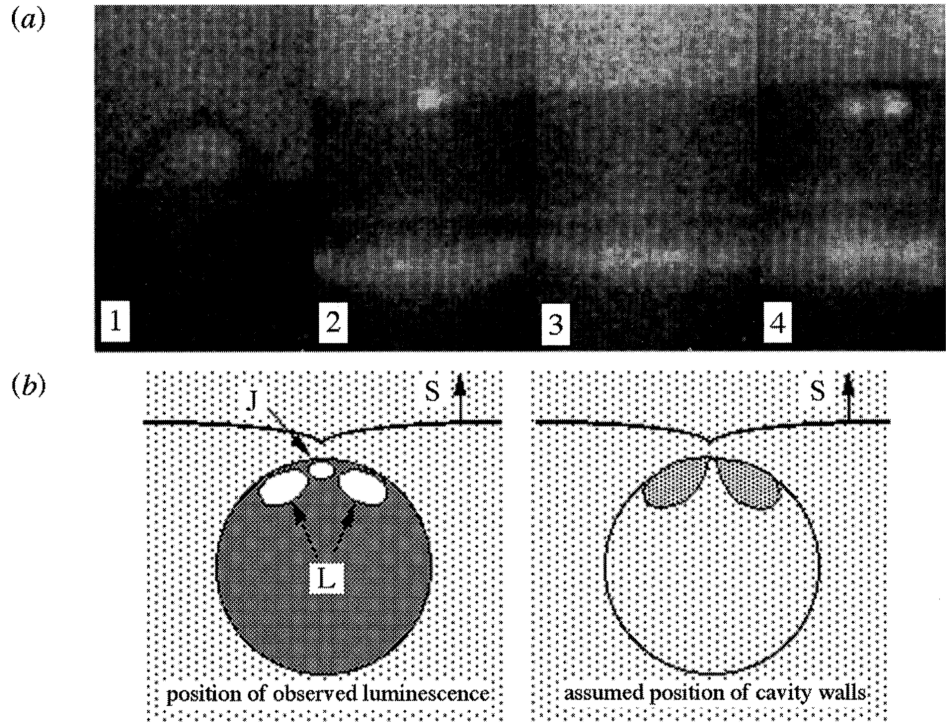

Figure 2.8: Light emission from the collapse of a 6 mm cavity under the influence of a 1.88 GPa incident shock wave. Taken from Bourne and Field.[5] (a) shows a time series in which a shock wave propagates upwards across a cavity, just visible in frame 1. Bursts of light are visible in frames 2 and 4. (b) shows diagrams of where the authors believed the light emission to emanate from in relation to the initial location of the cavity.

periments of Dear, Bourne and Field[4,167], the gel sheets used were cast from a 12 % by weight mix of gelatin in water, and were of thickness 3 mm.

This two dimensional technique has been used to examine single cavity collapse in detail.[7,167] Cavities collapse to form a high-speed jet perpendicular to the shock front, with a shock travelling ahead of it, which strikes the leeward cavity wall producing a shock wave in the liquid and leaving two lobes of gas. These lobes form a pair of counter-rotating vortices that travel downstream behind the shock. Of particular interest, luminescence has been observed[5,7,167] during shock driven cavity collapse at high shock magnitudes (see for example figure 2.8). This luminescence can be seen to be divided into two distinct bursts, the first corresponding to the compression of gas underneath the jet tip at impact (frame 2 in (a), J in (b) in figure 2.8) and the second to heating of gas in the remaining

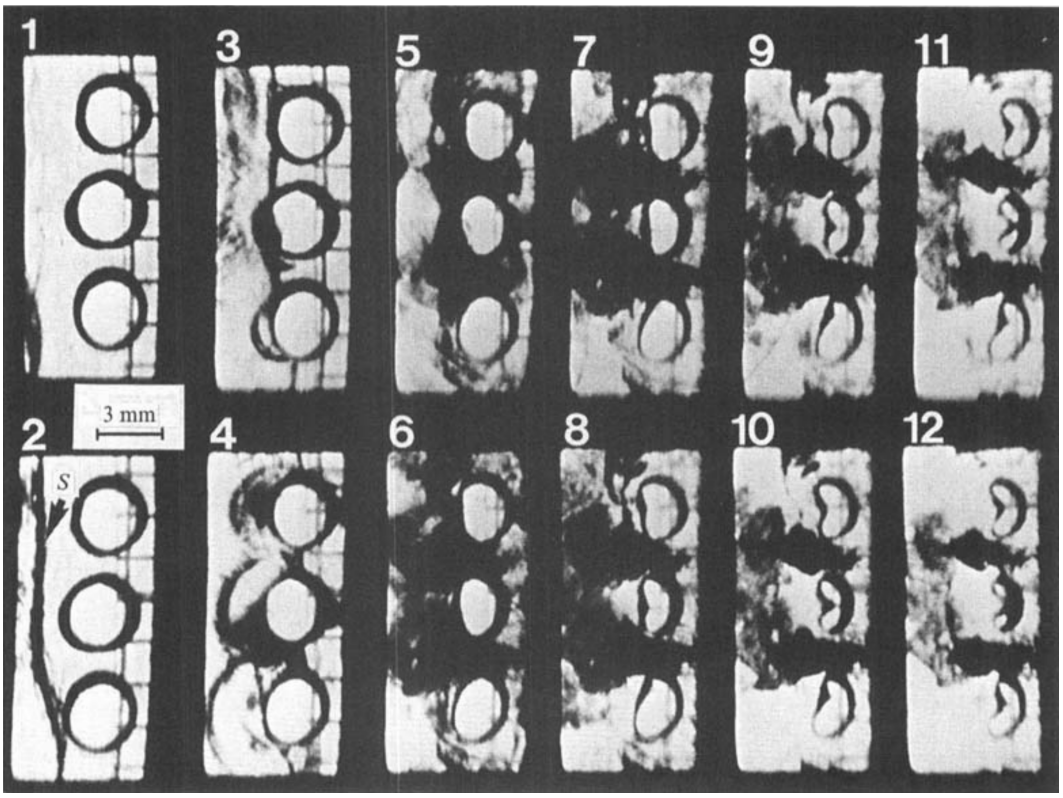

Figure 2.9: Collapse of an array of three cavities in a line parallel to the shock front, taken from Dear and Field.[4] Shock wave propagates from left to right. The jets in the outer cavities can be seen to point away from the centre of the arrangement.

lobes (frame 4 in (a), L in (b) in figure 2.8). The source of light emission was attributed by the authors to hydrodynamic heating in the case of the first light flash, and adiabatic heating in the second.[5]

Of particular interest to the present work, a number of studies have looked at the interaction of shock waves with multiple cavities.[4,7,113,166] Dear and Field[4] looked at a number of arrangements, for example three cavities in a line parallel to the shock front (figure 2.9). As can be seen, in this case it was found that cavitation clouds formed between the cavities, and the jets of the outer cavities diverged from the centre of the arrangement. Dear and Field attributed this to the collapse of the formed cavitation bubbles, which produced shocks that influenced the collapse of the outer cavities through asymmetric shock loading. Bourne and Field[168] suggested that a more likely cause was the influence of the free

surface of the gel close to the outer cavities. Other work[168,169] has suggested that when two cavities are in close proximity, in a line parallel to the shock front, the restriction to the flow between the cavities leads to an imbalance of pressure on the cavities, causing the jets to point inwards towards the centre of the arrangement. This result was also substantiated numerically be Lauer *et al.*[165]. Other arrangements studied by Dear and Field include three cavities perpendicular to the shock front, six cavities in a triangular array, with the apex towards the shock and away from it, and nine cavities in a square. Swantek and Austin[166] looked at two cavities in a line perpendicular to the shock front and four cavities in a diamond array, but at a lower incident shock pressure of approximately 40 MPa. It was found that in multiple cavity arrays upstream cavities can offer significant shielding to downstream cavities and deflect the shock, causing it to strike subsequent cavities asymmetrically. Without a driving shock wave, other studies have looked at the interaction of multiple (spherical) bubbles when cavitated in close proximity, using laser nucleation,[170,171] or spark generation.[172] Whilst no incident shock is involved in these cases, when these bubbles collapse they produce strong shock waves. These shocks can collapse adjacent bubbles, producing characteristic shock-cavity effects such as high-speed jetting.

As the cavities are cut from solid gel sheets, the method as previously outlined permits the testing of cavity geometries less commonly occurring in nature. Bourne and Field[167] studied the interaction of a shock wave with a square, semi-circular, triangular and elliptical cavity. For shock waves striking a flat face, it was found that two jets form at the corners of the cavity, which eventually join to form one central jet. The speed with which these jets join is related to the angles of the corners, with more acute angles leading to slower joining speeds. For an elliptical cavity, it was found that the jet formed continues to travel in the direction of the shock and not in the direction of the longest axis of the cavity.

The collapse of cavities by shock waves in the vicinity of solid particles has also been examined.[5,168] It has been found that the presence of solid particles can offer some shielding to cavities if placed upstream of them, or speed up the collapse if placed downstream as the reflected shocks from the particle strike the leeward cavity wall during collapse. In the case of a cavity and a particle placed side by side, it has been shown that when the two are sufficiently far apart the cavity collapses with a jet directed away from the particle, as the shocks reflected from the particle strike the cavity in addition to the incident shock wave. As the cavity is moved closer however, the impingement of the flow in between the two begins to become the dominant factor, and the jet direction reverts to pointing towards the particle.

Experiments in mediums other than gelatin (or water) have also been conducted, for example using nitro-glycerine in the study of explosive ignition.[7,112] Outside of the pseudo two-dimensional setup, Haas and Sturtevant[173] looked at light and heavy cavities in a gas, using thin plastic membranes and soap bubbles.



CHAPTER 3

NUMERICAL METHODS

The numerical methods used in this thesis to model the collapse of cavities are described. A front-tracking approach is employed, whereby tracked curves are used to model the interface between different media, with Eulerian methods used to model the bulk flow. A key difficulty of this method is in the detection and resolution of tangles in the tracked curves; the methods used to resolve this issue are also outlined. The equations of state used to model the materials employed in this thesis are described.

3.1 INTRODUCTION

In this chapter, the numerical methods used in this work to model cavity collapse will be described. These methods are by no means unique to this work; the front-tracking software as used in this study was developed primarily at The State University of New York at Stony Brook (USA) over a period of decades, under the supervision of James Glimm. The reader is referred to the many papers released by that group for a more comprehensive overview of the method.[174–178] This research was developed into the open source software package *FronTier*, which is available online[179], although the code as used in the present work was significantly altered from this online version. The research presented in this work also utilises the same methods as the work of Hawker and Ventikos[1,2] into shock

driven cavity collapse, a review of which was given in the previous chapter. This work is also an excellent source of additional information on the methods used in this research.

3.2 THE FRONT-TRACKING APPROACH

Numerical simulations in this study are conducted using a 'front-tracking' methodology. Within this method, contact discontinuities between different media are tracked explicitly using Lagrangian hyper-surfaces, referred to as 'fronts'. These fronts are overlaid on an underlying Eulerian mesh, which is used to model the bulk flow[174]. The fronts break the domain up into separate regions, called components, between which no numerical differencing takes place. All propagation of waves between components is handled entirely by the update to the fronts. During the update to the bulk flow, any states required from cells within other components are extrapolated from within the current component.[180] This therefore allows separate components to be modelled with entirely different equations of state, and even different physics, if required. A key additional advantage of this method is the elimination of numerical diffusion of the interface, a significant difficulty in problems of this type. An example schematic of a front-tracking simulation is given in figure 3.1.

Within a single time step, the update to the flow may be broken into two separate steps. Firstly, the points on the fronts are propagated. This is described in detail in section 3.2.1. This completed, the bulk flow is updated, using shock capturing methods[174]; this step is described in section 3.2.2. The equations of motion to be solved are given by Euler's equations[178,181] (3.1),

$$\begin{aligned} \frac{\partial \rho}{\partial t} + \nabla \cdot \left(\rho \boldsymbol{u}\right) &= 0 \\ \frac{\partial \left(\rho \boldsymbol{u}\right)}{\partial t} + \nabla \cdot \left(\rho \boldsymbol{u} \otimes \boldsymbol{u}\right) + \nabla p &= 0 \\ \frac{\partial E}{\partial t} + \nabla \cdot \left[\left(E + p\right) \boldsymbol{u}\right] &= 0 \end{aligned} \tag{3.1}$$

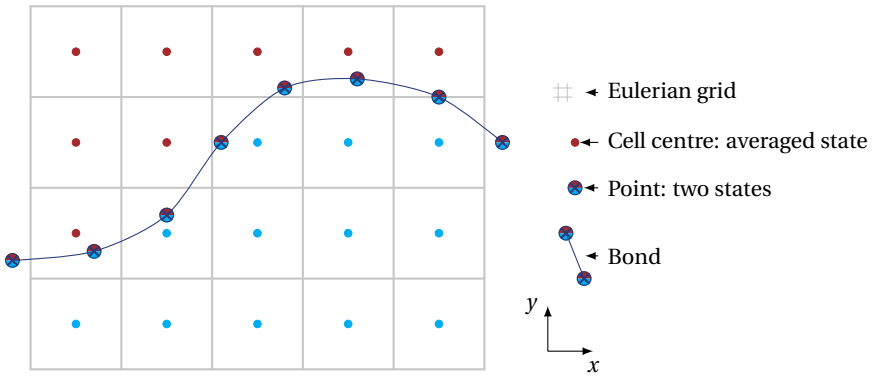

Figure 3.1: Example schematic of a front-tracking simulation in two dimensions. A curve, made up of bonds, is shown dividing two different regions (coloured red and blue). Each point on the curve has two states, describing the flow on either side of the curve.

where ρ is the density, $\boldsymbol{u}$ is the velocity, and p is the thermodynamic pressure. E is the specific total energy, and is related to the specific internal energy (e) as:

$$E = e + \frac{1}{2}\left|\boldsymbol{u}^2\right|. \tag{3.2}$$

This system describes the laws of conservation of mass, momentum and energy, and is closed via an equation of state. With the addition of viscosity and heat conduction, equations 3.1 become the full Navier-Stokes equations.[181] In *FronTier*, if used these terms are accounted for in a separate step, after the update to the bulk flow. This step uses a central difference explicit Euler scheme, with heat conduction modelled using Fourier's law.[182] Surface tension may also be applied in simulations, simply modelled as a pressure jump across the interface, related to the curvature of the front. Curvature is calculated using the method of Jiao,[183] and is an expensive task computationally.

Hawker[2] presented a comprehensive study into the effect of heat conduction, viscosity and surface tension on single cavity collapse, concluding that none of these processes significantly influenced the dynamics of the process. Why this is so can be seen by analysing the conditions at jet impact; at this point the Reynolds number and Weber number of the liquid are approximately 2.5×10^5 and 4×10^5 respectively for a 1 GPa shock

wave striking a cavity.* The problem is thus dominated by inertial forces. Non-Euler terms are therefore not included in simulations conducted in this study.

During simulations, the time step is chosen based on the Courant-Friedrichs-Lewy (CFL) criterion,[184] in one dimension given by equation 3.3,

$$\Delta t \leq c\frac{\Delta x}{u} \tag{3.3}$$

where c is the Courant number, Δx is the cell width and u the velocity. The time step may be set by either the front propagation or the bulk flow hyperbolic solver. A Courant number of 0.75 is used; this value was found to provide the best balance between speed and stability. As described by Hawker[2], the method used to model heat conduction may become unstable for very small grid dimensions. An additional time step restriction is thus implemented when heat conduction is modelled[2], which can be a more severe restriction on time step increments than the CFL criterion under these circumstances.

A significant disadvantage of the front tracking method, similar to other methods of this type, is that movement of the interface can lead to unphysical crossings, or 'tangles', which must be resolved before simulation can continue. This substantially increases the complexity of the problem as it leads to numerous special cases, each of which must be dealt with individually. This is discussed in section 3.2.1.3. As an additional issue, as the front is propagated points on curves can bunch together (increasing computation time), or become overly separated (which breaches the CFL condition, affecting stability). This therefore requires the implementation of redistribution algorithms, described in section 3.2.1.4.

From the base of *FrontTier*, we as a group have made extensive changes to the code to improve its accuracy, functionality and usability, and to reduce errors. A number of

*Based on a liquid density of 968 kg/m^3, jet width of 120 μm, liquid velocity of 2090 ms^{-1}, gas velocity of 1570 ms^{-1}, dynamic viscosity of 1.002×10^{-3} kg/s·m and surface tension 72.75×10^{-3} Nm^{-1}. The gas density is 14 kg/m^3.

the changes made by Hawker to fix errors in the code are outlined in his thesis[2], while improvements made to the user interface of the code are outlined in section 3.4.

Du *et al.*[185] compared front-tracking to a series of other methods for modelling interfaces, building on a similar study by Rider and Kothe[186]. It was found that Front tracking performed at least as well as particle methods, but was better than Volume of Fluid (VOF), level set, or capturing schemes. It was noted that front tracking was also computationally faster than particle methods, as significantly fewer points were required per cell to model the interface.

3.2.1 Front propagation

Within the front-tracking software used in this study, tracked fronts are simply a collection of geometric objects, describing the location of a contact line between different components[175,178]. This collection consists of points in 1D, curves in 2D and surfaces in 3D. The combined collection of fronts is referred to as 'the interface'. A curve is a connected list of 'bonds', where a bond is a piecewise linear connection between adjacent points. A surface is a collection of triangles[177], which are connectors between three adjacent points. The boundaries of curves are a particular type of point called 'nodes', while the boundaries of surfaces are a type of curve called 'node-curves'. Curves only intersect at nodes, while surfaces only intersect at node-curves. Associated with each point on a front are two states, left and right, describing the state of the flow on either side of the point. All points on a front are given the same left-right orientation when the front is created, which is then maintained for the duration of the simulation.

There are three basic steps to the update of the interface in any simulation[178]. Firstly, the positions and states of the points on the fronts are updated. Once completed, any crossings of fronts must be interrogated, and unphysical points removed. The points may also be redistributed in this step. Finally, if this is a parallel simulation a communication

step must be completed, where information is shared with adjacent subdomains.

The first part of this process is the update to the position and states of the points on the interface. This algorithm is performed for every point, every time step. In the implementation used in this work, this is broken into two steps, normal and tangential to the front[187]. The normal update, described in section 3.2.1.1, solves a one-dimensional projection of system (3.1) in the direction normal to each point, and updates the position and states of the points. The tangential update (section 3.2.1.2) then solves the flow equations in the orthogonal direction, using standard shock capturing methods. As two states are associated with each point, the tangential update is performed on both sides of each point. No update to the position of the points is conducted in the tangential update.

It should be noted that this method does not take into account the curvature of the front, or the change in the normal direction over the course of the time step. Both of these effects are incorporated into the solution indirectly through the tangential update, and as the normal direction is recalculated every time step. However, the solver will only be accurate to first order close to the interface.[178] The splitting of the method into a normal and tangential update also introduces a first order error.[178]

3.2.1.1 Normal propagate

Prior to propagation of the points in the normal direction, the normal direction itself must be found for each point. This is currently calculated using the Weighted Least Squares Polynomial Fitting (WLSP) algorithm developed by Jiao.[183] In areas of large curvature the solution to this algorithm may become multi-valued, leading to erroneous results. Under these conditions the algorithm is therefore replaced by a first order approximation. This method simply calculates the normal to the secant joining the two adjacent points.

The normal propagate algorithm solves a Riemann problem in the direction normal to the point at position $\boldsymbol{p}$, at time t. A Riemann problem is defined as an initial value prob-

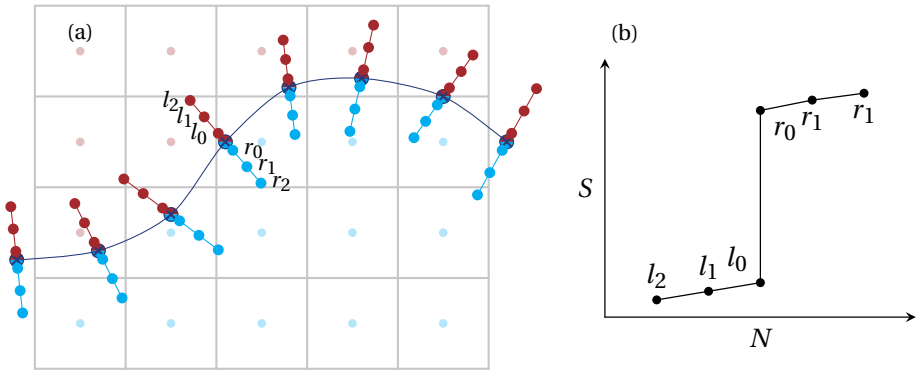

Figure 3.2: Stencils for the normal propagate. (a) shows example normal stencils for a number of points on the interface. (b) shows a monotonic interpretation of the states S interpolated from the underlying grid in the normal direction **N**, for one of these stencils. States l_0 and r_0 are the left and right states associated with the point on the interface. All points on a front have the same left-right orientation.

lem with a single discontinuity, separating two regions of constant state.[178] The required variables to be computed are: the speed of the point in the normal direction u_N, and the states on either side of the front S_{left} and S_{right} at the updated time $t + \Delta t$. To achieve this, the states along a stencil in the normal direction $\boldsymbol{N}$ are first interpolated from the underlying Eulerian grid. States are evaluated at positions $p_i = p \pm i\Delta n\boldsymbol{N}$ for $i = 0, 1, 2$, where $i = 0$ are the vertex states. The spacing Δn is related to the underlying grid by equation 3.4,

$$\Delta n = \left(\sum_{i=1}^{d} \left(\frac{N_i}{\Delta x_i} \right)^2 \right)^{-\frac{1}{2}}, \tag{3.4}$$

where Δx_i is the mesh spacing in the coordinate directions, N_i the components of the normal vector in the coordinate directions and d is the spatial dimension of the flow.[178] This therefore gives a total of 6 points in the stencil, 3 on either side of the point. An example of these stencils calculated for a number of points on the interface is shown in figure 3.2 (a). Based on these interpolated values, the van Leer limiter[188] is used to calculate the slopes on either side of the front, for example:

$$\delta s_r^i = \text{sgn} \min \left(\left| \frac{s_r^{i+1} - s_r^{i-1}}{2} \right|, \left| s_r^{i+1} - s_r^i \right|, \left| s_r^i - s_r^{i-1} \right| \right) \tag{3.5}$$

where δs_r^i is the slope at position i on the right (r) hand side of the front. (sgn) is the

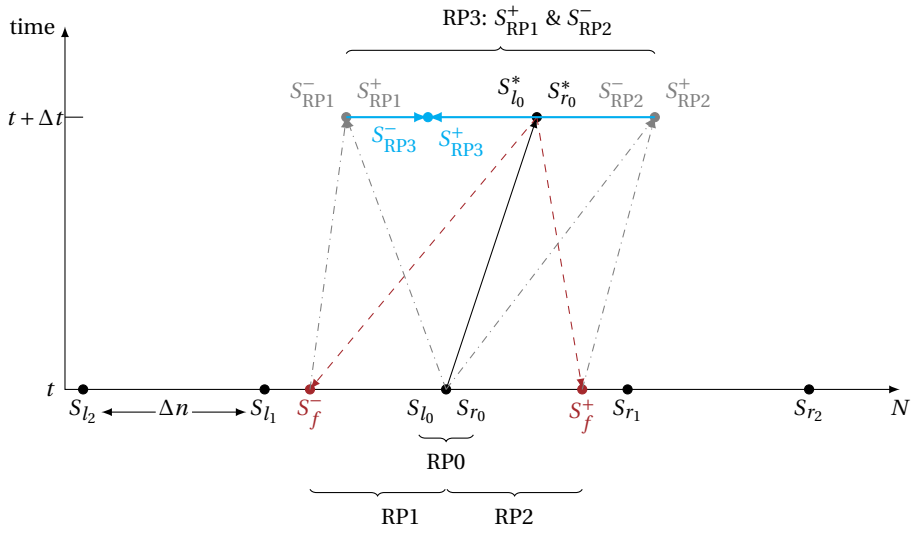

Figure 3.3: Schematic of the algorithm used for the normal propagate, to move a point on the interface at time t to its new position at time $t+\Delta t$. Initial states either side of the interface are S_{l_0} and S_{r_0}. Final states at new time are S^-_{RP3} and S^+_{RP3}.

common sign of the three differences if all agree in sign, zero otherwise[180]. This yields a piecewise linear profile, that is monotonic on either side of the front (figure 3.2 (b)).

The update to the point, based on the monotonic stencil proceeds as in figure 3.3. This is essentially a predictor-corrector type algorithm, and is nominally second order. Firstly, a Riemann problem is solved (RP0), just using the states on the front S_{l_0} and S_{r_0}. This yields the characteristic speed of the contact u^*_{RP0}, and midstates $S^*_{l_0}$ and $S^*_{r_0}$. From these states, the limits of the region along the stencil that would affect the new point over the change in time step are found, using the method of characteristics at time $t+\Delta t$. Using this method, the midstates computed from the Riemann problem solution are used to approximate the characteristic slopes. Where these slopes cross the stencil at time t, the values are interpolated from the stencil to give two new states, S^-_f and S^+_f. This process is represented by the red dashed lines in figure 3.3. States S^-_f and S_{l_0} are then used as the input to a new Riemann problem (RP1), yielding new states S^-_{RP1} and S^+_{RP1}. Similarly, states S_{r_0} and S^+_f are used to produce new states S^-_{RP2} and S^+_{RP2}. These two Riemann problems are represented by the grey dot-dashed lines in figure 3.3. Finally, states S^+_{RP1} and S^-_{RP2} are

used as the input to a final Riemann problem, to yield the final states S^{-}_{RP3} and S^{+}_{RP3}, and velocity u^{*}_{RP3}. This is represented by the thick blue lines in figure 3.3. The final velocity is then given by $u_N = \left(u^{*}_{\mathrm{RP1}} + u^{*}_{\mathrm{RP3}}\right)/2$. The updated position of the point can be calculated as equation 3.6[178,180].

$$\boldsymbol{p}_{(t+\Delta t)} = \boldsymbol{p}_t + u_N \boldsymbol{N} \Delta t \tag{3.6}$$

3.2.1.2 Tangential propagate

The tangential propagate operates on the states produced by the normal propagate, in order to account for the movement of waves along the interface. This is done by solving a tangential projection of system (3.1), on either side of the front using standard shock capturing schemes[178]. Further details of these schemes are given in section 3.2.2. Stencils for each calculation are only populated from one component, with the spacing Δs between points calculated as equation 3.7,

$$\Delta s = \left(\sum_{i=1}^{d} \left(\frac{T_i}{\Delta x_i} \right)^2 \right)^{-\frac{1}{2}}, \tag{3.7}$$

where T_i is the component of the tangential vector in the coordinate directions. In 3D, the tangent to a point is a plane, and two tangential update steps must be performed on either side of the point, in orthogonal directions. In this case, the first vector is chosen to be the direction of the velocity shear across the interface, which must always be tangential to the interface.

In 2D simulations, the update is performed using the Monotonic Upstream-centered Scheme for Conservation Laws (MUSCL)[188], as on the underlying grid. For axisymmetric and 3D simulations the simpler Godunov scheme is used to improve the stability of the simulation (see section 3.2.2 for further details).

3.2.1.3 Untangling

One of the challenges of front-tracking as an approach is that the interface may become tangled as it propagates. These tangles correspond to the pinch-off or merger of separate sections of fluid. Without explicit handling, this will lead to non-physical volumes in the solution. These intersections must therefore be identified and rectified each time step. In *FronTier*, two different algorithms are implemented, grid-free and grid-based untangling. In both cases, the untangle step is performed after the update to the position of the points on the interface, but before the update to the states on the underlying grid. This is because it is essential that the position of the interface is fully resolved prior to the update to the interior states [189].

Grid-free untangling was first described in detail by Glimm *et al.* [189], and is the method used in this thesis in 2D and axisymmetric simulations. In this method, a number of assumptions are made on which the algorithm is based. Firstly, it is assumed that each point on a curve has crossed another curve at most once over the course of the time step. To ensure this is true, when a tangle is detected the entire time step is completely repeated with progressively smaller time increments, until only one point on the front has crossed another front over the course of the time step. Additional assumptions are (i) that each unphysical component has at least one cross point on its boundary, excluding the possibility that a front completely reverses itself, (ii) that tangled fronts actually cross, and not just intersect, and (iii) that nodes do not overlap over the course of the time step. This last condition is handled in a separate algorithm. Based on these conditions, the first step in the algorithm is to detect crossing points on fronts. To achieve this, a list of the bonds on the interface is created, and intersections are checked for within each grid cell on the underlying mesh. New points are then inserted at these cross-points, with states found by interpolation from the joining fronts. Inspecting the component regions that bound each new point, the unphysical component is then identified and deleted.

In the grid-based scheme[180,190], the vertices of the grid cells on the underlying mesh are labelled with the component that they belong to. Additionally, the edge of each cell where a front crosses is recorded, along with the component information relating to that front. Based on this information, components are checked for consistency within each cell, and unphysical sections removed. The entire interface can then be discarded, and rebuilt based on the stored information. This method is simpler and more robust, and is thus used for three-dimensional simulations. However, as noted by Du[185], the replacement of the interface within a cell by a linear segment leads to errors of order $O(\Delta x^2)$ in the position of the front.

3.2.1.4 Redistribution

As the points on the interface are propagated, over time points will begin to diverge or converge. This inevitably leads to a poorer representation. To rectify this, points on the interface are periodically redistributed along the interface. To achieve this in 2D[178,185], starting from a node, new points are added along each curve at an equal distance, set to 75% of the computational mesh size in this work. The mesh size is calculated using equation 3.7, with the tangent direction evolving along the curve. The old points may then be deleted. As this process tends to smooth out sharp perturbations on the interface, in this work it is only performed every five time steps.

In three dimensions, redistribution is considerably more complicated. In this case, local operations are performed on the triangular elements, merging small triangles and splitting larger ones. Triangles with poor aspect ratios are also adjusted[178].

3.2.1.5 Parallel communication of the interface

In order to reduce computation time, simulation domains in this work are divided into a series of parallel subdomains, with a maximum of 200,000 cells present within each sub-

domain. Parallel communication in *FronTier* is handled using the Message Passing Interface (MPI) standard. At the start of each time step, at the edges of subdomains ghost cell regions of width 4 grid cells are created from information from adjacent subdomains. This enables each subdomain to complete the time step without the need for information from adjacent subdomains. At the end of each time step, the last step in the propagation of the interface is therefore the synchronisation of the subdomains with their neighbouring regions. This is achieved by clipping the interface to remove the ghost cell regions, before joining the interface across adjacent subdomains. New ghost cell regions may then be recreated from the joined interfaces[178].

3.2.2 Hyperbolic solvers

Once the positions and states of the fronts have been found, the next step in the time step update is the coupling of the grid with the interface[178]. This step is needed because the algorithm for the propagation of the interface requires the interpolation of states from the grid at arbitrary locations. In 2D, a list is created of the crossings of the interface with the dual mesh, created by the joining of the centres of grid cells. While this is a comparatively simple process, it adds significantly to the computational run time of simulations[178]. Based on this list of crossings, the dual grid and the points on the front, a triangulated grid is created, whereby triangles are used near to the interface, and rectangles are used away from the interface. Triangles do not cross the interface. Based on this grid, linear interpolation can be used in triangular cells, and bilinear in rectangular cells. In 3D, the creation of this grid is computationally too expensive, and thus cells are created on a need to use basis[178].

After the creation of the triangular grid, the states on the Eulerian grid can be updated using shock-capturing methods. This is achieved using the MUSCL solver[188], with an additional slope limiter as described by Colella[191]. The MUSCL solver is a Godunov-type

scheme, whereby a Riemann problem is solved at each inter-cell boundary. The solution of each Riemann problem constructs a flux across the inter-cell boundary; these fluxes are then differenced in each spatial direction within each cell to update the cell states, and the solution is advanced in time. While the original work by Godunov[192] assumed the state data to be piecewise constant within each cell, the MUSCL solver reconstructs the state data as piecewise linear within each cell, while preserving monotonicity (see equation 3.5). This improves the method to second order spatial accuracy. The original implementation by van Leer[188] performed the calculation in Lagrangian coordinates, before remapping the result onto the Eulerian grid. The method as proposed by Colella[191], and utilised in this work, is a purely Eulerian implementation of this method.

In this work an exact Riemann solver is used to calculate the fluxes through each cell. With this implementation, shock waves are captured to first order accuracy, with shocks distributed over approximately two grid cells. The update is performed in one-dimensional sweeps, with the order of the sweeps alternated every time step to provide higher order accuracy[193,194]. In each directional sweep, the update is broken down into two steps, to improve efficiency. The first step updates all cells, ignoring the interfaces. In the second step, states are then recomputed for cells whose domain of dependence overlaps the interface. No interpolation is performed across the front, and missing points are filled in as ghost cells extrapolated from the correct component.

Once the cell states have been updated within each subdomain, the final step in the process is the communication of this information with adjacent subdomains in parallel simulations. This process is completed in a similar fashion to that described in section 3.2.1.5.

3.3 EQUATIONS OF STATE

In order to close system 3.1, and to provide a relationship between different thermodynamic properties an equation of state (EOS) is required for each material in a simulation. In this study, comparatively simple equations of state are used. Only three materials are modelled: air, water and the hydrogel used in the experiments.

3.3.1 Air

Air in this study is modelled using the ideal gas equation of state:

$$p = \rho R_{\text{specific}} T. \tag{3.8}$$

where ρ is the density, p is the pressure and T is the temperature. A value of $R_{\text{specific}} = 287.058\,\text{J}\,\text{kg}^{-1}\text{K}^{-1}$ is used ($\gamma = 1.4$). This equation is accurate under moderate conditions, but as pressures and temperatures are increased this accuracy diminishes. This is partially because more complex effects such as dissociation and ionisation are not accounted for. As these processes absorb energy, predicted temperatures will therefore be overestimates and only semi-quantitative. However, as explained by Ball[3] and studied by Tully[195], the overall hydrodynamics are dominated by the equation of state for the liquid, and general trends will thus be modelled accurately using the ideal gas EOS.

3.3.2 Water

The modelling of water has generally been conducted using either the Tait[3,124,148,150] or the stiffened polytropic equation of state[1,157,196]. The Tait equation[197] approximates water as:

$$p = B\left[\left(\frac{\rho}{\rho_R}\right)^{\gamma} - 1\right] \tag{3.9}$$

where p is the pressure, ρ_R is a reference density at which the pressure falls to zero, and B and γ are constants. In the work of Ball[3], $B = 3.31 \times 10^8\,\text{Pa}$ and $\gamma = 7$. Note it is not pos-

p_∞ (Pa)	Γ	$R\left(\mathrm{J kg^{-1} K^{-1}}\right)$	e_t	$E_\infty\left(\mathrm{J kg^{-1}}\right)$
6×10^8	3.4	1700	-1.8×10^{-6}	7.456×10^6

Table 3.1: Fitted parameters for water in the stiffened polytropic equation of state, as used by Hawker[1,2]

sible to calculate temperature using this equation, and thus it cannot be used for front-tracking.

The stiffened polytropic equation[198] is given by equation 3.10:

$$\begin{aligned} p + (\Gamma+1)\, p_\infty &= \Gamma\rho\,(e + E_\infty) \\ RT &= \frac{p+p_\infty}{\rho} + \Gamma e_t \rho^\Gamma \end{aligned} \tag{3.10}$$

where p is the pressure, T is the temperature, ρ is the density, e is the specific internal energy, p_∞ is the stiff pressure constant, $\Gamma = \gamma - 1$ is the Grüneisen exponent where γ is the ratio of specific heats, R is the gas constant, e_t is the thermal energy factor and E_∞ is the energy translation factor. In the work of Hawker[1], the terms in these equations were fitted to the experimental data of Nagayama[199] and to IAPWS-95[200], such as to match water as closely as possible. The parameter E_∞ was fitted such that the internal energy was zero at the triple point. These fitting parameters are given in table 3.1. The simulations presented in chapter 4 of this thesis use the stiffened polytropic equation of state, with these parameters.

Figure 3.4 compares the two equations of state to the experimental results of Nagayama[199]. Also shown is the Los Alamos shock Hugoniot data[201], which covers a higher intensity parameter space. As can be seen, while both the Tait equation and the stiffened polytropic equation show good agreement to the data up to approximately 5 GPa, beyond this point the stiffened polytropic equation drops away from the curve significantly. The Tait equation maintains good affinity to the data up to approximately 20 GPa, but then gradually deviates. Clearly the stiffened polytropic EOS as used in this study becomes

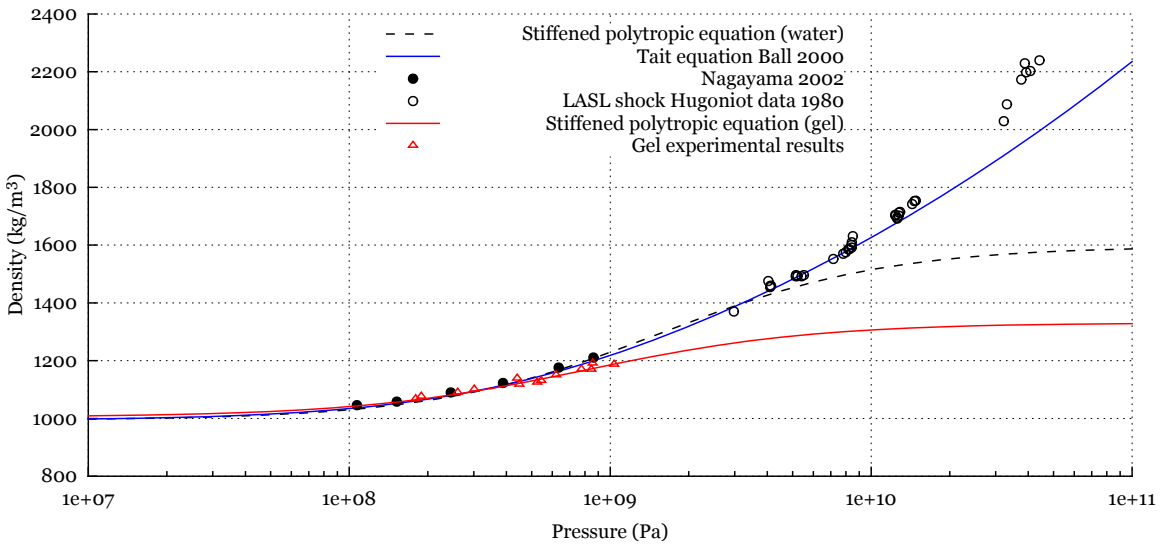

Figure 3.4: Comparison between the Tait[3] and stiffened polytropic EOS, and experimental shock Hugoniot data for water[199,201]. Also shown are our own experimental results, measured in gellan gum, and the stiffened polytropic EOS fitted to that data[202].

progressively less suitable at high pressures. However, it is beyond the scope of this study to fully investigate the effect of this on the presented results.

3.3.3 Hydrogel

As described in detail in chapter 5, experimental results in this work are not conducted in water, but in a viscoelastic hydrogel,[†] that acts in a manner very similar to water when shocked. A full description of this hydrogel is given in section 5.4. To improve the accuracy of simulations when matching to experimental results, the parameters of the stiffened polytropic EOS outlined in section 3.3.2 have been fitted to experimental shock data in this material, using a least squares approach[202]. The experimental results and fitted principal Hugoniot are shown in red in figure 3.4, and the matched parameters are given in table 3.2. It should be noted that whilst in figure 3.4 these parameters appear to give a less representative curve, these parameters give a much closer match when comparing other Hugoniot parameters, for example shock velocity and density.

[†]Gellan Gum (Sigma Aldrich, Phyta Gel^{TM})

p_∞ (Pa)	Γ	$R\left(\mathrm{Jkg^{-1}K^{-1}}\right)$	e_t	$E_\infty\left(\mathrm{Jkg^{-1}}\right)$
3.48×10^8	6.17	1159	0	-3.46×10^5

Table 3.2: Fitted parameters for the hydrogel in the stiffened polytropic equation of state.

3.4 IMPROVEMENTS TO THE USER INTERFACE

One of the key bodies of work conducted at the beginning of this project was the development of a more advanced user interface (UI) for *FronTier*. This software is extremely powerful for the study of shock-cavity interactions, and applicable to the study of a wide variety of other phenomena. However, the UI for the code consists of a simple text file, into which specific commands may be inserted. The number of problem types available to the user is comparatively limited, with any modification to this requiring complex additions to the underlying C code. This made the modelling of anything other that the most simple of geometries prohibitively difficult.

To address this issue, an additional feature in *FronTier* has been utilised, whereby simulations that crash may be restarted from 'restart files' periodically saved out by the code. These files contain a full set of information on the location and states of the fronts, as well as the states on the underlying grid. Reverse-engineering these files, it is thus possible to create and run simulations, without using the conventional input scripts to the code. This provides a comparatively simple way to improve the functionality of the code, without making wholesale changes to the complex and inextensible code itself. A flow diagram illustrating how the new user interface interacts with the code is shown in figure 3.5. Input files are now replaced by Python input scripts, which interact with an extensive Python library that builds the restart files and other inputs required to run simulations. By using Python scripts the running of large arrays of simulations, for example for the running of large parametric studies, is trivialised. To reduce the complexity of building full simulations within individual input files, a library of commonly used problem types

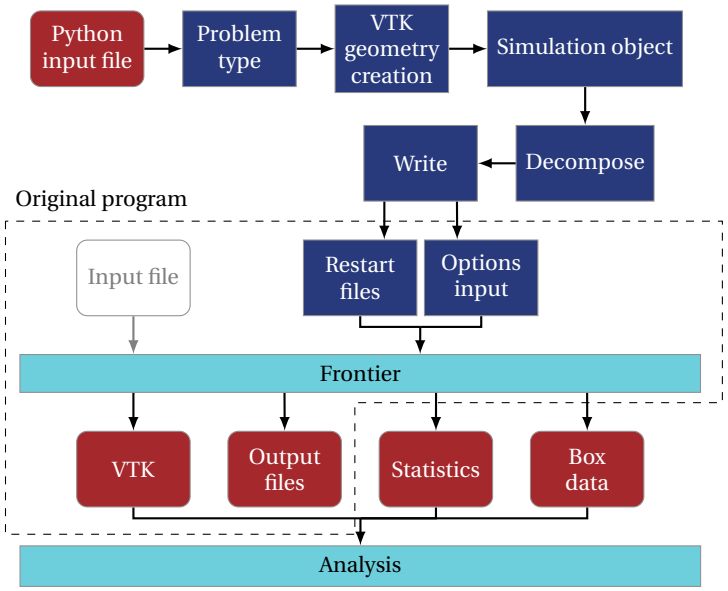

Figure 3.5: Flow diagram of the user interface. By utilising the 'restart' facility of *FronTier*, the basic input files can be replaced by a much more powerful python interface, without a need to make significant modifications to the underlying code.

is maintained. Additions to this library are simple to add. Once the required components and curve locations have been specified by the Python input files and problem types, a geometry library built around the Visualization ToolKit (VTK) libraries is used to calculate the required states at curve points and grid locations. This fully specifies a simulation, which can then be decomposed into individual subdomains for parallel simulations, and written to file.

Through this improved user interface, a number of previously unmodellable problems have now been successfully studied. Examples include the implementation of complex shock profiles, for example taken from experimental results, and the study of cavities attached to walls.

3.5 POST PROCESSING METHODS

In addition to the user interface as outlined in section 3.4, an extensive post processing library has been built for the analysis of simulated results. With modifications made to the

C code, it is now possible to record statistics over the course of simulations, for example the variation in peak pressures or temperatures in specific components over time. One important addition is the implementation of 'boxes' in the domain, in which the average conditions are monitored. These boxes may be placed anywhere in the domain, and can be of any size. By monitoring the conditions in the cavity, and in a box immediately downstream of the cavity, this method allows accurate calculation of cavity collapse times and water hammer shock pressures.

The main data files produced by *FronTier* are VTK files, detailing the hydrodynamic states within each cell and the location of the interface, for each time step. The analysis of these files, and the creation of the image sets presented in this work from them is done using the VisIt visualisation tool.[203]



CHAPTER 4

NUMERICAL MODELLING OF MULTI-CAVITY COLLAPSE

In this chapter, the shock-driven collapse of multiple-cavity arrays is explored. An array of two cavities, one placed behind the other in relation to the incident shock is studied in detail. While the first cavity collapses in the same way as a single cavity, the collapse of the second is found to be driven primarily by the water hammer shock from the first cavity. This process is dependent on the separation distance between the cavities, with the shape and speed of the main transverse jet changing substantially with separation distance. The effect of the relative size of the two cavities is also explored, revealing additional complex effects, such as the entrainment of one cavity into the jet of another. Through a triangular array of three cavities, peak pressures almost 40 times higher than the incident shock pressure are seen.

4.1 INTRODUCTION

This chapter presents a computational study of the interaction of shock waves with multiple cavity arrays. This work is taken directly from a recently published paper, 'Computational modelling of the interaction of shock waves with multiple gas-filled bubbles in a liquid', by myself, B. Tully, N. Hawker and Y. Ventikos[204] (Copyright: 2015, AIP Publishing). Additionally, many of the ideas presented in this chapter are the subject of a recently filed patent[205]. As discussed in section 2.4, there has been very little research on multi-cavity

effects in shock cavity interactions, despite the substantial influence that inter-cavity effects have on any real-world applications involving this process. In this chapter, these multi-cavity effects are studied in detail, for a number of specific cases. Complex inter-cavity effects are revealed, with particular arrangements demonstrating a greater level of energy focusing than hitherto seen in shock cavity interaction studies.

The numerical methods used in this chapter are as outlined in chapter 3, with the gas inside the cavities modelled as air, using the ideal gas EOS (section 3.3.1). The liquid is modelled as water, using the stiffened polytropic equation of state (section 3.3.2). Terms used to describe processes are as outlined in section 2.4.3.

All arrangements presented in this chapter are modelled in 2D, with a reflecting boundary on the axis of symmetry used to model half the domain, with the exception of those in sections 4.2.2.2 and 4.3.3. As many previous experiments[4,166,167] conducted on this subject have used a two-dimensional technique, this allows direct comparison with previous experimental results. The use of a reflecting boundary reduces computational cost. To enable direct comparison to previous numerical studies, the incident shock is modelled as an infinite step shock of pressure 1 GPa in all cases, giving a density behind the shock of 1222.9 kg/m^3. The downstream fluid is initialised at standard temperature and pressure, with a density of 993.9 kg/m^3. The initial density of the gas is 1.184 kg/m^3. All times given are relative to the time of first impact of the incident shock wave on the closest of the cavities.

4.2 GRID INDEPENDENCE AND VALIDATION

4.2.1 Grid independence

Prior to conducting a full numerical study of multi-cavity shock wave interactions, a thorough study of the effect of spatial resolution was conducted to ensure that grid indepen-

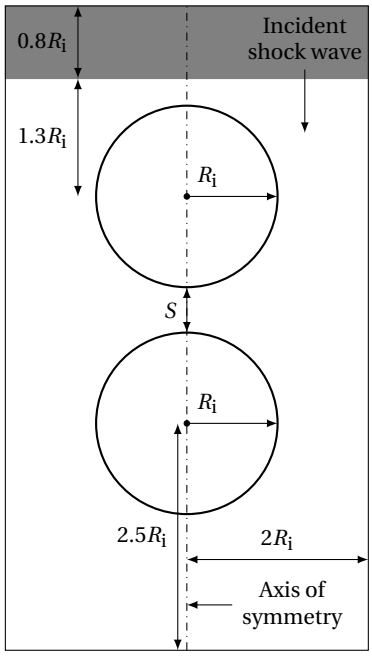

Figure 4.1: Diagram for the simulation of two cavities in a line orientated parallel to the direction of incident shock propagation.

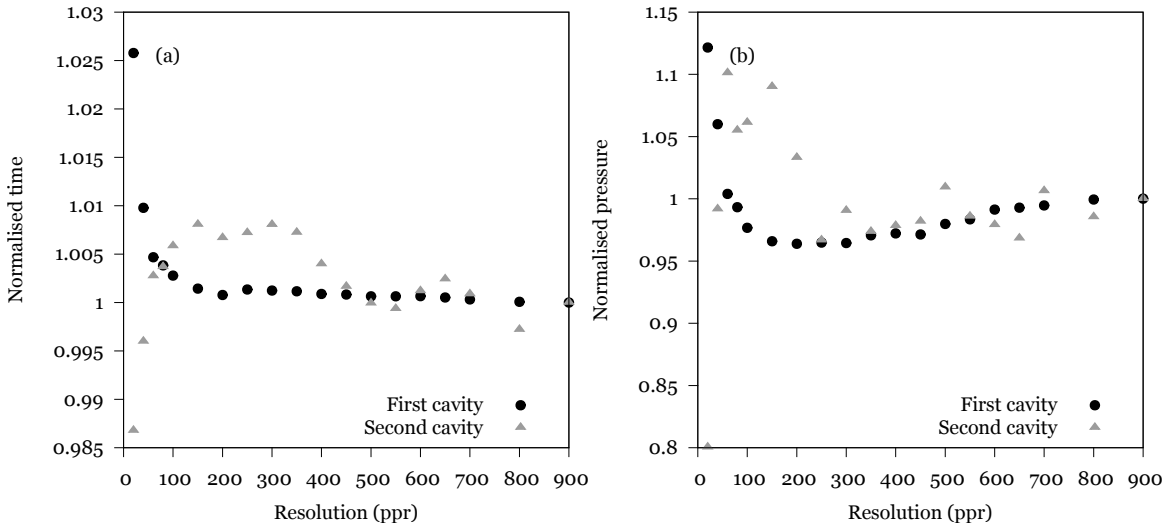

Figure 4.2: The effect of grid resolution. (a) First phase collapse time. (b) Water hammer shock pressure. Values are normalised by the value at 900 ppr.

dence was achieved. The test case used is shown in figure 4.1, and consists of two cavities of initial radius $R_i = 0.5$ mm separated by a distance S, placed in a line perpendicular to the front of a shock wave of amplitude 1 GPa. An in depth study of this arrangement is given in section 4.3. The relative separation distance between the cavities S/R_i was cho-

sen to be 0.5. Resolutions tested varied from 20 cells per linear cavity radius, or points per cavity radius (ppr), to 900 ppr.

To quantify the level of grid independence achieved two metrics are presented: the variation in first phase collapse time of the two cavities (figure 4.2 (a)), and the effect of resolution on the water hammer shock pressures following jet impact (figure 4.2 (b)). In both cases, the values presented have been normalised by the value at 900 ppr to aid comparison. The first phase collapse time is defined as the time between the impact of the incident shock on the cavity, and the impact of the ensuing jet on the leeward cavity wall. As can be seen, whilst there is evidently more scatter in the values for the second cavity, this metric is easily resolved for both cavities, a resolution of 100 ppr being sufficient to match the timings at 900 ppr to within 1 %. More variation is evident in the case of the water hammer shock pressures. This is particularly the case in the second cavity values, where oscillations in the solution suggest the result may not be fully converged at 900 ppr, although the variation is small at high resolutions. Compared to the values at 900 ppr, at 400 ppr first phase collapse times are both within 0.4%, while water hammer shock pressures are within 3%. These values were deemed sufficiently accurate, and this resolution is thus used for the following results presented. At this resolution simulations take approximately 24 hours to run, split across 18 processors.

4.2.2 Validation

4.2.2.1 Comparison with previous experimental results

For the single cavity case, the quantitative comparison of the method used in this study to previous experimental and numerical results was conducted by Hawker and Ventikos[1], with good agreement for metrics such as cavity collapse time and jet velocity shown. For further validation, comparison is made to the work of Dear and Field[4], which was briefly discussed in section 2.4.5. This study looked at arrays of cylindrical cavities trapped be-

tween two glass plates. Figure 4.3 compares select images from the collapse of a triangular array of cavities by a 0.26 GPa shock wave, visualised experimentally by Dear and Field[4] and modelled numerically in this study. As can be seen, despite this being a highly complex problem with many competing factors, there are substantial similarities between the two. In this arrangement, due to the presence of the leading cavity the second level of cavities are partially protected from the incident shock. As a result, the cavities are affected more strongly by the shock away from the axis of symmetry of the arrangement, and the resultant jets point in towards the centre of the arrangement. When the leading cavity collapses, the resultant water hammer shock also strikes these cavities, leading to the formation of a second jet in both cavities. Comparing the images (a) in figure 4.3, which show the collapse after the water hammer shock has struck the cavities, these effects can clearly be seen.

Images (b) in figure 4.3 show the collapse at a further advanced state. In the numerical study, it can be seen that the combination of water hammer shock impact and asymmetrical incident shock impact in the second layer of cavities leads to the formation of very narrow jets that strike the back wall of the second layer cavities. Although image (b.1) is inconclusive regarding the details of the collapse, the outline of the cavities shows significant similarities to the numerical study. Also of note is the asymmetrical jet formation in the outside cavities in the third layer, which can also be seen in both the numerical and the experimental study.

In addition to these similarities, there are some differences between the numerical and experimental studies. Of particular note is that the speed of collapse predicted by the numerical study is substantially faster than in the experiment. For example, the time difference between images (a.1) and (b.1) in figure 4.3 is 8.5 μs, compared to a time difference of 1.04 μs between (a.2) and (b.2). There are a number of possible reasons for this discrepancy. While the numerical study models the shock wave pressure profile as con-

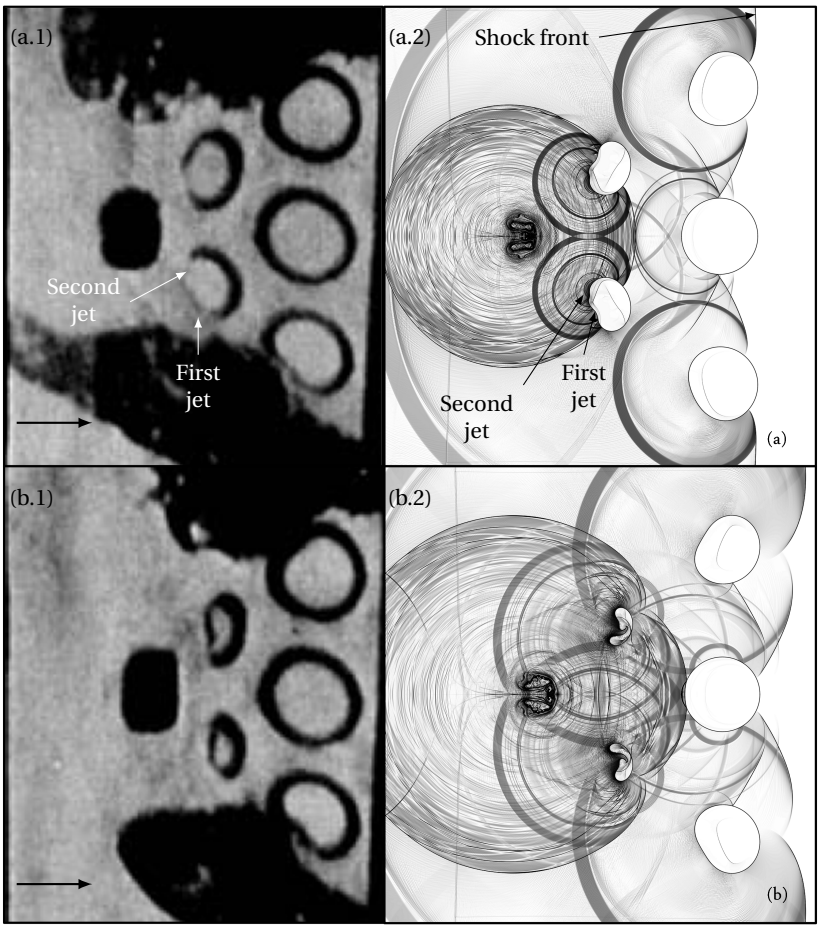

Figure 4.3: Collapse of a triangular array of cavities by an incident shock wave: experimental results (a.1, b.1) and the present study (a.2, b.2), shown using numerical Schlieren, where $n_s = \left|\nabla(\rho)\right|$. Black arrows show the direction of incident shock propagation. Experimental image (b.1) 8.5 µs after (a.1), numerical image (b.2) 1.04 µs after (a.2). Experimental result taken from Dear and Field[4].

stant, the profile of the experimental shock wave is unknown, with pressures behind the shock front likely to vary considerably over time. Additionally, the experimental shock wave is propagating through a narrow channel between glass blocks (for a similar setup, see figure 2.7 (b)). This is likely to have a substantial influence on the propagation of the shock waves.

Another factor of note, that could lead to a much slower collapse, is the presence of free surfaces close to the cavity array in the Dear and Field experiment. As discussed in section 2.4.5, this effect is illustrated more clearly in another case studied by Dear and

Field[4], that of a 0.26 GPa shock wave striking three cavities in a line parallel to the shock front (figure 2.9). In our own analysis of this arrangement, on impact of the incident shock on the cavities, reflected rarefactions form in the liquid, which overlap and strike the other cavities. This has the effect of slowing the collapse of the inner lobes in the outer cavities. As a result, on impact of the main transverse jets on the leeward cavity walls, the inner lobes of the outer cavities are substantially larger than the outer lobes. This is clearly evident in figure 4.4, which compares the study of the same problem by Lauer *et al.*[165] to our own analysis. As can be seen, the two studies are very similar. By contrast, in the Dear and Field[4] study the inner lobes of the outer cavities were found to collapse *faster* than the outer lobes. This was originally attributed to the collapse of cavitation bubbles between the cavities, although Bourne and Field[168] suggested that a more likely cause was the influence of the free surface of the gel close to the outer cavities. This theory was further justified by Lauer *et al.*[165], who by adding free surfaces to the simulation showed that the rarefactions produced by the interaction of the incident shock with the free surfaces slowed the collapse of the outer cavities, to such an extent that the outer lobes collapsed more slowly than the inner lobes, with the collapse taking approximately 4.0 µs (80%) longer. In the presence of free surfaces, we also observe a reversal in relative lobe size at jet impact in the outer cavities (not shown).

Given the presence of this effect in other arrangements in Dear and Field[4], it is likely that it is also present in the triangular array of cavities shown in figure 4.3. This would lead to a substantial reduction in collapse velocity, possibly helping to explain the difference in inter frame time between simulation and experiment. The rarefactions caused by the presence of the free surfaces may also be the cause of the large dark regions present at the edges of the cavity array in figure 4.3, which could be clouds of cavitation bubbles.

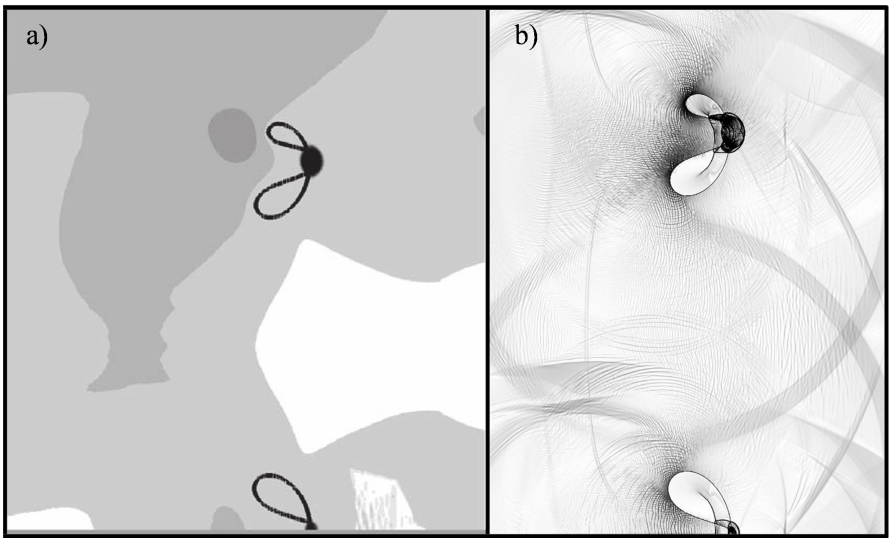

Figure 4.4: Array of three cavities in a line parallel to a 0.26 GPa shock, 4.5 µs after shock impact. Reflected portion of domain not shown. Image (a) shows the numerical result of Lauer *et al.*[165], image (b) the present study.

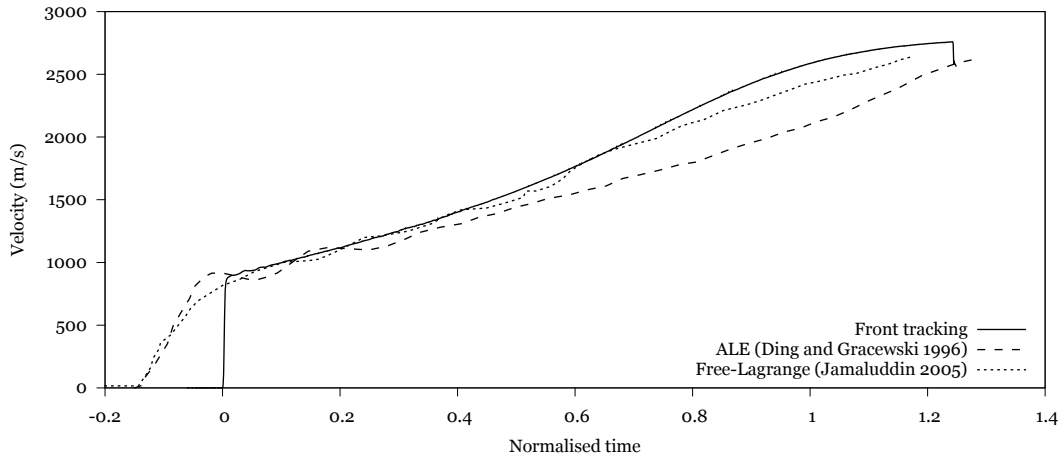

Figure 4.5: Jet velocity vs time for a 1 GPa incident shock wave striking a spherical cavity, simulated using axisymmetric coordinates. Comparison between the front tracking result and other studies.[146,149] The lines have been shifted horizontally to align them in time. Times normalised as $t_{\text{norm}} = \frac{t v_s}{2R_i}$ to allow direct comparison between result sets.

4.2.2.2 Comparison with previous numerical studies

As part of a wider study, Ding and Gracewski[146] analysed the variation in jet velocity with time for the interaction of a shock wave with a spherical cavity, for a number of cavity radii and shock pressures, using an axisymmetric setup. This work was subsequently repeated by Jamaluddin[149], using the Free-Lagrange-Method (FLM). For further validation,

comparison is made here between our results and those of Ding and Gracewski[146] and Jamaluddin[149], for the specific case of the collapse of a 1.0 mm radius spherical cavity struck by a 1.011 GPa incident shock wave. Our comparative simulation models a 0.5 mm radius cavity struck by a 1.0 GPa incident shock wave, also using an axisymmetric setup. As shown by Ding and Gracewski[146], jet velocities reached during collapse are independent of the size of the cavities. Timings may thus be compared across different radii by using a normalised time $t_{\text{norm}} = \frac{t v_s}{2R_i}$, where t is the time, v_s is the incident shock velocity and R_i is the initial radius of the cavity. Although the incident shock pressures are very similar for the different result sets, as different equations of state are used for the different methods the shock velocities will differ. These values have therefore been inferred from Hugoniot equations, and the conditions as published in these papers.

Figure 4.5 shows how the velocity of the tip of the jet changes during the first phase of the collapse process for each of the different simulations. In order to allow easier comparison between the different results, the lines have been shifted horizontally to align them in time. As can be seen, the front tracking solution correctly predicts a sharp increase in velocity at the point of shock impact on the cavity, consistent with the solution of the Riemann problem at this point to within 3%. By comparison, the other solutions predict a much more gradual increase. However, beyond this point the jet is predicted to accelerate in a similar manner by all three methods. There is particularly close agreement between the front-tracking and FLM simulations. Jamaluddin notes in his work that the roughness present in the FLM curve is due to artifacts introduced by the refinement and de-refinement algorithms used in his code.

4.3 TWO CAVITIES

As a natural extension of the collapse of a single cavity as modelled by Hawker and Ventikos[1], the first multi-cavity case explored is that of two cavities, with the second placed

directly behind the first at a separation distance S (see figure 4.1). Of particular interest in this study was the interdependence of the cavities, and whether the stacking of cavities relative to the incident shock could be used to intensify collapse, as predicted by Lauer[165]. In the particular case modelled, the relative separation distance $S/R_i = 0.5$. The initial radius R_i has been set to 0.5 mm.

In order to elucidate the flow in both the liquid and the gas regions, in each frame two images are shown. The first shows the data in just the gas regions of the simulation. This in turn is displayed using two methods, with the left-hand-side of the image being a plot of the magnitude of the gradient of the density ($|\nabla\rho|$), giving a numerically generated Schlieren image, and the right-hand-side being a plot of the pressure. This arrangement is repeated in the second image, which shows the data for the liquid regions of the simulation.

4.3.1 Analysis of the collapse

On contact of the incident shock on the first cavity, collapse proceeds in an identical manner to that of a single cavity, as detailed in section 2.4.3. As suggested by Lauer *et al.*[165], the collapse of the second cavity follows the same process as that of the first, driven instead by the water hammer shock from the first cavity. In the Lauer study, the collapse of the second cavity was observed to be more intense than that of the first, leading to higher peak pressures during collapse. While these observations are also seen in the present study, substantial additional complexity in the collapse of the second cavity is observed. This is evident in figures 4.6 to 4.8, which follow the collapse of the second cavity.

The first cavity water hammer shock has an average magnitude of 3 GPa on formation (approx. 10 GPa peak) and may be viewed as a shock wave emanating from a point source directly below the first cavity. Although this shock weakens as it spreads, on impact on the second cavity a main transverse jet is formed in the cavity with a significantly flatter

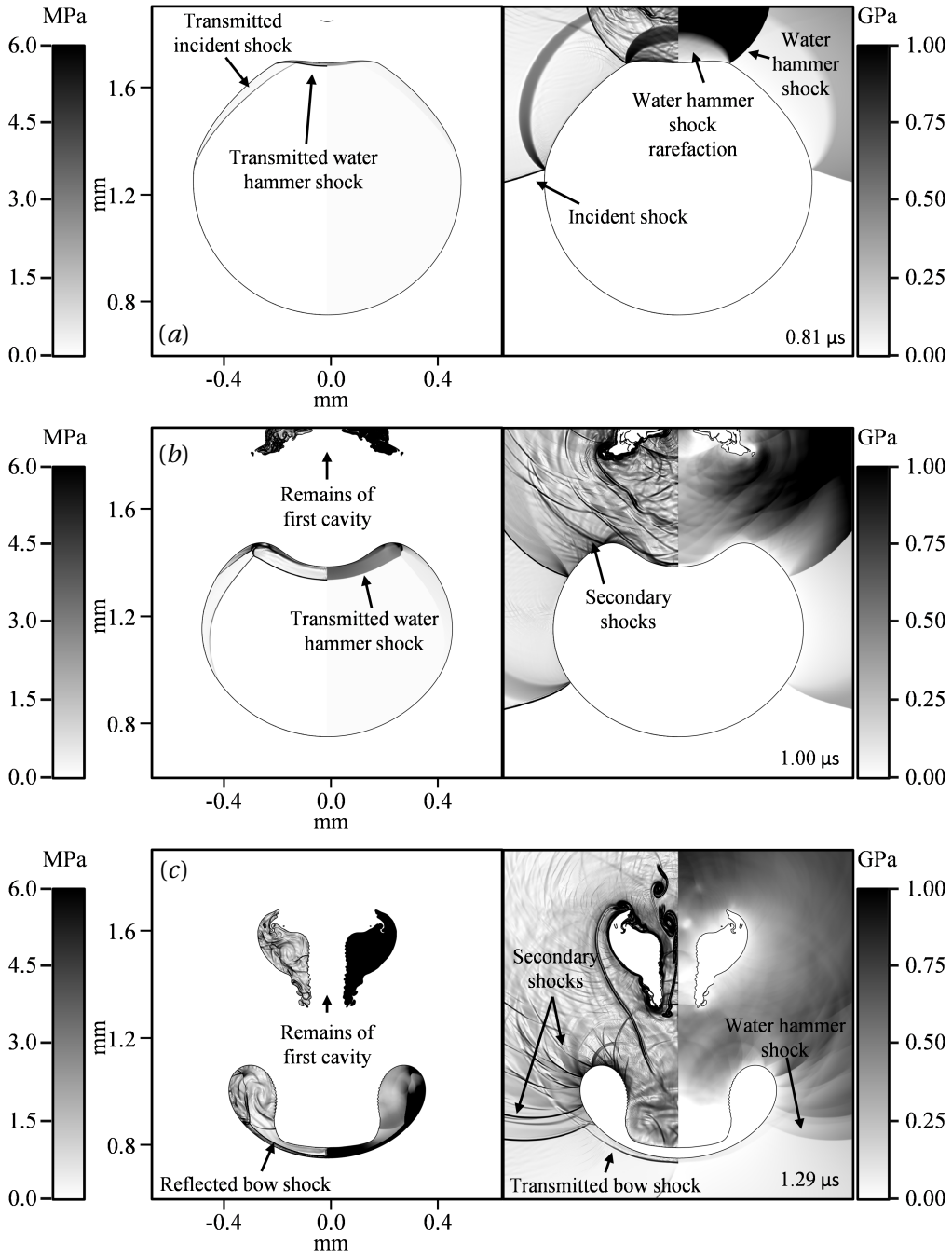

Figure 4.6: Jet formation in the second cavity of the arrangement shown in figure 4.1. Collapse of first cavity as in figures 2.4 and 2.5. In each frame, the left-hand image shows the flow in the gas, while the right-hand image shows the flow in the liquid. On both sides, the left half shows a numerically generated Schlieren plot ($|\nabla\rho|$), the right half the pressure field. Left side scale bar corresponds to left side image. Times relative to the time of first impact of the incident shock on the first cavity. (a) impact of the first cavity water hammer shock on the second cavity. The incident shock strikes the second cavity prior to this point. (b) Mid way through jet formation in the second cavity, at the point at which secondary shocks strike the second cavity. (c) Immediately before impact of the, now almost square, main transverse jet on the leeward cavity wall. The reflected and transmitted bow shocks can be seen in the gas and liquid images respectively.

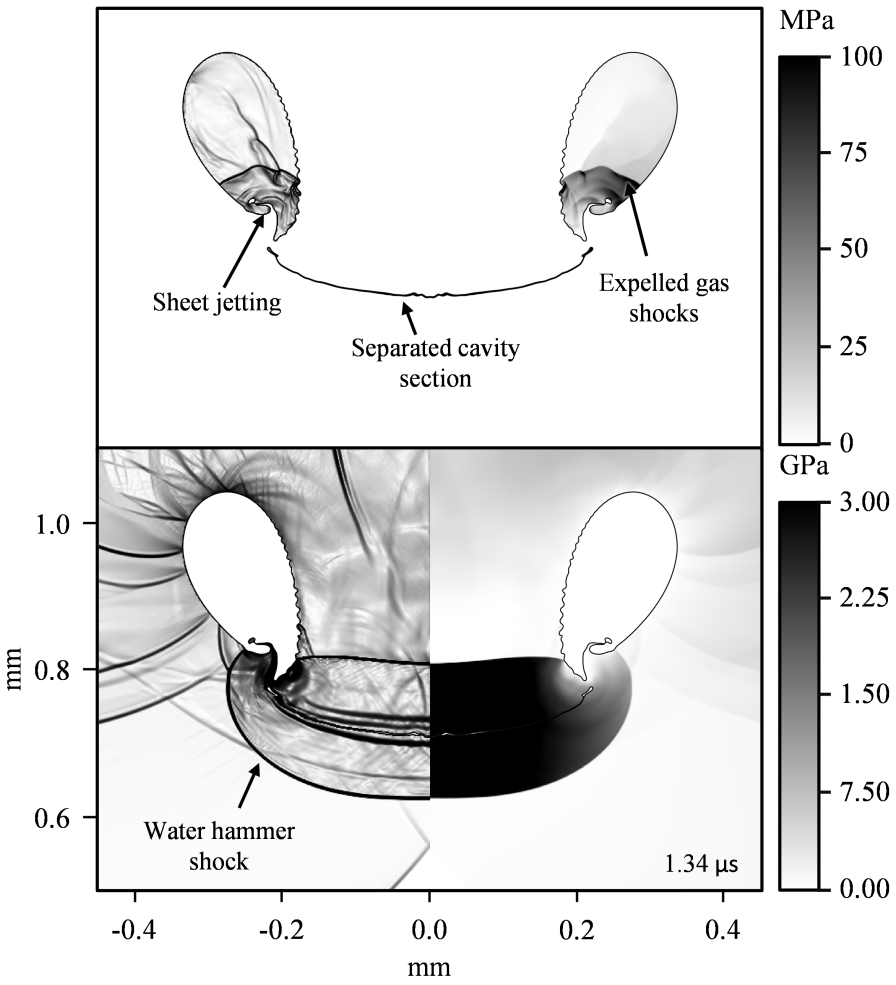

Figure 4.7: Collapse of the second cavity after water hammer shock formation. Plots shown as in figure 4.6, with the gas-phase on the top and the liquid phase on the bottom.

leading edge, and a higher velocity than the single cavity case. This process can be seen in figure 4.6. On impact on the leeward cavity wall, a larger region of gas is trapped and as a result a wider water hammer shock is formed (figure 4.7).

Further differences are caused by the secondary shocks from the collapsing first cavity, secondary shocks being defined as shocks emitted during collapse after the water hammer shock has been formed. These shock waves tend to be significantly stronger than the water hammer shock, but due to passing through the rarefaction fan formed by the impact of the water hammer shock on the second cavity are of much lower magnitude at the

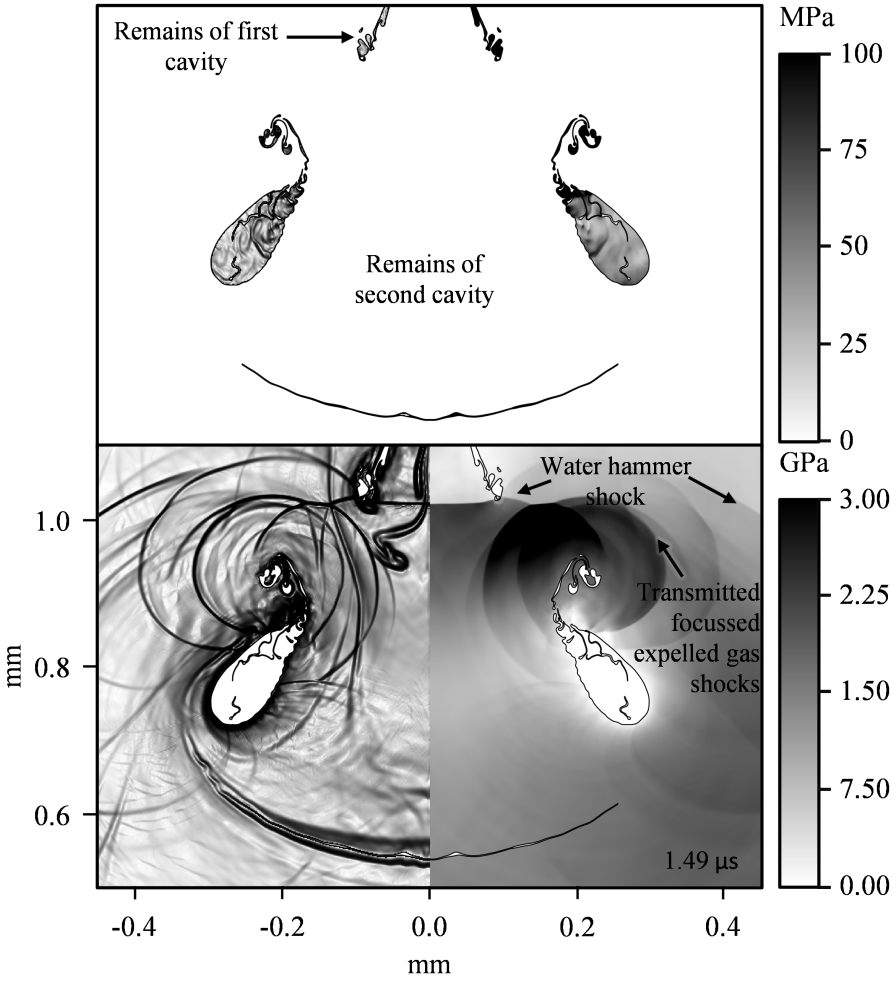

Figure 4.8: Collapse of the second cavity after the expelled gas shocks have reached the top of the lobes. Plots shown as in figure 4.7. The transmitted focussed expelled gas shocks can be seen forming in the liquid.

point of impact. As can be seen in figure 4.6 (b), these shock waves strike the sides of the jet first, steepening its profile.

Another effect, not present in these images but seen in other simulations, is the entrainment of parts of the first cavity into the jet of the second. This is driven by the close proximity of the two cavities and the low pressure behind the jet as it forms, which causes the gas sections to re-expand. As the water hammer shock from the second cavity expands, together with the transmitted expelled gas shocks, it re-collapses these sections of gas, forming further shock waves. This leads to the formation of very high pressures

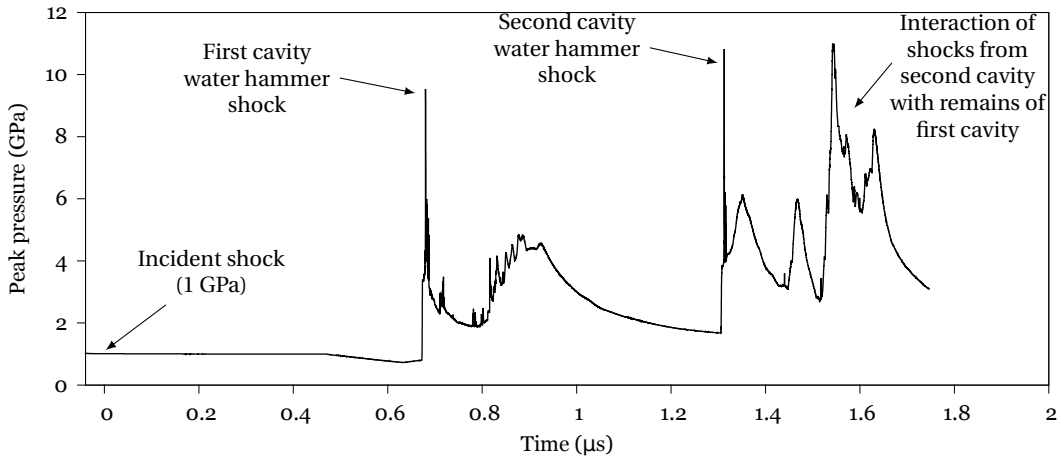

Figure 4.9: Variation of the peak overall pressure in the domain with time for the arrangement of figure 4.1 ($S/R_i = 0.5$, $R_i = 0.5\,\text{mm}$).

in the gas, as well as very high pressures in the liquid as these shock waves interact with the collapsing water hammer shock. This behaviour is the result of a long chain of small, complex events, and consequently is difficult to resolve or characterise fully.

The intensification of the second cavity collapse relative to the first is illustrated in figure 4.9, which shows the variation in peak pressure over time for the simulation. As can be seen, the peak pressure in the second cavity water hammer shock is slightly higher than in the first cavity collapse. However, further peaks of substantial magnitude are seen after the formation of the second cavity water hammer shock. These peaks correspond to the overlap of the water hammer shock and secondary shocks upstream of the second cavity, and the interaction of these shocks with the remains of the first cavity (see for example figure 4.8).

4.3.2 Effects of inter-cavity distance

The collapse of the second cavity is strongly dependent on the distance between the cavities. This is illustrated in figure 4.10, which shows how the shape of the jet varies with the inter-cavity distance. S/R_i values of 0.2, 0.5, 1.5 and 2.5 are shown. As can be seen, when the cavities are far apart the main transverse jet forms in a similar manner to the single

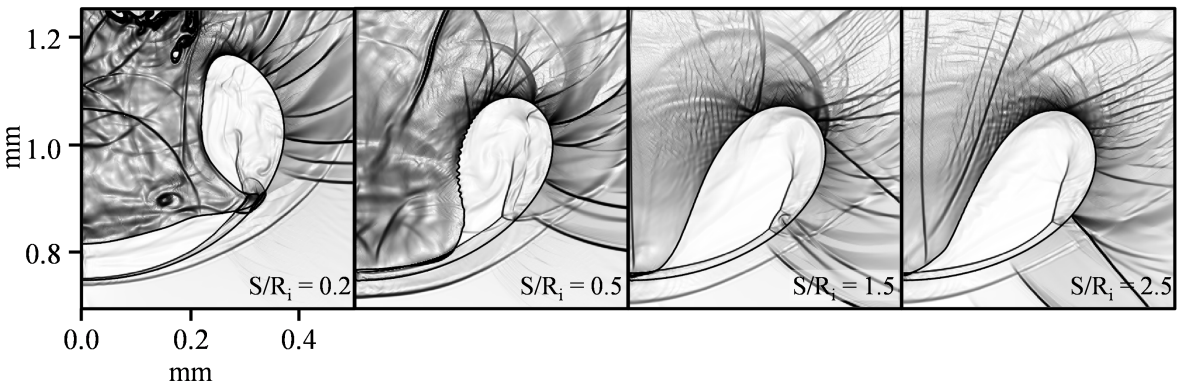

Figure 4.10: Numerical Schlieren plots of the main transverse jet of the second cavity at the point of jet strike, for S/R_i values of 0.2, 0.5, 1.5 and 2.5. $R_i = 0.5$ mm. The sides of the jet can be seen to steepen as the initial distance between the cavities is reduced.

cavity case. However, as the cavities are moved closer to each other, the sides of the jet steepen and the tip of the jet flattens. If the cavities are moved sufficiently close, the sides of the jet go beyond the vertical, the top of the cavity folding in on the centre. At this shock pressure, this effect is predicted to occur for S/R_i values of 0.5 or below. One of the key influencing factors in this process is the first cavity water hammer shock, which initiates collapse. As the shock expands, it spreads out and the radius of curvature increases. Thus, when the cavities are moved further apart the radius of curvature of the shock on impact on the second cavity is greater and it more closely resembles a planar wave. As a result, the second cavity collapse becomes more like that of the first cavity. Conversely, when the cavities are close together initially a much narrower jet is formed.

Figure 4.11 illustrates how the tip of the main transverse jet moves during collapse. Plots shown are for the first cavity, which collapses in an identical manner for all separation distances studied, and the second cavity for S/R_i values of 0.2 and 2.5. On contact of the driving shock wave on the cavity wall, a sharp increase in velocity is seen. Due to the greater magnitude of the water hammer shock relative to the incident shock, this initial rise is substantially larger in the second cavity than the first in both cases. Comparing the second cavity curves, when the separation distance is smaller the magnitude of the initial

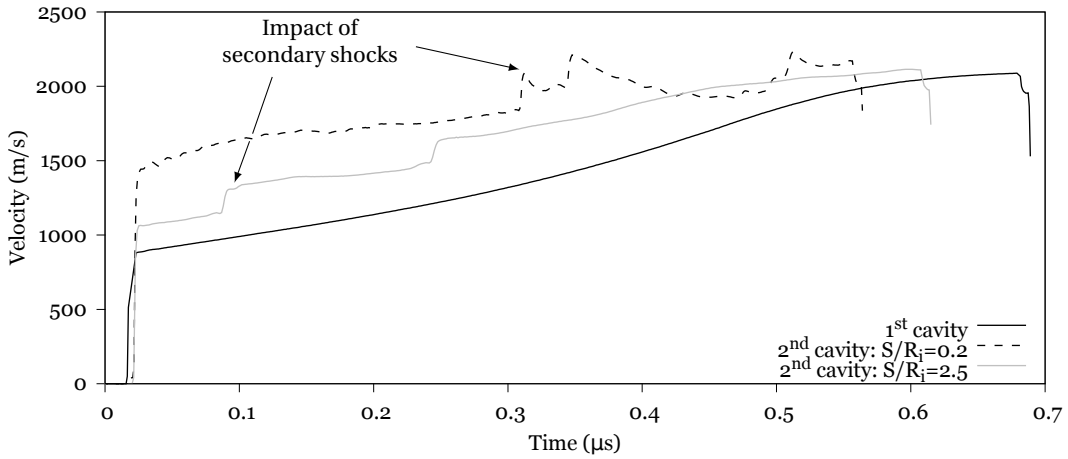

Figure 4.11: Change in velocity of the tip of the main transverse jet over time in both cavities of the arrangement of figure 4.1. S/R_i values of 0.2 and 2.5 shown. $R_i = 0.5\,\text{mm}$.

increase in jet velocity in the second cavity is larger. This is due to a higher water hammer shock pressure on impact, as the shock is curved and thus weakens as it spreads.

Following this initial impact, as the jet forms the flow is focussed, causing it to accelerate. This acceleration is substantially smoother in the first cavity than in the second in both cases, with the velocity continuing to increase smoothly up until the point immediately before jet impact. In the second cavity, clearly evident in figure 4.11, the impact of secondary shocks from the collapse of the remains of the first cavity leads to further step changes in collapse velocity. Due to their higher initial magnitude, these shocks travel with a higher velocity than the water hammer shock. Thus, as the cavity separation distance is increased, the impact of the secondary shocks on the second cavity occurs sooner after water hammer shock impact. As these shocks coalesce over time, in the $S/R_i = 2.5$ case the velocity curve follows a comparatively smooth trend following this impact. By comparison, in the $S/R_i = 0.2$ case the second cavity is struck by a series of shock waves and rarefactions, leading to a more complex velocity profile.

Figure 4.12 shows the effect of separation distance on the collapse times and water hammer shock pressures in the second cavity. Collapse times and pressures are presented

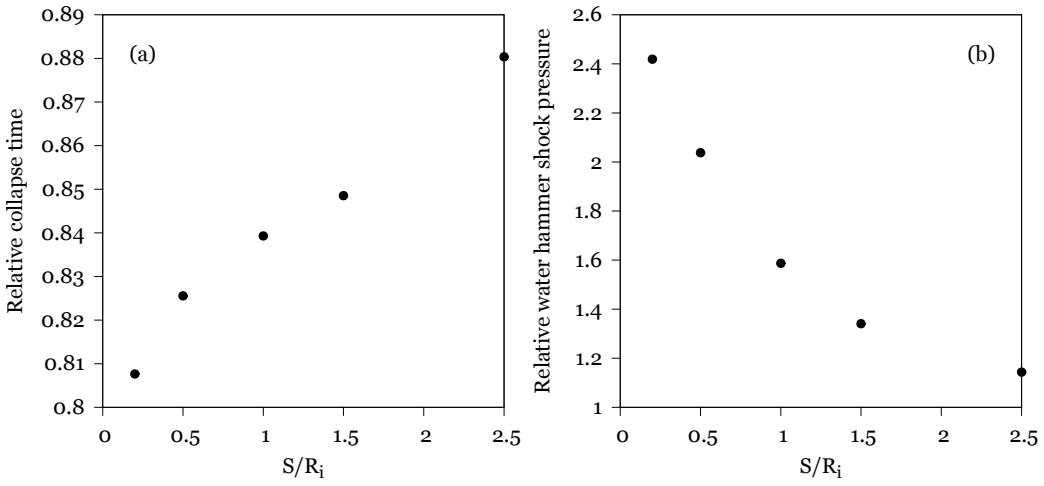

Figure 4.12: (a) collapse time in the second cavity, relative to the first. (b) peak water hammer shock pressures after the second cavity jet strike, relative to the first cavity water hammer shock pressure.

relative to the first cavity values. As can be seen, the second cavity collapse is faster than the first in all cases presented. This is due to the substantially larger initial increase in velocity, although the first cavity maintains a higher average acceleration beyond this point. As the cavities are moved closer to each other, the collapse time of the second cavity decreases. This is again primarily due to the larger initial increase in velocity on shock impact. As evident in figure 4.12 (b), the effect of this reduction in collapse time is a significant increase in water hammer shock pressure in the second cavity, with higher pressures being achieved at closer separation distances.

4.3.3 Cylindrical vs Spherical cavities

Outside of this section and section 4.2.2.2 all cases given in this chapter are modelled in planar 2D, in order to allow more direct comparison with published experimental results. However, as most applications of cavity collapse involve spherical cavities, comparison is presented here between 2D and axisymmetric simulations of the same two cavity arrangement. In both cases, $S/R_i = 0.5$, and the resolution is 400 ppr. As outlined in section 2.4.3.2, for the single cavity case Hawker and Ventikos[1] demonstrated that axisymmetric

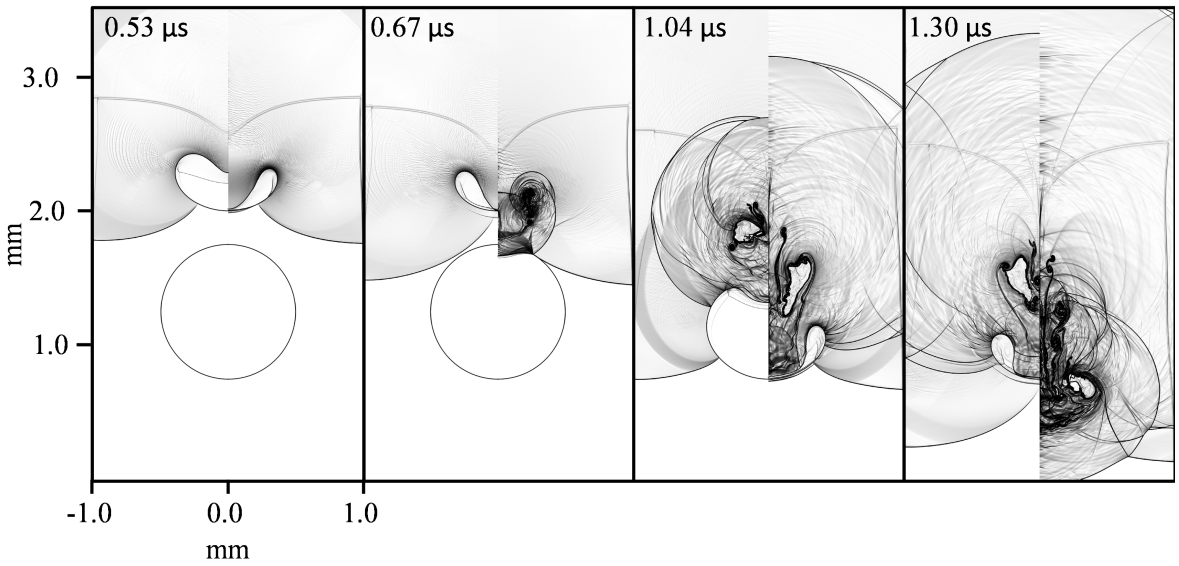

Figure 4.13: Numerical Schlieren images detailing the collapse of the arrangement shown in figure 4.1 in a 2D (left) and axisymmetric (right) simulation. Cavity collapse can be seen to be substantially faster in the axisymmetric case. $S/R_\mathrm{i} = 0.5$, $R_\mathrm{i} = 0.5\,\mathrm{mm}$.

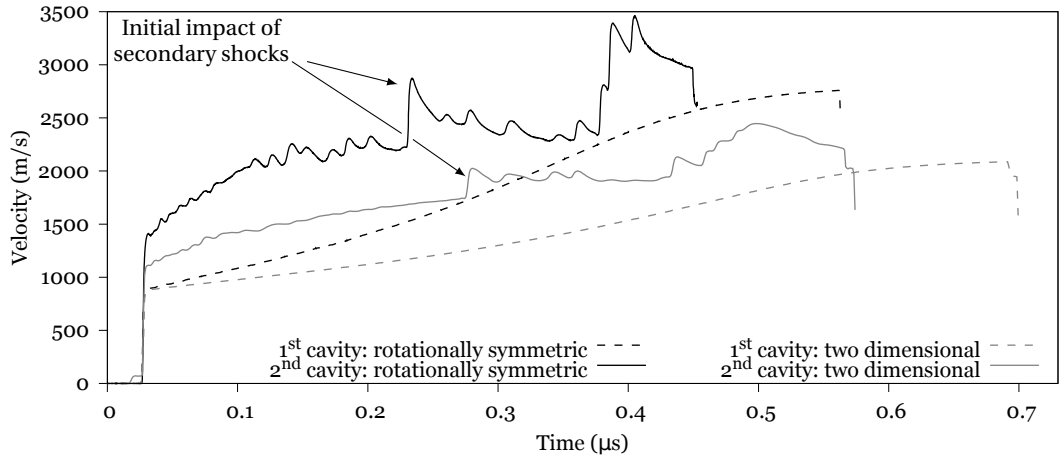

Figure 4.14: Change in velocity of the tip of the main transverse jet over time, during the first phase of cavity collapse, for a 2D and axisymmetric simulation of the arrangement of figure 4.1. $S/R_\mathrm{i} = 0.5$, $R_\mathrm{i} = 0.5\,\mathrm{mm}$.

and fully three dimensional computations produce almost indistinguishable results.

Numerical Schlieren images comparing both simulations are given in figure 4.13. As can be seen, the collapse of both the first and second cavity is substantially faster in the axisymmetric case, although the jet shape and general dynamics of the collapse remain largely unchanged. The increase in jet speed in the axisymmetric case is unsurprising; in

the axisymmetric case the flow is focussed onto a point during main transverse jet formation, as opposed to a line in the 2D case. This leads to a substantial increase in focusing and thus a higher jet speed.

The effect on the velocity of the collapse is further illustrated by figure 4.14, which shows how the velocity of the jet tip changes for both the first and second cavity in both studies. Comparing the plots for the first cavities, it can be seen that the initial rise due to incident shock impact is the same in both cases. Due to the greater level of focusing, the acceleration of the jet is substantially faster in the axisymmetric case beyond this point. This faster acceleration translates into a stronger water hammer shock, leading to a larger initial increase in jet velocity in the second cavity compared to the 2D case. Likewise, the acceleration of the second cavity jet beyond this point is greater in the axisymmetric result. Additionally, further spikes in jet velocity, caused by the impact of secondary shocks from the first cavity collapse on the second cavity jet tip, are of a larger magnitude in the axisymmetric case. Comparing the times between initial shock impact and jet impact, it is found that the collapse is 20 % faster in the first cavity, and 22 % faster in the second cavity.

4.3.4 Effect of relative cavity size

From the analysis of the collapse of two cavities of equal size, it is clear that inter-cavity effects play a substantial role in the collapse process. In particular, the shielding of the second cavity by the first prevents the collapse of the second cavity by the incident shock wave, allowing the stronger first cavity water hammer shock to collapse the second cavity at a later point, leading to different collapse dynamics.

As a more extreme case of shielding, figure 4.15 shows the effect of substantially reducing the size of the second cavity relative to the first. The arrangement is modelled with a radii ratio R_1/R_2 of 5, and a relative separation distance S/R_1 of 0.2, where R_1 is the

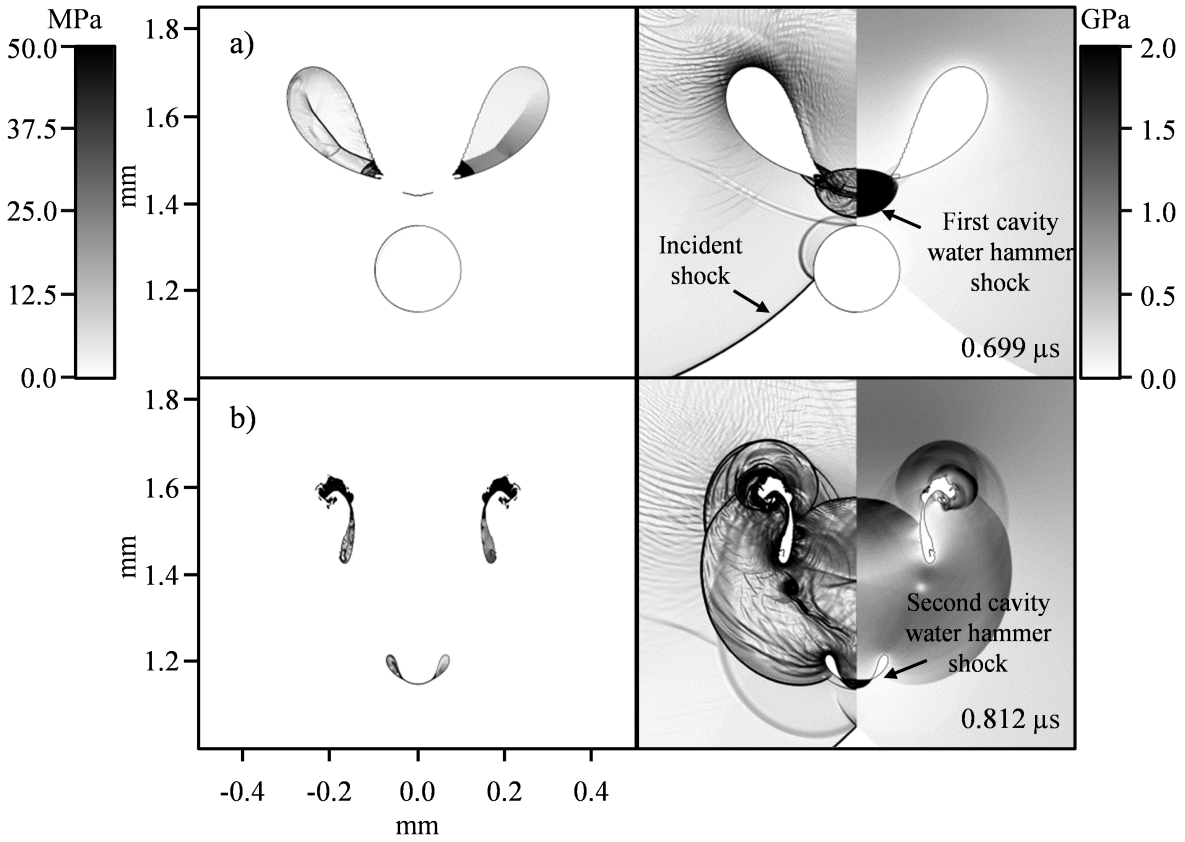

Figure 4.15: The effect of decreasing the size of the second cavity relative to the first ($R_1/R_2 = 5$, $S/R_1 = 0.2$, $R_1 = 0.5$ mm). Plots shown as in figure 4.6. (a) Collapse of the second cavity, after impact by the incident shock but before impact by the water hammer shock. (b) Water hammer shock formation in the second cavity.

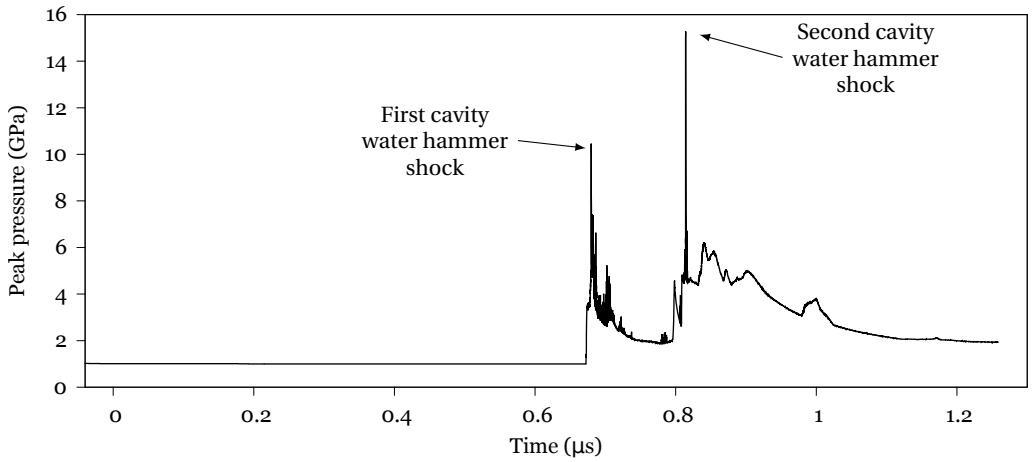

Figure 4.16: The effect of decreasing the size of the second cavity relative to the first: variation in peak overall pressure with time. $R_1/R_2 = 5$, $S/R_1 = 0.2$, $R_1 = 0.5$ mm.

initial radius of the first cavity, and R_2 that of the second. S is as in figure 4.1. This gives a resolution in the second cavity of 80 ppr. R_1 is 0.5 mm. As demonstrated by figure 4.15 (a), with this greater level of shielding the incident shock has little effect on the second cavity. As a result, the collapse is driven entirely by the first cavity water hammer shock. Once the water hammer shock strikes the second cavity, collapse proceeds in a similar manner to a single cavity, as shown in figure 4.15 (b). However, clearly evident in figure 4.16, which shows the variation in peak overall pressure with time for the simulation, peak water hammer shock pressures in the second cavity collapse are now significantly higher, relative to the case of two equally sized cavities (figure 4.9). This effect is further highlighted by figure 4.17, which shows how the peak pressure achieved varies with S/R_1 and R_1/R_2. These simulations were conducted at the slightly lower resolution of 50 points per small cavity radius, and pressures are presented scaled by the peak pressure achieved at $R_1 = 1.01R_2$ for each separation distance. Although these results are at an insufficient resolution to be fully predictive, the general trend suggests an increase in peak pressure as R_1 becomes larger than R_2, with the effect most pronounced at close separation distances. For $S \gtrsim 0.4R_1$, minimal increase in pressure is observed with an increase in R_1/R_2.

Figure 4.18 demonstrates the converse case, where the first cavity is substantially smaller than the second ($R_1/R_2 = 0.2$, $S/R_2 = 0.2$, $R_2 = 0.5\,\text{mm}$). As seen in figure 4.18 (a), the smaller size of the first cavity relative to the second offers substantially less protection for the second cavity, and second cavity collapse is thus driven by both the incident shock, which leads to the formation of a wider, slower main transverse jet, and the first cavity water hammer shock, which forms a narrower, faster jet down the centre of the cavity. Of significant note, clearly evident in figures 4.18 (b) and (c), with this arrangement the entirety of the first cavity becomes entrained in the main transverse jet during collapse of the second cavity. On impact of the jet on the leeward cavity wall this leads to the formation of a number of high pressure spikes in the peak overall pressure plot (figure

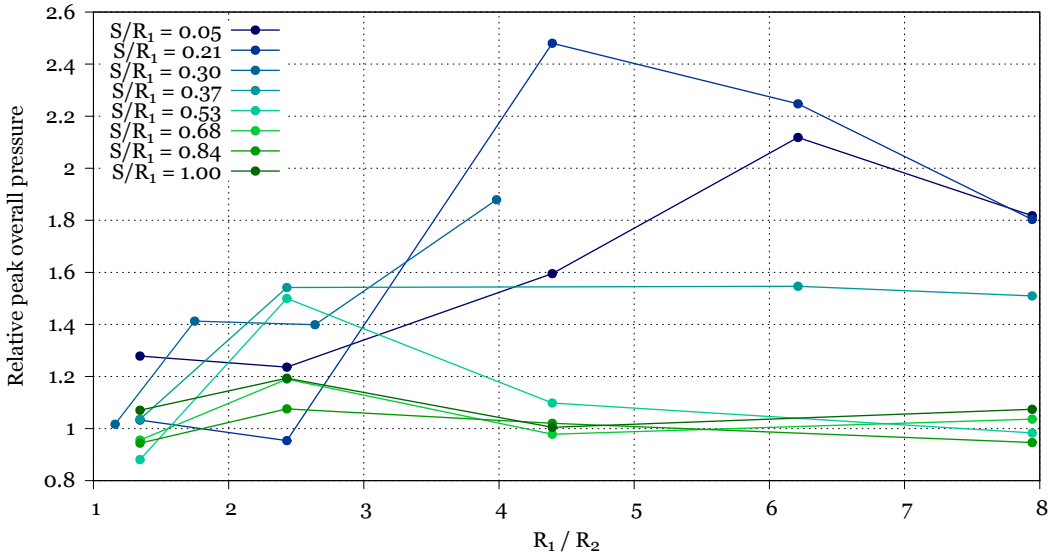

Figure 4.17: Variation in peak overall pressure achieved with S/R_1 and R_1/R_2, for $R_1 > R_2$. Pressures are scaled relative to the pressure achieved at $R_1 = 1.01R_2$ for each value of S/R_1.

4.19), as the water hammer shock developed interacts with the first cavity remains. This process can be seen in figure 4.18 (c), which shows the collapse of the second cavity after impact of the main transverse jet.

Thresholds for parameters for entrainment are illustrated by figure 4.20. As in figure 4.17, these simulations were conducted at a resolution of 50 points per small cavity radius. In the plot, the light grey region shows the combination of parameters where some entrainment of the first cavity is seen. The dark grey region shows where the extreme case of complete entrainment is observed. $R_{\max} = \max(R_1, R_2)$. For a separation distance of $S > 0.4R_{\max}$ no entrainment is observed, regardless of the radius ratio. Below this value, for very high radius ratios complete entrainment is observed for most separation distances. Likewise, for very close separation distances, some entrainment is observed regardless of radius ratio. Between these extremes, full entrainment is likely to occur if $R_2 > 3R_1$ if the cavities are within $S \lesssim 0.2R_2$.

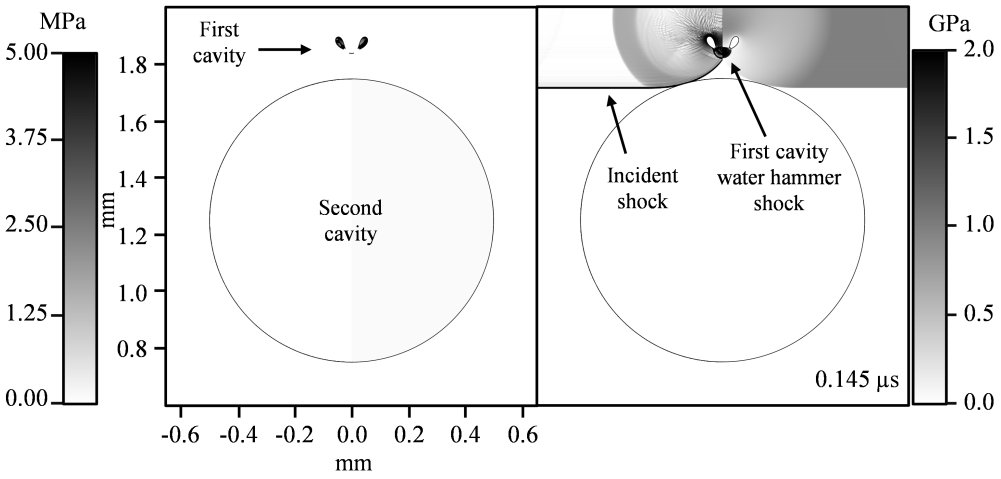

(a) Impact of the incident shock on the second cavity.

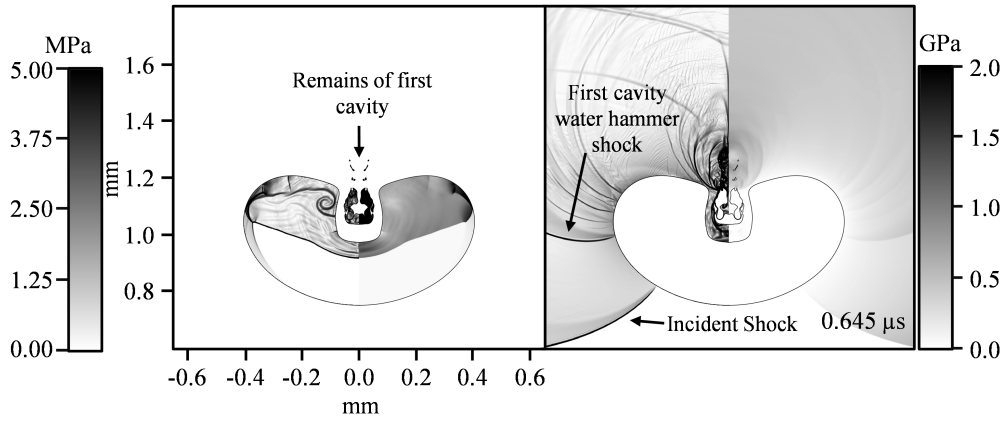

(b) Main transverse jet formation in the second cavity. The entirety of the smaller first cavity becomes entrained in the main transverse jet of the second cavity.

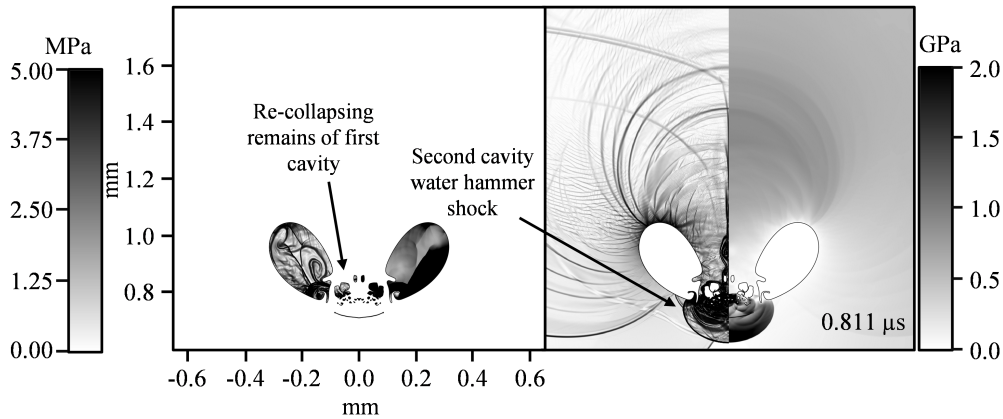

(c) Water hammer shock propagation during the collapse of the second cavity. The water hammer shock can be seen re-collapsing the remains of the first cavity.

Figure 4.18: The effect of decreasing the size of the first cavity relative to the second ($R_1/R_2 = 0.2$, $S/R_2 = 0.2$, $R_2 = 0.5\,\text{mm}$). Plots shown as in figure 4.6.

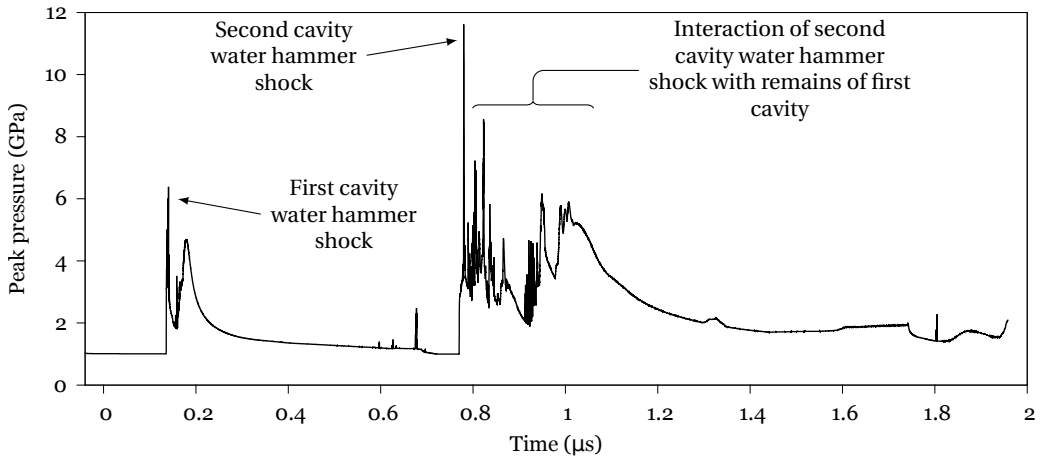

Figure 4.19: Variation in peak overall pressure with time for the case where $R_1/R_2 = 0.2$, $S/R_2 = 0.2$ and $R_2 = 0.5\,\text{mm}$.

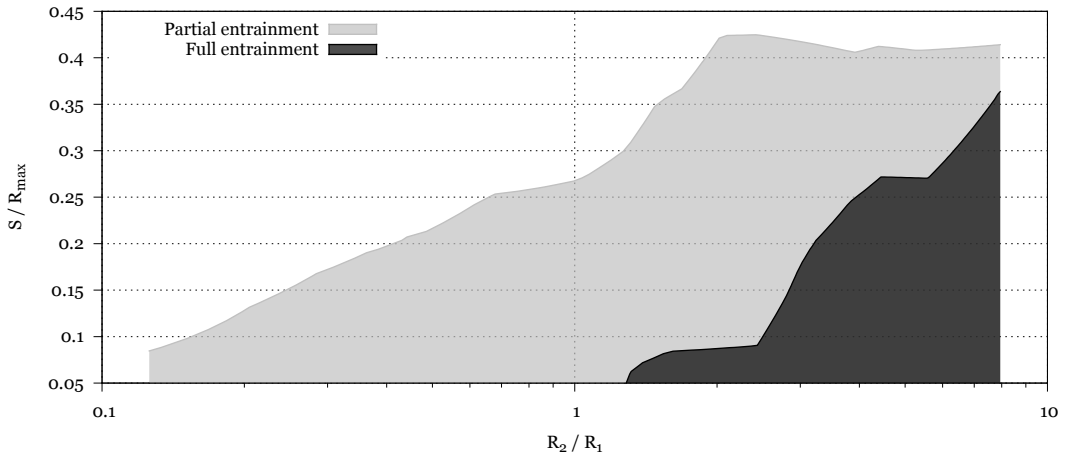

Figure 4.20: Threshold contours for partial and complete entrainment of the first cavity within the second. $R_{\max} = \max(R_1,\, R_2)$

4.4 FOCUSING TRIANGULAR ARRAY

As shown by the study of two cavities in a line, shielding effects may play a significant role in even simple multi-cavity arrangements. As suggested by Tomita *et al.*[169] and later by Bourne and Field[168] and Lauer *et al.*[165], when two cavities are placed side by side in close proximity there is substantial impingement of the flow in between the cavities. From the study of single cavity collapse[1], some of the strongest shocks in the process are formed when the remaining lobes of the cavity collapse, following jet impact on the leeward cav-

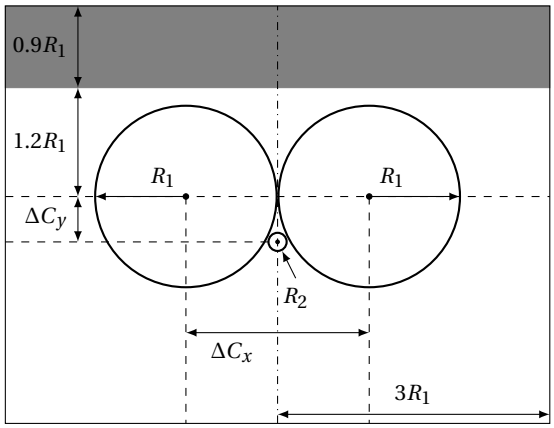

Figure 4.21: Diagram of the focusing triangular array configuration. Two cavities of radius R_1 are placed next to each other, separated by a centre-to-centre distance ΔC_x. Behind these cavities, a smaller cavity of radius R_2 is placed on the centre-line between the cavities, separated by a centre-to-centre distance of ΔC_y. Grey section demarcates the high pressure region initialised behind the incident shock wave.

ity wall. An arrangement that capitalises on these processes to enhance the intensity of collapse is shown in figure 4.21. A triangular array of cavities is placed with two of the cavities substantially larger than the third, and placed ahead of it with regard to the incident shock. The gap between the cavities is reduced to a small size to minimise the flow between the cavities. In the particular arrangement presented, $\Delta C_y/R_1 = 0.5$, $\Delta C_x/R_1 = 2.02$, $R_1/R_2 = 10$ and $R_1 = 0.5$ mm.

4.4.0.1 Grid independence

Due to the differing length scales of this arrangement over and above those in section 4.2.1, a new set of grid independence comparisons have been performed (see table 4.1). The metrics used are: the large cavity first phase collapse time (the time between the first impact of the incident shock on the large cavities and the impact of the main transverse jet on the leeward cavity walls); the large cavity second phase time (the time between jet impact and the impact of the expelled gas shocks on the top of the inner lobes); the small cavity first phase time and the peak overall pressures in the simulation. As the collapse dynamics of the small cavity are very different from that of the large cavities, to be ex-

	200 ppr	400 ppr	580 ppr	800 ppr	1000 ppr
Large cavity first phase time (ns)	685.5	687.3	688.3	690.0	691.3
Large cavity second phase time (ns)	219.6	217.7	216.7	212.5	208.7
Small cavity first phase time (ns)	3.95	5.20	4.70	4.64	4.80
Peak overall pressure (GPa)	18.52	23.39	27.48	40.92	35.96

Table 4.1: Grid independence results for the collapse of the arrangement shown in figure 4.21.

plored shortly, the small cavity first phase time is defined as the time between the initial collapse of the top of the cavity, which gives the peak overall pressure in the simulation, and the time at which the main transverse jet strikes the leeward cavity wall, producing the peak water hammer shock pressure.

As can be seen in table 4.1, all metrics bar the peak overall pressure are reasonably well matched between resolutions, although due to the complexity of the problem true grid independence is very difficult to achieve. The large cavity sheet jetting, which drives the collapse of the small cavity, is particularly difficult to resolve, with increased resolution leading to a continuous increase in the complexity of breakdown. However, all key features in the collapse process, such as the envelope of the sheet jetting, the movement of the expelled gas shock and the collapse process in the small cavity are well resolved at higher resolutions.

In order to resolve as much detail as possible in the small cavity, the analysis of the collapse process will be given at 1000 points per large cavity radius, giving a total of 13.8 million cells in the simulation. At this resolution, simulations take approximately 4 days to complete, split across 48 processors. Compared to the values at 800 ppbr, the small cavity first phase collapse time at this resolution is 3.3% longer, while the peak over-

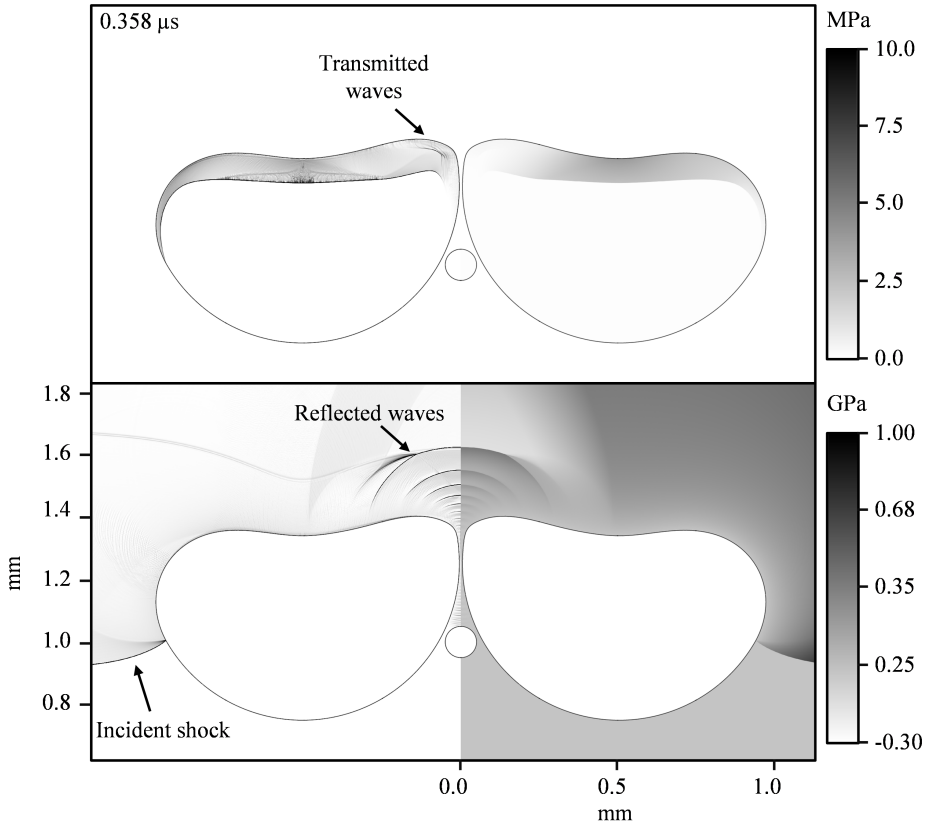

Figure 4.22: Collapse of the arrangement of figure 4.21, after impact of the incident shock on the larger cavities. Plots shown as in figure 4.6.

all pressure is 13.7% lower. These numbers give some indication of the errors in the values presented in this section, although true quantification of the accuracy of the solution is not easily achieved.

4.4.0.2 Analysis of collapse

The following analysis discusses the case of a 1 GPa shock striking the arrangement of figure 4.21. In a similar manner to the collapse of a single cavity in free space, the impact of the incident shock wave on the two larger cavities begins the formation of a main transverse jet in each cavity. However, due to the proximity of the cavities, the rarefaction fans overlap and come in contact with the inner lobe of the opposite cavity. This causes an area of negative pressure to form upstream of the cavities on the central line of

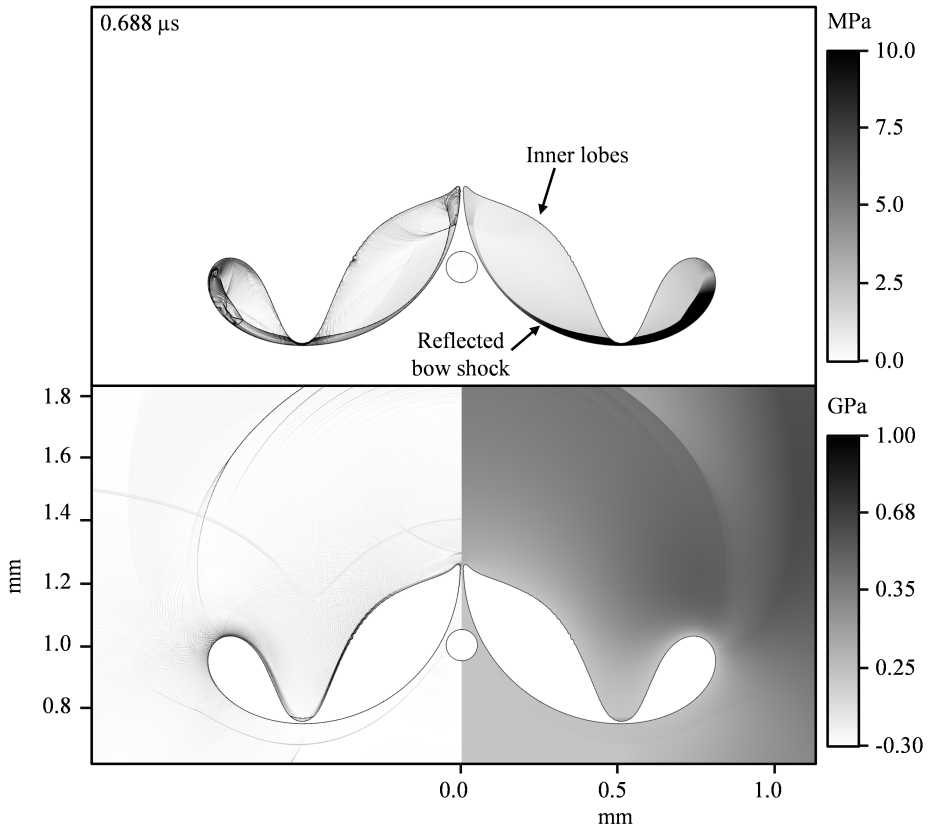

Figure 4.23: Collapse of the larger cavities of figure 4.21, prior to impact of the main transverse jets on the leeward cavity walls. Plots shown as in figure 4.6.

symmetry, a rarefaction wave to be transmitted into the cavities, and reflected shocks to form in the liquid at the cavity interfaces. These reflections overlap to create a small area of high pressure, before contacting the opposite cavity and reflecting once more to form an overlapping region of rarefaction. As can clearly be seen in figure 4.22, this process forms a series of waves that propagate both up, away from the cavities, and down, towards the smaller cavity. Additionally, a series of transmitted waves are formed in the gas, which coalesce to form a single shock. A result of these effects is that the incident shock is dramatically reduced in magnitude in between the cavities. This provides significant protection for the small central cavity, which largely remains unaffected until much later on in the collapse process, and greatly slows the collapse of the inner lobes. As the shock continues to propagate around the outside of the cavities at a normal rate, the outside

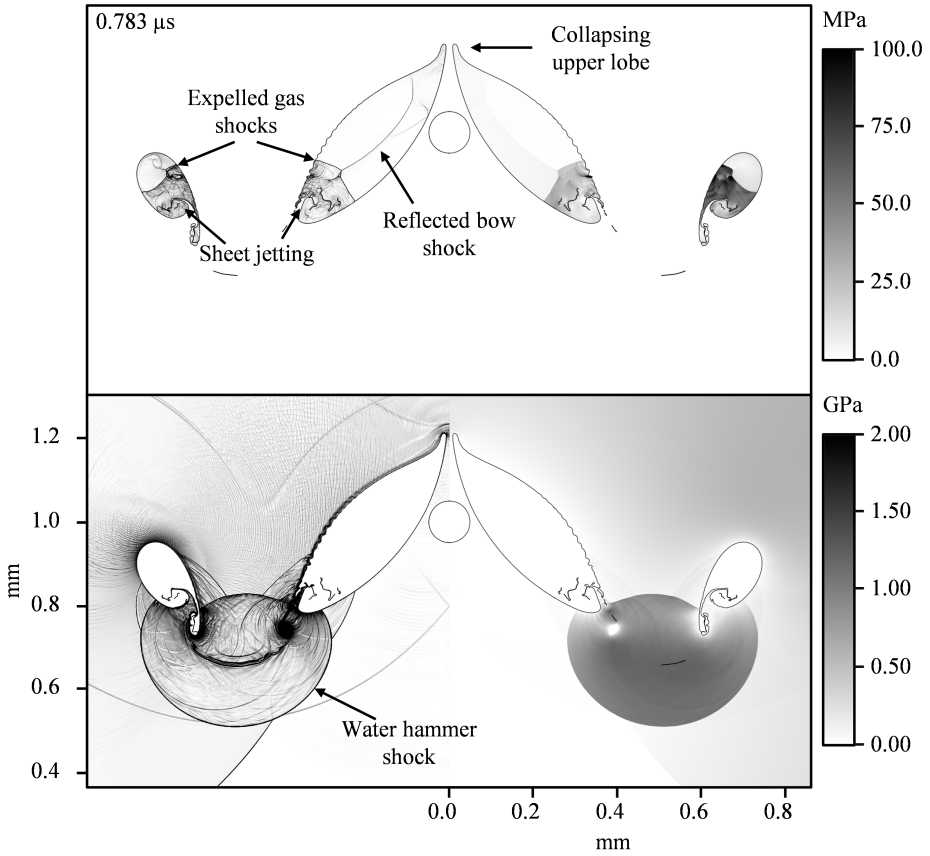

Figure 4.24: Propagation of expelled gas shocks, sheet jetting and water hammer shocks after impact of main transverse jets in larger cavities of figure 4.21. Plots shown as in figure 4.6.

lobes of the cavities thus collapse far more quickly than those on the inside. As a consequence, after the impact of the main transverse jet on the leeward cavity walls the inner lobes are substantially larger than in the single cavity case (see figure 4.23).

Due to the protection it is afforded by the larger cavities, the smaller central cavity avoids contact with the incident shock, and is instead collapsed by the shock waves produced by the collapse of the inner lobes of the larger cavities. Specifically, these shocks are the expelled gas shocks and the shocks produced by the sheet jetting (see figure 4.24). This protection, followed by intense collapse by multiple shock waves, leads to a very substantial increase in the pressures developed in the collapse.

On formation, the expelled gas shocks and sheet jetting shocks travel rapidly up the

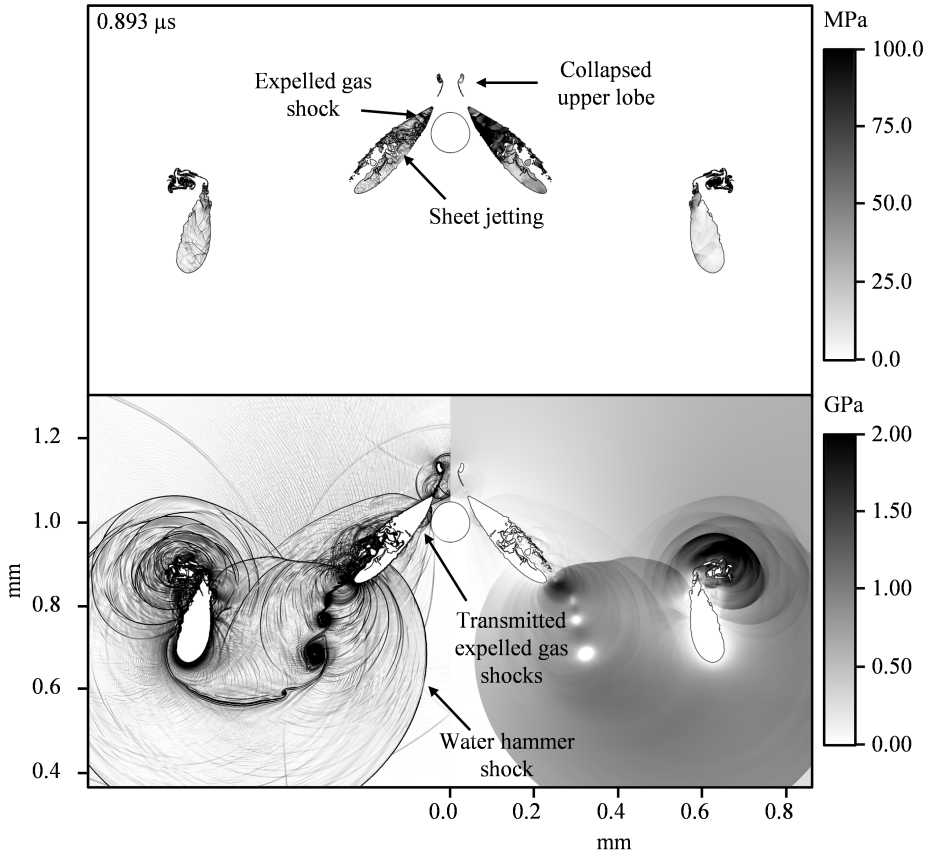

Figure 4.25: Collapse of the upper lobes and formation of transmitted expelled gas shocks in the larger cavities of figure 4.21. Plots shown as in figure 4.6.

lobes of the large cavities, interacting with the cavity walls as they go. The sheet jetting is very unstable and begins to break the lobes up into small sections, as well as form relatively strong shock waves through compression of small areas of trapped gas. This process leads to the formation of sheet-jetting 'bow-shocks' that travel ahead of the sheet jetting as it travels up the lobes. Rather than consisting of one uniform shock front, these shocks are made up of a series of small shock waves that coalesce to form a region of high pressure. The net result of this process is that a complex region of high pressure (approx. 75 MPa) forms behind the expelled gas shock fronts, driven by the sheet jetting which continues to break up the cavities as it travels. As this process is happening, the top of the inner lobes continue to collapse, decreasing the size of the lobes and reducing the tip to a sharp point (figure 4.24).

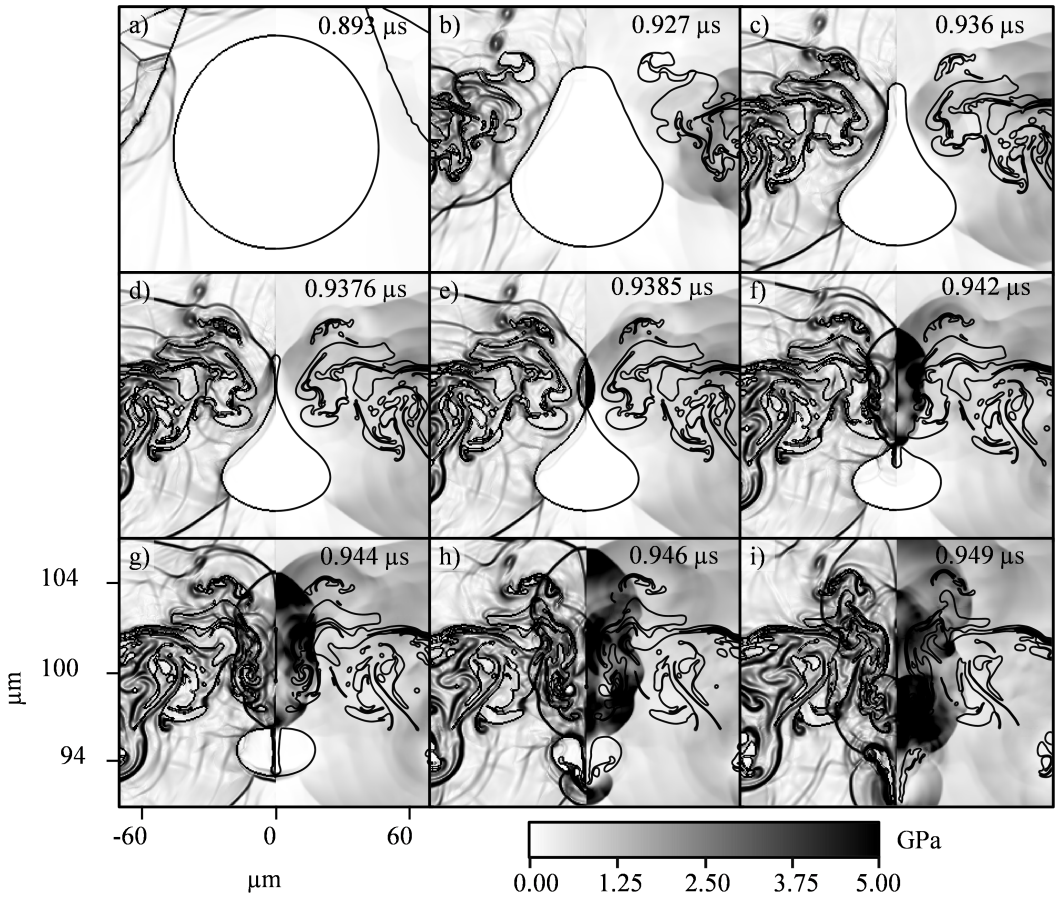

Figure 4.26: Collapse of the small cavity of figure 4.21, following formation of the transmitted expelled gas shocks in the larger cavities. In each image, the left side shows a numerical Schlieren plot while the right side shows the pressure in both the liquid and gas phase.

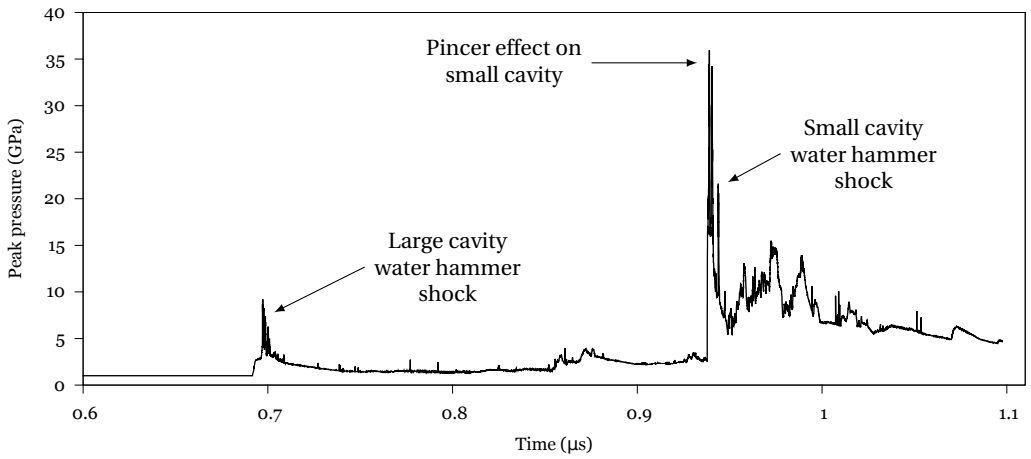

Figure 4.27: Variation of the peak overall pressure with time for the arrangement of figure 4.21. Values presented vary by approximately ±14% with grid resolution across high resolution results.

As the expelled gas shocks reach the top of the inner lobes, the area of high pressure behind propagates through the cavity walls and strikes the small cavity on either side with a pressure of approx. 300 MPa. This can be seen in figure 4.25. These shocks form a small bow shock in the small cavity, and cause the interface to begin to move inwards. During this time, the expelled gas shocks themselves reach the top of the lobes, forming the transmitted expelled gas shocks (approx. 1.6 GPa on formation) which also strike the cavity on either side with a pressure of around 500 MPa. The collapse of the small cavity from this point is shown in figure 4.26. As the sheet jetting continues to propagate in the inner lobes of the large cavities, more and more gas is forced into the top of the lobes, leading to the formation of a continuous series of shocks which strike the small cavity (a - d). Additionally, new areas of high pressure are continually created as the lobes break down and small sections of gas are compressed. Coupled with the collapse of the top of the lobes, on impact with the small cavity the sheet jetting thus consists of a mass of small gas sections surrounded by very high pressure liquid (see for example b). This accelerates rapidly towards the small cavity due to the low pressure created by the inward movement of the small cavity walls. This strikes the small cavity on either side with a 'pincer' like effect, leading to rapid compression of the top of the cavity (b). Pressures of the shocks striking the cavity during this part of the process are consistently around 2 GPa, with peak pressures of approx. 4 GPa. The upper section of the cavity rapidly compresses to a very thin section (c - e), with pressures in and around the gas reaching a peak of 36 ± 5 GPa (e). This corresponds to the largest peak in the graph of peak pressures in the simulation, given in figure 4.27, giving a five fold increase in pressure ratio compared to the single cavity peak water hammer shock pressure of 6.8 GPa, and a 36-fold increase in pressure relative to the incident shock. This extremely high magnitude area of pressure drives a narrow main transverse jet into the cavity (f), which subsequently strikes the leeward cavity wall (g). The average velocity of the jet is approximately 9100 ms^{-1}. The water hammer shock formed (h), reaches a peak pressure of 21 ± 3 GPa (the subsequent peak shown in figure

4.27).

4.5 CONCLUDING REMARKS

Using the methodology outlined in chapter 3, this chapter has studied in detail the collapse of multi-cavity arrays under the influence of driving shock waves. This work has built upon the work of Hawker and Ventikos [1] into single cavity collapse, revealing a rich level of additional complexity. Within this complexity, it has been shown that significant intensification of conditions can be achieved under the right conditions. As with the work of Hawker and Ventikos, the results of this chapter raise some significant questions. Perhaps the most important of these questions is: of the effects shown, which are seen in reality? In the next chapter, an experimental setup is outlined, which aims to answer this question.



CHAPTER 5

EXPERIMENTAL METHODS

The experimental methods used in this work are described. A single-stage light-gas gun is used to produce high pressure (approximately 1 GPa) shock waves in hydrogel blocks, into which cavities are cast. The ensuing collapse of the cavities is captured using high speed imaging, with light detection diagnostics used to record any light emission produced. A hydrophone is utilised to measure pressures. Image analysis techniques may be used to build simulations that are matched to experimental results.

5.1 INTRODUCTION

As discussed in chapter 2, much of the experimental work done in the field of shock-bubble interactions has utilised a quasi-two dimensional technique, whereby cylindrical cavities are cut from thin hydrogel sheets. The sheets are then compressed between clear PMMA plates, before being collapsed by a shock wave, formed either by a gas gun or an explosive charge. As the bonding in the hydrogel is relatively weak, it is assumed that the pressure of the incident shock wave is sufficient to overcome the chemical bonding and that the hydrogel acts in a manner very similar to water. The casting of cavities in hydrogel allows for accurate control of both the size and placement of cavities, with very good temporal stability. The cylindrical cavities are viewed on-axis, allowing imaging of

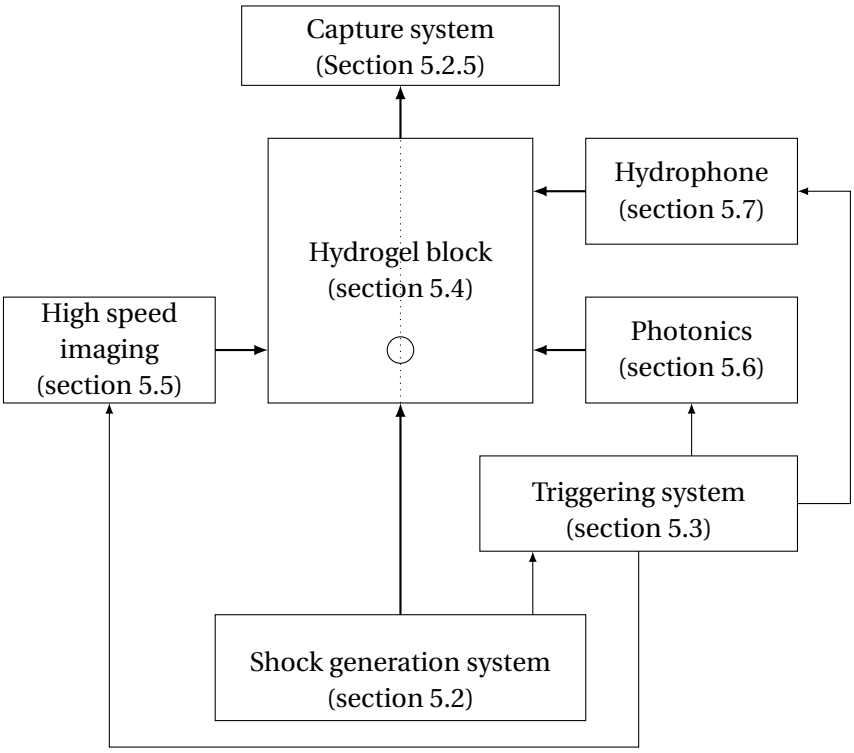

Figure 5.1: Schematic of the experimental setup

the inside of the cavity. Using this method, high speed images of the collapse of single and multiple cavity arrays have been recorded in a number of different configurations[4,166], including observations of light emission during collapse[5,7,167].

This chapter describes a similar experiment, in which strong shock waves produced by a single-stage light gas gun are used to collapse air-filled cavity arrays held in hydrogel blocks. As in the work of Dear and Field, high speed imaging is used to capture the cavity collapse and light emission (section 5.5). However, additional diagnostics are utilised, including temporal and frequency resolving optical diagnostics (section 5.6) and pressure measurement (section 5.7). A top-level schematic of the experimental setup is given in figure 5.1. The shock generation system is described in section 5.2, with the triggering system used described in section 5.3. Target design and manufacture are detailed in section 5.4. With the experimental results collected, analysis techniques may be used to develop simulations that are matched to those results. The methods employed in this process are

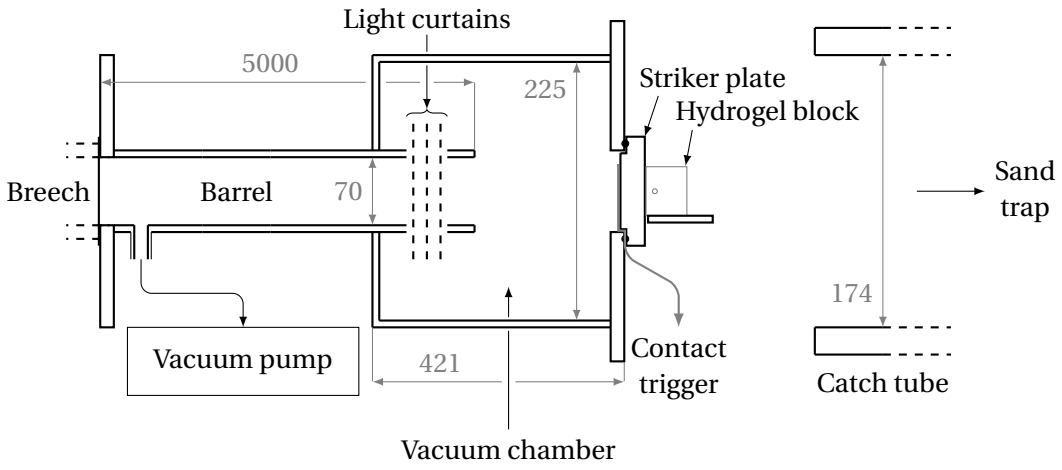

Figure 5.2: Diagram of the gas gun setup (not to scale). Shock waves are created by the firing of projectiles from a 70 mm bore light-gas gun into an aluminium striker plate, behind which the target hydrogel block is placed. Dimensions in mm.

outlined in section 5.8.

5.2 SHOCK GENERATION SYSTEM

In this experiment, shock waves are produced using a single-stage 70 mm bore light gas gun (diagram figure 5.2, photograph figure 5.3). This gun has a barrel length of 5 m, a barrel wall thickness of 35 mm and is made of manganese steel. Projectiles fired from the gun are impacted against an aluminium striker plate, behind which the target hydrogel block is placed. The gun is fired through the use of a bursting-diaphragm breech (section 5.2.1). In order to increase the velocity of the projectile and reduce the intensity of any light flash produced by the impact of the projectile on the striker plate, the barrel is evacuated prior to the shot, to approximately 0.8 Torr. Projectile velocity is measured using a light curtain array (LCA) situated at the end of the barrel (section 5.2.2).



Figure 5.3: Photograph of the gas gun setup.

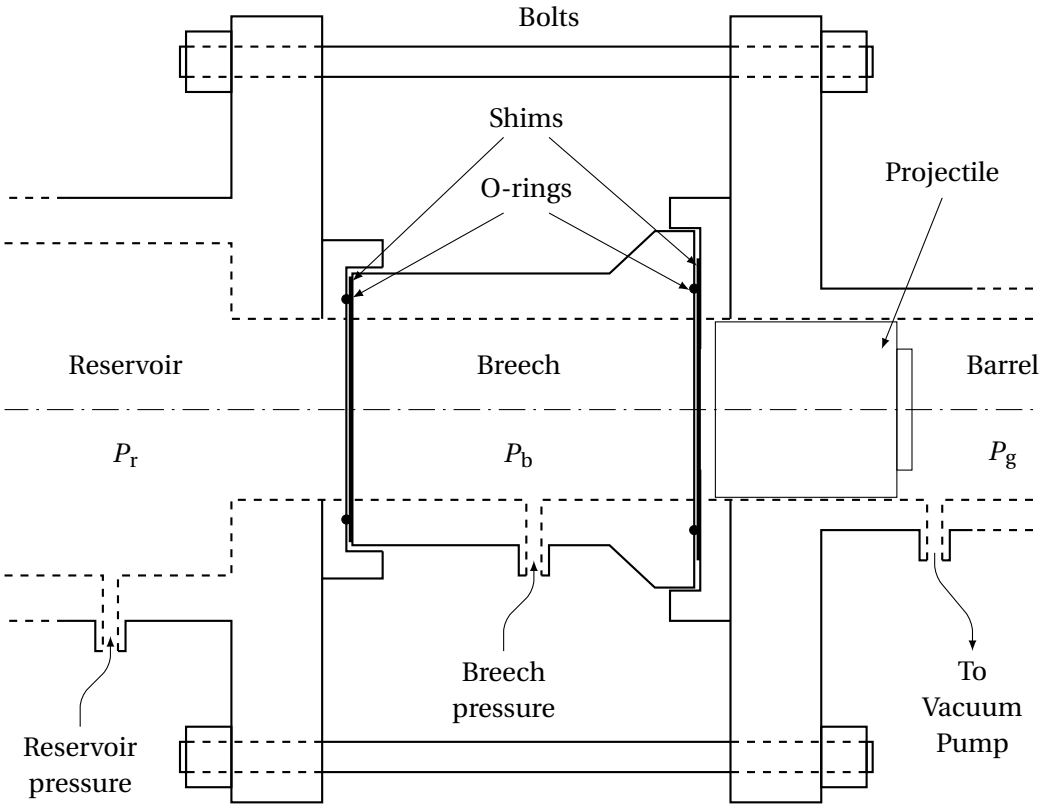

Figure 5.4: Diagram of the gas gun breech. This utilises a double-shim, bursting diaphragm system.

5.2.1 Breech design

The gas gun is fired using a bursting-diaphragm breech system (see figure 5.4). This utilises a removable breech, which is placed between the barrel and the reservoir of the gun. Brass or steel shims of a known bursting pressure P_{burst} are secured between the breech and the reservoir, and between the breech and the barrel. Once the breech and shims are in place, the system is tightened using four large bolts to prevent leakage. The barrel is then evacuated to pressure P_{g} and the reservoir and breech filled to pressures P_{r} and P_{b} respectively with either Nitrogen or Helium gas, such that P_{r} is the desired driving pressure and the following conditions are satisfied:

$$\begin{aligned} P_{\text{r}} &> P_{\text{b}} > P_{\text{g}} \\ P_{\text{r}} - P_{\text{b}} &< P_{\text{burst}} \\ P_{\text{b}} - P_{\text{g}} &< P_{\text{burst}} \end{aligned} \tag{5.1}$$

To fire the gun, P_{b} is lowered such that $P_{\text{r}} - P_{\text{b}} > P_{\text{burst}}$, causing the rear shim to burst. This leads to a sharp increase in P_{b} such that $P_{\text{b}} - P_{\text{g}} > P_{\text{burst}}$, which bursts the front shim causing the projectile to be launched. The principal advantage of the double-shim system adopted here is that it allows any firing pressure (P_{r}) between P_{burst} and $2P_{\text{burst}}$ to be used.

5.2.2 Light curtain array

The light curtain array (LCA) located at the end of the barrel consists of three emitter - detector pairs (Honeywell S&C IR-emitting diode, 880nm, TO-46; Honeywell S&C Optoschmitt Detector, TO-46), located 30 mm apart along the barrel axis. When a projectile passes through each emitter-detector pair, the light incident on the detector is blocked. As both the distance between the beams and the length of the projectile are known, this may be used to calculate the velocity of the projectile. Light curtain signals are recorded on a Tektronix DPO3034, 300 MHz 2.5 GS/s Oscilloscope. An example output from the

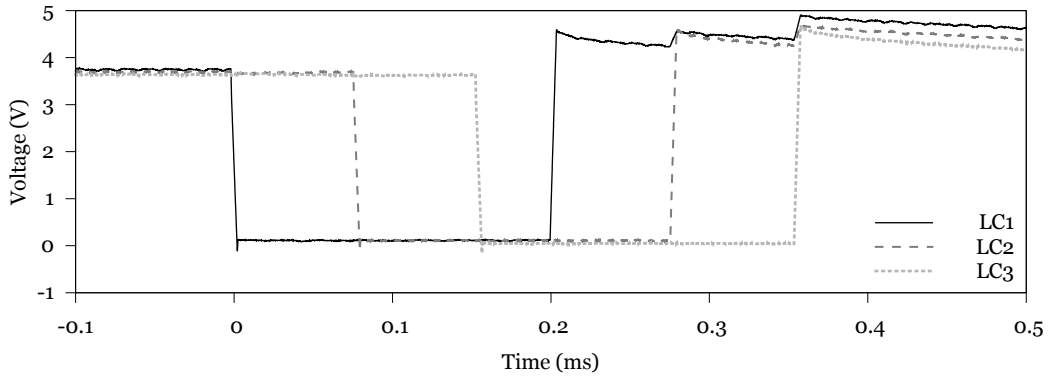

Figure 5.5: Example output from the light curtain array. As a projectile passes through the array, the signal to the sensors is blocked. If the distance between the detectors is known, this can be used to calculate the velocity of the projectile

LCA is given in figure 5.5. For each light curtain, the projectile is deemed to be at the light curtain at the time at which the signal falls below 2 V, and to have passed the light curtain at the time at which the signal rises again above 2 V. The signal rise time for each emitter-detector pair is 4 μs.

5.2.3 Projectile design

The projectile used consists of a 50 mm diameter, 15 mm thick mild steel disk, held within a 70 mm diameter nylon 6 tube. The first design of this projectile is shown in figure 5.6 (a). This consisted of a 75 mm long hollow nylon 6 tube with a 10 mm deep, 50 mm diameter recess at the front into which the steel projectile was superglued. Once in place, 5 mm of the steel protruded beyond the nylon. The approximate total mass of the projectile was 390 g, although this was batch dependent. At velocities exceeding 400 ms^{-1} it was found that the nylon section of these projectiles was fracturing in the barrel of the gun prior to impact. This lead to inconsistent results, possibly due to the broken projectiles tumbling on exit from the barrel.

A second, more robust design is shown in figure 5.6 (b). This design has a solid core, and mass removed from the outside to reduce weight. The total projectile mass is approx-

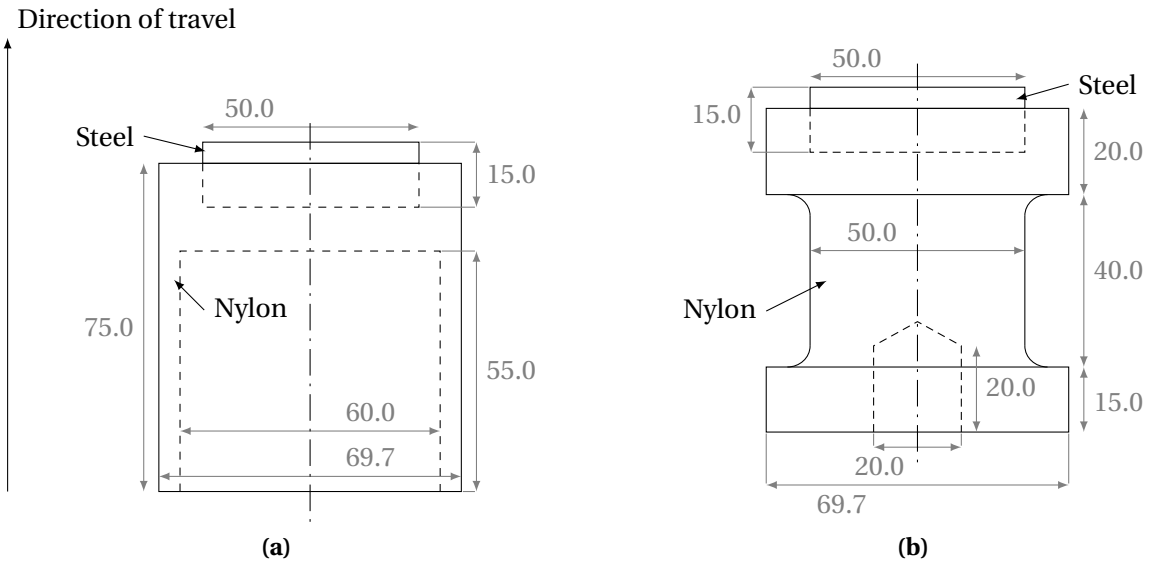

Figure 5.6: Projectile configurations. (a): First design (b): Second design. Dimensions in mm.

imately 450 g. High speed imagery at the point of barrel exit verified that this projectile design has sufficient strength to withstands shot velocities up to 600 ms^{-1}. An HDPE version of the projectile, of approximate mass 415 g, was found to be capable of withstanding shot velocities of at least 700 ms^{-1}.

5.2.4 Striker plate assembly

Shock waves in the target hydrogel block are produced by the impact of the projectile against an aluminium striker plate of thickness 25 mm, behind which the hydrogel is placed (see figure 5.7). The striker plate is used to seal the vacuum chamber such that the gun barrel may be evacuated, with an o-ring placed between the striker plate and vacuum chamber to prevent leakage. Additionally, the plate provides an impedance matching layer between the steel projectile and hydrogel. Estimates, based on the solution of Riemann problems at the interfaces between the materials, suggest that the use of the aluminium plate increases the pressures in the hydrogel block by approximately 30%, relative to the direct impact case.

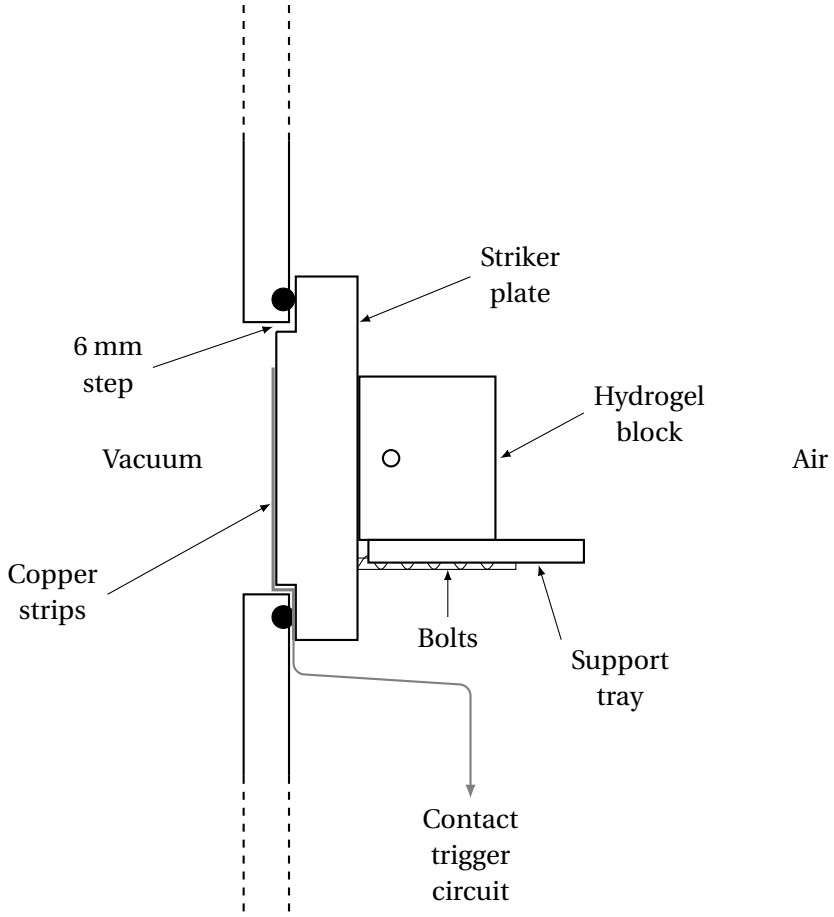

Figure 5.7: Expanded view of the striker plate assembly (see figure 5.2). Projectiles impact the striker plate from the left, leading to the formation of shock waves which propagate from left to right into the target hydrogel block

The impact of the projectile on the aluminium striker plate can lead to the formation of a bright flash of light. This is possibly due to the presence of a small pocket of air trapped between the two surfaces, as the vacuum chamber can only be evacuated to 0.8 Torr. The high pressures and temperatures caused by the compression of this gas may be sufficient to cause light emission from the gas itself, or to ignite the aluminium on the face of the striker plate. To reduce the influence of this flash on the light detection diagnostics, a 6 mm step has been incorporated into the design of the striker plate. This removes any direct line of sight between the light flash inside the vacuum chamber and optical diagnostics situated outside the vacuum chamber until after the striker plate has

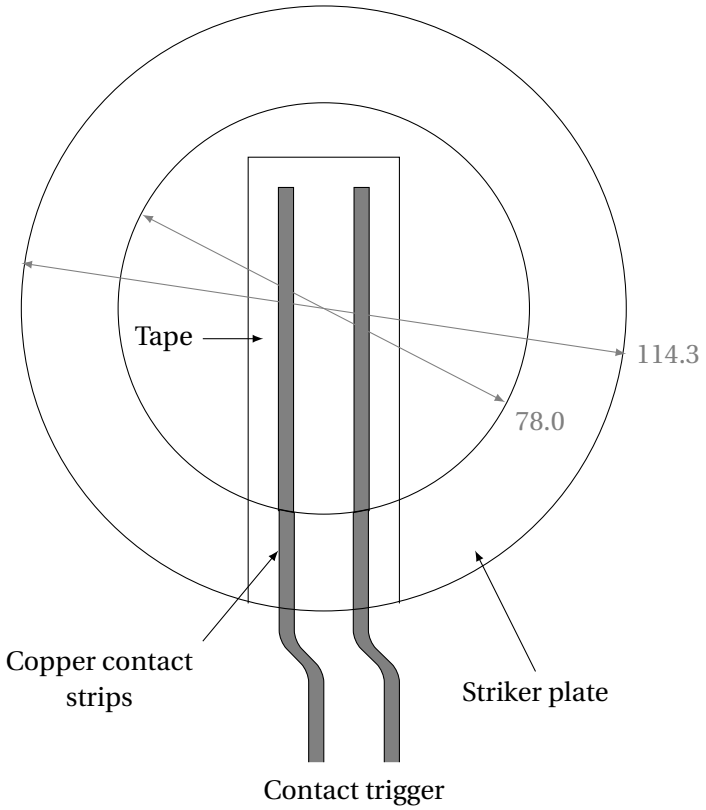

Figure 5.8: Frontal view of the striker plate. Copper strips are taped on to the front of the striker plate, such that an electrical connection is made when the steel projectile makes contact. This may be used to trigger diagnostics. Dimensions in mm.

moved away from the vacuum chamber. This takes approximately 100 µs from the point of projectile impact, which is sufficient to separate the impact flash temporally from the cavity light emission, which ceases at most 30 µs after projectile impact.

On the impact-side of the striker plate, two copper strips are attached (figure 5.8). These are connected to the triggering circuit and provide a completed electrical connection when the steel projectile strikes the plate. More detail on the triggering system is given in section 5.3.

To support the hydrogel block behind the striker plate, a PVC support tray is used. The tray sits on two 50 mm M6 bolts, which are screwed into the back face of the striker plate. The tray is positioned a small distance away from the striker plate to prevent any shock

propagation within the tray. The hydrogel may then be placed on the tray, directly against the back face of the striker plate as shown in figure 5.7. Care is taken to eliminate any air bubbles trapped between the two during this process.

5.2.5 Containment and debris collection

Protection of diagnostic equipment is achieved though the use of a rectangular mild-steel primary containment vessel, which is secured over the end of the barrel and target hydrogel block before each shot. The outside width of the primary containment is 1350 mm, the outside length is 1270 mm, and the outside height is 1540 mm. The thickness is 12 mm. A mild steel tube of outside diameter 193.7 mm, thickness 10 mm and length 820 mm attached to the back of the primary containment funnels any debris from the shot out of the primary containment and into a sand trap behind. The primary containment is mounted on rails, and can be moved backwards away from the end of the barrel to allow access to the end of the barrel. All imaging and light detection diagnostics are situated outside the primary containment; events are observed through three port windows of diameter 100 mm. These windows are situated in-line with the hydrogel, with one window on each side and one above. The windows used for light detection diagnostics (Global Optics) are made of fused silica and are of thickness 10 mm, while the window used for imaging diagnostics is made of laminated glass and is of thickness 11.4 mm. The primary containment and sand trap, as well as much of the diagnostic equipment such as cameras and light detection equipment, are contained in a much larger secondary containment chamber, which is shut with an inter-locking system prior to each shot. This prevents the gun from being fired whilst the doors to the secondary chamber are open.

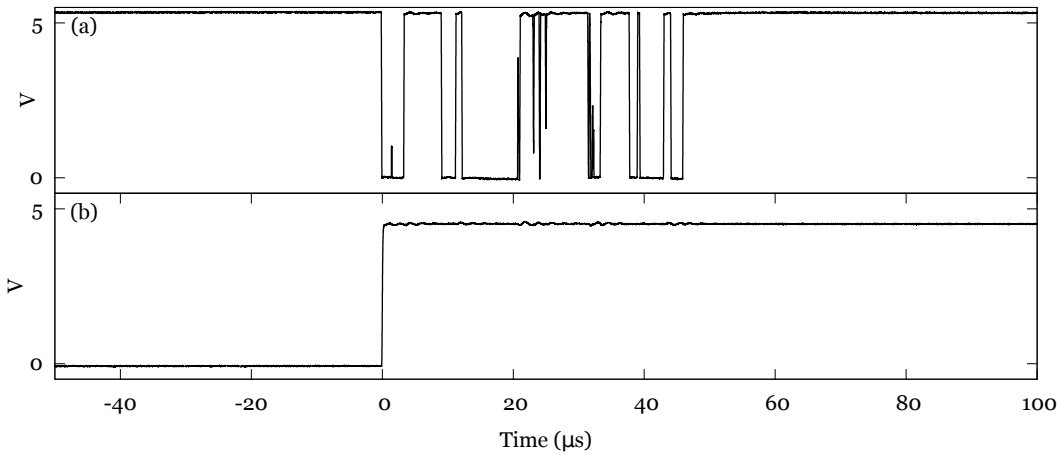

Figure 5.9: Contact trigger: example triggering signal. (a): output from the Schmitt-trigger buffer chip (b): output TTL produced by circuit.

5.3 TRIGGERING SYSTEM

To trigger diagnostics, two copper strips of thickness 0.051 mm are taped on to the impact face of the aluminium striker plate using double sided tape (figure 5.8). The strips are of width 5 mm, length 120 mm, and spaced 9 mm apart (all lengths approximate). One strip is held at 5 V, while the other is pulled to ground. In addition to securing the contact strips, the tape also serves as an insulating layer to prevent electrical contact through the aluminium. The impact of the steel projectile on the copper strips closes the circuit, which results in the generation of a TTL-compatible trigger signal.

To produce a TTL-compatible trigger signal from the raw signal from the contact strips, a circuit based on a 555 timer chip is used (see figure A.1). This chip is set up to operate in monostable mode, such that the output is a single positive pulse of length $t_p = 516\,\mu s$. A Schmitt-trigger buffer chip is incorporated into the circuit between the copper strips and the 555 timer chip, to perform contact debouncing and signal conditioning. Full details of the circuit may be seen in section A.1. With this circuit, diagnostics are triggered 160 ns after first contact of the projectile on the striker plate. An example TTL signal from the contact trigger is given in figure 5.9.

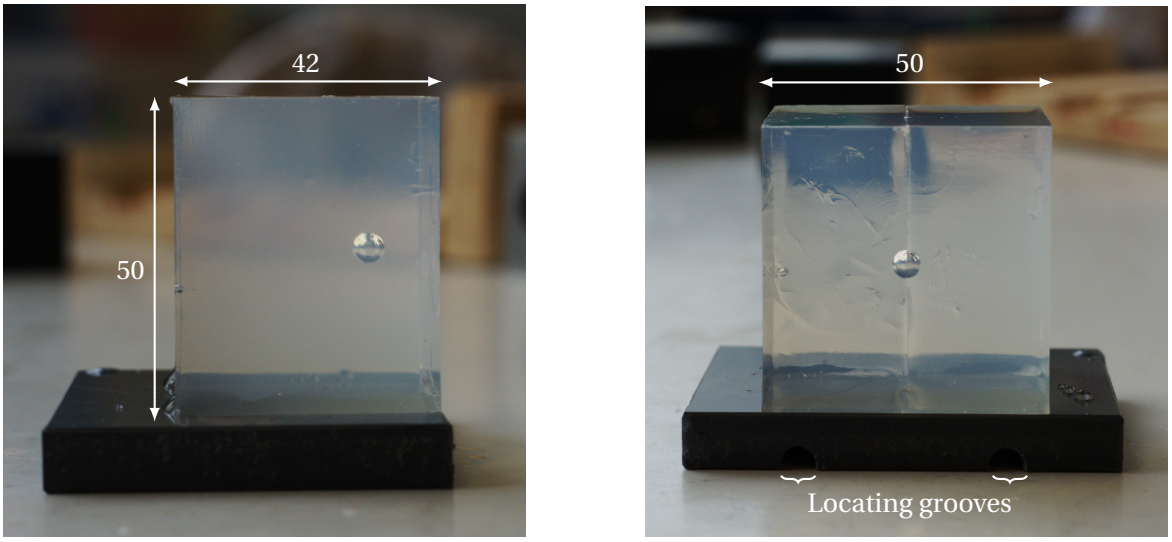

(a) **(b)**

Figure 5.10: Hydrogel block containing single 5 mm diameter spherical cavity on support tray. (a): Side view (b): front view.

5.4 TARGET DESIGN AND MANUFACTURE

As in the work of Dear *et al.*[4], cavities are created in this study by the method of casting in hydrogel blocks. However, in a modification to the work of Dear and Field cavities are cast into the face of two hydrogel block halves, which are then placed against each other to create three dimensional cavities in the centre of a complete hydrogel block (see figure 5.10). In such a way the casting of spherical cavities is made possible. The experiment is designed such that the entire hydrogel block is struck by the incident shock wave, and the hydrogel halves are made sufficiently thick that reflections from the outer surfaces of the blocks do not influence the cavity during collapse.

5.4.1 Hydrogel

The hydrogel used in this study is gellan gum (Phytagel^{TM}, Sigma-Aldrich). This was chosen because of its ease of handling and optical clarity. The hydrogel is made up by heating 0.5 % gellan gum by weight with degassed deionised water to 90 °C, adding 0.05 % CaCl

salt before allowing the solution to cool to 50 °C. The mixture is stirred during heating and cooling. At 50 °C, the mixture is poured into moulds and allowed to cool completely to room temperature, setting at 30 °C. Once fully set, lids are placed on the moulds to prevent dehydration; the hydrogel may then be refrigerated for several days if required. The particular hydrogel and salt concentrations were chosen to produce a clear gel that was sufficiently strong to maintain its shape without support. The water is degassed prior to the making of the hydrogel using an aspirator vacuum pump (Cole-Parmer #35031-10).

5.4.2 Moulds

Images of the hydrogel moulds are given in figure 5.11. Each mould consists of a rectangular tube of internal cross section 42 mm x 50 mm and length 177 mm. This tube is made up of two perspex plates and two aluminium plates which slot together. Into this tube are placed two end blocks, each of which consists of an aluminium back plate which is pushed against the end of the tubes; an aluminium block of length 30 mm and cross section 41.95 mm x 49.95 mm; and a removable Delrin face plate of thickness 10 mm which is bolted on to the aluminium block (figure 5.11 (a) and (b)). The aluminium block and face plate have been sized such that they may slide freely in the tube, whilst preventing leakage. To cast cavities in the hydrogel blocks, stainless steel ball bearings or Delrin cylinders are glued into the Delrin face plates (figure 5.11 (c)). This allows the casting of spherical or cylindrical cavities, respectively. The easily exchanged face plates are thus the only part of the moulds specific to any particular cavity configuration. A spacer may be placed between the aluminium block and back plate, to adjust the thickness of the hydrogel block produced (figure 5.11 (b)).

When pouring the hydrogel into the moulds, one of the side plates in the tube is removed, and the hydrogel poured directly into the mould. Care is taken not to entrain bubbles during pouring. The hydrogel is then allowed to set fully before the side piece is

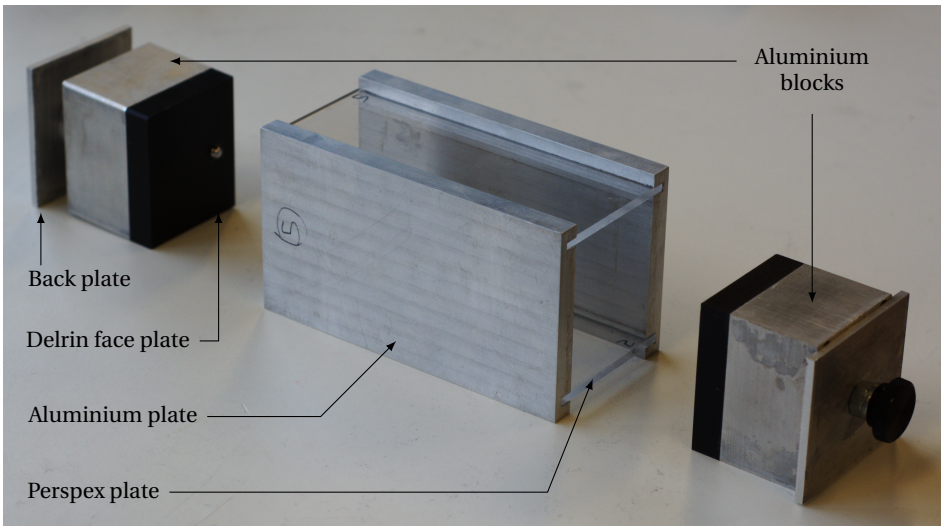

(a)

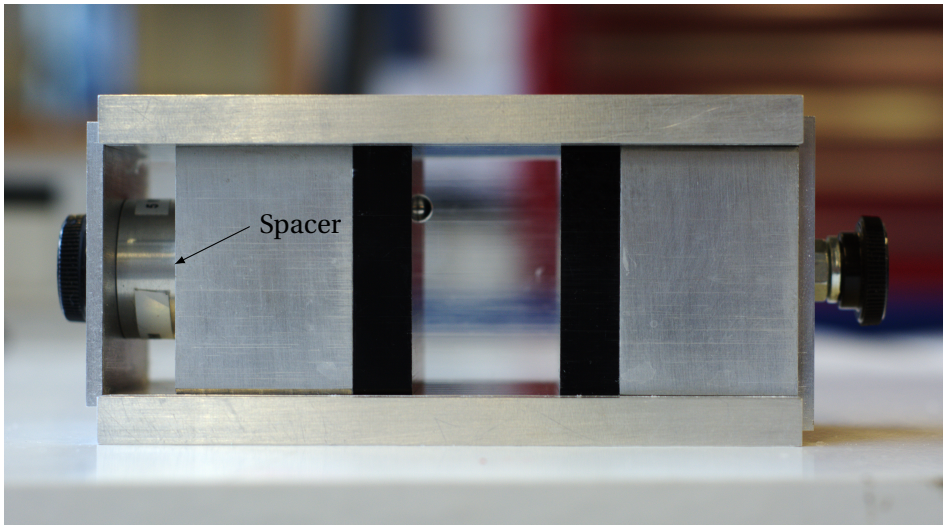

(b)

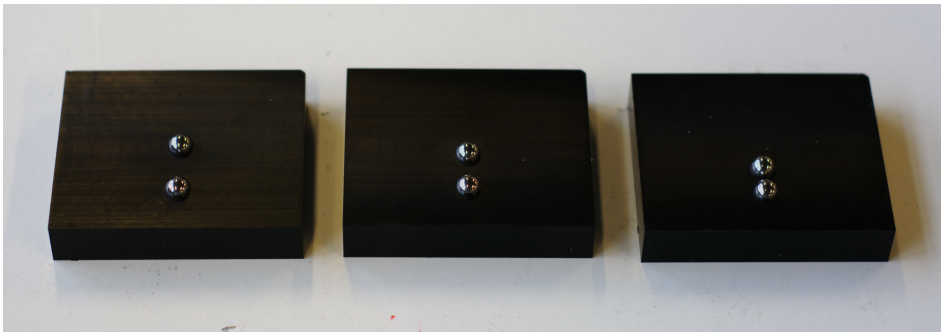

(c)

Figure 5.11: Images of the hydrogel moulds. Each mould consists of an assembled rectangular tube, into which end blocks are placed. To pour the hydrogel, one side of the tube is removed. Two moulds are required to create a complete block for testing. (a): Exploded view of a single sphere mould. (b): Combined single sphere mould. (c): Double 5 mm sphere Delrin face plates.

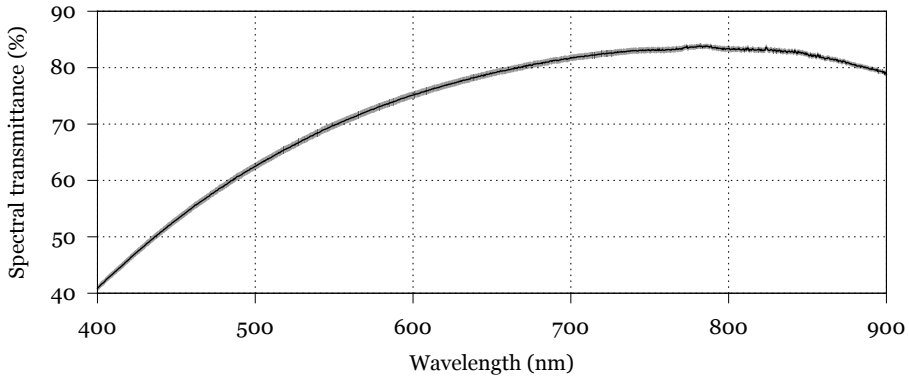

Figure 5.12: Calculated spectral transmittance (T_{sample}) of a 25 mm thick block of hydrogel. Shaded region shows the errors, calculated as in equation 5.5.

replaced, to allow for shrinkage in the hydrogel as it cools.

5.4.3 Light transmission through hydrogel

Figure 5.12 shows the spectral transmittance of a 25 mm block of hydrogel. As can be seen, spectral transmittance drops off significantly at shorter wavelengths. These measurements were made on a Varian 50 Bio UV/Visible spectrometer, with the hydrogel set in polystyrene cuvettes (theconsumablescompany.com 4ml square push cap tube polystyrene), with a sample width of 10.1 mm. To account for the effect of the cuvette, the measured spectral transmittance was compared to that of deionised water in the same cuvettes, for which the spectral transmittance T_{water} is known. The spectral transmittance of the hydrogel T_{gel} is calculated as:

$$T_{\text{gel}} = \frac{T_{\text{gel, cuvette}}}{T_{\text{water, cuvette}}} T_{\text{water}} \tag{5.2}$$

where $T_{\text{gel, cuvette}}$ is the measured spectral transmittance of hydrogel in the cuvette, and $T_{\text{water, cuvette}}$ is the spectral transmittance of water in the cuvette. This assumes that the index of refraction of the hydrogel and water are the same; based on hydrophone measurements (see section 5.7), the index of refraction of the hydrogel has been measured to be within 1% of the measured value for water. This corresponds to approximately a 0.1%

difference in the calculated spectral transmittance of the hydrogel, which is considerably less than other uncertainties in the spectral transmittance measurement.

To scale the spectral transmittance of the cuvette up to the full thickness of a hydrogel block the Beer-Lambert law[206] can be used,

$$T = e^{-\alpha l} \tag{5.3}$$

where α is the attenuation coefficient and l is the sample length. Applying this equation to the spectral transmittance within the cuvette and at the required thickness, the spectral transmittance T_{sample} can be found:

$$T_{\text{sample}} = T_{\text{gel}}^{(l_{\text{sample}}/l_{\text{cuvette}})} \tag{5.4}$$

where l_{cuvette} is the thickness of the hydrogel within the cuvette (10.1 mm), and l_{sample} is the thickness at which the transmission is to be found.

Errors in the calculation of the spectral transmittance of the cuvette $\left(e_{T_{\text{gel}}}\right)$ are calculated as the standard error, comparing multiple different combinations of hydrogel samples and water samples. This error is scaled to account for thickness using equation 5.5, producing the errors as shown in figure 5.12.

$$e_{T_{\text{sample}}} = \left| \left(\frac{l_{\text{sample}}}{l_{\text{cuvette}}} \right) T_{\text{gel}}^{(l_{\text{sample}}/l_{\text{cuvette}}-1)} e_{T_{\text{gel}}} \right| \tag{5.5}$$

5.5 IMAGE CAPTURE

5.5.1 High-speed imaging

A diagram of the setup used for imaging and light detection is shown in figure 5.13. A Specialised Imaging SimX 16 high speed camera is used to view the cavity collapse through a 50 R / 50 T plate beam splitter (Edmund Optics #46-583, 127x178 mm), which splits light equally between the imaging and light detection setups. The camera is capable of

acquiring sixteen 1280 × 960 pixel black and white images, at a maximum effective frame rate of 200 Mfps. A key advantage of this camera is that a separate CCD is used for each frame. This enables individual control of the timing, exposure and gain for each frame. A Sigma DG 70-300mm Macro lens is used with the camera. The iris is held fully open, at an f-number of $f/4.0$.

The camera is utilised with and without external illumination. When illumination is required, the hydrogel block is back-lit using a 200 W pulsed diode laser (Cavilux SMART, Cavitar Ltd.). This laser has a 25 µs maximum pulse length, a 640 nm centre wavelength and an approximate bandwidth of 7 nm.* As this light source is relatively narrow band, it is possible to prevent light from the illumination source being detected by the light detection setup by using suitable bandpass filters. The output from the laser is directed through a liquid light guide and collimator, on to the hydrogel block. This enables imaging of the cavity wall during collapse, as well as shock waves as they pass through the hydrogel. As light passes through the hydrogel block, gradients in the density of the medium refract the light. If the light is refracted through a sufficiently large angle it will not be captured by the camera; in such a way shock waves passing through the hydrogel appear as dark lines in the captured images. As density gradients are extreme at shock fronts, no knife-edge is required to block refracted light, as used in a conventional schlieren imaging system.

Behind the incident shock front, the system as described to this point is too sensitive to gradients in density, and the images appear black. To reduce this sensitivity, the output of the laser is directed through a 100 mm diameter, 120 grit ground glass diffuser plate (Edmund Optics). In addition to improving the uniformity of the light source, this scatters the light as it passes through the plate, meaning that light is incident on the hydrogel block from a cone of angles, rather than in a single column. As such, light may reach the camera lens even if it is diffracted through a large angle, and the sensitivity of the system

*Full width at half height

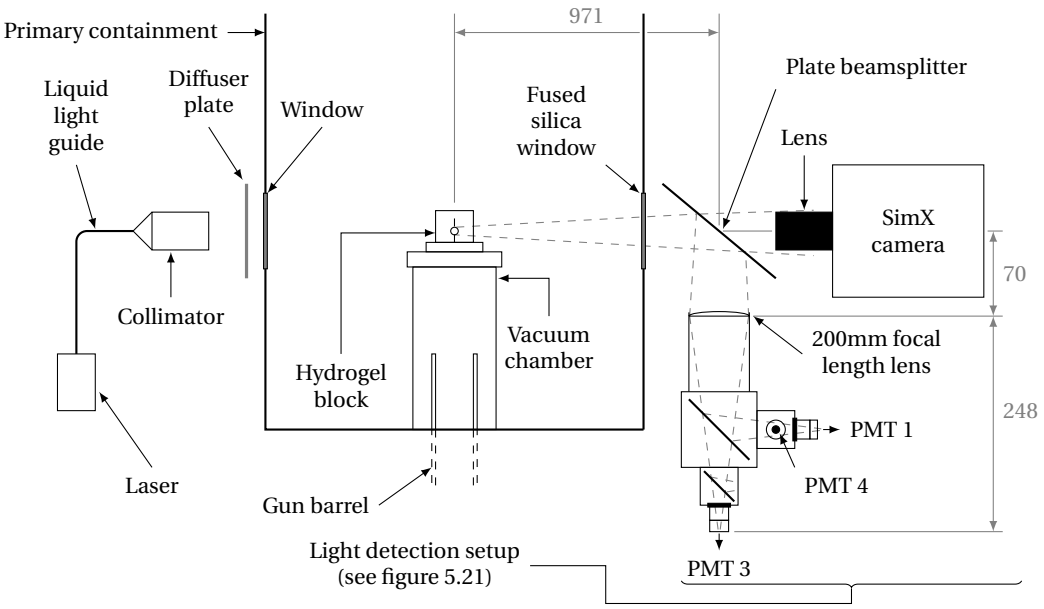

Figure 5.13: Diagram of the imaging and light detection setup, top-down view (not to scale). Dimensions in mm.

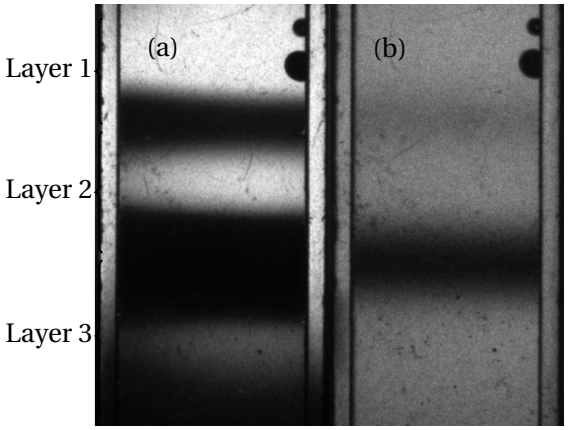

Figure 5.14: Effect of diffuser plate on sensitivity of high-speed imaging to density gradients. Images show a cuvette of sugar water with three distinct regions of different density. The interfaces between the layers can be seen as two dark bands in the images. In image (b), more of the diffuser plate is illuminated than in image (a). This can clearly be seen to reduce the sensitivity of the imaging system, decreasing the thickness of the dark bands.

is reduced. An example of the effect of the diffuser plate on the imaging sensitivity is given in figure 5.14. This figure shows two images of a cuvette of sugar water, which has been made up to create three distinct layers of differing density. As can be seen, the gradient in density at the interfaces between the layers leads to the formation of thick black bands

in the images. By illuminating more of the diffuser plate, and thus increasing the maximum angle with which light is incident on the cuvette, the sensitivity of the system is substantially reduced.

When no external illumination is used, light emission from cavities during collapse may be imaged. The inter-frame time of the camera is reduced to zero to ensure all light is captured. If back-lighting is used but with reduced intensity, simultaneous imaging of the shock formation during cavity collapse and cavity light emission is possible.

5.5.2 Rear-view imaging

In addition to the side-on imaging of the hydrogel block as described in section 5.5.1, by using a mirror placed behind the hydrogel block the collapse may be viewed from the rear. This mirror is sacrificial, and is replaced for every shot. A diagram of the setup used to achieve this is shown in figure 5.15. To illuminate the images taken using this setup, the Cavitar light source and collimator are moved to the spare port on the light detection setup (see section 5.6). Light from the source is then focussed by the field lens via the mirror on to the hydrogel block, before reflecting from the aluminium striker plate, back on to the mirror and into the camera lens. In order to prevent uneven reflections from the striker plate, the face of the plate is roughened prior to the shot to a matt finish. The brightness of the source can be altered by adjusting the focus of the collimator.

5.5.3 Long-exposure photography

In an alternate imaging setup, the SimX is replaced by a Nikon D7100 DSLR camera, with the same Sigma lens as used with the SimX. No external lighting is used. In this setup, a single long exposure image may be taken of light emission during cavity collapse. This allows the colour of the light emission to be observed. As it is not possible to trigger the DSLR sufficiently quickly to use the contact trigger, it is triggered manually immediately

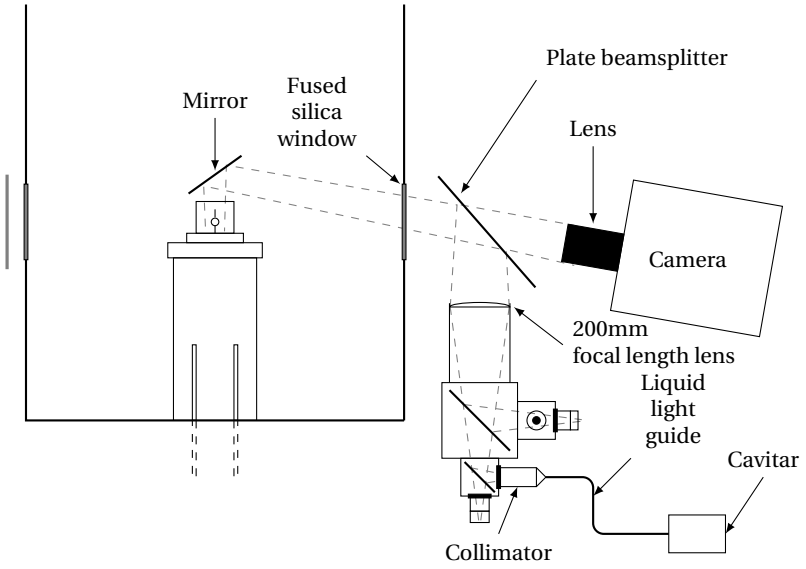

Figure 5.15: Diagram of the setup used for rear-view imaging and light detection. When lighting is used, the Cavitar laser is shone through one of the PMT ports. The light reflects through the system of beamsplitters onto the striker plate, where it is reflected back onto the camera lens.

before the shot.

5.5.4 Calculation of image dimensions

In order to calibrate the spatial length scales of the experimental images, a set of frames are taken after each shot of a calibration plate (Thorlabs, R2L2S1P Positive NBS 1963A Resolution Target). The plate is placed directly against the striker plate, such that the markings are located the same distance from the camera as the centre of the cavity. A SimX calibration frame of the plate is shown in figure 5.16. As can be seen, the plate is marked with a number of blocks, each consisting of 5 lines of a known equal thickness and spacing. The particular blocks used for the calibration are shown in red in the figure. The marked numbers on the plate, upside down in this frame to align the larger blocks with the imaging area, denote the cycles per mm of the adjacent blocks. To use the plate to calculate the size of the frame, the blocks in the frame must first be located. This is done using a Canny edge detector[207,208] to locate the edge of the individual lines. A Watershed algorithm[207] is then used to fill the areas of the frame inside the edges. This done,

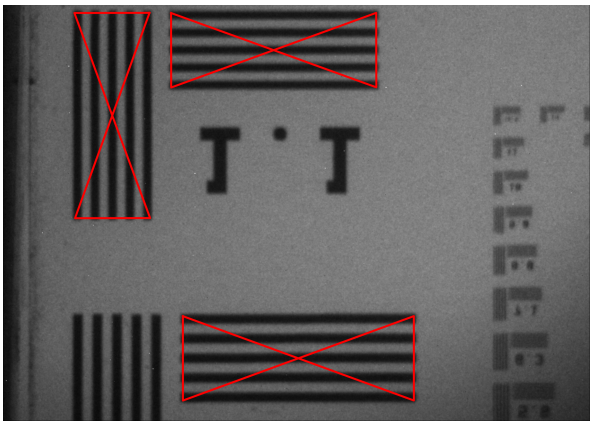

Figure 5.16: A SimX calibration frame of the calibration plate (Thorlabs, R2L2S1P Positive NBS 1963A Resolution Target), upside down to align the largest blocks with the imaging area. Red boxes show the blocks used to calculate the size of the frame.

the lines can be extracted from the frame. Extra features in the frame, for example the numbers adjacent to the lines, may be removed by inspection of the aspect ratio of each feature. Once the individual lines have been found, they are grouped by length and orientation, such that each block of five lines is a single entity. The corners and orientation of these blocks can then be found, which are subsequently passed on to the next stage of the algorithm.

Once the location of each of the blocks is known, traces may be interpolated from the frame orthogonal to the lines in each block, an example of which is shown in figure 5.17. In this study, 50 traces are interpolated from the plate per block, and up to four blocks are used from the plate. As can be seen in figure 5.17, although the lines on the plate consist of discrete dark bands with sharp interfaces, the interpolated traces approximate a cosine wave. This is primarily because the camera is focused on the cavity inside the hydrogel, whereas the plate is placed in air. The refraction of the hydrogel adjusts the focus of the frame, such that the plate appears blurry. To fit a curve to these traces, a least squares method is used where the function to be minimised is:

$$J(\mathbf{p}) = \sum_{i=0}^{N-1} e_i^2(\mathbf{p}) \tag{5.6}$$

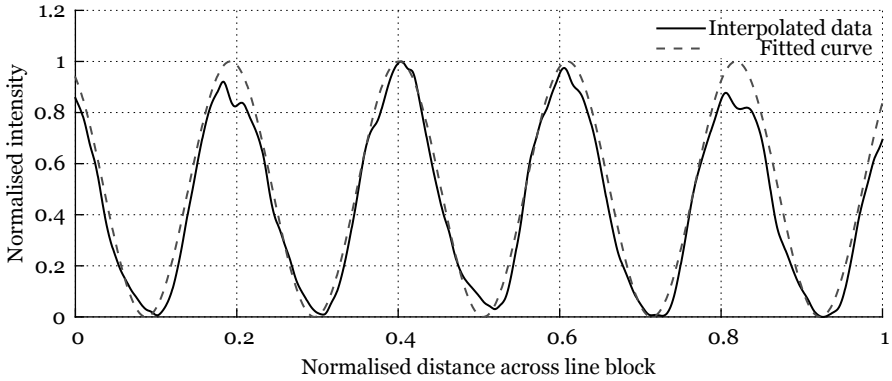

Figure 5.17: A normalised interpolated line from the calibration block, and a least squares fitted cosine wave.

where:

$$e_i(a,b,x_i,y_i) = \left\| y_i - \cos\left(\frac{2\pi x_i - b}{a}\right) \right\|. \tag{5.7}$$

x_i is the normalised distance across the line block at point i, and y_i is the corresponding normalised intensity. The fitted result is shown in figure 5.17 as the dashed line. The division of the found wavelength (a) by the cycle size of the block gives a pixels-per-mm conversion factor for the frame. Calculation of this value for all traces in the frame yields the average pixels-per-mm value for the frame. This process is repeated for all frames in the series.

5.5.4.1 Error handling

If the pixels per mm value for a single trace is p_t, the associated error (e_{p_t}) is given by the standard deviation from the least-squares fit σ_{p_t}. For each frame, the pixels per mm of the frame p_f is the mean of the pixels per mm for each trace. One measure of the error in this value is the standard error. For n traces this value is:

$$e_{f_1} = SE_f = \frac{\sigma\left(p_f\right)}{\sqrt{n}} \tag{5.8}$$

where $\sigma\left(p_f\right)$ is the standard deviation in the measured value for the frame. This assumes that the variation in the measured value is normally distributed. Alternatively, another measure of the error in the calculation per frame is the combined error of σ_{p_t} for all traces.

As all measurements of σ_{p_t} may be assumed to be independent and random, they may be summed in quadrature:

$$e_{f_2} = \frac{\sqrt{\sum_{i=0}^{n-1} \sigma_{p_{t_i}}^2}}{n}. \tag{5.9}$$

In this study, the maximum value of e_{f_1} and e_{f_2} is chosen as the error in the calculation of the pixels per mm for the frame.

5.5.5 Calculation of shock velocity

One particularly important metric that may be inferred from the high-speed images is the velocity of any shock waves as they propagate across the hydrogel block. The first step in this process is to locate the position of the shock wave in each frame in the image series. To achieve this, a linear cut is taken of each image frame in the x direction (see the red line in figure 5.18 (a)). An interpolation algorithm may then be used to calculate the pixel intensity as a function of position as a continuous and normalised curve, as in figure 5.18 (b). As can be seen, shock waves crossing the images from left to right are detectable in the interpolated traces as sharp changes in image intensity. These sharp changes can be used to locate the shock wave in each image. To achieve this, a two stage step finding algorithm is used. The first stage breaks the interpolated plot into a series of separate steps, which may be passed individually to the second algorithm (see for example the red dashed lines in figure 5.18 (b)). In such a way it is possible to analyse multiple shock waves from the same trace. The second stage algorithm takes the step sections as calculated in the first stage algorithm, and processes them more accurately to find the 10%, 50% and 90% points on the shock front, as well as the lower and upper limits (blue points in figure 5.18 (b)). An example of the application of the shock finding algorithms to a set of images is given in figure 5.19. On each image, the location of the shock wave as found at a number of positions in the y direction (i.e. vertical) in the image are shown.

For each y position, once the shock front has been located in the images, at each time

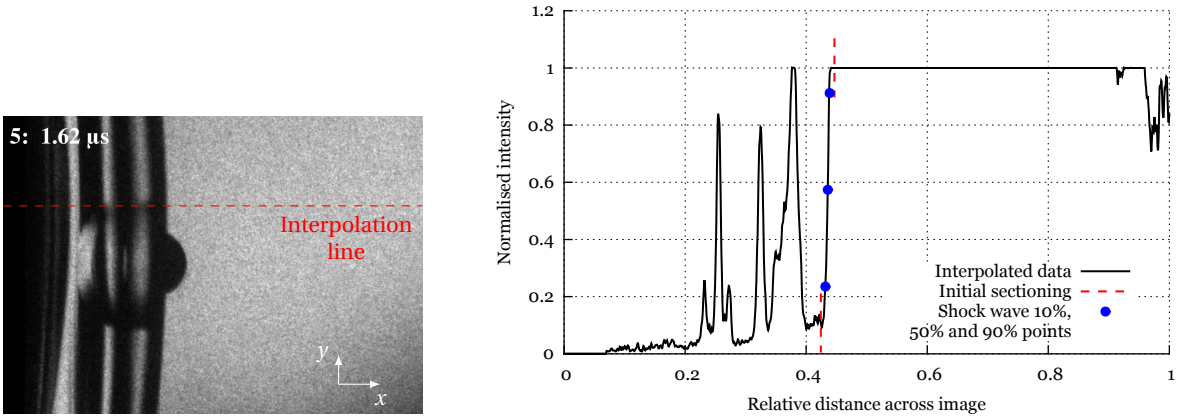

Figure 5.18: (a): SimX image showing a shock wave passing over a single cavity cast within a hydrogel block. The image intensity is interpolated along the red dashed line. (b): The interpolated line from (a). The red dashed lines denote the step limits located by the first stage of the step-finding algorithm. The blue dots mark the 10%, 50% and 90% step locations as found by the second stage of the algorithm.

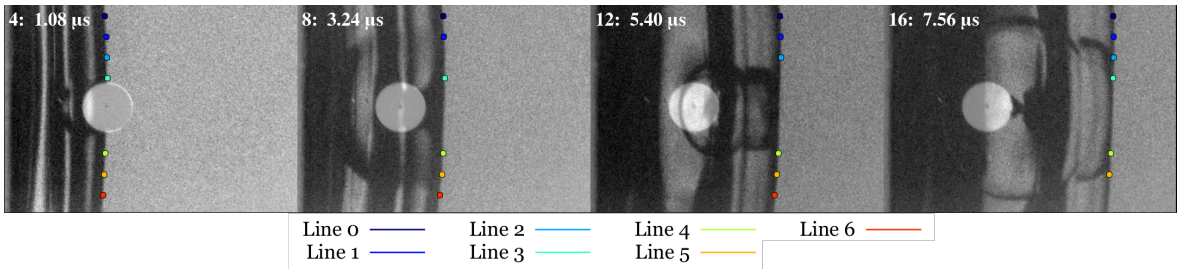

Figure 5.19: Example image array. The location of the shock at various heights in the hydrogel as found by the shock finding algorithm are marked on the images.

the distance of the shock (x_i) from some reference x coordinate x_{ref} can be found as:

$$x_i = 1 \times 10^{-3} \frac{x_{i,\text{pixels}}}{p} \text{ m} \tag{5.10}$$

where p is the pixels per mm value as calculated in section 5.5.4, and $x_{i,\text{pixels}}$ is the distance of the shock wave from x_{ref} in pixels. The error associated with the position of the shock at a particular time for a particular y position is then calculated as:

$$e_{x_i} = 1 \times 10^{-3} \sqrt{\left(\frac{e_{x_{i\text{pixels}}}}{p}\right)^2 + \left(\frac{x_{i\text{pixels}} e_p}{p^2}\right)^2} \tag{5.11}$$

where the error in the position of the shock wave in pixels ($e_{x_{i\text{pixels}}}$) is approximated as the average of the difference between the 90% and 50% position, and the 50% and 10%

Function	Mean residual (m)	Residual standard deviation (m)
Linear	7×10^{-4}	3×10^{-4}
2nd order polynomial	2.2×10^{-4}	7×10^{-5}
3rd order polynomial	1.9×10^{-4}	5×10^{-5}

Table 5.1: Mean residuals for different fitting functions when least-squares fitted to shock position data.

position. The error in the calculation of pixels per mm (e_p) is the value as found in section 5.5.4.1.

The position of the shock front at each time known, the velocity of the shock is found by differentiation of the position data. This is accomplished using central differences, apart from the first and last points where forward and backward differences are used respectively. Prior to differentiation, functions may be fitted to the position data using a least squares approach; small inaccuracies in the location of the shock wave in the SimX images can lead to large errors in the velocity data once differentiated if this is not done. Table 5.1 compares mean residuals for different fitting functions. For each shot, the residual is calculated for each y position as $\sqrt{\sum \left(x_i - x_{i,\text{fit}}\right)^2}$, where $x_{i,\text{fit}}$ is the fitted location of the shock wave at the same time as x_i. The residual value for the shot is then calculated as the mean over all y positions. The values as presented in table 5.1 are simply the mean and standard deviation, comparing the residuals across all shots. As can be seen, the lowest residuals are achieved using third order polynomial functions. This is in part because incident shocks in the experimental results can both accelerate and decelerate within the same shot. An example of this method applied to shock positional data is given in figure 5.20 (a), with the corresponding differentiated shock velocity lines shown in figure 5.20 (b). The final shock velocity curve ($u_s(t)$, shown in black in 5.20 (b)) is calculated as the mean across all lines at each point in time, with the errors calculated as the 95% confidence intervals.

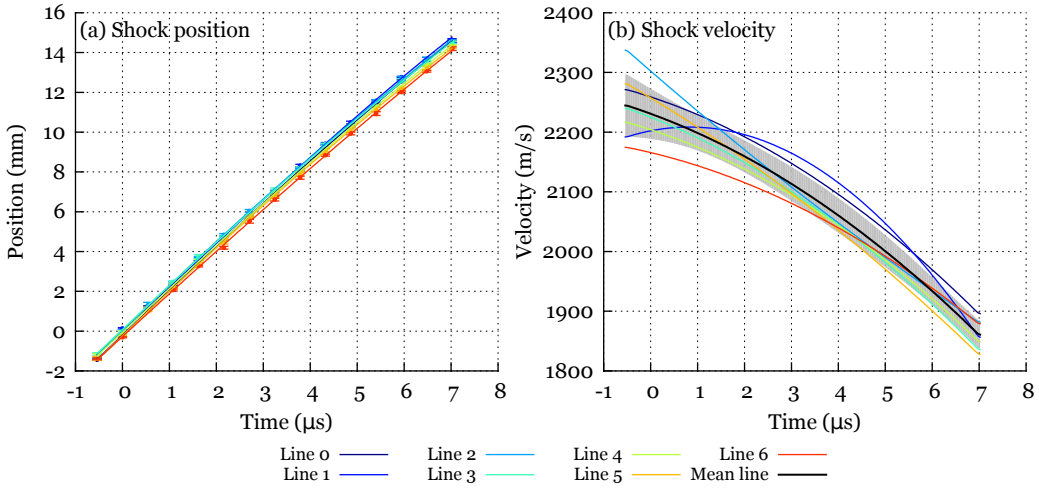

Figure 5.20: (a): variation in shock position with time, at the positions in the hydrogel block shown in figure 5.19. Fitted polynomial lines also shown for each position in the hydrogel. (b): Corresponding shock velocity curves, differentiated from the fitted lines.

5.5.6 Conversion of shock velocity to pressure

If the equation of state is known, the pressure of a shock front can be calculated from its velocity using the Rankine-Hugoniot equations. In this work, a stiffened polytropic EOS is assumed for the hydrogel, with variables fitted to experimental data as described in section 3.3.3. Utilising equation 3.10 and the Rankine-Hugoniot conditions, the density immediately behind the shock ρ_1 can be found from the shock velocity u_s as:

$$\begin{aligned}
\rho_1 &= \frac{1}{2}\frac{D+u_s^2 B}{E+u_s^2 C}\sqrt{\left(\frac{1}{2}\frac{D+u_s^2 B}{E+u_s^2 C}\right)^2+\frac{u_s^2 A}{E+u_s^2 C}} \\
A &= -\rho_0^2(C+1) \\
B &= \rho_0(1+\Gamma) \\
C &= \frac{\Gamma}{2} \\
D &= \left(p_0+p_\infty\right)(1+\Gamma) \\
E &= \Gamma\left(E_\infty+e_0+\frac{p_0}{\rho_0}\right)
\end{aligned} \tag{5.12}$$

where p_0, ρ_0 and e_0 are the ambient pressure, density and internal energy respectively, and all other variables are as in table 3.2. Particle velocity u_1 and pressure p_1 can then be

PMT number	Model	Gain (μ)	Bandpass filter (nm)	Calibration constant (W/m/V)
1	H11526-01-NF	40254	405	4430 ± 170
3	H11526-20-NF	40254	520	1664 ± 62
4	H11526-20-NF	40254	760	5925 ± 120

Table 5.2: PMT models and bandpass filters used for light detection

found from the Rankine-Hugoniot equations,

$$u_i = \frac{u_s\left(\rho_1 - \rho_0\right)}{\rho_i}$$
$$p_1 = p_0 + \rho_0 u_s^2 - \rho_1 \left(u_1 - u_s\right)^2 \tag{5.13}$$

The ambient pressure p_0 is assumed to be 1.013 bar, and the hydrogel is assumed to be initially at rest.

5.6 LIGHT DETECTION

Light detection from cavity collapse is performed using using avalanche photodetectors (APDs), photomultiplier tubes (PMTs), or an integrated spectrometer. PMTs offers greater sensitivity and temporal resolution, but at the expense of greater complexity and risk of damage. Voltages are recorded using a Tektronix DPO3034, 300MHz 2.5 GS/s Oscilloscope.

5.6.1 Photomultiplier tube

Light detection using PMTs is achieved using the setups as shown in figures 5.13 and 5.15 for side-on and rear-view detection respectively. Light from cavity collapse is reflected by an Edmund Optics plate beamsplitter on to the PMT array, a more detailed view of which is given in figure 5.21. The light must also pass through a fused silica window on the primary containment. Within the PMT array, a 75 mm diameter, 200 mm focal length fused

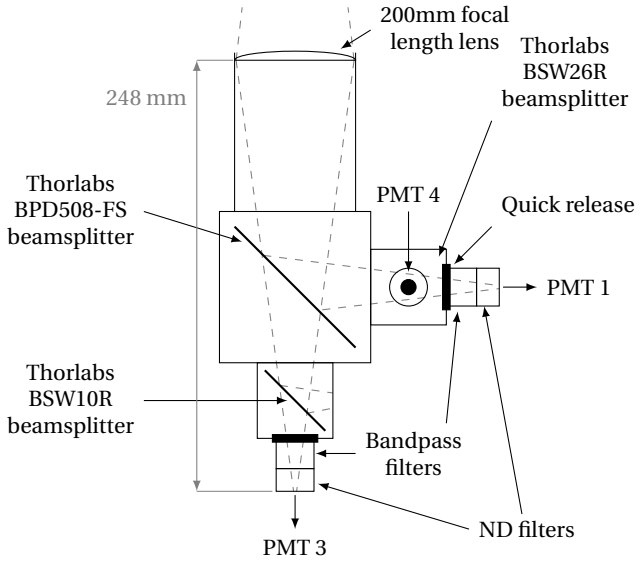

Figure 5.21: Detailed view of the PMT array. Light from cavity collapse is focussed by the field lens onto a series of beamsplitters, which split the light on to 4 different PMT ports. Only three of the PMT ports are used.

silica field lens (Thorlabs) is used to focus light on to three PMT modules, via a series of beamsplitters. The models of the PMTs used are given in table 5.2. Each PMT has a different 10 nm bandpass filter placed in front of it (Thorlabs or Edmund Optics), and thus only monitors the variation in light emission with time over a narrow band of wavelengths. By comparing this variation across the different wavelength bands, information about the variation of the spectrum of the emitted light over time can thus be inferred.

The spectral working range of the two PMT models used are illustrated by figure 5.22, which shows the representative cathode radiant sensitivity of the modules. All three PMTs have an inbuilt time gating system, a temporal resolution of approximately 0.6 ns, and a sensor diameter of 8 mm. This sensor diameter gives an approximate field of view of diameter 34 mm. Neutral density filters (Thorlabs, mounted UV fused silica reflective) are used to moderate the intensity of the light incident on the sensors.

In order to control the inbuilt time gating system of the PMTs, an additional circuit is required. This circuit receives the positive TTL pulse produced by the contact trig-

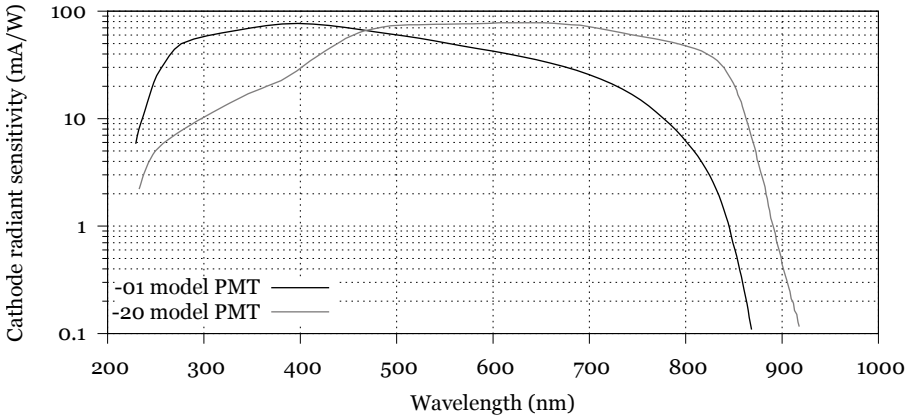

Figure 5.22: PMT cathode radiant sensitivity (χ) (representative data, supplied by Hamamatsu).

ger circuit, and outputs a substantially shorter TTL pulse, which sets the gating time for the PMTs. Much like the contact trigger circuit, this circuit utilises a 555 timer set up in monostable mode. A 500 Ω variable resistor allows adjustment of the pulse length, and is set to give a 40 µs pulse. This is sufficiently long to capture light emission from cavity collapse, whilst minimising the exposure of the PMTs to the impact flash at later times. Full details of the circuit used to trigger the PMTs, as well as the circuit used to detect errors in the functioning of the PMTs are given in appendix section A.2. These circuits were designed and built by Dr. Phillip Anderson.

5.6.1.1 Calculation of power

For a particular shot, s, for a particular PMT, the output voltage generated by the PMT over time (t) in volts ($V_s(t)$) is related to the spectral radiant flux[209] $\left(\Phi_{\lambda,s}(\lambda,t)\right)$ of the light incident on the light detection system (units W/nm), adjusted for transmission through the hydrogel, by the following equation:

$$V_s(t) = R l_s(V_s)\,\mu \int_0^{\infty} \chi(\lambda)\,\Phi_{\lambda,s}(\lambda,t)\,f_s(\lambda)\,f_{BP}(\lambda)\,d\lambda. \tag{5.14}$$

In this equation λ is the wavelength of the incident light (nm); R is the load resistance of the scope (50 Ω); l_s is the linearity of the response, which is dependent on the voltage but approximately equal to 1.0 below 0.9 V (see section 5.6.1.3); μ is the gain of the PMT;

$f_s(\lambda)$ is the combined spectral transmittance of the light detection system and hydrogel; and $f_{BP}(\lambda)$ is the spectral transmittance of the bandpass filter used. $\chi(\lambda)$ is the cathode radiant sensitivity of the PMT in A/W, and is defined as the current generated by the photocathode per unit power at a given wavelength. The variation of $\chi(\lambda)$ with wavelength for typical PMT modules is shown in figure 5.22. As the bandwidths of the bandpass filters used are so narrow, equation 5.14 may simplified by assuming that $\chi(\lambda)$, $\Phi_{\lambda,s}(\lambda)$ and $f_s(\lambda)$ do not vary with wavelength over the bandwidth of the bandpass filter, and take the values at the wavelength of peak spectral transmittance of the bandpass filter $s(\lambda_{BP})$, $\Phi_{\lambda,s}(\lambda_{BP})$ and $f_s(\lambda_{BP})$. Equation 5.14 can then be written as

$$V_s(t) \approx R I_s(V_s)\, \mu s(\lambda_{BP})\, \Phi_{\lambda,s}(\lambda_{BP}, t)\, f_s(\lambda_{BP}) \int_0^\infty f_{BP}(\lambda)\, d\lambda. \tag{5.15}$$

Prior to the calculation, voltages are first filtered to reduce the effect of noise. This is achieved using a Savitsky-Golay[210] filter, with a window size of 51 points (20.4 ns). This method fits successive sub-sets of adjacent data points to low (in this case 5th) order polynomials using linear least-squares. It was determined empirically that this method provided the optimal reduction in noise levels whilst preserving the underlying data.

5.6.1.2 Calibration

The quantities μ, $s(\lambda_{BP})$ and $f_s(\lambda_{BP})$ are not known accurately in equation 5.15, and the system must therefore be calibrated before use. This is achieved using the arrangement shown in figure 5.23. A Bentham CL6 II calibrated light source (clear bulb), powered by a Bentham 605 supply provides light input into the system. This device is calibrated to produce a known irradiance in units of W/m^2/nm, at a distance of 5.5 mm from the exit of the device. An iris is placed at this distance, with a known area. The spectral radiant flux of the light incident on the system ($\Phi_{\lambda,c}(\lambda)$) in units of W/nm is thus known. The light that passes through the iris is focussed by a 150 mm focal length, fused silica field lens, via the plate beamsplitter, onto the PMT array. The 150 mm focal length lens replaces the

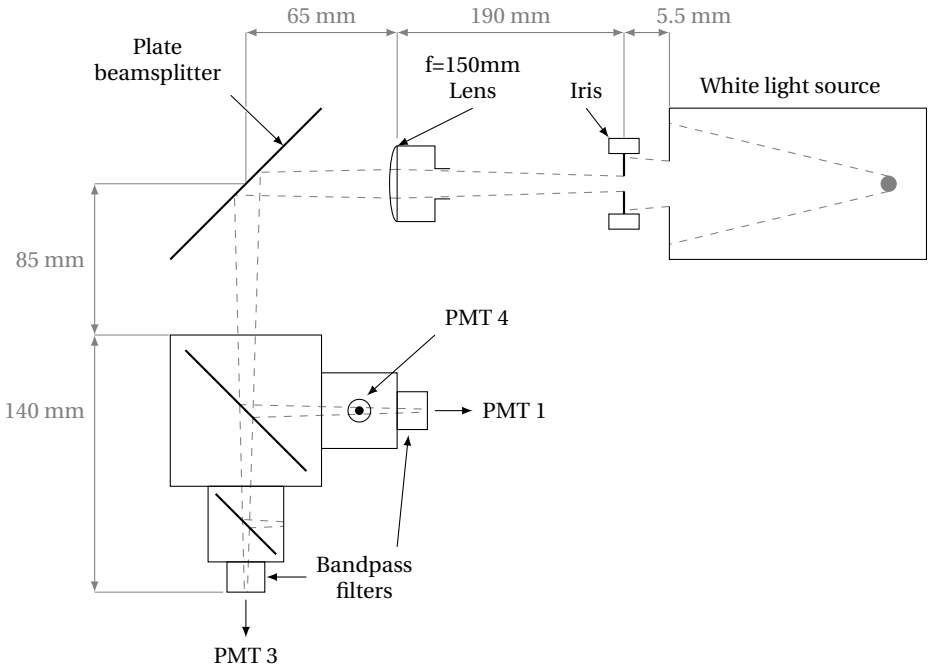

Figure 5.23: Diagram of the setup used to calibrate the PMT array.

200 mm lens as used in the experiment, as the distances are too short to allow use of the larger lens. By shortening the distances in the calibration setup, much more light can be captured by the system, and more accurate measurements made. As the thickness of the two lenses are approximately the same, it is assumed that the spectral transmittance of the two lenses is the same.

As $\Phi_{\lambda,\mathrm{c}}(\lambda)$ is known, by measuring the voltage V_c recorded by the PMTs using the system of figure 5.23, with a number of bandpass filters with peak wavelengths λ_BP, V_c can be related to $\Phi_{\lambda,\mathrm{c}}(\lambda_\mathrm{BP})$ for each filter as

$$V_\mathrm{c} \approx R l_\mathrm{c}(V_\mathrm{c})\, \mu s(\lambda_\mathrm{BP})\, \Phi_{\lambda,\mathrm{c}}(\lambda_\mathrm{BP})\, f_\mathrm{c}(\lambda_\mathrm{BP}) \int_0^\infty f_\mathrm{BP}(\lambda)\, d\lambda. \tag{5.16}$$

where $l_\mathrm{c}(V)$ is the linearity of the calibration measurement and $f_\mathrm{c}(\lambda_\mathrm{BP})$ the spectral transmittance of the calibration setup at $\lambda = \lambda_\mathrm{BP}$. Comparing this equation to equation 5.15, it can be seen that $\Phi_{\lambda,\mathrm{s}}(\lambda_\mathrm{BP}, t)$ is then given by

$$\Phi_{\lambda,\mathrm{s}}(\lambda_\mathrm{BP}, t) = \frac{V_\mathrm{s}(t)}{V_\mathrm{c}} \frac{l_\mathrm{c}(V_\mathrm{c})}{l_\mathrm{s}(V_\mathrm{s})} \frac{f_\mathrm{c}(\lambda_\mathrm{BP})}{f_\mathrm{s}(\lambda_\mathrm{BP})} \Phi_{\lambda,\mathrm{c}}(\lambda_\mathrm{BP}). \tag{5.17}$$

Comparing figure 5.23 to figure 5.13, the only filter terms present in f_s not present in f_c are the transmission through the hydrogel $(f_{s,gel})$, the transmission through the fused silica window $(f_{s,window})$ and the transmission through any neutral density filters used in the experiment $(f_{s,ND})$. Equation 5.17 can thus be written as

$$\Phi_{\lambda,s}(t) = \frac{C_{BP} V_s(t)}{l_s(V_s) f_{s,ND} f_{s,gel}} \text{ W/nm} \tag{5.18}$$

where C_{BP} is a calibration constant given by

$$C_{BP} = \frac{\Phi_{\lambda,c} l_c}{V_c f_{s,window}} \text{ W/nm/V.} \tag{5.19}$$

C_{BP} incorporates the spectral transmittance of the lens, the beamsplitters and bandpass filter used. This calibration is therefore specific to a particular PMT, at a particular gain setting, on a particular port on the PMT array, with the particular bandpass filter used. The ports as used for the calibration are as shown in figure 5.21. Measurements of the calibration constants were made twice with an iris diameter of 2.95 $\pm$0.02 mm and once with an iris diameter of 1.96 $\pm$0.02 mm. The mean constants at the pertinent wavelengths for this study are given in table 5.2.

If the source is assumed to emit isotropically, the emitted spectral intensity can be calculated from equation 5.18 by accounting for the solid angle over which the light from the source is detected,

$$I_{\lambda,s}(t) \approx \frac{C_{BP} V_s(t)}{l_s(V_s) f_{s,ND} f_{s,gel}} \cdot \frac{d_{lens}^2}{\pi r_{lens}^2} \text{ W/nm/sr.} \tag{5.20}$$

In this equation d_{lens} is the distance of the lens from the emitted light, and r_{lens} is the radius of the lens. This assumes that $r_{lens} \ll d_{lens}$, a reasonable approximation in this case. The error in the emitted spectral intensity $e_I(t)$ is calculated as equation 5.21,

$$e_I(t) = \left|I_{\lambda,s}(t)\right| \sqrt{\left(\frac{e_C}{C_{BP}}\right)^2 + \left(\frac{e_V(t)}{V_s(t)}\right)^2 + \left(\frac{e_l}{l_s}\right)^2 + \left(\frac{e_{f,combined}}{f_{s,combined}}\right)^2} \tag{5.21}$$

where $f_{s,combined}$ is the combined transmission through all filter terms and e_C is the error in the measurement of the calibration constant, etc. The errors in the PMT voltages $e_V(t)$ are given in section 5.6.1.4.

5.6.1.3 Linear range

At moderate light levels, the current produced by the PMT is linearly proportional to the incident radiant flux. However, the output current begins to deviate at high light levels. This deviation from a linear response is primarily due to the PMT anode and cathode characteristics, and is independent of the wavelength of the light[211].

To calculate the linearity, each PMT was placed approximately 52 mm away from a pair of strobing LEDs. These LEDs were programmed to flash sequentially, and then synchronously, with each flash lasting 250 µs. The gate time for the PMT was set to 250 µs for each flash, and all three pulses were captured on the oscilloscope on the same trace. For each measurement, 570 repetitions of this pattern were averaged to improve the signal-to-noise ratio (SNR). Blackout curtains were used to minimise errors caused by room light leakage. To vary the intensity of the light incident on the photocathode, different neutral density filters were placed in front of the photocathode, and the aperture of an iris placed between the LEDs and the photocathode was varied. ND 2.0, 1.0 and 0.3 filters were used. For each PMT, the gain was set to 40.2×10^3.

The spectral radiant flux of the light incident on the photocathode is related to the voltage recorded on the PMT as:

$$V_1 = l_1(V_1) \cdot C_\mathrm{a} \int_0^\infty \Phi_{\lambda,1}(\lambda)\, C_\mathrm{b}\, d\lambda \tag{5.22}$$

$$V_2 = l_2(V_2) \cdot C_\mathrm{a} \int_0^\infty \Phi_{\lambda,2}(\lambda)\, C_\mathrm{b}\, d\lambda \tag{5.23}$$

$$\begin{aligned} V_3 &= l_3(V_3) \cdot C_a \int_0^\infty \Phi_{\lambda,3}(\lambda)\, C_\mathrm{b}\, d\lambda \\ &= l_3(V_3) \cdot C_a \int_0^\infty \left[\Phi_{\lambda,1}(\lambda) + \Phi_{\lambda,2}(\lambda)\right] C_\mathrm{b}\, d\lambda \\ &= l_3(V_3) \cdot C_a \left[\int_0^\infty \Phi_{\lambda,1}(\lambda)\, C_\mathrm{b}\, d\lambda + \int_0^\infty \Phi_{\lambda,2}(\lambda)\, C_\mathrm{b}\, d\lambda\right] \end{aligned} \tag{5.24}$$

where $\Phi_{\lambda,1}(\lambda)$ is the spectral radiant flux of the light from the first pulse, etc. and C_a and C_b are constants taking into account the other terms in the equation. It is assumed that

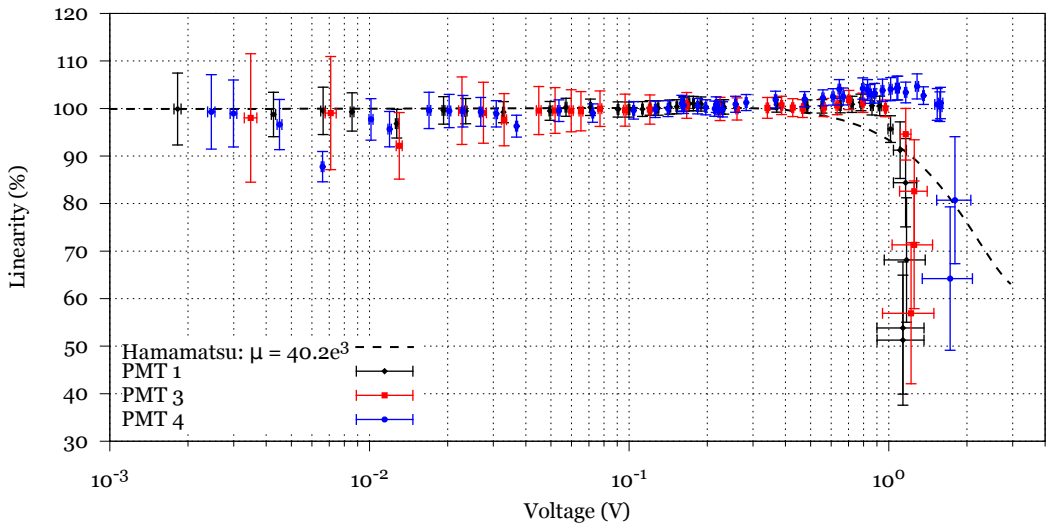

Figure 5.24: Linearity of the three PMT modules. Dashed line shows typical Hamamatsu supplied results at at gain of 40.2×10^3 .[212]

$\Phi_{\lambda,3}(\lambda) = \Phi_{\lambda,1}(\lambda) + \Phi_{\lambda,2}(\lambda)$. If the linearity of the first two pulses is assumed to be 1.0

$$l_3 = \frac{V_3}{V_1 + V_2}, \tag{5.25}$$

and the linearity can be calculated. Figure 5.24 shows the results for each of the PMT modules using this method. As can be seen, these results suggest that the PMT response is linear up to approximately 0.9 V. Scatter in the data below 20 mV is due to poor signal to noise ratio (see section 5.6.1.4).

5.6.1.4 Noise levels

The variation in the SNR of the PMTs with recorded voltage is shown in figure 5.25. These measurements were made using the same setup as figure 5.23, with ND filters and the iris used to vary the intensity of the light incident on the PMTs. The noise value at each voltage was taken to be the standard deviation in the recorded voltage for each measurement.

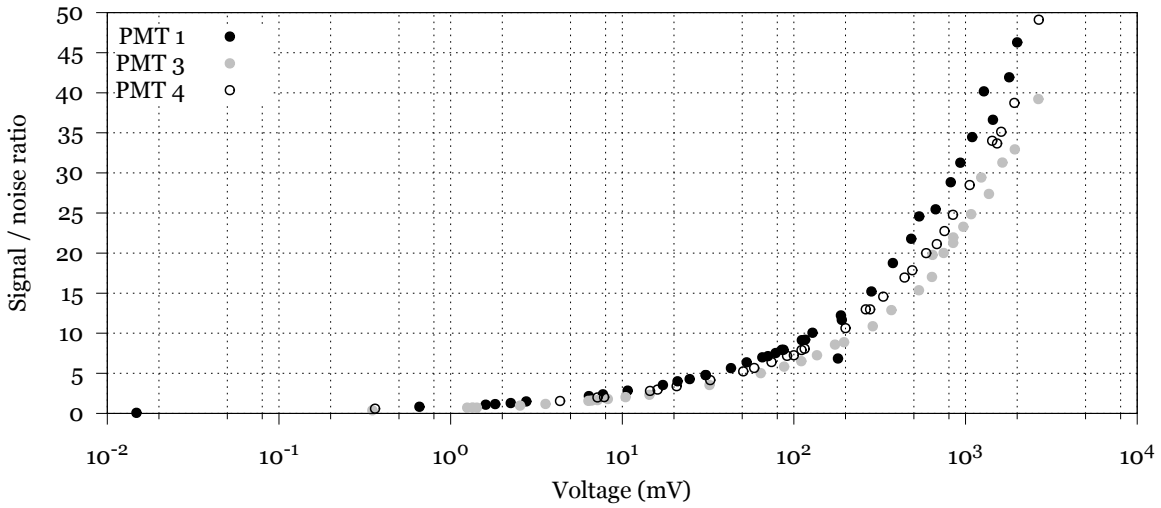

Figure 5.25: Variation in PMT signal-to-noise ratio with output voltage.

5.6.2 Avalanche photodetector

As a simpler alternative to the PMT array, a single APD is also used for light detection. The APD (Thorlabs APD110A2/M) is UV-enhanced, with a 200 nm to 1000 nm working range and a 1 mm diameter sensor. The temporal resolution of the APD is approximately 20 ns. The light from the emitting source is focussed on to the sensor using a fused silica 75 mm diameter field lens, with a 150 mm focal length (Thorlabs LA4372). This lens is placed 900 mm from the centre of the cavity, giving a 5 mm diameter field of view. If a larger field of view is required, for example for multi-cavity arrangements, this lens is replaced by a 50 mm Nikon camera lens. This lens is placed 800 mm from the centre of the cavity, and has an aperture of approximately 13.9 mm. The iris is held fully open, giving an f-number of $f/1.8$. This increases the field of view to approximately 16 mm, but reduces the amount of light captured. Different filters may be placed in front of the APD, including 10 nm bandpass filters and neutral density filters. To reach the APD, the light must also pass through the fused silica window on the primary containment.

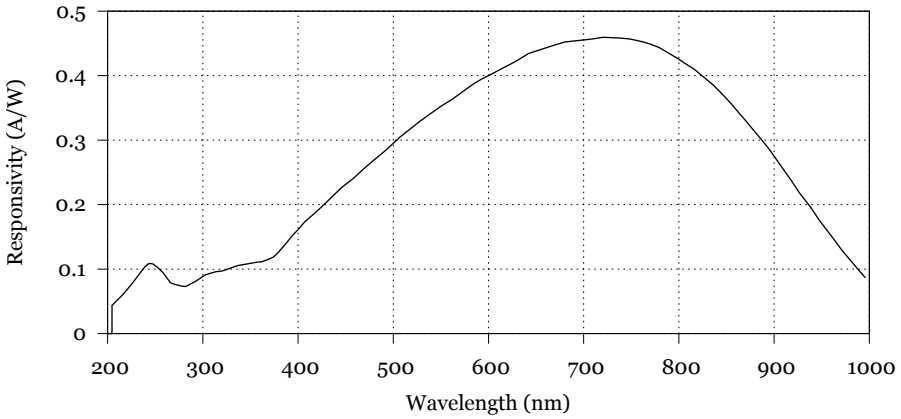

Figure 5.26: Variation of APD responsivity (χ) with wavelength of incident light (representative data, supplied by Thorlabs).

5.6.2.1 Calculation of incident radiant flux

When terminated with a 50 Ω load, the voltage $V(t)$ measured by the APD is related to the detected spectral radiant flux from the light source ($\Phi_\lambda(\lambda)$) as

$$V(t) = \frac{1}{2} MG \cdot l(V) \int_0^\infty f(\lambda)\, f_{\mathrm{BP}}(\lambda)\, \Phi_\lambda(\lambda)\, \chi(\lambda)\; d\lambda \tag{5.26}$$

where M is a multiplication factor dependent on the room temperature, but factory set to 50; G is the gain of the APD, set to 100 kV/A; $f(\lambda)$ is the cumulative spectral transmittance of any filters placed in front of the sensor, $f_{\mathrm{BP}}(\lambda)$ is the spectral transmittance of the bandpass filter used, l is the linearity and $\chi(\lambda)$ is the responsivity of the APD (units A/W). The spectral response of a typical APD of this model is given in figure 5.26. As in equation 5.15, this equation can be simplified by assuming $f(\lambda)$, $\Phi_\lambda(\lambda)$ and $\chi(\lambda)$ do not vary over the bandwidth of the bandpass filter, taking values of $f(\lambda_{\mathrm{BP}})$, $\Phi_\lambda(\lambda_{\mathrm{BP}})$ and $\chi(\lambda_{\mathrm{BP}})$ where λ_{BP} is the wavelength of maximum spectral transmittance of the bandpass filter. The emitted spectral intensity can then be calculated as

$$I_\lambda(\lambda_{\mathrm{BP}}, t) = \frac{2V(t)}{MG \cdot l(V) \cdot f(\lambda_{\mathrm{BP}})\, \chi(\lambda_{\mathrm{BP}})} \frac{1}{\int_0^\infty f_{\mathrm{BP}}(\lambda)\, d\lambda} \cdot \frac{d_{\mathrm{lens}}^2}{\pi r_{\mathrm{lens}}^2}\ \mathrm{W/nm/sr} \tag{5.27}$$

Model	Ocean Optics QE65000 Pro
Grating	HC1 300 line composite blaze
Filter	OFLV-QE 200 - 950 nm
Bandwidth	200-978 nm
Slit	200 μm
CCD	Ocean Optics S7031: 1044 bins
Minimum acquisition time	8 ms

Table 5.3: Ocean Optics 65 Pro spectrometer details

5.6.3 Spectroscopy

Spectroscopy in this experiment is achieved using an Ocean Optics 65 Pro spectrometer, the details of which are given in table 5.3. This spectrometer uses a Czerny-Turner design, and is used to measure a single integrated spectrum of all light emission during the 8 ms acquisition time. A graph of the responsivity of the spectrometer is given in figure 5.27. The setup used to capture the light emission from the cavity collapse is shown in figure 5.28. A 75 mm diameter, 150 mm focal length fused silica lens (Thorlabs) is placed to focus the light from the cavity collapse onto a 0.22 NA single strand optical fibre, which feeds into the spectrometer. The light from the collapse must also pass through a fused silica 10 mm thick window on the primary containment.

As there is a delay of approximately 100 μs between the input trigger signal and the start of data acquisition, the spectrometer is triggered from the light curtain array at the end of the gun-barrel.

5.7 Pressure measurement

To measure the pressure within the hydrogel block, a fibre-optic probe hydrophone (FOPH) is used (figure 5.29). This was built by Dr. Phillip Anderson, based on a design

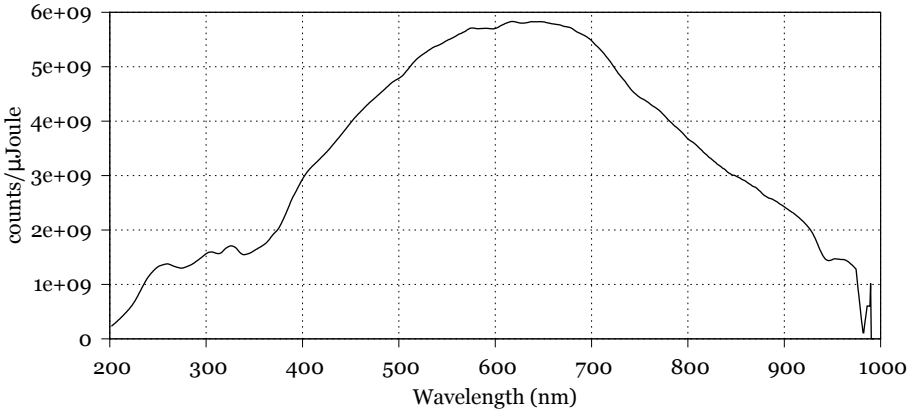

Figure 5.27: Spectrometer responsivity (factory calibration)

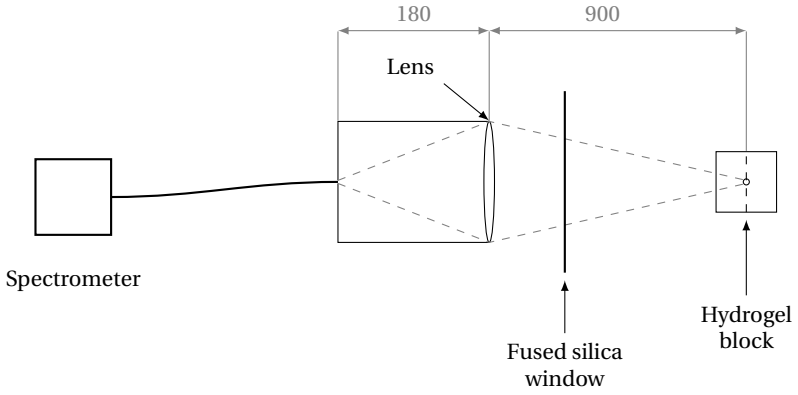

Figure 5.28: Schematic diagram of the spectroscopy setup. Dimensions in mm.

by Parsons *et al.*[213] This system measures the density of the medium at a point in space over time, by utilising the accompanying change in the index of refraction. To achieve this, light from a 1 W, 850 nm laser (QPhotonics QFLD-850-1000M) is passed through a 2 x 2 multi-mode fibre-coupler (Gould Fiber Optics 15-22500-50-66640) into a multi-mode, 100 μm beam core optical fibre (Gould Fiber Optics 64-02522-30-05001), which is placed in the medium. The output from the laser is kept constant using an Arroyo (6340 ComboSource) driver. The proportion of the light reflected back up the fibre, which is related to the difference between the index of refraction of the fibre-tip and the medium, is then recorded on a silicon fixed gain detector (Thorlabs, PDA10A-EC) attached on the other side of the fibre-coupler. From this data the density, and so the pressure, may subsequently be inferred. As only ~ 0.3% of the light is reflected back up the fibre, no damage

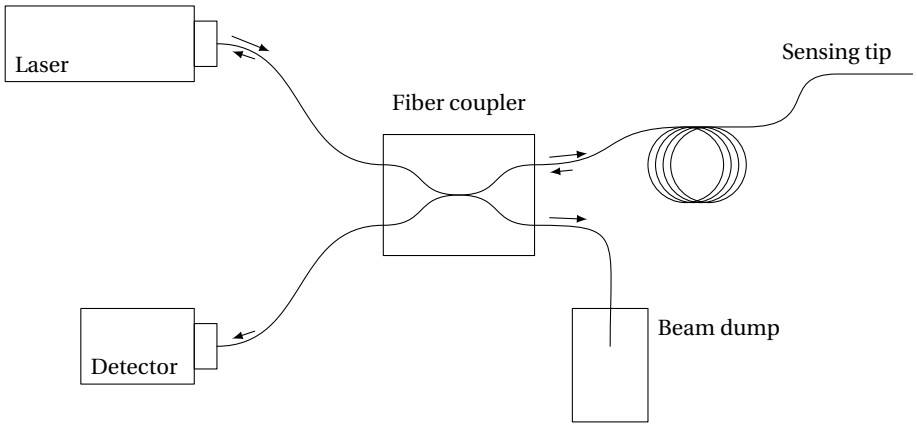

Figure 5.29: Schematic diagram of the fibre-optic probe hydrophone. Arrows show direction of light propagation

is sustained by the detector or laser. The typical effective noise level from this device is approximately 50 MPa, primarily caused by uncertainties in the measured voltages. The key advantage of this system is that it allows measurement of much higher pressures than conventional needle hydrophones. Additionally, only the cheaply replaceable tip of the optical-fibre is placed in the medium, thus avoiding damage to more expensive parts.

5.7.1 Calibration

To obtain accurate readings, the FOPH must be re-calibrated prior to each shot. The end of the fibre must be re-cleaved (Thorlabs, XL411) to ensure the end of the fibre is undamaged, and orthogonal to the fibre axis. To calibrate the FOPH, the measured voltage V is assumed to be linearly related to the reflectivity at the fibre tip ($R(n)$):

$$V = gR(n) + S \tag{5.28}$$

where S is an offset due to cross-talk in the fibre-coupler and g is the gain. The reflectivity is:

$$R(n) = \left(\frac{n_f - n}{n_f + n}\right)^2 \tag{5.29}$$

assuming a normal reflection at a two-medium interface, where n is the index of refraction of the medium and n_f the index of refraction of the fibre. dn/dp is approximately 2

orders of magnitude larger than dn_f/dp,[213] and n_f is thus assumed to be constant under all conditions. By measuring the voltage for a number of materials with known index of refraction (typically air and a calibration oil), the gain g and offset S may thus be inferred. To obtain the index of refraction of the medium to be measured, equation 5.28 can be inverted:

$$n(V) = n_f \cdot \frac{1-J}{1+J} \qquad (5.30)$$
$$J = \sqrt{\frac{(V-S)}{g}}.$$

Once the calibration is completed, the fibre is placed in the hydrogel, at an angle of approximately 45° to the vertical. This angle generates a rise time of approximately 35 ns in the signal.

5.7.2 Conversion to density and pressure

Conversion from index of refraction to density is achieved using the Gladstone-Dale relation,[214]

$$\frac{n(t)-1}{\rho(t)} = \text{constant}. \qquad (5.31)$$

As the ambient conditions (ρ_o, n_o) are known, the density of the medium $\rho(t)$ can be calculated as

$$\rho(t) = \rho_o \cdot \frac{n(t)-1}{n_o-1}. \qquad (5.32)$$

This equation is valid up to densities of 1220 kg/m^3.[215,216]

To calculate pressure from density, an additional piece of information is required, commonly an equation of state. Alternatively, if the velocity of the shock front is known, the pressure at the front may be inferred from the Rankine-Hugoniot conditions as in equation 5.13. The ambient pressure p_0 is assumed to be 1.013 bar, and the hydrogel is assumed to be initially at rest. Shock velocity is inferred from SimX images, as described in section 5.5.5. Each successive point behind the shock is treated as a new shock, with the

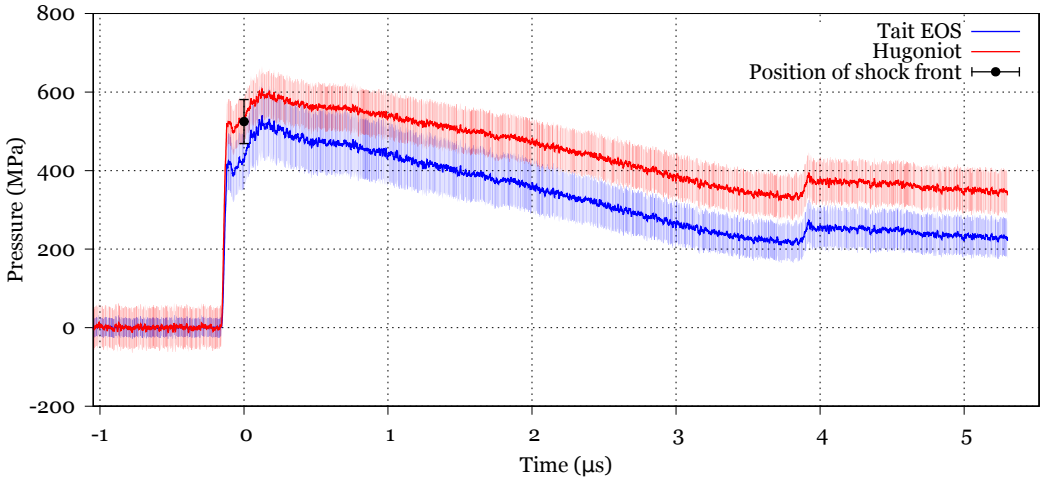

Figure 5.30: Comparison between methods for calculation of shock pressure. Red line shows the results calculated using equations 5.13, blue using the Tait EOS (equation 3.9). Shaded regions show the calculated errors in the presented measurements. The black point is the position at which the front of the shock is deemed to lie, with the time inferred from SimX images as the time at which the shock passes the tip of the fibre. Calculated pressure at the shock front in this case is 520 MPa.

particle velocity and pressure recalculated using equation 5.13, assuming ambient conditions ahead of the point, and the shock velocity as calculated at the shock front. This calculation is strictly only valid at the shock front, however as shown in figure 5.30, which compares pressure curves as found using the Tait EOS (equation 3.9) and equations 5.13, applying equations 5.13 to the full curve yields a pressure profile that is very similar in form to that found using the Tait EOS, but is shifted to be more accurate at the shock front. Pressures are thus presented in this work using this method. Also shown in figure 5.30 is the inferred position of the front of the shock. The time of this point is found as the time at which the shock wave contacts the tip of the fibre, interpolated from the SimX images.

5.8 Comparisons between simulated and experimental results

Once experimental measurements have been obtained, matching simulations may be produced that can be compared back to those results. This process achieves two things. Firstly, the process allows validation of the numerical methods used to produce those simulations. Secondly, if simulations match experimental results to sufficient accuracy, they can offer further insights into the processes at work, due to the much greater level of detail available.

In this work, the development of matching simulations is achieved in a semi-automated fashion, with image analysis techniques used to infer the locations of features such as cavities or shock waves from experimental images. The methods used to to achieve this are briefly outlined in sections 5.8.1 and 5.8.2. With the shock fully defined and the geometry of the simulation specified, everything is known that is required to run the simulation. The result is a number of calculated values and data sets, which may then be compared back to the original experiment. This is then a test of the accuracy of the code, as well as the validity of the assumptions made to set up the simulation in the first instance. A key part of this process is the inference of reliable metrics from experimental results, which may then be compared to simulations. One particularly important metric is the time at which the high speed jet strikes the leeward cavity wall, which is not directly observable in experimental results. A method used to infer this metric from the propagation of water hammer shocks is described in section 5.8.3.

5.8.1 Creation of comparative simulations from experimental results

In order to produce a simulation that matches to an experimental result, a significant number of metrics must be either measured from that experiment, or inferred from those

measurements. Of critical importance are the images of the cavities before and during the shot, the size of which are inferred as described in section 5.5.4. Together, these image sets may be used to fully define the geometry of the matching simulation, as well as calculate shock velocity using the methods outlined in section 5.5.5. The shock velocity and position data as found may then be used to calculate both the shape of the leading edge and the conditions behind the incident shock at the time at which the simulation is to be initialised, if an equation of state is assumed. This calculation is summarised in section 5.8.2. The location and sizes of the cavities in the image are inferred using image analysis techniques. Specifically, a Canny edge detector algorithm[207,208] is used to locate the edges of the cavities in the image, and a watershed filling algorithm[207] is then used to fill the enclosed regions. The centroid, radii and rotation of these filled regions define the ellipses used to model the cavities.

The final critical piece of information used in producing matched simulations are the equations of state used to model the hydrogel and the air in the cavities. In this study, a stiffened polytropic EOS is used to model the hydrogel (see section 3.3.3), and the air is modelled as an ideal gas (section 3.3.1). The hydrogel is assumed to be initially at standard temperature and pressure, with a density of $1005\,\mathrm{kg/m^3}$. The initial density of the air is assumed to be $1.18\,\mathrm{kg/m^3}$.

5.8.2 Calculation of the incident shock state

An important aspect of the creation of comparative simulations to experimental results in this work is the setup of the incident shock. Although the velocity, and therefore the density, of the shock can be inferred from the SimX images, as a hydrophone is not used in all shots the temporal profile of the incident shock is not generally known. However, as will be shown in section 6.2, the profile of the incident shock does not change substantially from shot to shot, or with magnitude. A normalised average trace is thus used, averaging

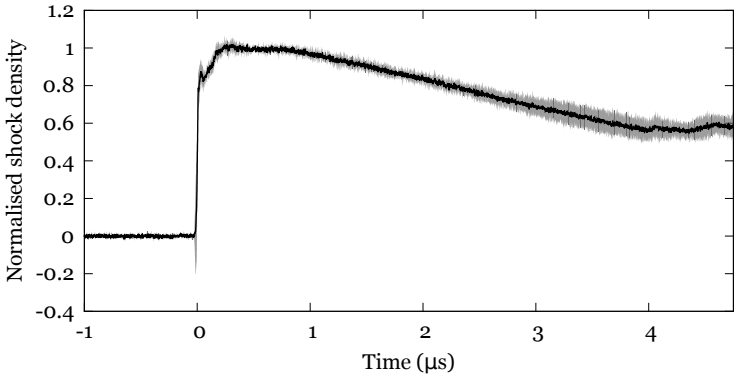

Figure 5.31: Variation in normalised incident shock density with time. Result is an average of four hydrophone traces at a projectile velocity of 395 ± 7 ms^{-1}. Shaded region shows the standard deviation across all traces.

across a number of hydrophone shots (see figure 5.31). This trace is then scaled, such that the density at the peak of the shock front matches the value inferred from the peak of the shock velocity curve, using equation 5.12. Pressures and particle velocities behind the shock front are calculated using the Rankine-Hugoniot relations, as described in section 5.7.2.

The assumption of a constant shock velocity at all points behind the shock front, and of treating each successive point as a new shock are unlikely to be fully accurate. This is thus a source of error in matched simulations. However, in the absence of a more complete picture of the conditions behind the incident shock they provide a rudimentary method to allow the creation of simulations. A comparison of the variation in shock velocity with time for an experiment and matched simulation is shown in figure 5.32. As can be seen, while the shock velocity is initially well matched, the experimental shock attenuates at a much faster rate, such that by the final frame the simulated shock velocity is approximately 20% higher. This difference is likely to be in part due to differences in the states behind the shock front, although other factors such as geometric spreading may play a role (see figure 6.1).

The shape of the incident shock can be inferred from the position data used to calcu-

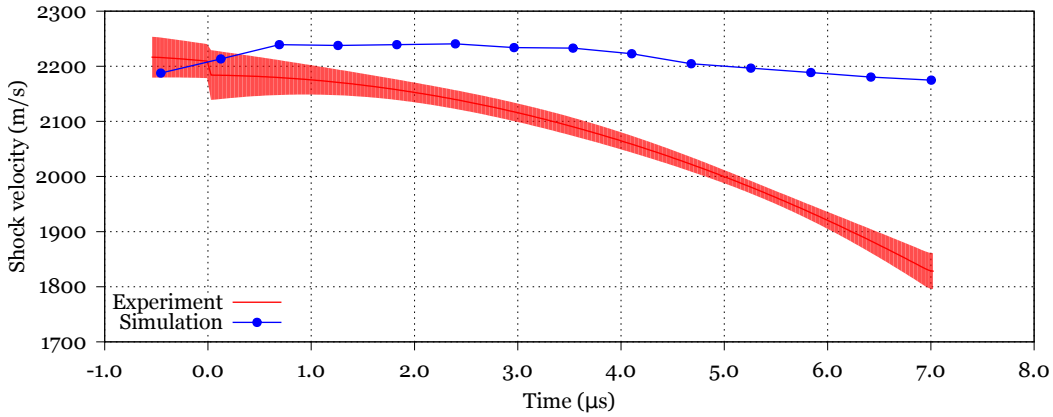

Figure 5.32: Variation in incident shock velocity with time for an example shot, as measured from experimental and simulated results.

late the shock velocity, as described in section 5.5.5. An ellipse is fitted to these points, using a least squares approach. The state of each point behind the shock is then set by the relative distance of the point from the edge of the ellipse, and the angle of the velocity vector set by the angle around the ellipse.

5.8.3 Inference of the time of jet strike from water hammer shocks

An important metric for comparison between simulations and experimental results is the first phase collapse times of cavities. As described in chapter 4, this metric is defined as the time between the point of contact of a driving shock on a cavity, and the time at which the resulting high-speed jet strikes the leeward cavity wall. Although comparatively simple, matching of this metric requires substantial accuracy in the numerical methods used, as well as the equation of state and the initial setup of the problem. It is thus a good metric to use for matching simulations to experimental results.

While readily available from simulated results, the calculation of the first phase collapse time from experimental measurements is more complex. Although the time of contact of the shock on the cavity is simple to infer from high speed images of the collapse, the propagation of the jet across the cavity is not visible in the images due to the curva-

ture of the spherical cavity walls. Additionally, as will be shown in chapter 6, the three dimensional structure of the incident shock significantly obscures the view of the collapse. One solution to this issue is to utilise the water hammer shock that propagates out from the point of impact of the jet on the leeward cavity wall (see section 2.4.3). This shock is clearly visible in experimental image sets, and is a spherically spreading shock that effectively propagates from a point source at the base of the cavity. By locating this shock at each point in time, it is therefore possible to infer the time at which the shock was formed by extrapolation of fitted lines. Through use of this method, the time of jet strike can be calculated in simulated results to within approximately 0.4% of the correct value. For experimental results, the position of the water hammer shock may be obscured by other features in the images, and the accuracy of the method diminishes. The more frames in which the water hammer shock can be seen, and the closer these frames are to the initial point of shock formation the more accurate a measurement can be made.

Due to the many additional shock waves present in the image sets of cavity collapse, automated detection of the position and shape of the water hammer shock in frames is not easily achieved. Therefore, to find the location of the water hammer shock at each time, a series of points are visually identified and manually selected from each image, along the edge of the water hammer shock. An ellipse can then be fitted to these points, using a least squares approach. The error function to be minimised is given by equation 5.33:

$$\begin{aligned} e_i(a,b,c_x,c_y,x_i,y_i) &= \|r_i - r_e\| \\ r_i &= \sqrt{(x_i-c_x)^2+\left(y_i-c_y\right)^2} \\ r_e &= \frac{ab}{\sqrt{(b\cos\theta)^2+(a\sin\theta)^2}} \\ \theta &= \cos^{-1}\left(\frac{y_i-b_y}{x_i-b_x}\right) \end{aligned} \tag{5.33}$$

where a is the radius of the ellipse in the x-direction, b is the radius in the y-direction, and

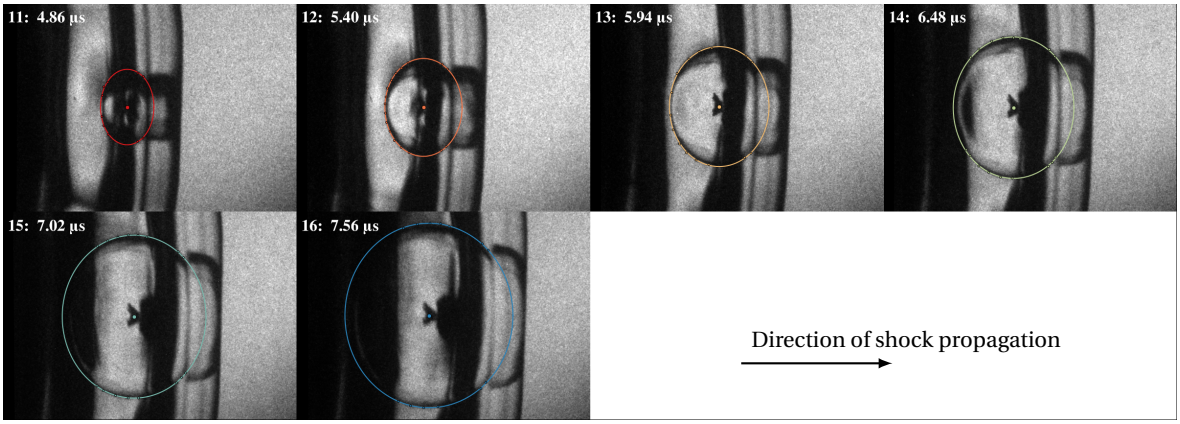

Figure 5.33: Array of SimX images of the collapse of a single spherical cavity, imaged from the side. Fitted ellipses are shown superimposed on the propagating water hammer shock in the frames.

c_x and c_y are the x and y locations of the centre of the ellipse respectively. An example of this approach applied to a set of SimX images is given in figure 5.33.

Once the ellipses have been found, to find the time of water hammer shock formation the ellipses are first overlaid with the same centre point (figure 5.34). This helps to take into account variations in shock propagation velocity with direction. The distance propagated by the water hammer shock at a number of angles may then be found by calculation of the radius of each ellipse at each angle. Finally, the fitting of functions to these points enables extrapolation of the time of formation of the shock, which is assumed to be the time at which the radius is equal to zero (figure 5.35). This time is slightly different for the different angles around the cavity, and the time of formation is therefore calculated as the mean time comparing all lines. The error in the measurement is calculated as the standard deviation.

One key aspect of this method is in the choice of function to be fitted to the ellipse radii. Table 5.4 compares the time of jet strike as calculated using different functions when applied to a simulated result. For the simulation in question, the time of jet strike was calculated using another method as 4.21 µs. As can be seen, the use of the function $r = (at + b)^c$ provided the most accurate fit, with an approximate value of $c = 0.9$ closely

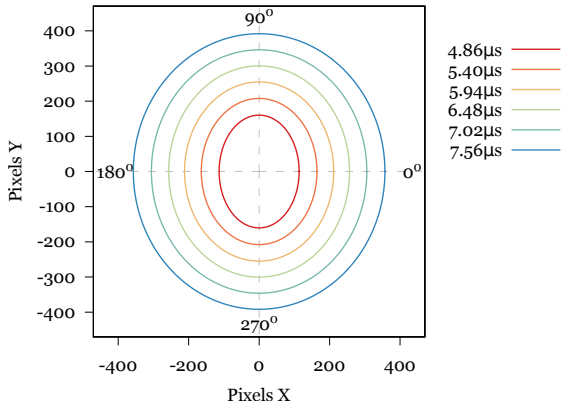

Figure 5.34: The fitted ellipses of figure 5.33, overlaid with the same centre location.

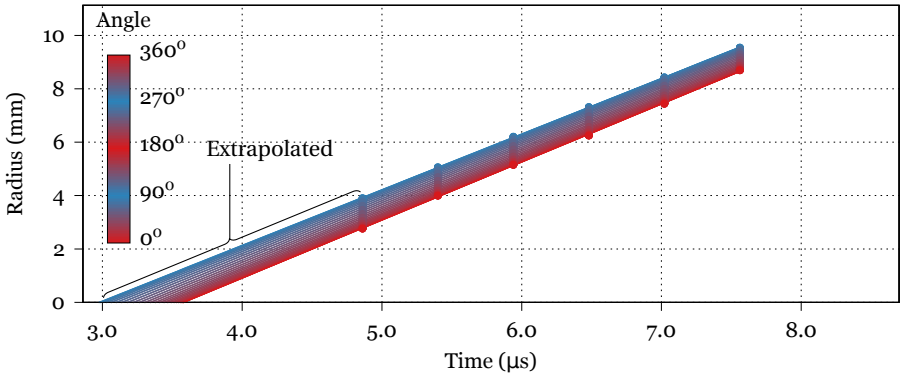

Figure 5.35: Straight lines fitted to the water hammer shock ellipses of figure 5.34. Extrapolation of these lines to the time when the radius is equal to zero enables approximate calculation of the time of formation of the water hammer shock and thus the time of jet strike in the cavity.

matching the data. The Sedov-Taylor blast wave solution[217] also provided a reasonable fit to the data, but was less accurate than a fitted third-order polynomial function. When applied to experimental results, the limited number of available frames shortly after the time of formation of the shock severely reduced the applicability of these functions, which require this information to produce an accurate fit. The only function that was found to be sufficiently robust to allow fitting of all shots was the linear trend $r = at + b$, and as a result this was the function used to fit the experimental data. As can be seen in table 5.4, as the shock deccelerates as it propagates this will lead to approximately a 3% underestimate of the time of water hammer shock formation.

Fitting function	Calculated jet strike time (μs)	Jet strike time error (μs)	Percentage difference (%)
$r = a(t-b)^{2/5} - c$	4.16	0.06	1.21
$r = at + b$	4.08	0.06	3.2
$r = at^2 + bt + c$	4.15	0.06	1.34
$r = at^3 + bt^2 + ct + d$	4.17	0.05	0.9
$r = (at + b)^c$	4.20	0.05	0.32

Table 5.4: Comparison between different fitting functions for the calculation of the time of jet strike from water hammer shock propagation in simulated results. Correct jet strike time 4.21 μs. The first function presented is the functional form of the Sedov-Taylor blast wave solution.[217]

5.9 SUMMARY

This chapter has outlined the setup used in this thesis for the experimental study of shock-driven cavity collapse. A single stage light gas gun is used to fire projectiles into an aluminium plate, behind which a hydrogel block is placed. This process creates high pressure shock waves in the hydrogel block, which go on to impact any cavities cast in the block. Prior to an experimental investigation into the collapse of cavities, in the next chapter this setup is utilised to characterise the propagation of the incident shock wave across the hydrogel block.



CHAPTER 6

SHOCK WAVE CHARACTERISATION

In this chapter, the propagation of the incident shock across the hydrogel block is studied. It is shown that the incident shock has a complex thee-dimensional structure, that partially obstructs the view of events occurring in the centre of the hydrogel block. The variation in incident shock velocity and pressure with projectile velocity are analysed.

6.1 INTRODUCTION

Before cavity collapse results are presented, in this chapter the conditions in which the cavities are placed are first explored. Of particular focus are the pressures and profiles of the incident shock, and how this varies with the velocity of projectiles fired from the gun. Shock pressure profiles are taken from cases in which no cavities were present within the hydrogel block, while shock velocities are taken from cases in which cavities were present, to increase the number of available data points.

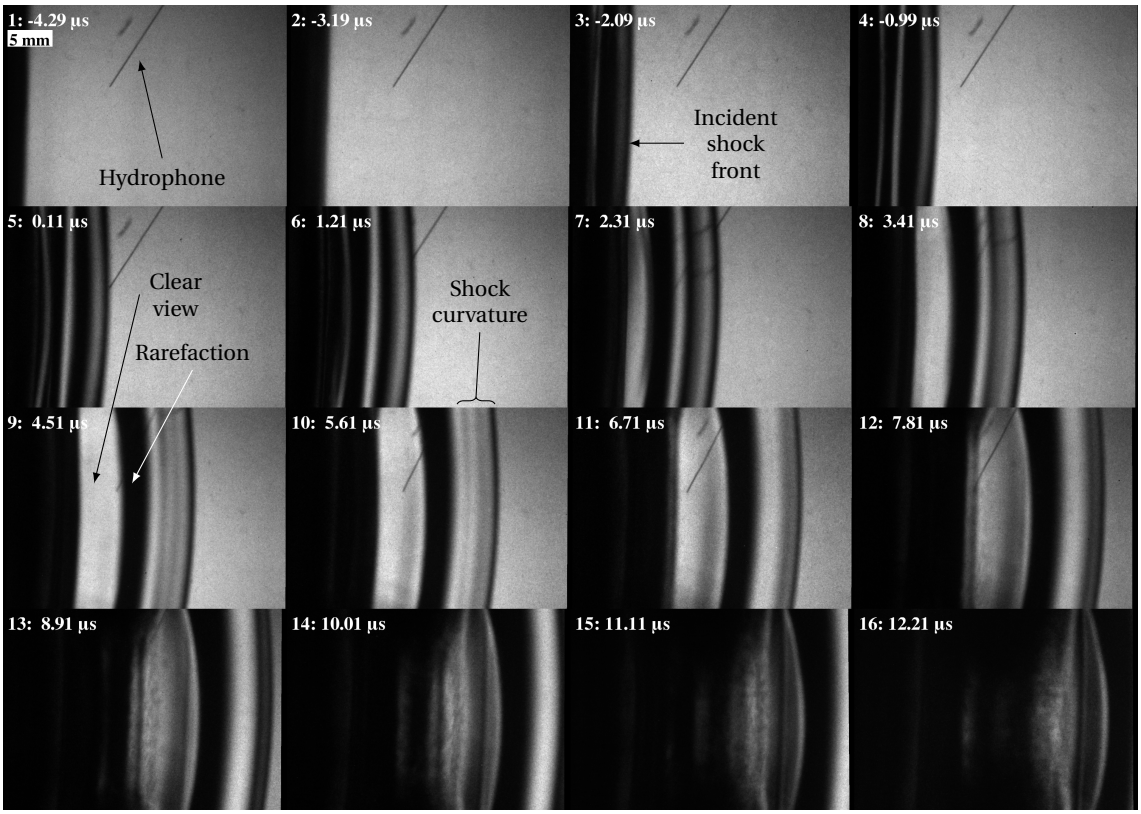

Figure 6.1: SimX image set of a shock wave propagating through a hydrogel block. A hydrophone is placed in the hydrogel, clearly visible as a thin line propagating down from the top of the images. Times referenced relative to the time of impact of the incident shock on the hydrophone tip. Shot velocity $392 \pm 4\ \mathrm{ms}^{-1}$.

6.2 RESULTS

A SimX image set of a shock passing through a hydrogel block, taken at a projectile velocity of $392 \pm 4\ \mathrm{ms}^{-1}$ is shown in figure 6.1. The images show a central section of the hydrogel block, with the striker plate just off screen on the left hand side. The shock wave can be seen propagating from left to right in the images as a series of dark bands, with significant structure behind the shock front. The fibre-optic probe hydrophone (FOPH, see section 5.7) has been placed in the hydrogel on the central line of the hydrogel block, with the tip approximately 10 mm from the striker plate. This is visible in the images as a thin dark line coming in from the top of the frame. The appearance of the shock as it passes across the hydrogel block is significantly altered by its three-dimensional structure. In

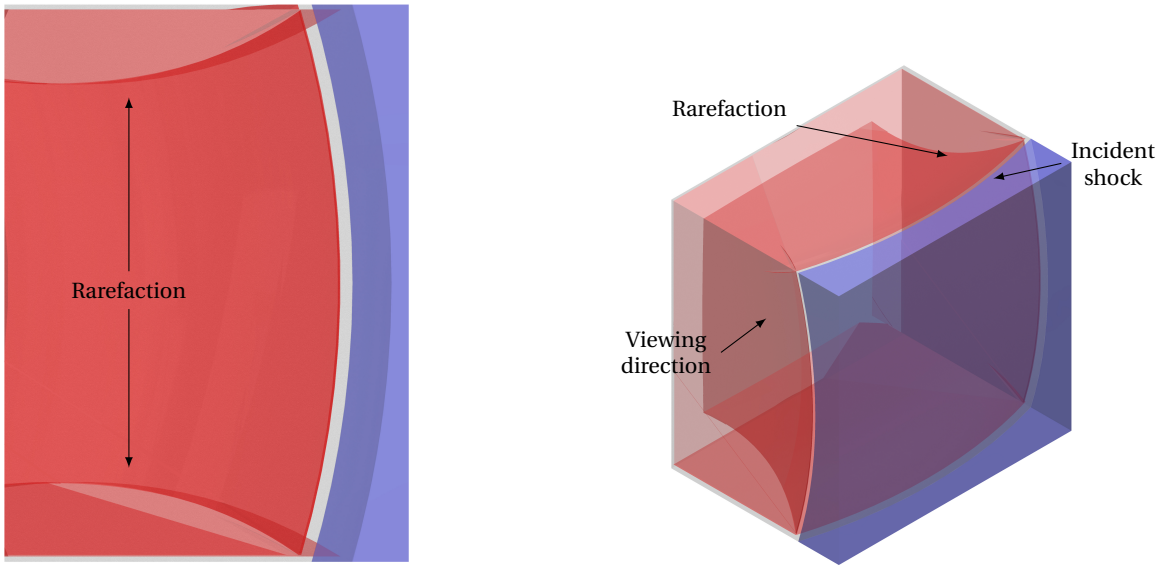

Figure 6.2: 3D schematic of the shock structures inside a hydrogel block. (a): Side view (b): Isometric view. Incident shock moving left to right.

particular, the curvature of the shock, clearly visible in all frames of figure 6.1, distorts the images immediately behind the shock front. This leads to the presence of a light band in the images (labelled in figure 6.1 as 'shock curvature'), through which any events occurring in the centre of the hydrogel are obscured. This is most easily seen in frames 6, 7 and 8, where the fibre tip can be seen to be initially entirely hidden by the shock, and then highly distorted. A second feature visible in all shots is a black band, which immediately follows the curved incident shock. This feature is not consistent with any significant density gradients seen on the FOPH trace, and we thus speculate that it is caused by the rarefactions which form on the edge of the hydrogel, as the shock wave propagates along the boundary. This feature almost completely blocks the view of events occurring on the centre-line of the hydrogel block, for a short distance behind the shock front. Together with the curvature of the shock, there is therefore a significant band in the images behind the leading edge of the shock wave within which events occurring in the centre of the hydrogel are obscured. The thickness of the shock-curvature band and the rarefaction band vary with the velocity of the shock. These features are further highlighted in figure 6.2,

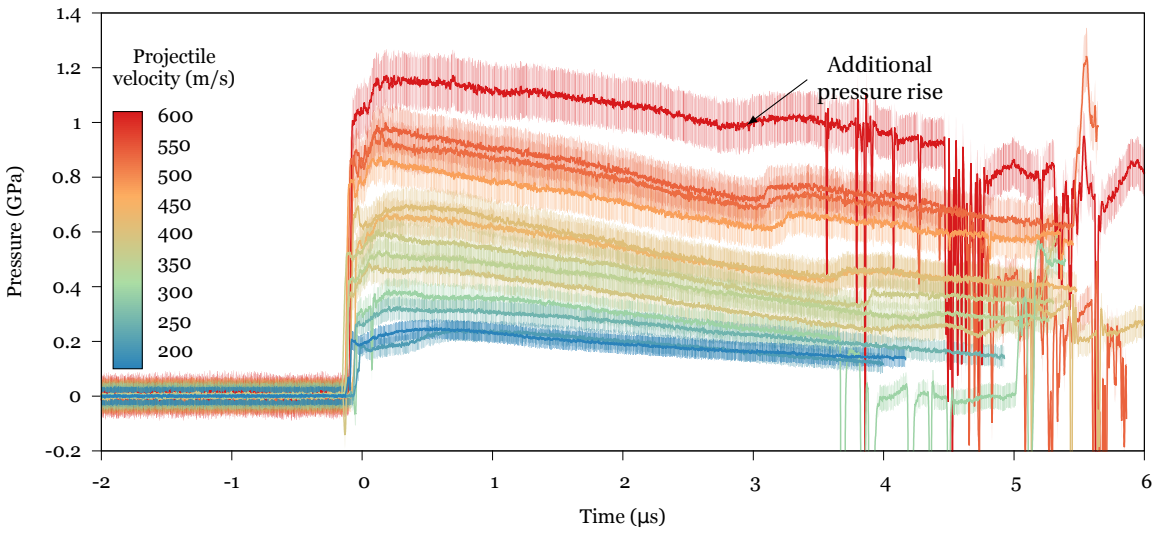

Figure 6.3: Variation in pressure with time, as recorded by the FOPH. Line colour varies with projectile velocity.

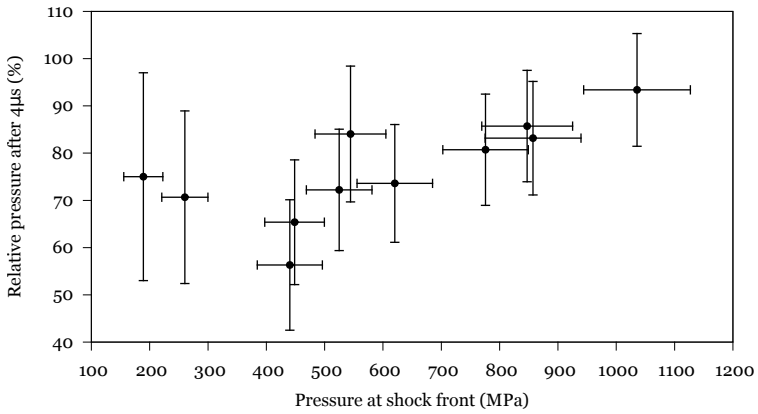

Figure 6.4: Pressure of the incident shock as recorded by the FOPH 4 μs after the shock front has passed, relative to the value at the shock front.

which shows a side-on and isometric representation of a hydrogel block within which a shock wave is passing. This figure is not directly taken from experimental or simulated results, and merely serves to illustrate the processes that we believe are occurring in the hydrogel block. Behind the rarefaction band, there is a section in which events occurring in the centre of the hydrogel block are clearly visible, before an additional dark region obscures the remainder of the process.

Figure 6.3 shows how the pressure varies with time for a number of different shots, as

recorded by the FOPH. The curves have been shifted in time, such that $t = 0$ is the time at which the shock wave passes the tip of the hydrophone, interpolated from the SimX images. In this plot, pressure has been calculated from density using the Rankine-Hugoniot equations, as outlined in section 5.7.2. In all cases, the hydrophone was placed 10 mm from the striker plate, on the central axis of the hydrogel. Lines are coloured by the projectile velocity for the shot in question. As can be seen, the incident shock consists of a sharp initial rise (rise time approx. 12 ns), followed by a comparatively slow drop-off; 4 μs after the shock front has passed the tip of the hydrophone (figure 6.4), pressures are at worst 50% reduced relative to those recorded at the shock front. This profile is thus well suited for the study of cavity collapse; as was used in chapter 4, sustained pressures behind the shock front are required for intense cavity collapse. Although the intensity of the incident shock increases with projectile velocity, this does not have a significant effect on the structure of the shock, which remains relatively consistent across all projectile velocities. Comparing across all pressure curves normalised by the value at the shock front, in the first 3 μs after $t = 0$ the mean standard deviation in the normalised pressure is 8%. Seen most clearly in figure 6.4, shock pressures remain slightly higher for longer at higher incident shock pressures, in part due to the presence of an additional pressure rise 3 to 4 μs after the shock front has passed. This feature is present in all profiles above approximately 300 m/s and is of an unknown origin. It is possible that this feature is caused by the reflection of waves within the setup, although the timings do not correlate with anything specific. Large spikes in the pressure profiles seen at late times are assumed to be caused by the fracturing of the fibre tip.

The variation in shock velocity with time for a number of shots is shown in figure 6.5, inferred from the SimX images as described in section 5.5.5. Each line shows the mean shock velocity and the equivalent shaded region shows the 95% confidence intervals, comparing across a number of y locations in the hydrogel block (see figure 5.18). As in

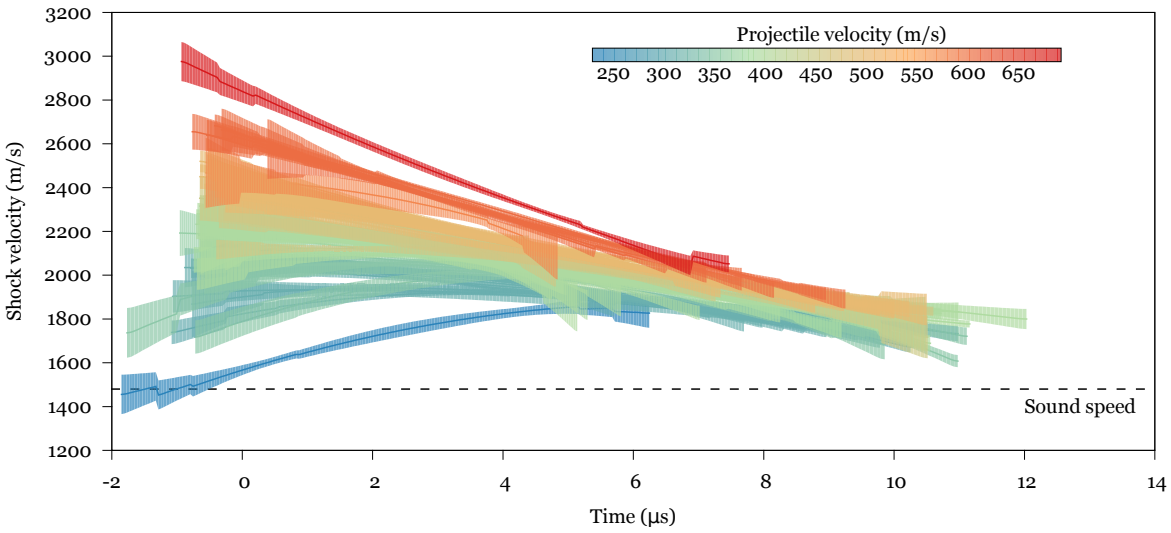

Figure 6.5: Variation in shock velocity with time, inferred from the SimX images. Line colour varies with projectile velocity. Each line shows the mean velocity across measurements taken at a number of positions in the hydrogel. Corresponding coloured regions show the 95% confidence intervals in the measurement.

figure 6.3, lines are coloured by the projectile velocity. In this case results are taken from shots in which cavities were cast in the hydrogel block, and $t = 0$ is defined as the time at which the shock wave first strikes the closest cavity (a position approximately 7.5 mm from the striker plate).* As can be seen, while the shock velocity at $t = 0$ increases consistently with projectile velocity, projectile velocity also has a significant influence on the shape of the velocity curves. At low projectile velocities, the shock is seen to initially accelerate, before decelerating at later times. As projectile velocity is increased, this initial rise is no longer observed, and the shock can be seen to be decelerating as soon as it enters the hydrogel. This perhaps suggests that at low projectile velocities the shock waves are not fully formed on first propagation into the hydrogel, although it is also possible that this effect is amplified by the use of fitted curves to calculate shock velocity. At late times, shock velocities can be seen to be converging on a single decelerating curve for all projectile velocities.

*For reference, using the stiffened polytropic parameters of table 3.2 a shock velocity of 3000 m/s corresponds to a shock pressure of approximately 1.6 GPa.

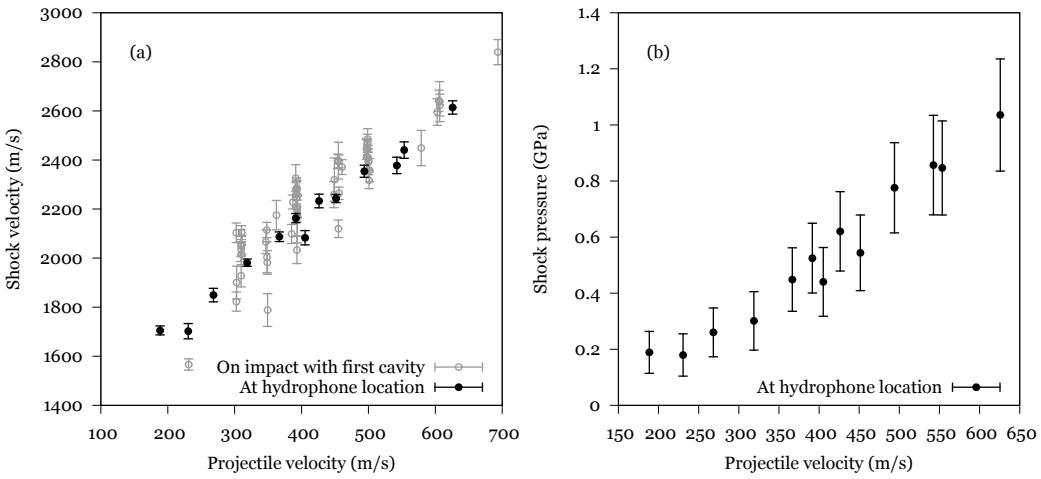

Figure 6.6: Effect of projectile velocity on shock velocity and pressure. (a) Shock velocity at the position of the FOPH tip and on impact on the first cavity, (b) Shock pressure as recorded by the FOPH, at the time at which the shock passes the FOPH tip.

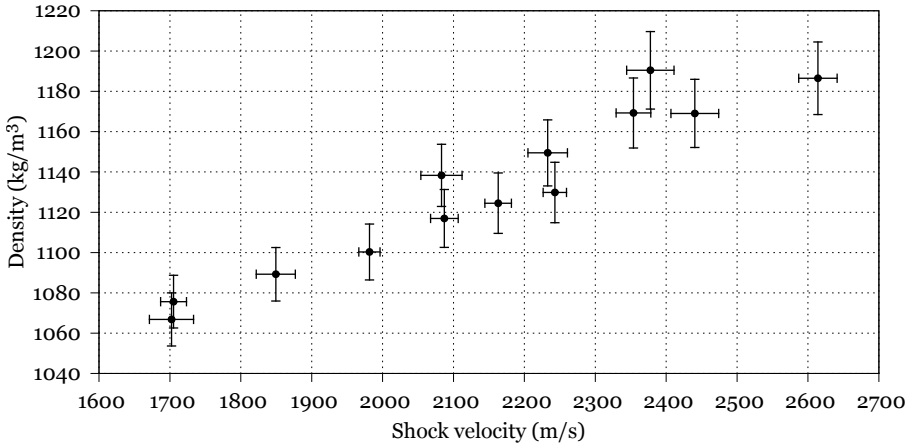

Figure 6.7: Variation in the density immediately behind the shock front with shock velocity. Densities measured using the FOPH.

To further clarify the effect of projectile velocity on the shock waves formed in the hydrogel block, pressures and velocities at the point of impact on the first cavity and hydrophone tip are shown in figure 6.6. Both pressure and shock velocity can be seen to increase monotonically with projectile velocity, with an approximately linear relationship between projectile velocity and shock velocity observed. Further information on the equation of state for the hydrogel may be inferred from figure 6.7, which shows how the density at the shock front varies with incident shock velocity.

6.3 DISCUSSION

As demonstrated in this chapter, the impact of projectiles on the aluminium striker plate leads to the formation of sustained pressure pulses within the hydrogel block, as required for the study of cavity collapse. Shock waves do not form as plane waves but are curved, and attenuate as they propagate. As would be expected, the rate of attenuation is greater at higher incident shock velocities, with the incident shock in fact seen to accelerate as it propagates at low projectile velocities. However, there is some evidence to suggest that while the pressure at the shock front reduces more quickly with time at higher projectile velocities, the pressure profile behind this front stays more consistent. These effects are likely to influence the collapse of cavities; as shown in figure 2.6, the pressures produced by cavity collapse are strongly related to the strength of the incident shock.

With the profile of the incident shock quantified over a range of driving pressures, in the next chapter results are presented for the most simple case, that of a single cavity.



CHAPTER 7

EXPERIMENTAL STUDY OF SINGLE CAVITY COLLAPSE

This chapter presents the interaction of a shock wave with a single cavity, using experimental and numerical results. Spherical and cylindrical cavities are compared, revealing that cylindrical cavities do not collapse in a two-dimensional manner in the experimental setup used. A detailed analysis of the collapse of a spherical cavity is then presented, showing that the cavity collapses to form a torus, emitting light in the process. This light emission consists of three separate peaks, with intensities that vary with shock pressure. The likely causes of these peaks are discussed. The spectra of the light emission is analysed.

7.1 INTRODUCTION

As shown in chapter 6, the experimental setup as described in chapter 5 leads to the formation of strong shock waves in the hydrogel block, with pressures in the region of 200 MPa to 1.3 GPa. In this chapter, these shock waves are utilised to collapse single cavities, cast into hydrogel blocks. No attempt is made to control the gaseous contents of the cavities, which thus contain air, initially at ambient conditions, with the addition of a small percentage of water vapour. A comprehensive discussion of light emission from hot air is given in appendix B.

To begin this chapter, comparison is first made between spherical and cylindrical cavities (section 7.2). A full analysis is then given of the collapse of a single cavity, including comparisons with simulated results (section 7.3). The influence of shock strength on the processes seen is discussed in section 7.3.4, and finally in section 7.3.5 the likely temperatures reached during cavity collapse are discussed.

7.2 Comparison between spherical and cylindrical cavities

As discussed in section 2.4.5, much of the experimental work that has been done on the subject of shock-driven cavity collapse has looked at short cylindrical cavities, held between plastic or glass plates. It is assumed that cavities in such a setup collapse in a two-dimensional manner (i.e. as infinitely long cylinders), as are studied in chapter 4. With this assumption, effects observed can be adjusted for the differences between 2D and axisymmetric collapse, as briefly discussed in section 4.3.3. Conclusions may then be made about spherical cavities, which tend to occur more readily in nature. By viewing cylinders on-axis, the problem of the curvature of the cavity wall, which effectively prevents imaging of events occurring in the gas inside spherical cavities, can effectively be eliminated.

To test the validity of the two-dimensional assumption, figures 7.1 to 7.3 show the collapse of a spherical cavity as well as 5 mm and 20 mm long cylindrical cavities, without external illumination. As can be seen, in all cases light emission is observed from the cavity. This is the shock-cavity equivalent of sonoluminescence, as was first shown by Dear *et al.*[7]. In each case, the light emission is shown as viewed from a number of different angles. These viewing angles do not correspond to the same physical shot, and for each image series not all images of the light emission are shown. Rather, the key light-emission structures as observed in each setup are given, with repeating frames and periods of no

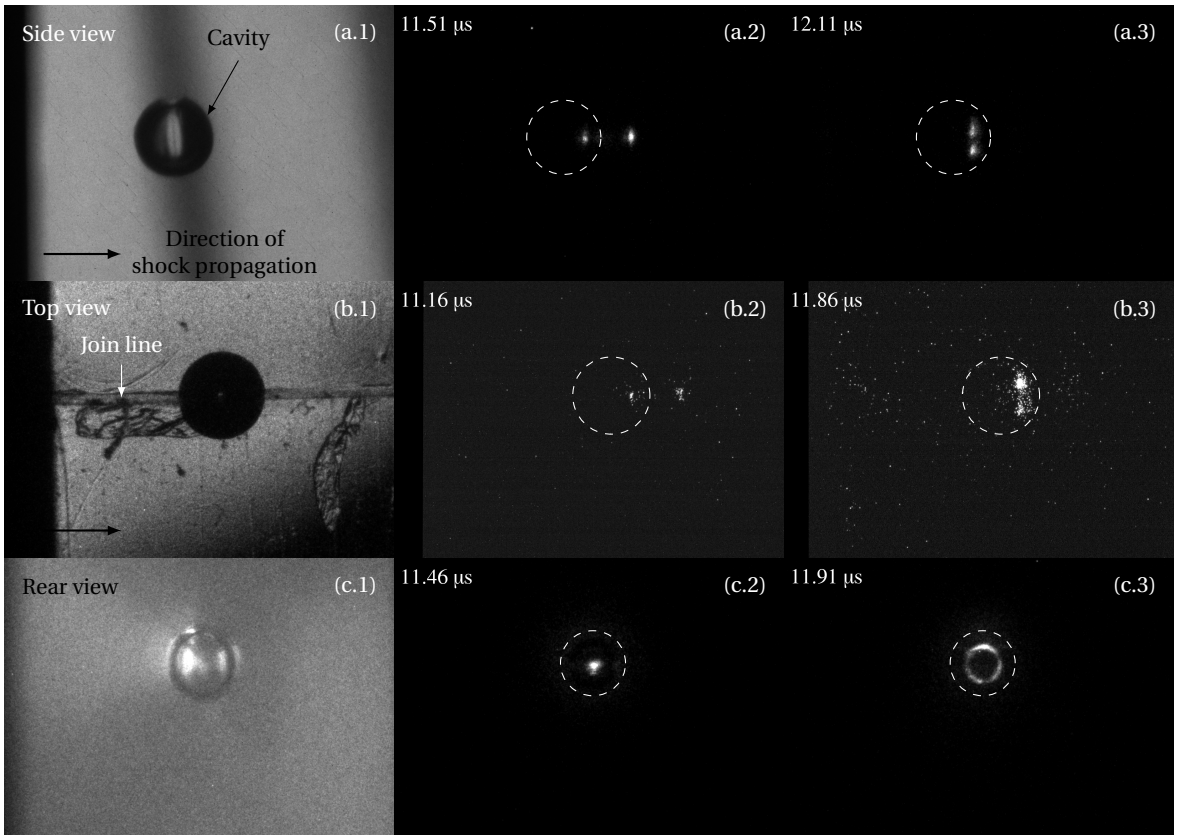

Figure 7.1: Images a.2 and a.3 show light emission from the collapse of a 5 mm diameter spherical cavity at a projectile velocity of 385 ± 4 ms^{-1}, viewed as shown in figure 5.13. Shocks propagate across images from left to right. No back-lighting is used, and image a.1 shows the position of the cavity in the gel before the shot. Image duration 0.2 μs. Images b.1 to b.3 show the results found using the same setup (projectile velocity 390 ms^{-1}, image duration 0.175 μs), but with the gel block rotated 90 degrees such that the join line between the hydrogel halves is visible. Images c1 to c.3 show results found using a mirror placed behind the gel (figure 5.15), with projectile velocity 392 ± 5 ms^{-1} and image duration 0.15 μs.

light emission removed. Times given correspond to the time of impact of the projectile on the striker plate.

Looking at the image sets, a number of features are immediately apparent in the structure of the light emission. In the case of the spherical cavities (figure 7.1), although the top-view images are of a much lower quality that those taken from the side, two separate bursts of light emission are seen in both image sets, with a qualitatively similar shape. These results correspond well to the rear-view images, which clearly show the light emission forming at single point, before propagating out into a toroidal shape. This result is

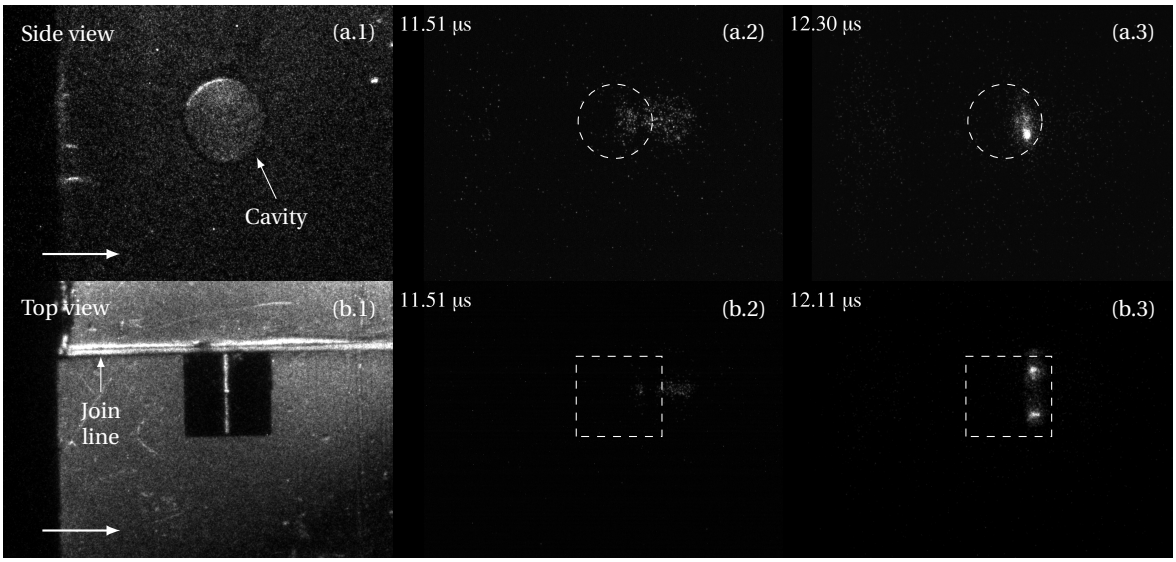

Figure 7.2: Light emission from the collapse of a 5 mm diameter, 5 mm long cylindrical cavity. Shocks propagate across images from left to right. Images as in figure 7.1. (a): projectile velocity 390 $\pm$ 2 ms^{-1}, frame duration 0.4 μs. (b): gel black rotated 90°, projectile velocity 388 $\pm$ 3 ms^{-1}, frame duration 0.2 μs. Arrows show direction of shock propagation.

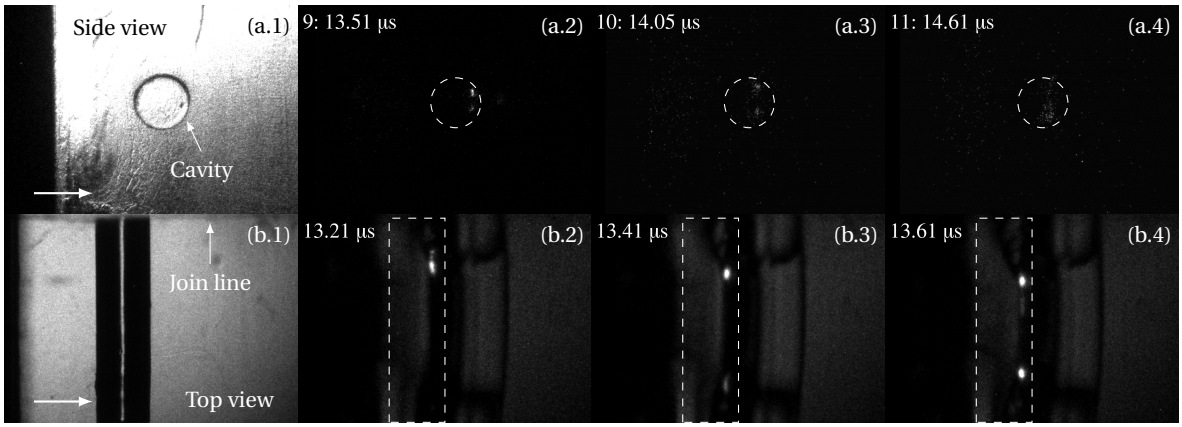

Figure 7.3: Light emission from the collapse of a 5 mm diameter, 20 mm long cylindrical cavity. Shocks propagate across images from left to right. Images as in figure 7.1. Shot (a) projectile velocity 391 $\pm$ 3 ms^{-1}, frame duration 0.55 μs. Shot (b) projectile velocity 392 $\pm$ 3 ms^{-1}, frame duration 0.2 μs. Arrows show direction of shock propagation.

consistent with an axisymmetric collapse process, as discussed in section 4.3.3.

In the case of the cylindrical cavities (figures 7.2 and 7.3), although the on-axis light emission appears to be reasonably similar in structure to the spherical case, the top-view images demonstrate that significant three-dimensional effects are occurring. This is most

clearly observed in figure 7.3, which shows the case of a 20 mm long cylinder. The light emission can be seen to start at the extremes of the cylinder, and then propagate in to the centre. This effect is consistent with the collapse of rectangular cavities (see for example[167]), where jets form at the corners of the cavity, and then migrate towards each other. The top-view images of the shorter cylinder case (figure 7.2 (b)) show the light emission concentrated at the extremes of the cylinder, possibly suggesting a similar process occurring.

While a two-dimensional collapse process may be achievable in other experimental setups, these results suggest that in the present case cylindrical cavities collapse as three dimensional entities. This significantly limits their usefulness within this study, as comparisons cannot be made to simulated results, which are restricted to axisymmetric and two-dimensional arrangements. As a result, results in the remainder of this work are restricted to the collapse of spherical cavities only.

7.3 Collapse of a single spherical cavity

In this section, the collapse of a single spherical cavity is explored, using both experimental and simulated results. In all cases, the cavity is of initial radius 2.5 mm, and is placed 10 mm from the the striker plate (see figure 5.7).

7.3.1 Analysis of the collapse

Figures 7.4 and 7.5 show the collapse of a single spherical cavity, viewed side-on and from the rear. The projectile velocities for the two shots were 393 ± 6 ms^{-1} and 394 ± 8 ms^{-1} respectively. For figure 7.4 the incident shock pressure, inferred from the incident shock velocity at the point of impact of the shock on the cavity, is calculated as 590 ± 40 MPa. As the incident shock velocity is not measurable from the images, the incident shock pres-

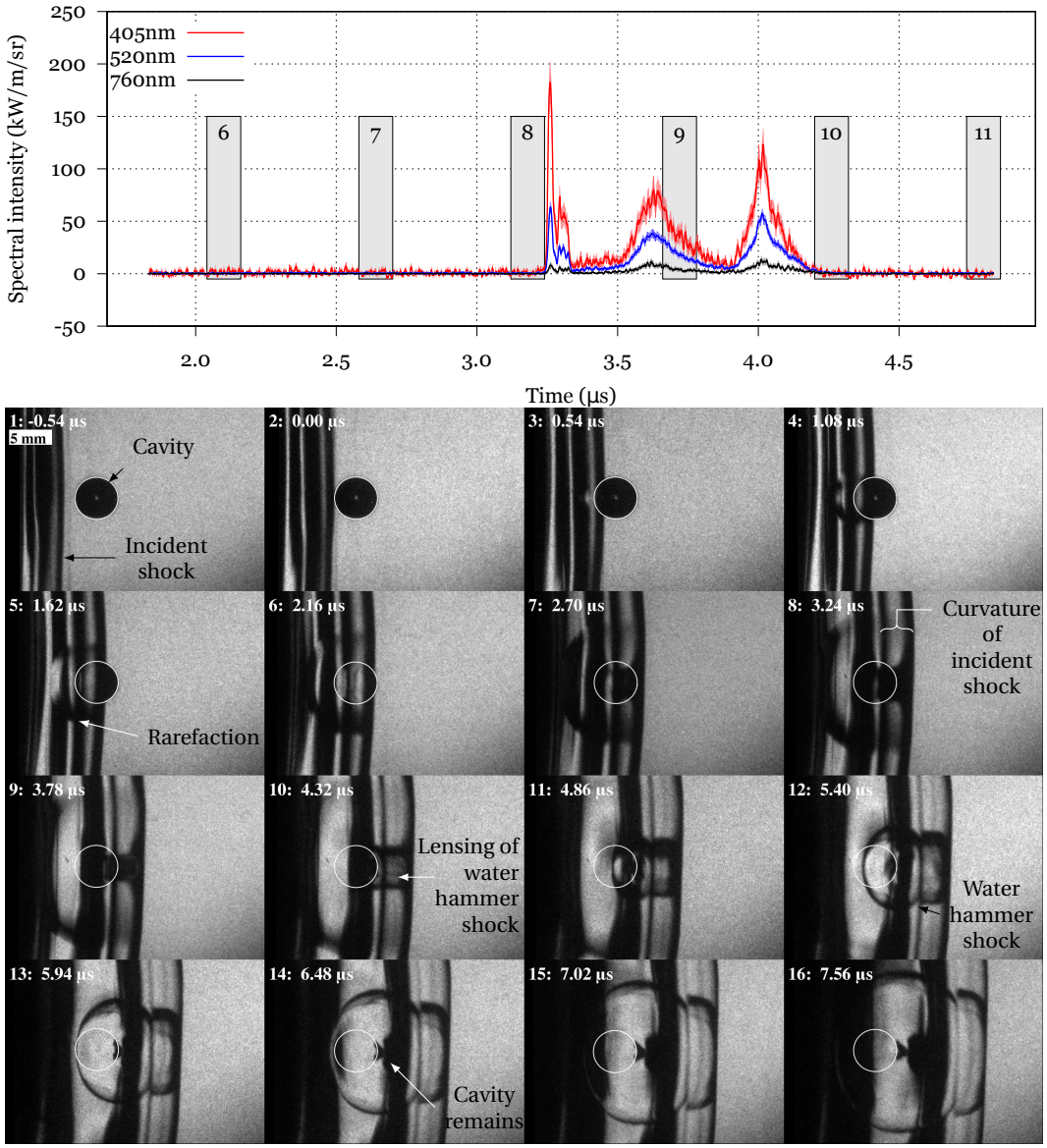

Figure 7.4: PMT traces and SimX images for the collapse of a single spherical cavity. Images taken from the side (figure 5.13). Projectile velocity 393 ± 6 ms^{-1}, incident shock pressure 590 ± 40 MPa. Numbered bars in PMT plot mark the times at which the corresponding SimX frames were taken. Displayed times referenced to time of first impact of incident shock on cavity.

sure is not known for figure 7.5, although as seen in figure 6.6, pressures are likely to be of similar magnitude to the side view case. For each figure, the graph displays the spectral intensity of light from the cavity, found using the PMTs at wavelengths of 405 nm, 520 nm and 760 nm, inferred from the recorded voltages for the shot as described in section 5.6.1. Below the graph, the image arrays show the frames taken of the collapse by the SimX 16

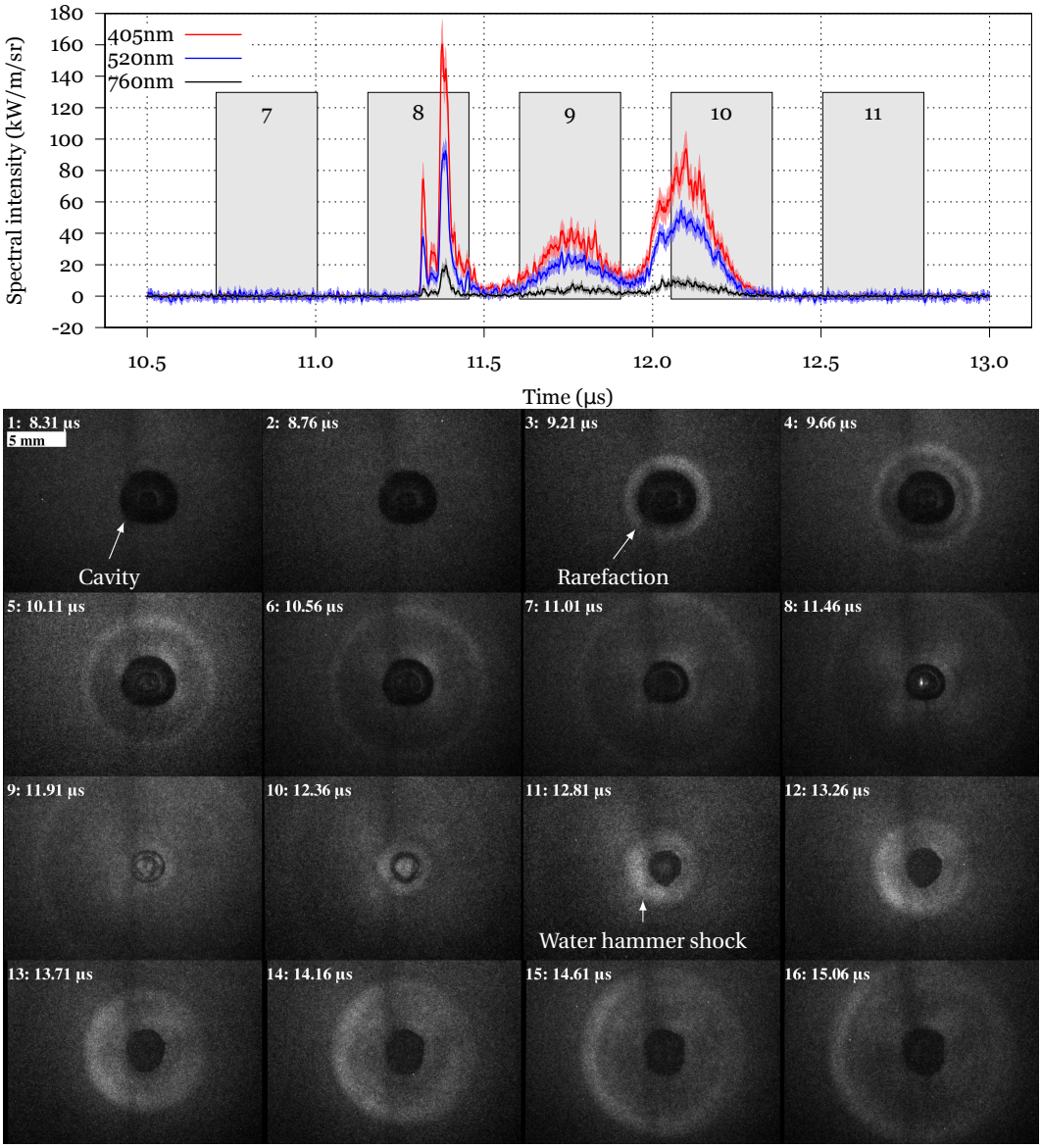

Figure 7.5: PMT traces and SimX images for the collapse of a single spherical cavity. Images taken from the rear, using a mirror as in figure 5.15. Projectile velocity $394 \pm 8\,\mathrm{ms}^{-1}$. Plots as in figure 7.4. Displayed times referenced to time of impact of projectile on striker plate.

camera. In figure 7.4, the displayed times are referenced to the time of first contact of the incident shock on the cavity, as measured from the SimX images. This time is not known for figure 7.5, and times are thus referenced relative to the time of impact of the projectile on the striker plate. The white bar at the top left corner of the first frame in both figures is a scale bar for reference. The time and duration of each frame is shown on the PMT

graphs as a series of labelled bars. The number of each bar corresponds to the number of the frame in the images below. The width of each bar shows the length of the exposure for the respective frame. The results of figure 7.4 were taken using the setup described in section 5.5.1, while the rear-view results of figure 7.5 were obtained using the setup described in section 5.5.2. In both cases, the SimX images were illuminated using the 200 W pulsed diode laser.

In the side-view images of figure 7.4, the bands in the images due to the curvature of the shock and the rarefaction at the gel edge, as described in section 6.2, are immediately apparent. Any events occurring within the curved region of the incident shock are obscured, with the images in this region consisting of a distorted image of the events occurring immediately to the left of the region. This lensing effect can most clearly be seen from frame 10 onwards. At this shock strength, this significantly impedes the view of the cavity collapse process. However, key features consistent with the results of Hawker *et al.* [1] and of chapter 4 are visible. On impact of the incident shock on the cavity, a reflected rarefaction forms. This wave is also present in the rear view images of figure 7.5, where a lighter circular region can be seen expanding from the cavity prior to any light emission. The cavity radius also begins to reduce, such that by the point of first light emission the radius is approximately 30 % smaller than its original value (frame 8, figure 7.5).

Looking at the PMT traces, in both shots the detected light emission can be seen to be temporally divided into three distinct peaks. The sources of these peaks are visible in the rear view images, but are more easily identified in figure 7.6, which shows the collapse of another single spherical cavity from the rear, this time without any additional illumination and with more frames over the period of light emission. Also shown is the corresponding APD trace, setup as described in section 5.6.2. In both figure 7.5 and figure 7.6 the first of the peaks is clearly visible as a single spot of light, approximately in the middle of the back wall of cavity. The spot of light is not perfectly round, but has some

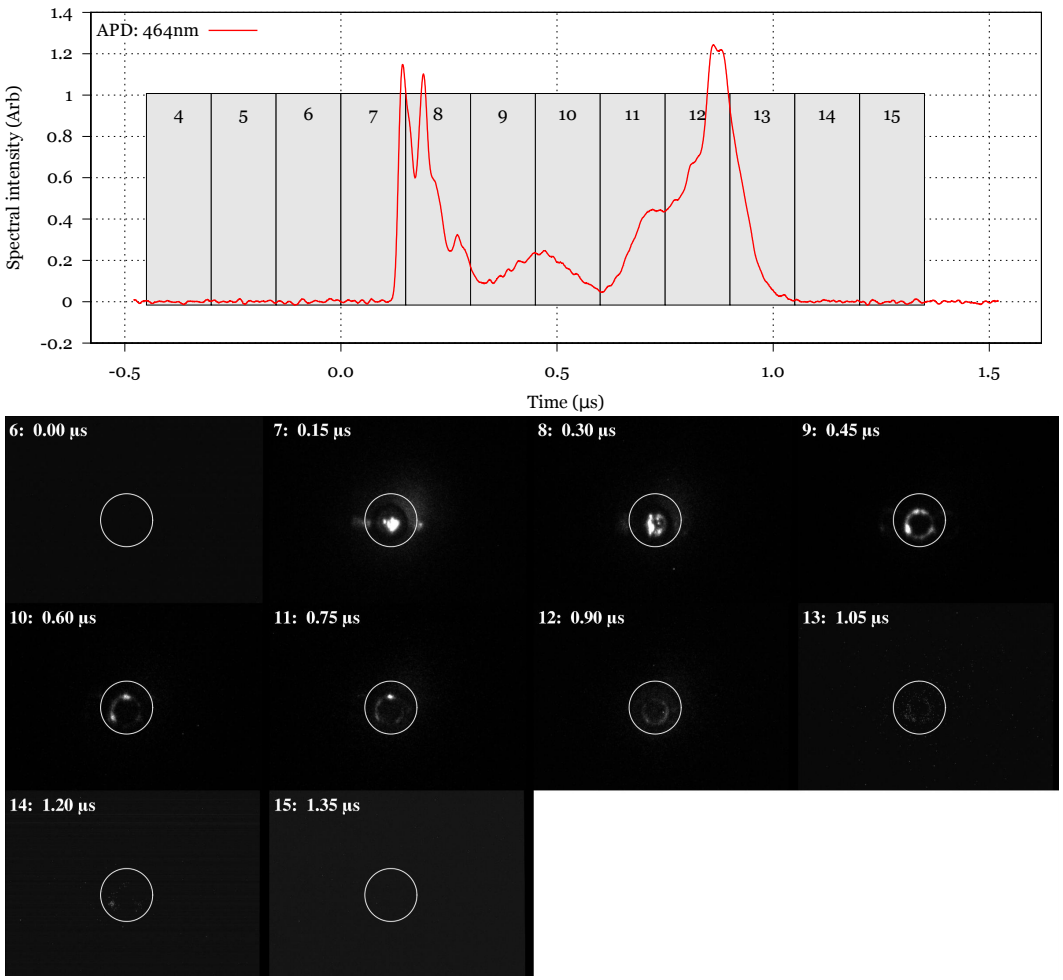

Figure 7.6: Light emission from the collapse of a single spherical cavity, imaged from the rear. No back-lighting. Projectile velocity $403 \pm 5\ \mathrm{ms}^{-1}$. Plot shows the APD trace as recorded for the shot, with frame timings marked as in figure 7.4.

structure, with an approximate radius of 0.3 mm in figure 7.5. In figure 7.6, this initial spot of light can be seen to progressively expand into a torus, which endures for almost a microsecond following formation. The timing of this torus corresponds to the period over which the second and third peaks occur. This ring of light is shown in figure 7.5 to form inside toroidal cavity walls, with the view through the centre of the cavity completely unimpeded.* This result is not unexpected; as shown in figures 2.4 and 2.5, which show the simulated collapse of a (cylindrical) cavity, when the main transverse jet strikes the leeward wall a pocket of gas is predicted to be compressed underneath the tip of the jet.

*The approximate outer radius of the torus in frame 9 of figure 7.5 is 1.25 mm.

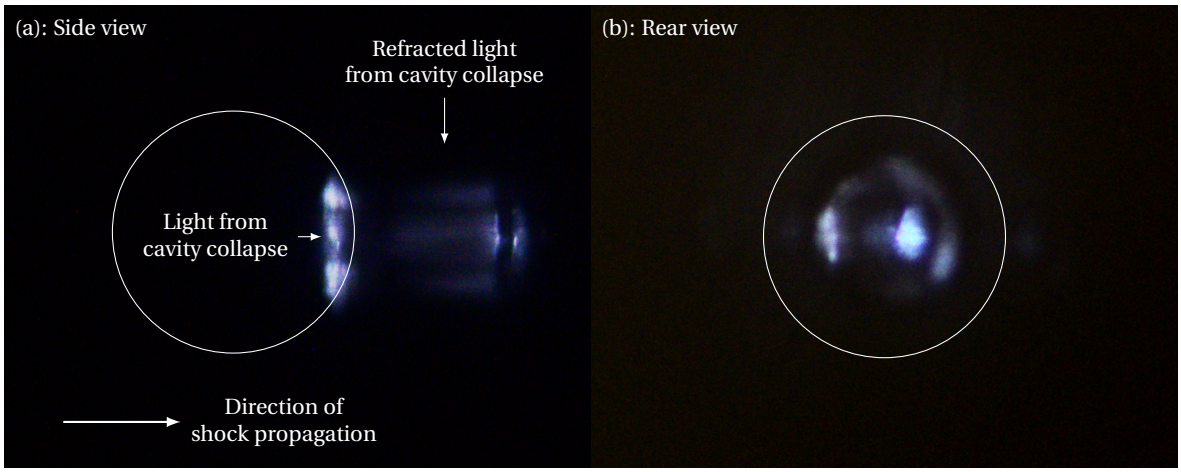

Figure 7.7: SLR long-exposure images of the collapse of a spherical cavity, taken from (a) the side and (b) the rear using a mirror, as described in section 5.5.3. White circles on images show the initial radius of the cavity in each case. Respective projectile velocities 386 ± 3 ms^{-1} and 388 ± 10 ms^{-1}. Exposure time 3 seconds, ISO 2000, white balance 3030 K. Apertures $f10$ and $f8$ respectively.

The remains of the cavity, which form a torus in the axisymmetric case, subsequently collapse as shock waves propagate out from the point of jet strike. These results thus suggest that the initial peak is caused by the impact of the jet on the leeward wall, while the second and third peaks correspond to the collapse of the toroidal cavity remains. The torus as shown in frame 9 of figure 7.5 is not perfectly smooth, possibly suggesting that the toroidal remains of the cavity collapse at different rates in different parts of the cavity. Comparing the structure of the light emission when viewed from the side and rear, the same three peak structure can be seen in both cases. This offers some indication that the structure of the light emission as detected by the PMTs is primarily caused by the emitting process, as opposed to the refractive effects of the incident shock, which would be expected to modify the light in different ways in different directions. Of additional note, the intensity of the light emission as observed in the SimX images does not always correspond to the level of spectral intensity as seen in the PMT traces (see for example frame 12 of figure 7.6). It is likely that this is in part due to the spectral response of the SimX camera.

Comparing the different PMT traces in figure 7.4, although the amplitudes vary with time, the light emission has a higher spectral intensity at lower wavelengths at all times.

This result is corroborated to some extent by figure 7.7, which shows long-exposure colour images of the collapse taken from the side and rear. In both images, the light emission can clearly be seen to have a blue tint, as would be expected from light emission that is more intense at lower (blue) wavelengths. Also visible in figure 7.7 (a) is a region downstream of the cavity in which the light emission from the collapse of the cavity is refracted towards the camera by the curvature of the incident shock. This is a feature also visible in SimX images of the light emission (see for example frame 11 of figure 7.12), and may lead to increases in the spectral intensity of the light emission as detected by the PMTs when the collapse process is viewed from the side. It is difficult to quantify the significance of this refracted light as it cannot be isolated from the light detected directly from the cavity, however the similarity in PMT traces when viewed from the side and rear in figures 7.4 and 7.5 may suggest that it is a relatively insignificant effect.

Following light emission, a spherically spreading shock wave is visible in figures 7.4 and 7.5. This shock wave is consistent with the water hammer shock formed by the impact of the main transverse jet on the back wall of the cavity, as discussed in section 2.4.3.1. As this shock propagates out from the cavity, the cavity remains endure. In the rear-view images of figure 7.5 the cavity can be seen to reform and regrow (frames 11 to 16), reaching a radius of approximately 2 mm 3.6 μs after first light emission. Looking at the side view images, the cavity does not return to its initial spherical shape, but exists as a complex mix of gas pockets, contained by the vortex ring produced by the action of the main transverse jet (see frames 13 to 16 of figure 7.4).

7.3.2 Repeatability

The repeatability of the light emission at particular shock pressures from the collapse of a single cavity can be seen in figure 7.8, which shows multiple PMT traces at approximately the same incident shock pressure, for a low pressure (approx. 600 MPa) and high pres-

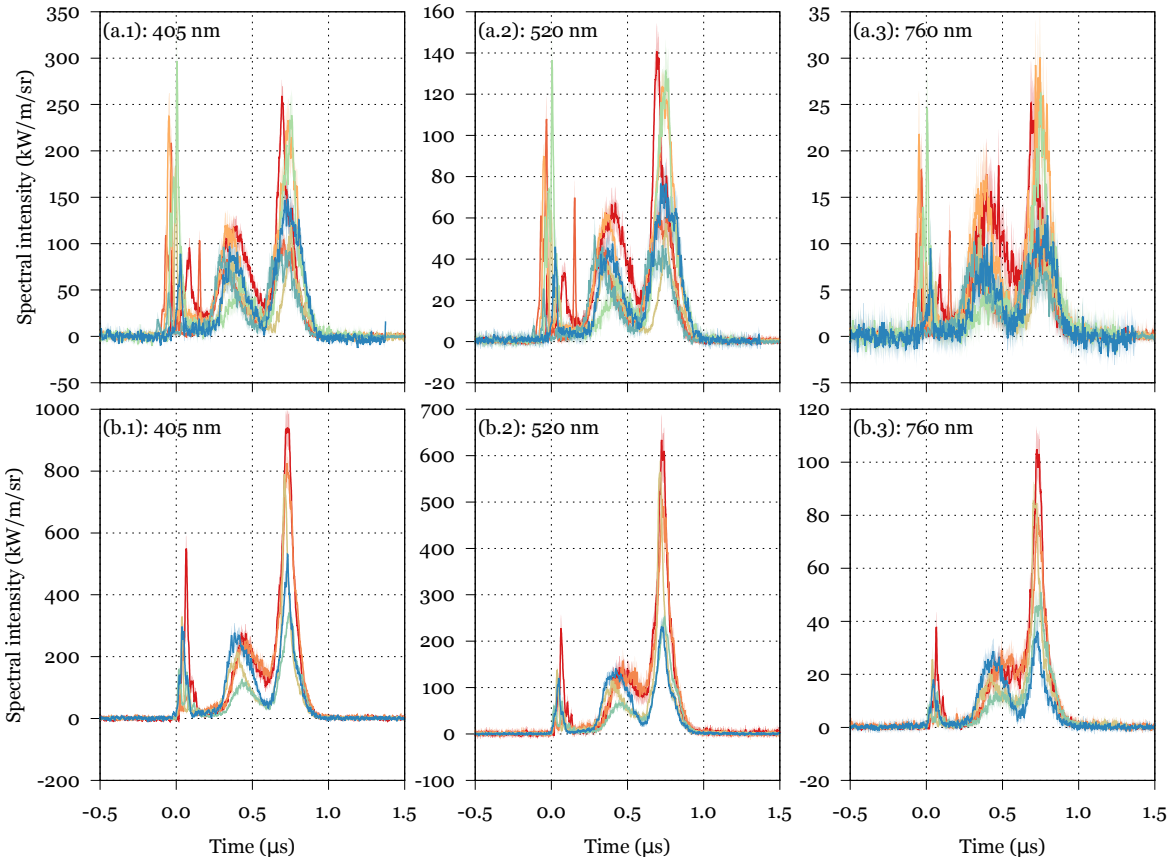

Figure 7.8: Overlaid PMT spectral intensities for a single cavity. (a) 7 traces at a mean incident shock pressure of 590 ± 30 MPa, (b) 5 traces at 810 ± 40 MPa. Traces aligned in time based on the time of final light emission to aid comparison. Line colours designate different shots.

sure (800 MPa) case. The traces have been shifted temporally to align the end of the light emission to aid comparison. Both single cavity results and the results obtained from the collapse of the first cavity in a two cavity array are shown; as discussed further in section 8.2, the first cavity in a two cavity array is found to collapse in a manner indistinguishable from the single cavity case. Looking at the plots, a number of key features are apparent. While there is some variability in the magnitude of the individual peaks, the general shape of the light emission is reasonably consistent at a particular shock pressure. The three peak structure, as discussed in section 7.3.1, is consistently returned in all cases, with the timings between the individual peaks and the overall width of the pulse found to stay fairly constant at a particular shock pressure. Overall pulse widths are constant to

within 5% at 600 MPa, and 2% at 800 MPa for the presented shots. Comparing the low pressure and high pressure case, the relative magnitudes of the peaks notably shifts as the pressure is increased. The magnitude of the third peak increases significantly at the higher pressure, becoming the brightest of the three. This effect is discussed further in section 7.3.4.

7.3.3 Comparison with simulation

To validate the numerical methods used in this work, and to provide further insight into the dynamics of cavity collapse, in this section comparison is made between experimental results and matched simulations. Simulations are conducted using the front-tracking approach, as outlined in chapter 3 and used extensively in chapter 4. As spherical cavities are used in the experimental results, simulations are modelled using axisymmetric coordinates. A stiffened polytropic equation of state is used to model the gel, with the fitted parameters of table 3.2. The air in the cavities is modelled as an ideal gas, with the effects of any water vapour in the gas neglected. Simulations are modelled from experimental results using the methods outlined in section 5.8, and are conducted at a resolution of 200 ppr.

Figure 7.9 compares the matching simulation to the experimental results of figure 7.4. As can be seen, the simulated incident shock is initially well matched to the experimental shock, but gradually overtakes it over time (compare frame 1 to frame 16). This is illustrated in figure 5.32, which compares the variation in experimental and simulated shock velocity with time for this shot. As can be seen, while the initial simulated shock velocity is well matched to the experimental result, the simulated shock velocity does not attenuate at the same rate. This difference may be partially caused by the assumptions used to model the incident shock, in particular the assumption that all points behind the shock are moving with the same effective shock velocity.

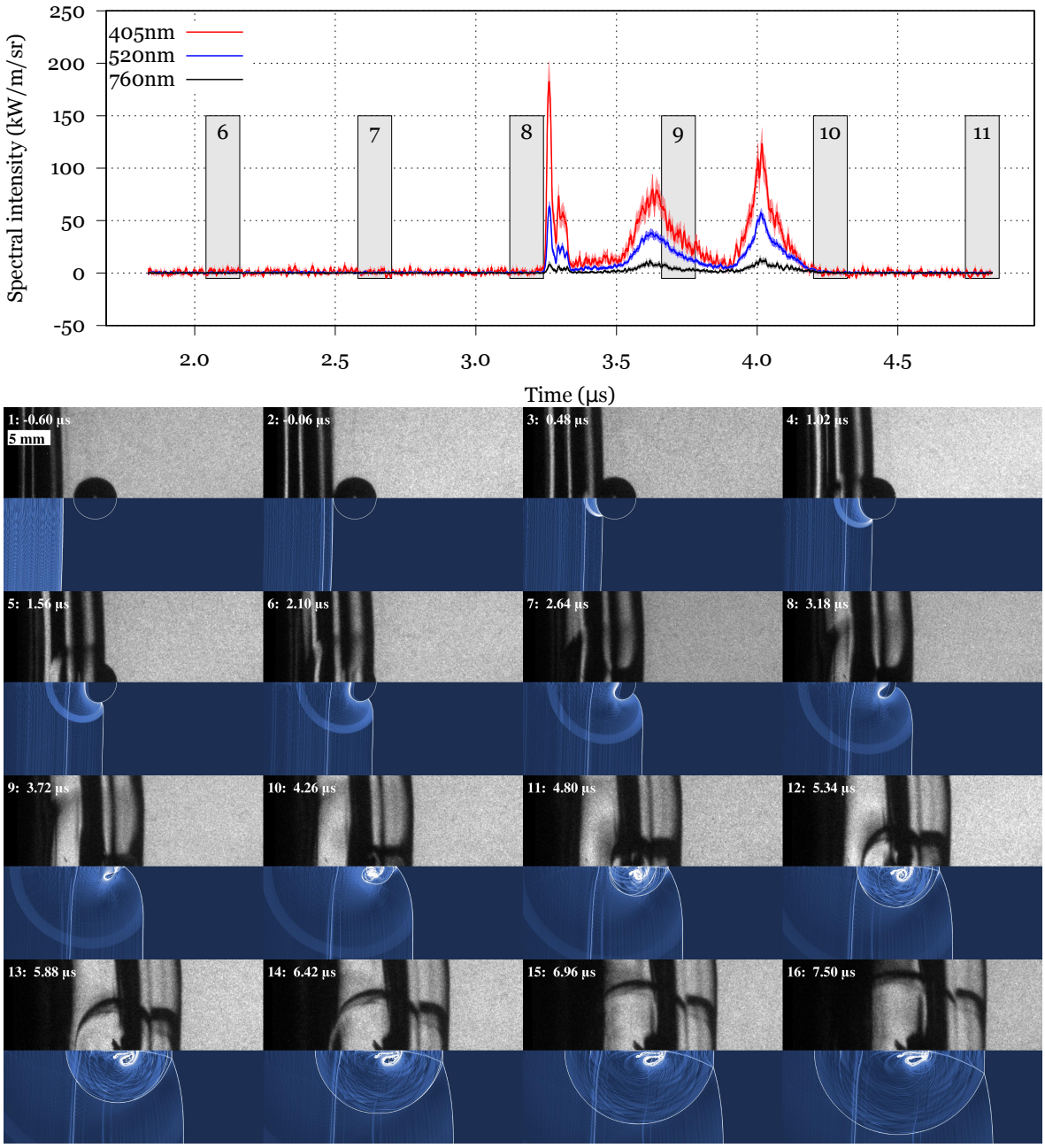

Figure 7.9: Comparison simulated results for the experimental results of figure 7.4. Experimental results shown at the top of each image, corresponding numerical results at bottom. Simulated images shown using $|\nabla\rho|$ as in chapter 4.

Although the main transverse jet is not visible in the experimental images in figure 7.9, other features present match closely to processes seen in the simulated result. In particular, the formation of the rarefaction wave from the impact of the shock on the cavity (frames 3 to 10), as well as the water hammer shock formed by the impact of the jet on the

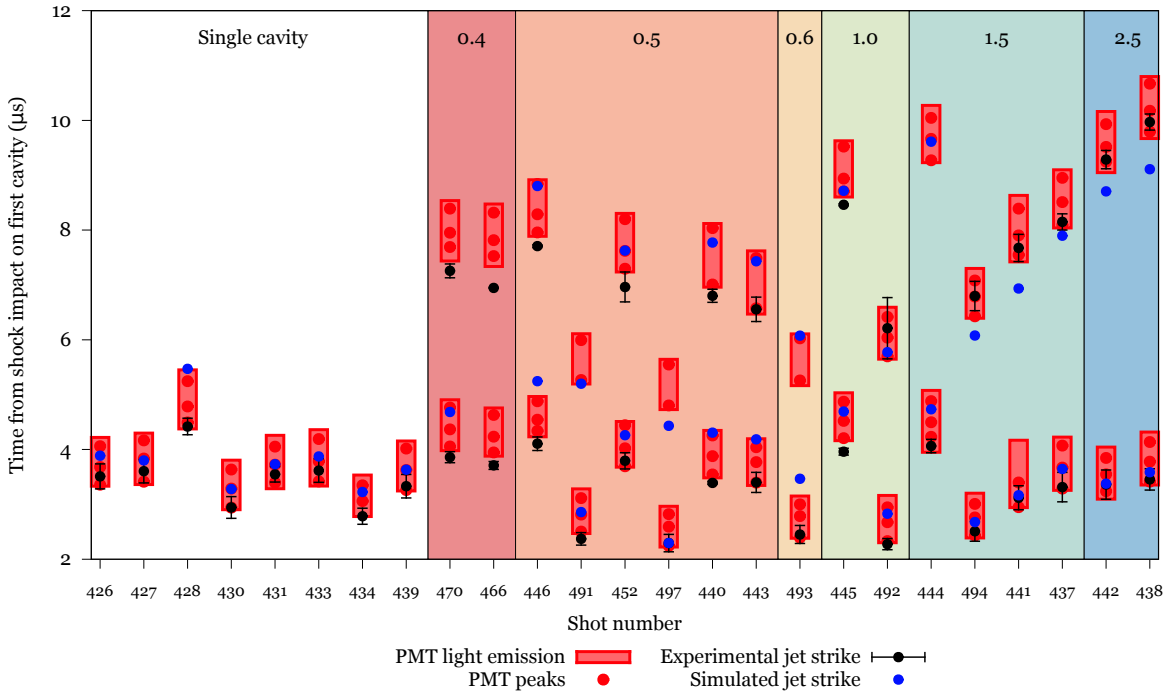

Figure 7.10: Comparison between light emission timings, experimental jet strike timings and simulated jet strike timings for a number of single and two cavity shots, covering a range of incident shock pressures. Experimental jet strike timings inferred from water hammer shock propagation, as described in section 5.8.3. Shots grouped by the separation distance between the cavities (S/R_i in figure 8.1), given at the top of each group.

leeward cavity wall (frames 10 to 16) are both closely matched. By frame 16, the simulated water hammer shock has expanded to a radius of 9.9 mm, compared to an experimental result of 9.4 mm, a difference of 5%. As the water hammer shock propagates away from the cavity, the cavity remains can also be seen to take qualitatively the same shape in the two result sets. Jet strike is predicted to occur approximately 0.4 µs later in the simulated result, a difference of 11% in the cavity collapse time. This may point to some inaccuracies in the numerical methods used, most notably the equation of state of the hydrogel (section 3.3.3), which may be too simple to capture the full complexity of the material, or be imperfectly fitted.

Figure 7.10 compares cavity collapse timings for a selected set of shots to equivalent timings as found in matched simulations. Within the plot, the red boxes show the pe-

riod of time during which light emission was detected on the PMTs for each shot. Within each red box, the red dots show the times at which peaks were seen in the PMT traces. Also shown for each experimental result is the calculated time of jet strike, as found from the propagation of the water hammer shocks using the methods outlined in section 5.8.3 (black dots). The times of jet strike for each cavity as found from matched simulations are shown with blue dots. Both single cavity and two cavity shots are shown in the plot, and the shots have been grouped by the relative separation distance between the cavities (S/R_i in figure 8.1). All times are referenced to the time of first contact of the incident shock on the first cavity in the arrangement. Comparing the times of light emission to the experimental jet strike times, it can be seen that the jet strike times line up consistently with the first peak of the light emission. This is illustrated further in table 7.1, which presents percentage differences between the two measurements. As can be seen, the percentage difference between the two result sets is on average less than the uncertainty in the experimental jet strike time measurement. This result therefore offers further evidence to suggest that the first peak of the light emission is caused by the impact of the main transverse jet on the leeward cavity wall. One caveat to this result is that (as discussed in section 5.8.3) the linear fit used to arrive at the experimental jet strike timings does not take into account the deceleration of the water hammer shock as it expands. Displayed experimental jet strike times in figure 7.10 are therefore likely to be slightly underestimated; however, a close correlation between first light emission and experimental jet strike was also seen when better fitting methods were applied, where it was possible to do so.

Comparing simulated and experimental jet strike times in figure 7.10, it can be seen that while timings are reasonably well matched in some cases, for a number of shots simulated jet strike timings are quite poor. Jet strike timings are matched most closely at higher incident shock pressures, when the collapse occurs earlier in time. In two cavity cases if the timings are correctly matched for one cavity they will not be so for the other.

Arrangement	Mean % difference	Standard deviation in % difference	Mean error in experimental jet strike time (%)
Single cavity	2.8	2.8	5.5
Two cavities: 1st cavity	-1.1	4.0	4.8
Two cavities: 2nd cavity	-0.8	4.6	2.5

Table 7.1: Percentage differences between the calculated experimental jet strike time, and the time of first light emission, for the different cavities presented in figure 7.10. Positive percentage difference when experimental jet strike time later than time of first light emission.

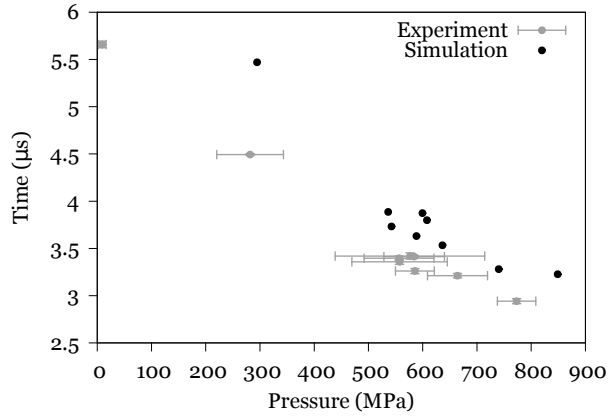

Figure 7.11: Variation in first phase collapse time with incident shock pressure for a single cavity.

The effect of incident shock pressure on the accuracy of the match between simulated and experimental results is seen more clearly in figure 7.11, which compares first phase collapse times for single cavity simulated and experimental results. The first phase collapse time, as in chapter 4, is defined as the time between the first contact of the incident shock on the cavity, and the time of jet strike on the leeward cavity wall. Given the result of figure 7.10, experimental jet strike times are inferred from PMT traces as the time of the first peak of light emission. Displayed pressures are the pressure of the incident shock on impact on the cavity.[†] As can be seen, simulated results are poorly matched at low

[†]For each shot, shock velocity does not vary with time in exactly the same way in the experimental and simulated result (see figure 5.32). Thus, by the time of impact of the incident shock on the cavity, the shock velocity, and therefore the pressure, will be slightly different. This means that simulation-experiment pairs do not line up vertically in figure 7.11.

pressures, but the quality of the match improves as the pressure is increased; percentage differences reduce from 20% at 300 MPa, to less than 10% at 800 MPa. The mean percentage difference between the two result sets is 13%, with a standard deviation of 4%. The large differences at low shock pressures are in part caused by the differences in how the shock velocity varies with time in the two result sets. At these low pressures, the incident shock initially accelerates as it propagates across the gel block (see figure 6.5). This phenomenon is not currently replicable in the simulated results, with simulated shock wave velocities reducing with time for all incident shock pressures. As a result, significant disparities can occur between the two result sets.

7.3.4 Effect of shock strength

As shown in figure 7.11, the strength of the incident shock strongly affects the timings of cavity collapse, reducing the collapse time of the cavity by half over the range of pressures studied. The effect of reducing the driving pressure on the dynamics of the collapse and the intensity of the light produced is shown in figure 7.12, which show the collapse of a cavity at the lower pressure of 280 ± 60 MPa. Because the relative timings of the processes at work in the gel during collapse vary at different rates with incident shock strength, less of the cavity is obscured by the shock wave in this image set, and more of the collapse process can be seen. Almost the entirety of the cavity is visible behind the incident shock wave from approximately frame 10 onwards. Light emission is visible in frame 11 as two small points at the base of the cavity, refracted as two thin lines by the curved incident shock. Two structures are visible in frame 12, with a shape and position that is consistent with the toroidal remains of the cavity; the approximate outer radius of this structure is 1.6 mm, compared to 1.3 mm for the outer radius of the torus at the equivalent point in the matched simulation. Light emission spectral intensities at this shock strength can be seen to be dominated by the first peak in the PMT trace, with magnitudes similar to those

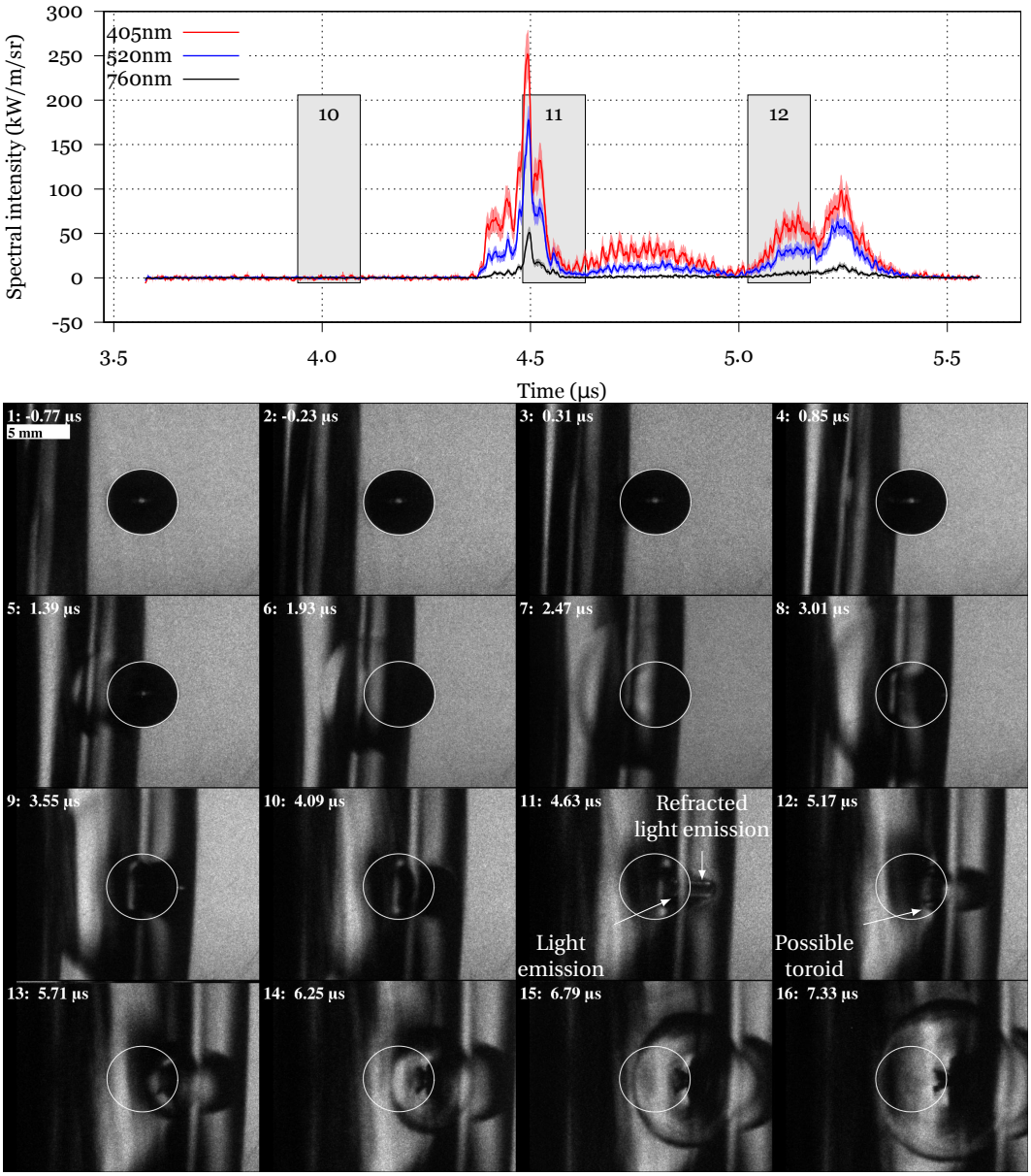

Figure 7.12: PMT traces and SimX images for the collapse of a single spherical cavity, at the lower pressure of 280 ± 60 MPa. Projectile velocity 300 ± 6 ms^{-1}. Results taken as in figure 7.4.

seen at 600 MPa, while second and third peak spectral intensities are reduced.

The effect of incident shock pressure on the structure of the light emission at a wavelength of 405 nm is shown in figure 7.13. As in figure 7.8, PMT traces are shown for both a single cavity, and the first cavity in a two cavity array. As can be seen, as the pressure is increased although the magnitude of all peaks increases the ratio of the different peaks

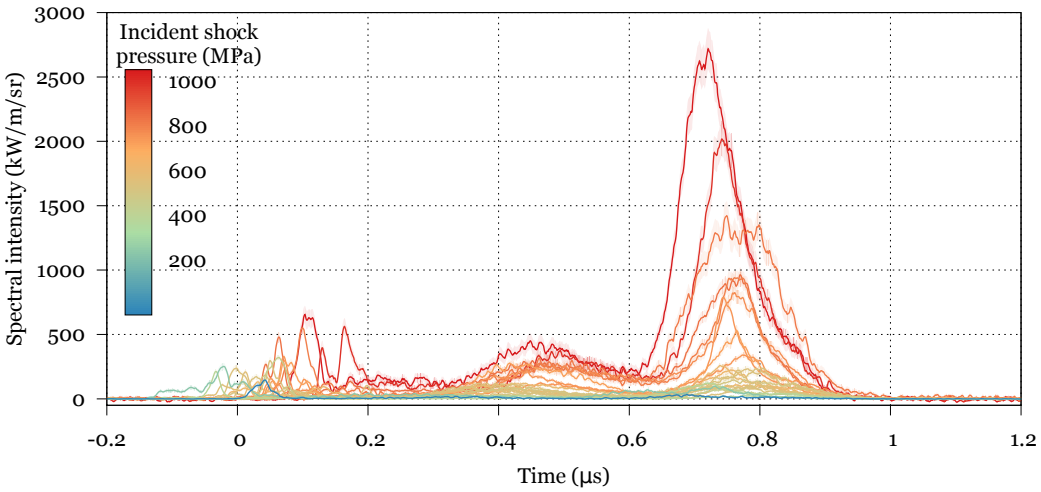

Figure 7.13: Overlaid PMT spectral intensities from the collapse of a single cavity at different incident shock pressures. Wavelength 405 nm. Traces aligned in time based on the time of first light emission to aid comparison.

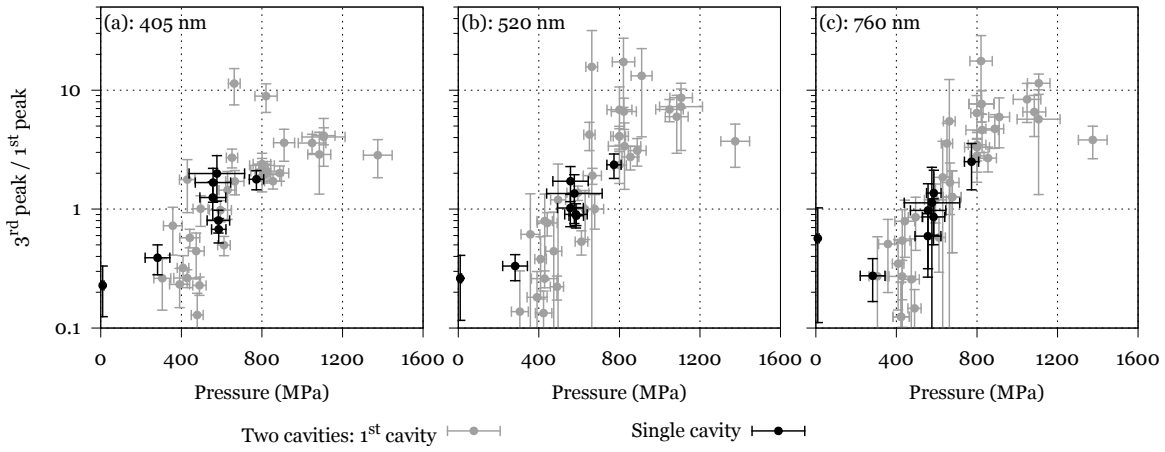

Figure 7.14: Ratio of first and third light emission peaks for the collapse of a single cavity. Also shown are the results for the first cavity in the two cavity array of section 8.2

changes. At very low pressures, the light emission is almost completely dominated by the first peak. As pressures are increased, the spectral intensity of the light emission from the first peak changes by factor of 10, but the spectral intensity of the third peak increases by a factor of 100. The third peak therefore progressively becomes the dominant source of light emission. This change in the relative magnitude of the peaks with incident shock pressure is shown more clearly in figure 7.14, which shows the variation in ratio between the third and first peak spectral intensities with incident shock pressure at the three dif-

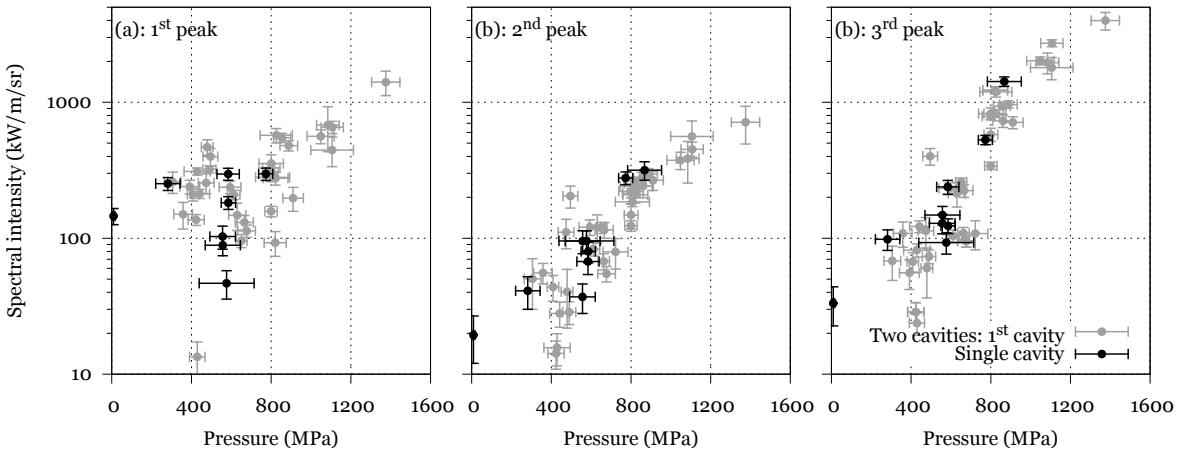

Figure 7.15: Variation in peak light emission spectral intensity with incident shock pressure for a single cavity arrangement, for each of the three peaks observed in the light emission traces. Wavelength 405 nm. Also shown are the results for the first cavity in the two cavity array of section 8.2

ferent wavelengths. Although there is substantial scatter in the data, a clear trend can be seen where at pressures below approximately 600 MPa the spectral intensity of the first peak is consistently higher than that of the third peak by up to a factor of 5, while at higher pressures the trend is reversed. This trend is seen at all wavelengths studied, with the increase in the ratio between the third and first peaks larger at higher wavelengths. This may suggest that the third peak has a larger area, but is cooler than the first at high incident shock pressures.

The effect of incident shock pressure on the absolute peak PMT spectral intensities is shown in figure 7.15. Results are shown for both a single cavity and the first cavity in a two cavity array, for each of the three peaks. As can be seen, second and third peak spectral intensities increase with incident shock pressure across the full range of pressures studied. By comparison, there is significant scatter in the first peak values below 600 MPa, although there is a notable trend beyond this point. Third peak spectral intensities increase by a factor of approximately 150 over the range of pressures studied. Together with the reduction in collapse time with incident shock pressure shown in figure 7.11, these results suggest that the conditions achieved during shock-driven cavity collapse do con-

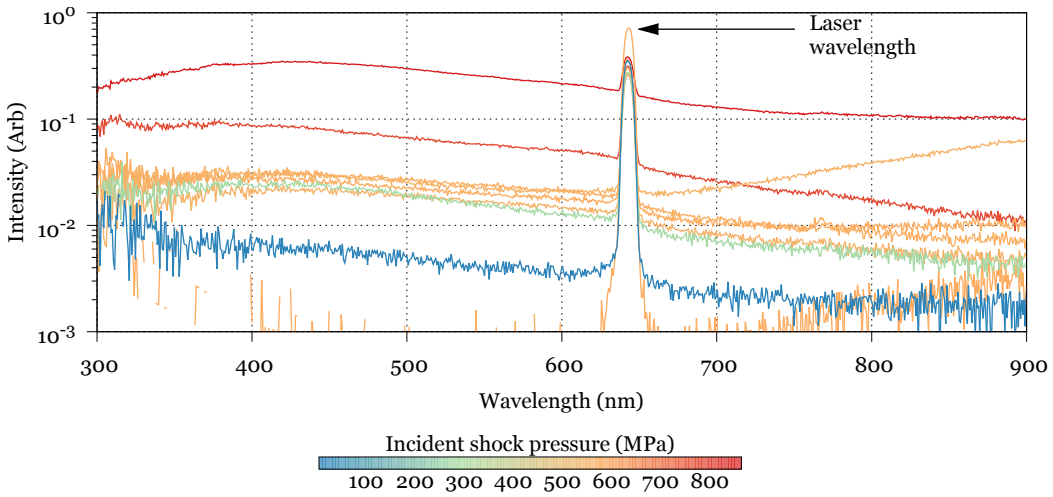

Figure 7.16: Variation in spectrum recorded by integrated spectrometer with incident shock pressure for a single cavity.

tinue to intensify as the incident shock pressure is increased, as was suggested by Hawker and Ventikos[1] (figure 2.6). Higher fidelity experimental techniques will be required to confirm this result, although some information as to the temperatures achieved may be found by comparing the PMT results at different wavelengths; this is done in the next section.

7.3.5 Temperature calculation

Looking at the relative magnitudes of the PMT traces for example in figure 7.4, it can be seen that the light emission varies in magnitude with wavelength in a consistent way. The light emission is more intense at shorter wavelengths, and progressively reduces in intensity as wavelength is increased. Although it is of course possible that the light emission consists of numerous peaks, three of which are at the wavelengths measured in this study, this trend is observed regardless of the wavelengths of the filters used, which lends support to the result that the spectrum of the light emission is generally broadband. Further support for this assertion is given by figure 7.16, which shows integrated spectra for the collapse of a single cavity, found using the methods outlined in section 5.6.3. As these

spectra are integrated over all times they have limited value in the calculation of temperatures. However, they offer further evidence to suggest that the light emission has a broadband spectrum, with no significant peaks observed. The one obvious exception to this result is the peak caused by the laser (640 nm central wavelength), clearly visible in the figure.

Looking at figure B.6 in appendix B, which shows how the spectra of the light emission is predicted to vary with different density-temperature combinations, to achieve a trend such as as seen in the PMT traces the light emission must be relatively close to the black-body limit. As will be shown in figure 8.19, simulations suggest conditions at jet strike ($\rho \approx 700$ kg/m^3, T $\approx 20,000 - 60,000$ K) that place the light emission inside the region in figure B.7 within which it would be expected to see a black-body spectrum, at the $\backsim 1$ mm sample depths seen in the experimental results. This assumption is clearly not valid for all points in time, as the temperatures will reduce to ambient conditions once the cavity has collapsed. However, the higher the intensity of the emitted light the more valid this assumption becomes, and a black-body model offers a reasonable first approximation for the spectrum of the light emission. With this assumption, the spectral intensity of the light emission at each point in time is given by the equation

$$I_\lambda(\lambda, t) = \kappa\alpha(t)\, L_{\lambda,\mathrm{BB},}(\lambda, t)\ \mathrm{W/m/sr} \tag{7.1}$$

where $L_{\lambda,\mathrm{BB}}$ is the black-body spectral radiance of the light emission in units of W/m^2/m/sr as given by Planck's law,

$$L_{\lambda,\mathrm{BB},}(\lambda) = \frac{2hc^2}{\lambda^5}\frac{1}{\exp(hc/\lambda k_B T) - 1}, \tag{7.2}$$

and α is the projected surface area of the emitting volume. κ is a non-dimensional constant, accounting for other effects such as the shape and structure of the emitting volume, and the emissivity of the plasma if a grey-body model is assumed. k_B is the Boltzmann constant, c is the speed of light, h is Planck's constant and λ is the wavelength. Simi-

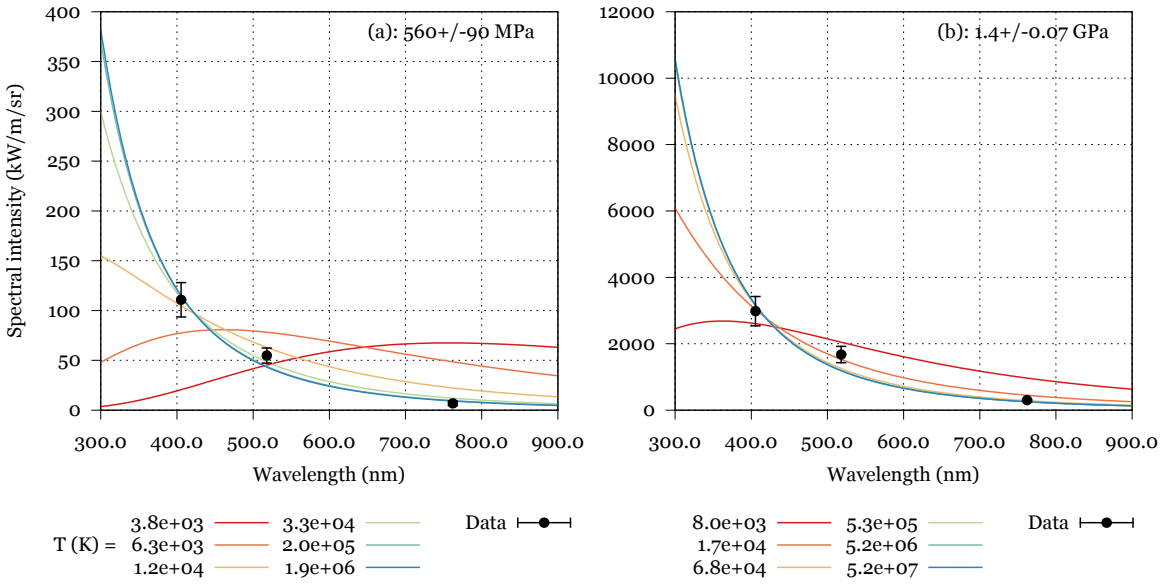

Figure 7.17: Fitted black-body curves for (a) a low spectral intensity (b) a high spectral intensity point, for different κ values. κ values decrease logarithmically from 0.01 (red line) to 1×10^{-7} (blue line).

lar methods have been used to infer temperatures in many previous studies, for example[218,219]. Neither the surface area or the emissivity are accurately known, but an order of magnitude estimation of α of 1×10^{-6} m^2 has been inferred from SimX images.

Although a least squares fitting routine may be used to fit the PMT spectral intensities at each point in time to equation 7.1 and thus infer temperature and $\kappa\alpha$, significant difficulties are encountered in doing so. Figure 7.17, which shows fitted black-body curves for different assumed values of $\kappa\alpha$, illustrates why this is the case. Looking for example at figure 7.17 (b), it can be seen that the data can be fitted with reasonable accuracy to a temperature of both 17,000 K and 52×10^6 K, if the area is permitted to take any value. In this case, these two values correspond to $\kappa\alpha$ values of 2×10^{-9} and 2×10^{-13} respectively. This is therefore a poorly constrained problem at high temperatures, and extreme, erroneous temperatures may be inferred by fitting routines if the fit is not constrained in some way. The clear remedy to this issue is the use of additional PMTs, particularly at wavelengths below 400 nm, although the poor transmission of the hydrogel at these wavelengths can

then become problematic (figure 5.12). A better solution still is the use of a full streak spectroscopy setup, at which point more sophisticated spectral approximations than a black-body model may be used.

Although it is unlikely to be possible to infer an accurate temperature from the PMT traces for the reasons just described, as can be seen in figure 7.17 there is a minimum temperature at which black-body curves reasonably approximate the data. This lower bound can be found by calculation of the lowest temperature at which the corresponding black-body curve approximates the data to within some limit. Based on the results of figure 7.17, this limit is set to be the point at which the relative error in the solution falls to within 10% of the solution. Figure 7.18 shows two examples of this analysis applied to single cavity PMT results. Looking at the figures, some evidence of the temperature and area traces mirroring each other is clear, particularly in figure 7.18 (b). This is unlikely to be physical; as the temperature traces effectively represent a lower bound, any increase in amplitude seen in the PMT traces is compensated for with an increase in area. This is further illustrated by figure 7.19, which shows the variation in fitted temperature and area with incident shock pressure, at the times of the three peaks in the spectral intensity traces. Particularly visible comparing figure 7.19 (a.3) and (b.3), no clear trend is visible in the temperature results with incident shock pressure, while fitted areas increase by almost three orders of magnitude over the same range.

The mean recorded temperature in both cases in figure 7.18 is approximately 18,000 K; this may represent the temperature limit beyond which the method used is not applicable. According to Zel'dovich *et al.*[220], at this temperature the air in the cavity should be almost completely dissociated into atoms, which are in turn appreciably ionised. Even if the black-body limit has not been reached, the spectrum should be dominated by broad-band spectra from photo-ionisation and bremsstrahlung processes (see appendix B). One interesting feature seen in both cases, and in fitted temperature traces generally is a no-

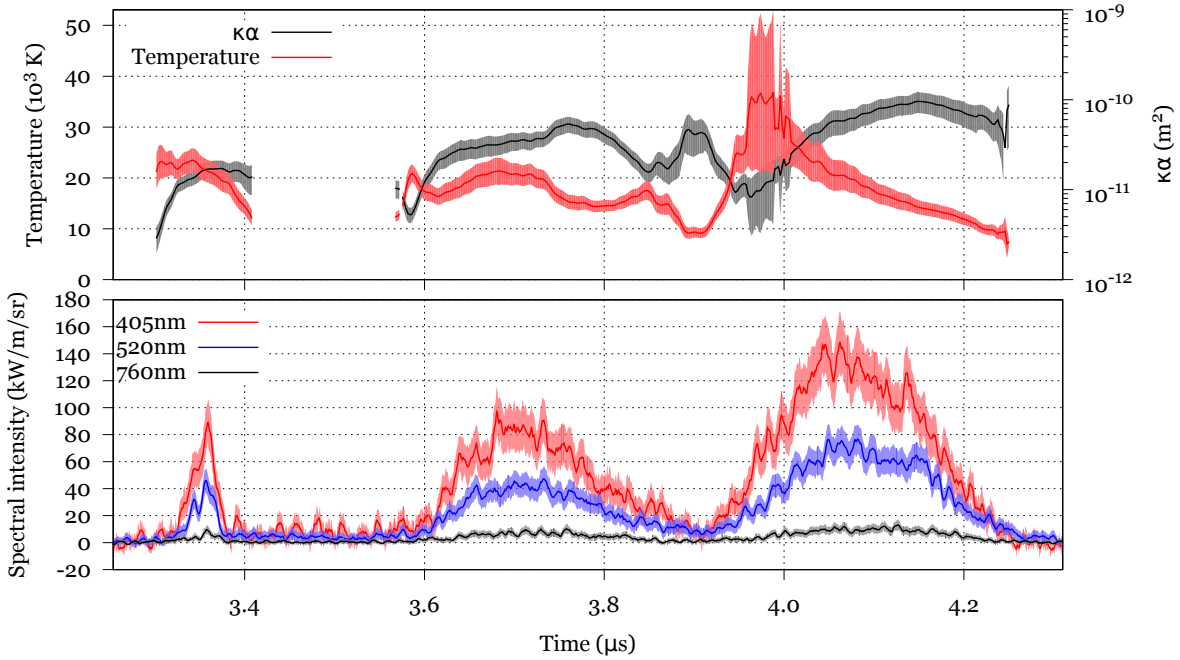

(a)

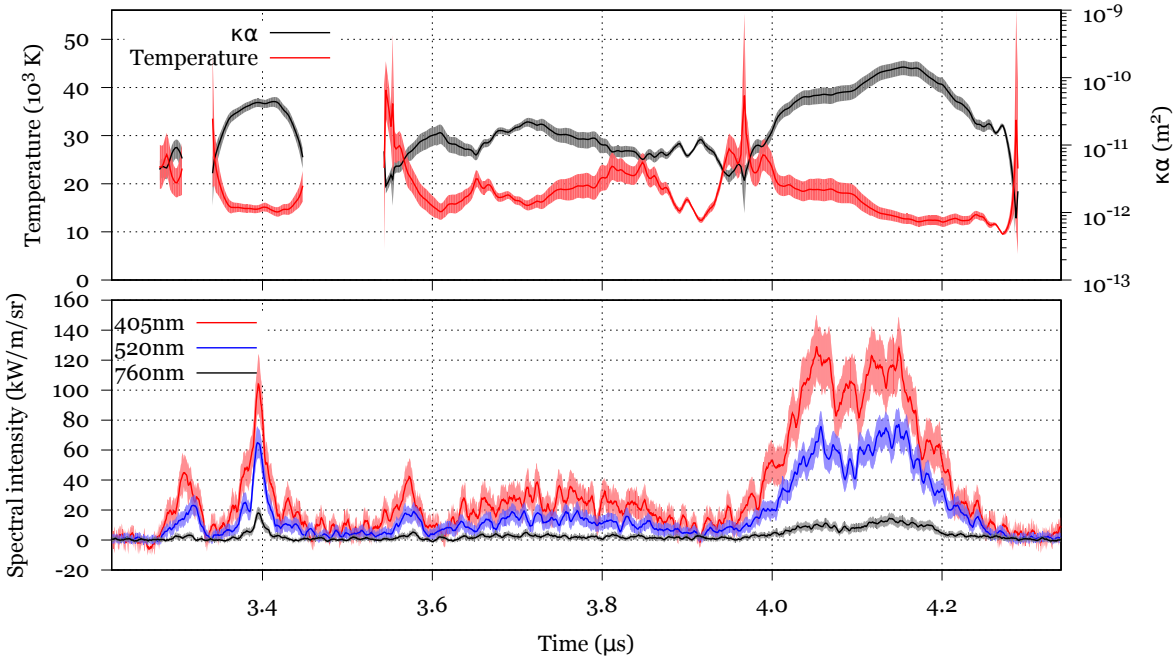

(b)

Figure 7.18: Two different examples of fitted temperature and area curves, inferred from the displayed PMT traces from the collapse of single cavities. Incident shock pressures 560 ± 90 MPa and 560 ± 60 MPa.

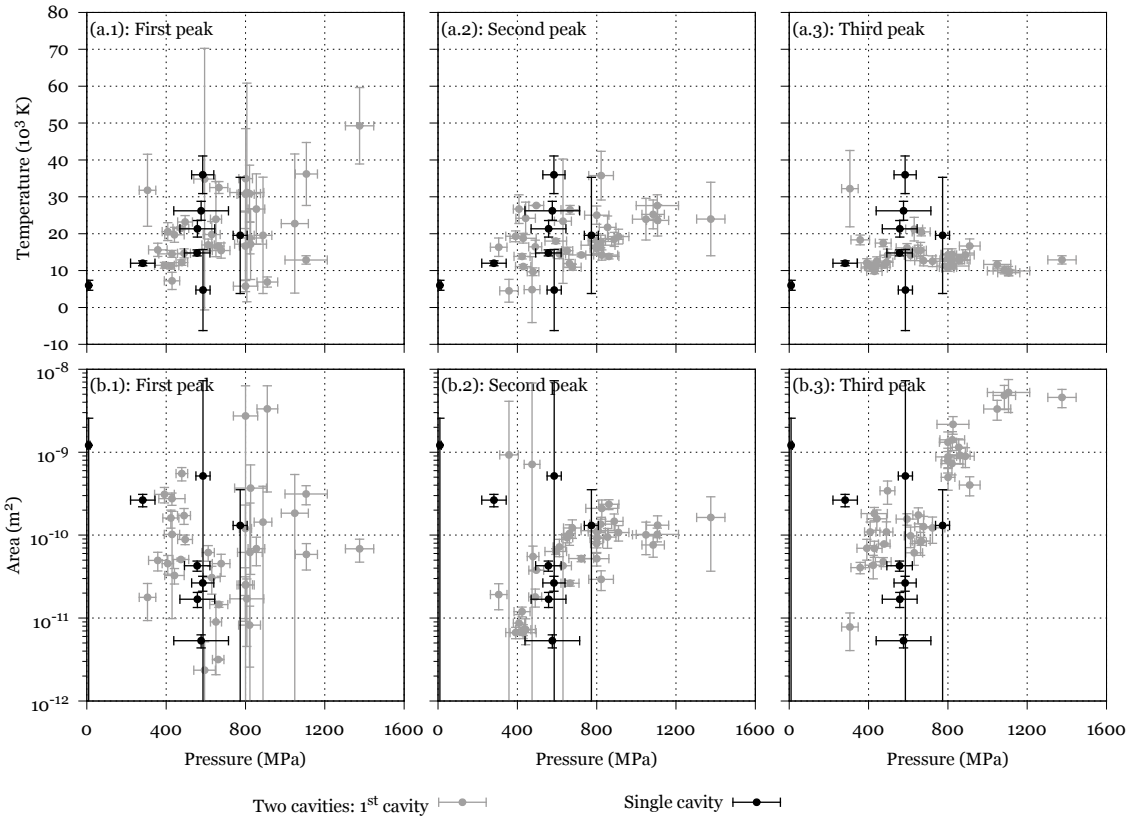

Figure 7.19: Variation in inferred temperature (a) and area (b) at PMT spectral intensity peaks with incident shock pressure, for the single cavity case. Also shown are the results for the first cavity in the two cavity array of section 8.2.

table peak in temperature, prior to the third peak in the corresponding PMT traces. This may suggest that minimum volume, when the shock waves propagating in the torus reach the top of the torus, recompressing the gas, does not correlate with the third peak in the PMT traces, but a point just before. Again, however, this result will need to be confirmed using more advanced experimental methods.

7.4 Discussion

This chapter has presented a comprehensive analysis of the collapse of a single cavity by an incident shock wave, using both experimental and simulated results. Before moving on to discuss more complex arrangements, the cavity collapse process as understood to

this point is briefly summarised.

On impact of the incident shock on the cavity, a reflected rarefaction is formed, and a main transverse jet forms in the cavity. This jet propagates across the cavity, striking the leeward wall. This process compresses a pocket of gas against the leeward wall, leading to ionisation of the gas and the emission of a burst of light with a broadband spectrum. The remains of the cavity at this point form a torus, which begins to collapse as shock waves from the point of jet strike propagate outwards in the gas. Also formed at this point is a strong spherical water hammer shock in the liquid. The collapse of the torus leads to a continuous period of light emission, seen as a ring in the images which propagates out from the point of jet strike. The highest temperatures are reached at the point at which the shock waves reach the top of the torus, although this is not the brightest part of the process due to the small area of the cavity at this time. Mean temperatures from the process are estimated to have a lower bound of approximately 18,000 K, with the experimental method used found to be insufficient to provide a more accurate estimate.

As the incident shock pressure is increased, both the timings of the collapse process and the structure of the light emission are seen to change. Collapse times progressively decrease, while the spectral intensity of the light emission increases. This may suggest that higher temperatures and densities are reached as the shock pressure is increased, although other factors, in particular the volume of the emitting region are likely to play a role. Additionally, the relative magnitude of the peaks varies with incident shock pressure. The spectral intensity of the first peak is highest at low shock pressures, but is overtaken as the shock pressure is increased. This may suggest that the most intense part of the collapse process is the collapse of the torus at pressures above approximately 600 MPa.



CHAPTER 8

EXPERIMENTAL STUDY OF MULTI-CAVITY COLLAPSE

This chapter presents an experimental and numerical study of the collapse of arrays of multiple spherical cavities by incident shock waves. Three arrangements are studied: an array of two cavities, one placed behind the other at a variable separation distance, a triangular array of three cavities and a triangular array of six cavities. In the case of the two-cavity array, significant increases in the spectral intensity of the light emission produced by the second cavity are observed at particular separation distances, relative to the single cavity case. The possible reasons for this increase are explored. The collapse of the three and six cavity arrays are seen to be highly complex, leading to light emission that is quite different from the single cavity case.

8.1 INTRODUCTION

In this chapter, the single cavity experimental results of chapter 7 are built upon, with a study of the collapse of multiple-cavity arrangements by incident shock waves. Specifically, the arrangements studied are a two-cavity array, where the distance between the cavities is varied, a three cavity triangular array and a six cavity triangular array. In all cases, the initial cavity radius R_i for all cavities is 2.5 mm, as was the case in the single cavity results. As only two-dimensional and axisymmetric simulations may be conducted us-

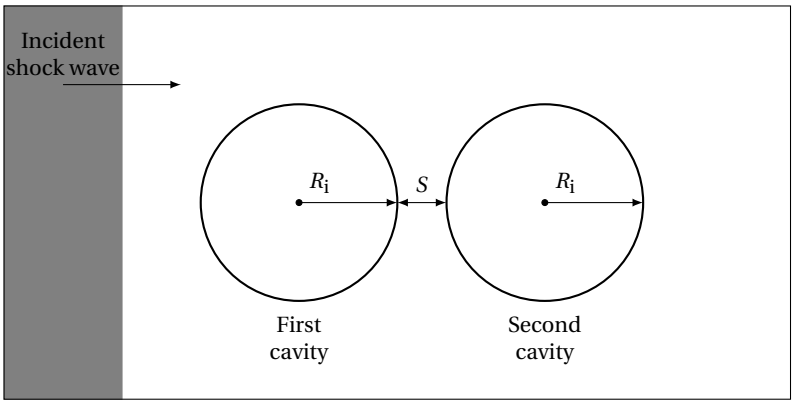

Figure 8.1: Diagram of the two-cavity experimental arrangement. Two cavities of initial radius R_i = 2.5 mm are placed separated by a distance S in a line parallel to the direction of incident shock propagation.

ing the front-tracking software employed in this study, only the two cavity arrangements are replicable in simulated results. Simulations of three and six cavity arrangements are therefore not presented in this chapter.

Of specific interest in this work was the question as to whether the conditions seen during cavity collapse could be amplified with the use of multiple cavity arrangements, as was shown in chapter 4, and whether this amplification held true at different incident shock pressures.

8.2 COLLAPSE OF A TWO-CAVITY ARRAY

This section presents a study of the collapse of a two-cavity array, a diagram of which is given in figure 8.1. As in chapter 4, two cavities of equal radius are placed in a line parallel to the direction of shock propagation. Both the distance between the cavities S and the incident shock pressure are varied.

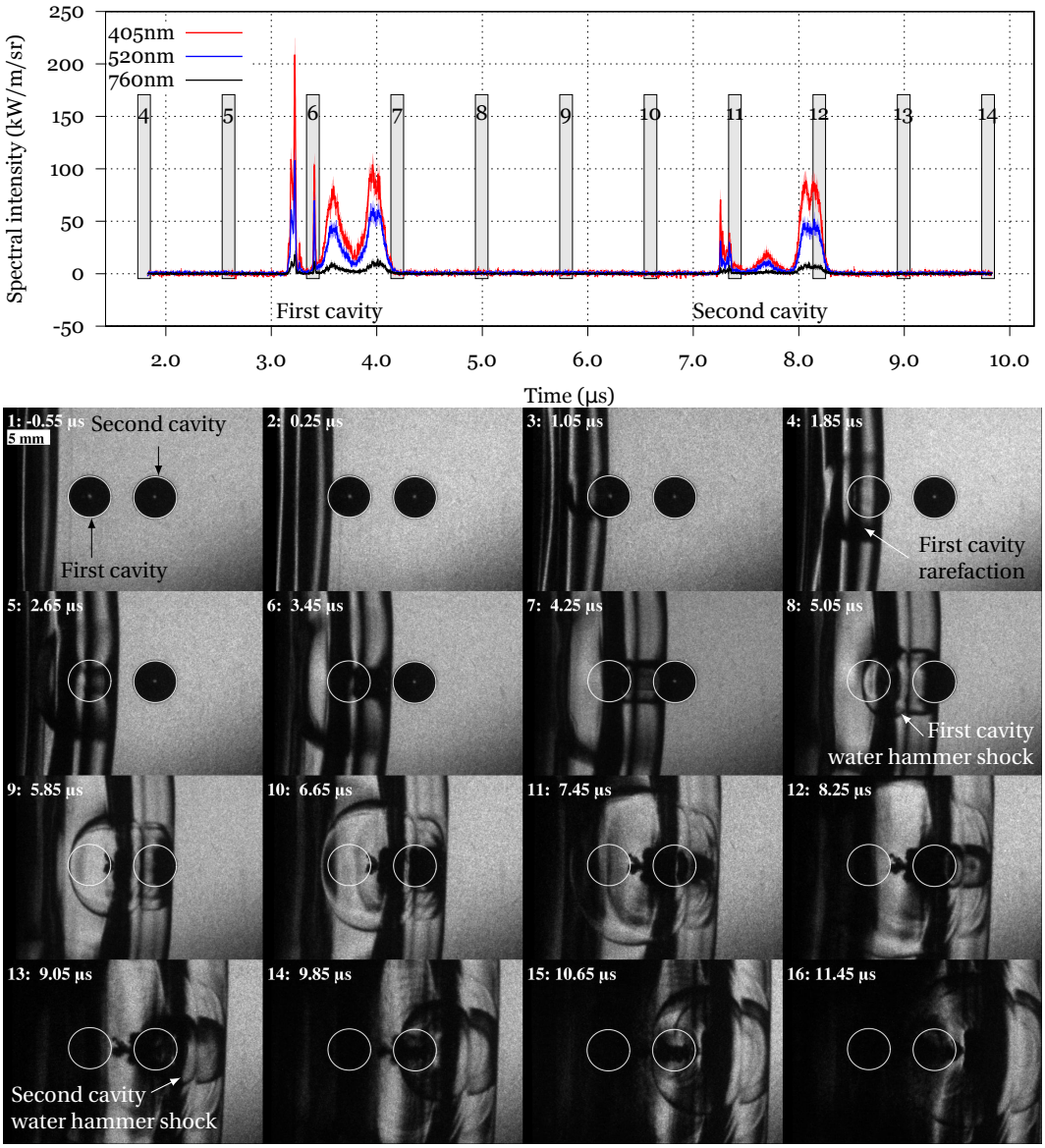

Figure 8.2: PMT traces and SimX images of a two-cavity array, $S = R_i$. Side view, incident shock pressure 610 ± 30 MPa, projectile velocity 387 ± 6 ms^{-1}. Images and plots as in figure 7.4.

8.2.1 Experimental results

Figures 8.2 and 8.3 show the collapse of a two-cavity array viewed from the side and from the rear respectively, for a separation distance of $S = R_i$. The incident shock pressure in figure 8.2 has been calculated from the incident shock velocity as 610 ± 30 MPa at the point at which the shock first contacts the first cavity. The projectile velocities for the two shots were 387 ± 6 ms^{-1} and 390 ± 8 ms^{-1} respectively. In both shots, the PMT traces can

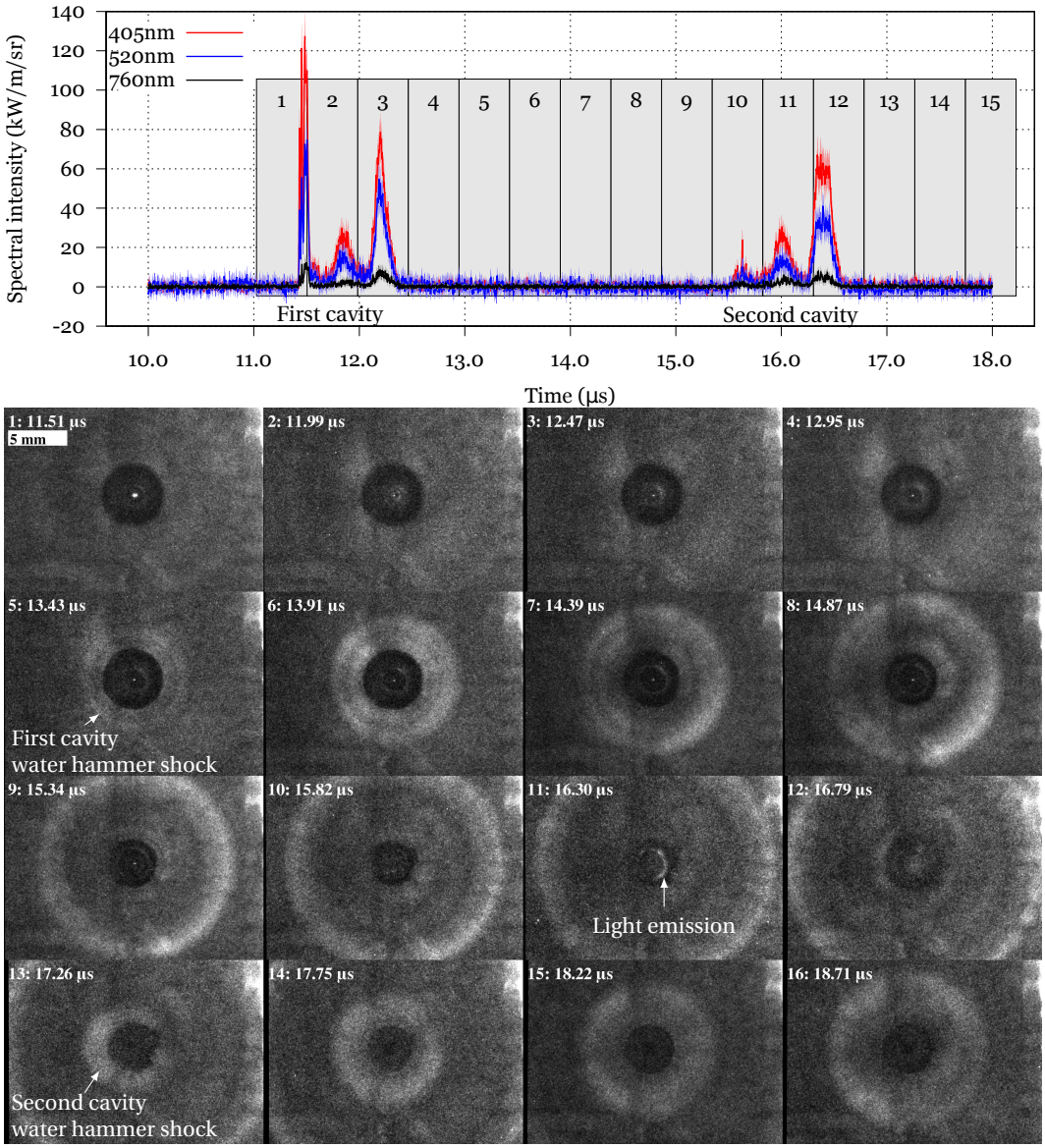

Figure 8.3: PMT traces and SimX images of a two-cavity array, $S = R_i$. Rear view, projectile velocity $390 \pm 8\ \mathrm{ms}^{-1}$. Images as plots as in figure 7.5.

be seen to be temporally divided into two distinct groups, with timings that agree well with the collapse of the two cavities. Looking at figure 8.2, the first cavity collapses in the same way as a single cavity. Cavity collapse timings are approximately the same as the single cavity results of section 7.3.1, and the corresponding PMT trace consists of three peaks, of the same magnitude as the single cavity case. The first cavity is obscured by the second in the rear view images (figure 8.3). This means that absolute PMT magnitudes

for this cavity are likely be slightly erroneous, as the light emission is captured through the second cavity. However, the water hammer shock, formed by jet strike in the cavity can be seen propagating out from the first cavity as a lighter circular region from frame 5 onwards.

As suggested in chapter 4, the collapse of the second cavity appears to follow the same fundamental process as the collapse of the first both figure 8.2 and 8.3. Although the collapse is largely obscured in the side-on images by the curved incident shock, the water hammer shock from the second cavity collapse is clearly visible in both image sets, propagating out from the cavity from frame 12 in the side on images, and frame 13 in the rear-view images. Also clearly visible in frame 11 of the rear view images is a partial torus of light emission. Approximately three quarters of the ring is visible in the image, with an approximate central radius of 1.4 mm. This frame lines up with the central peak of the second cavity PMT traces, which can be seen to be of a similar structure to the single cavity case for both shots, but with lower peak spectral intensities. In particular, the first peak of the PMT traces are reduced in intensity by approximately a factor of 3. In simulated results, it was seen that the second cavity was collapsed by a combination of the first cavity water hammer shock and the incident shock, which does not strike the cavity on-axis due to the protection afforded by the first cavity. Additionally, both the incident shock and the water hammer shock attenuate as they propagate (see for example figure 6.5), leading to reduced shock pressures on impact on the second cavity at large separation distances. It seems likely therefore that at this separation distance the addition of the water hammer shock is not sufficient to compensate for the reduction in the incident shock strength on impact, leading to a less intense collapse in the second cavity.

8.2.2 Effect of separation distance

Figures 8.4, 8.5 and 8.10 show how the PMT traces and SimX images vary with a progressive decrease in the separation distance between the cavities. Looking at figure 8.4, which shows the collapse of a two-cavity array at the larger separation distance of $S = 1.5R_i$, the dynamics of the collapse process and the structure of the light emission are similar to the $S = R_i$ case (section 8.2.1). The light emission from the second cavity begins 0.8 µs later in this case, which is consistent with the increase in the separation distance between the cavities. The light emission maintains the same structure, but is approximately 40% dimmer than the single cavity result (figure 7.4). Water hammer shocks are clearly visible from the collapse of both cavities.

Figures 8.5 and 8.6 show the collapse of a two-cavity array at the closer separation distance of $S = 0.5R_i$ from the side and rear. As can be seen, at this separation distance the structure of the light emission changes significantly. While the first cavity collapse is approximately the same as the single cavity case, the second cavity light emission now consists of two peaks, the first approximately 20 times more intense than the equivalent peak in the single cavity result. The event responsible for this peak in the PMT traces is clearly visible in both figure 8.5 and figure 8.6, but is most clearly seen in figure 8.7, which shows the light emission from the side, without any external illumination. Within the figure, the light emission is visible in frames 10 and 11 as a single very bright spot of light, approximately located on the leeward cavity wall at the point of jet strike, a result also observed in frame 12 of figure 8.5. This light emission is heavily refracted towards the camera by the curvature of the shock, greatly increasing the area of the light emission as observed by the camera and the PMTs. A different view of this event is visible in frame 9 of figure 8.6, which shows the collapse of the same arrangement, viewed from behind. The light emission can be seen to consist of a large ellipse with a major and minor radius of approximately 1.15 mm and 0.94 mm respectively. Compared to the observed

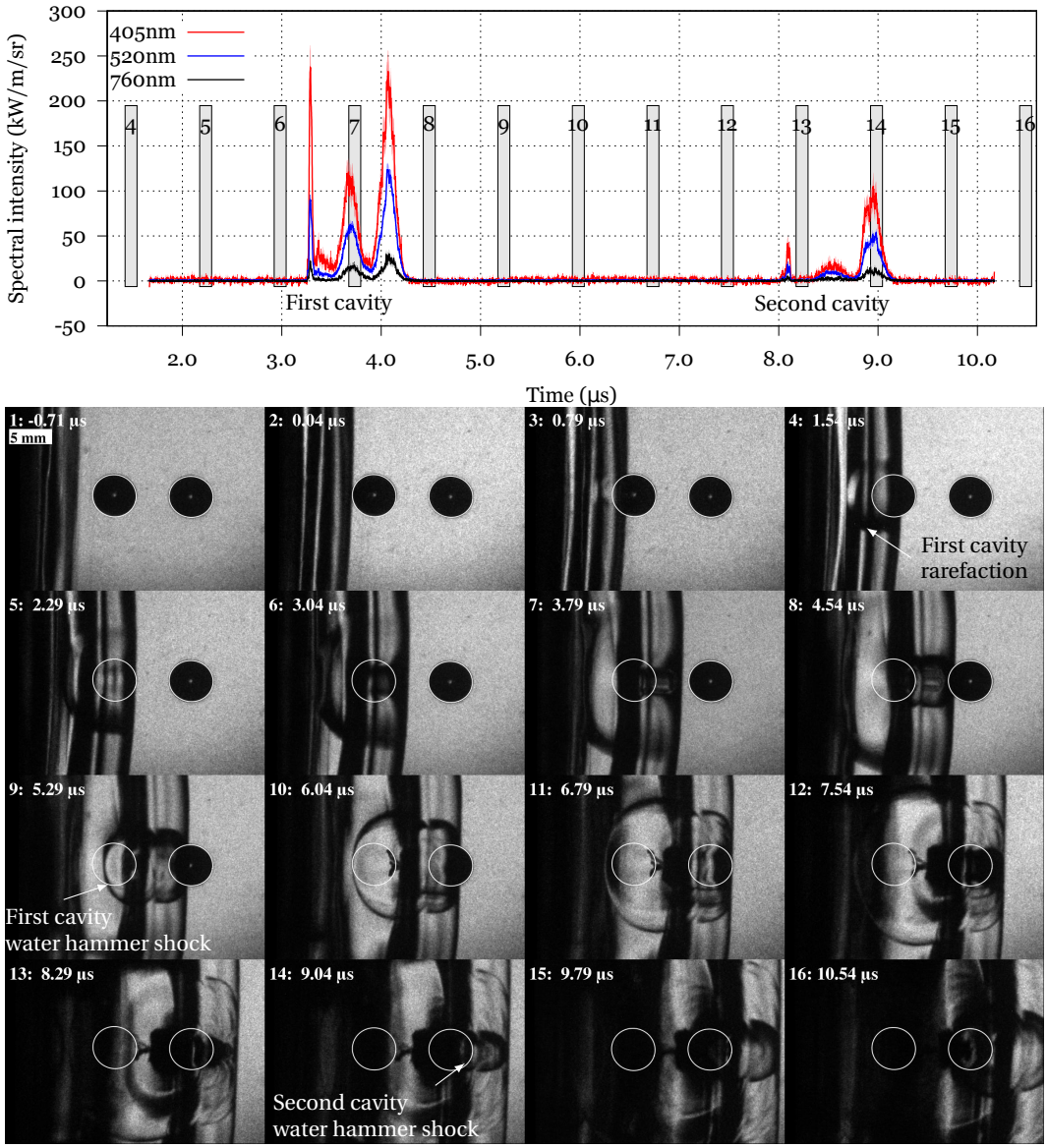

Figure 8.4: PMT traces and SimX images of a two-cavity array, $S = 1.5R_i$. Side view, incident shock pressure 590 ± 50 MPa, projectile velocity 393 ± 7 ms^{-1}. Images and plots as in figure 7.4.

single cavity light emission at jet strike, this light emitting volume is approximately three times thicker when viewed from the side, and has an area roughly 12 times larger when viewed from behind. This difference is likely to be due to the large increase in the width of the main transverse jet at the point of impact in the second cavity at close separation distances. This effect was shown for a cylindrical cavity case in figure 4.10, and also holds true for spherical cavities (see for example figure 8.8). For the simulation matched to the

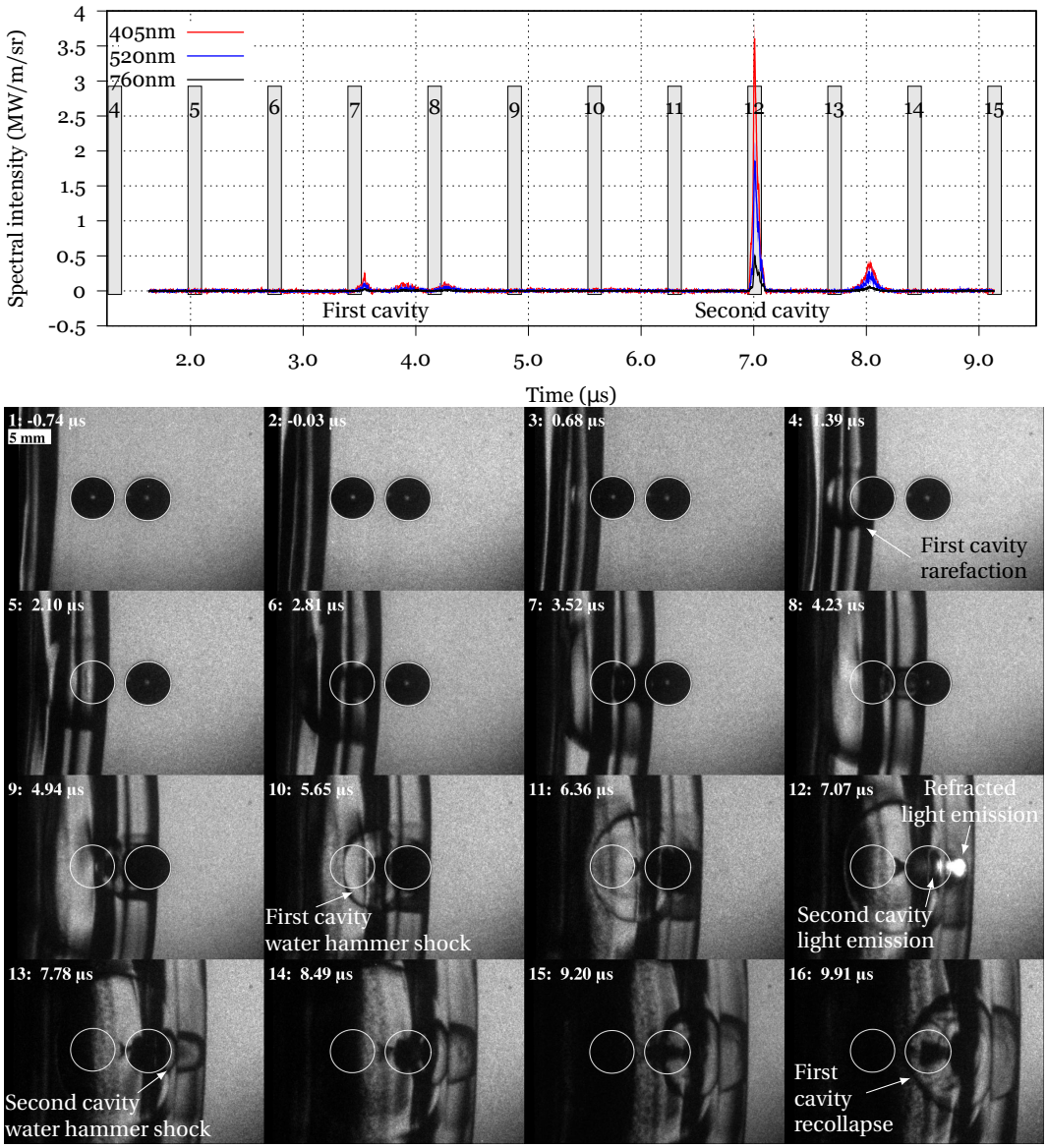

Figure 8.5: PMT traces and SimX images of a two-cavity array, $S = 0.5R_i$. Side view, incident shock pressure 470 ± 40 MPa, projectile velocity 385 ± 7 ms^{-1}. Images and plots as in figure 7.4.

experimental result of figure 8.5, the second cavity jet at the point of impact is approximately 2 times as wide as for the first cavity, leading to a four times increase in the emitting area. This increase in emitting area is likely to be a significant factor in the increase in the amplitude of the light emission seen, although, as shown in figure 8.8, the depth of the emitting region is still predicted to be comparatively thin at the point of jet strike. This therefore does not fully explain why the light emission as seen in the SimX images when

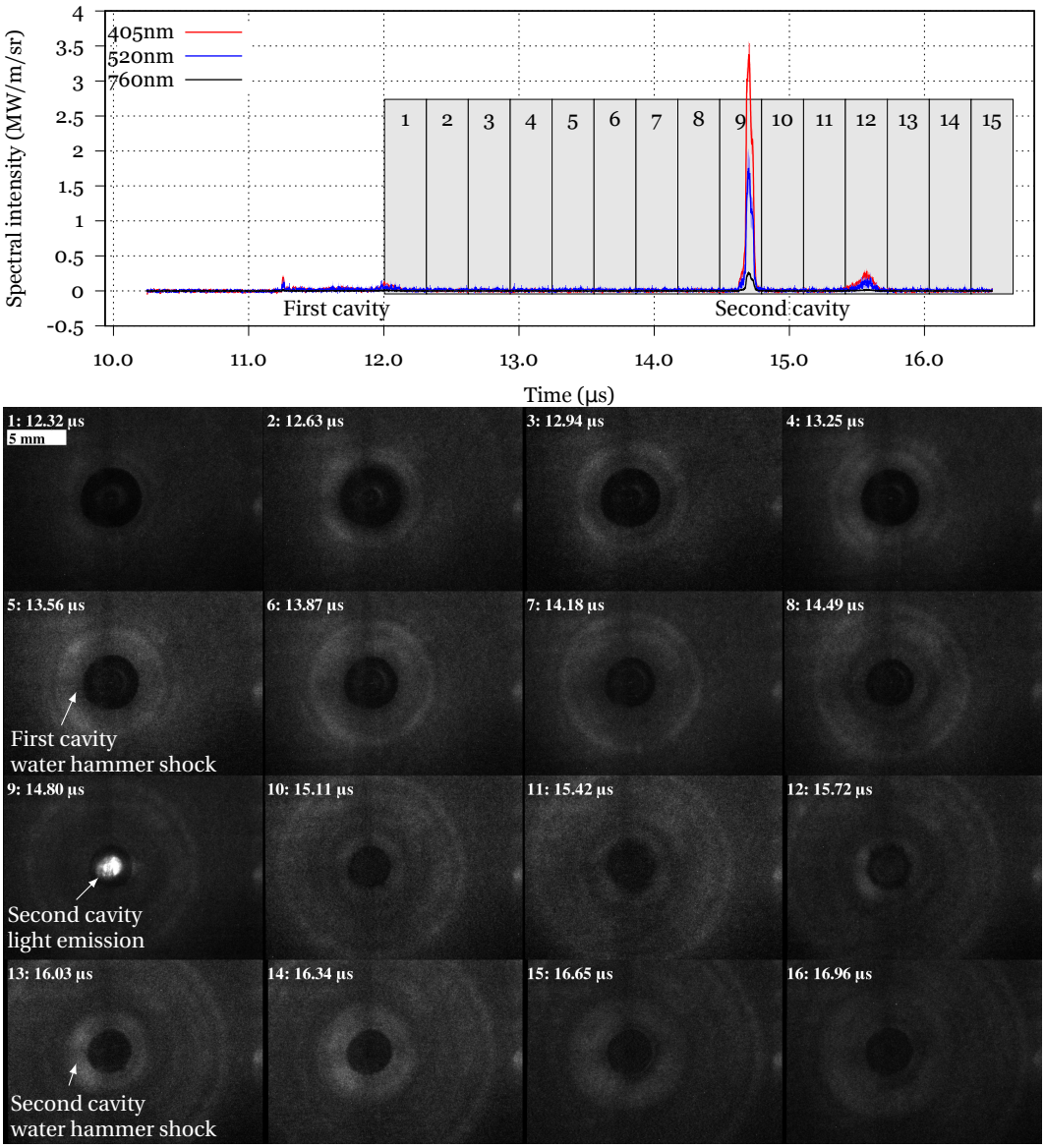

Figure 8.6: PMT traces and SimX images of a two-cavity array, $S = 0.5R_i$. Rear view, projectile velocity $391 \pm 8\,\mathrm{ms}^{-1}$. Images and plots as in figure 7.5.

viewed from the rear is so much brighter, requiring a reduction in the intensification of the camera of a factor of 4 to prevent saturation of the images.

Following the large peak in the PMT traces, an additional peak is seen approximately 1 μs later, roughly twice as intense as the single cavity case. It is possible that this peak is caused by the recollapse of the first cavity remains, which have moved approximately 3.5 mm downstream by the point of second cavity jet strike, but may also be the equivalent

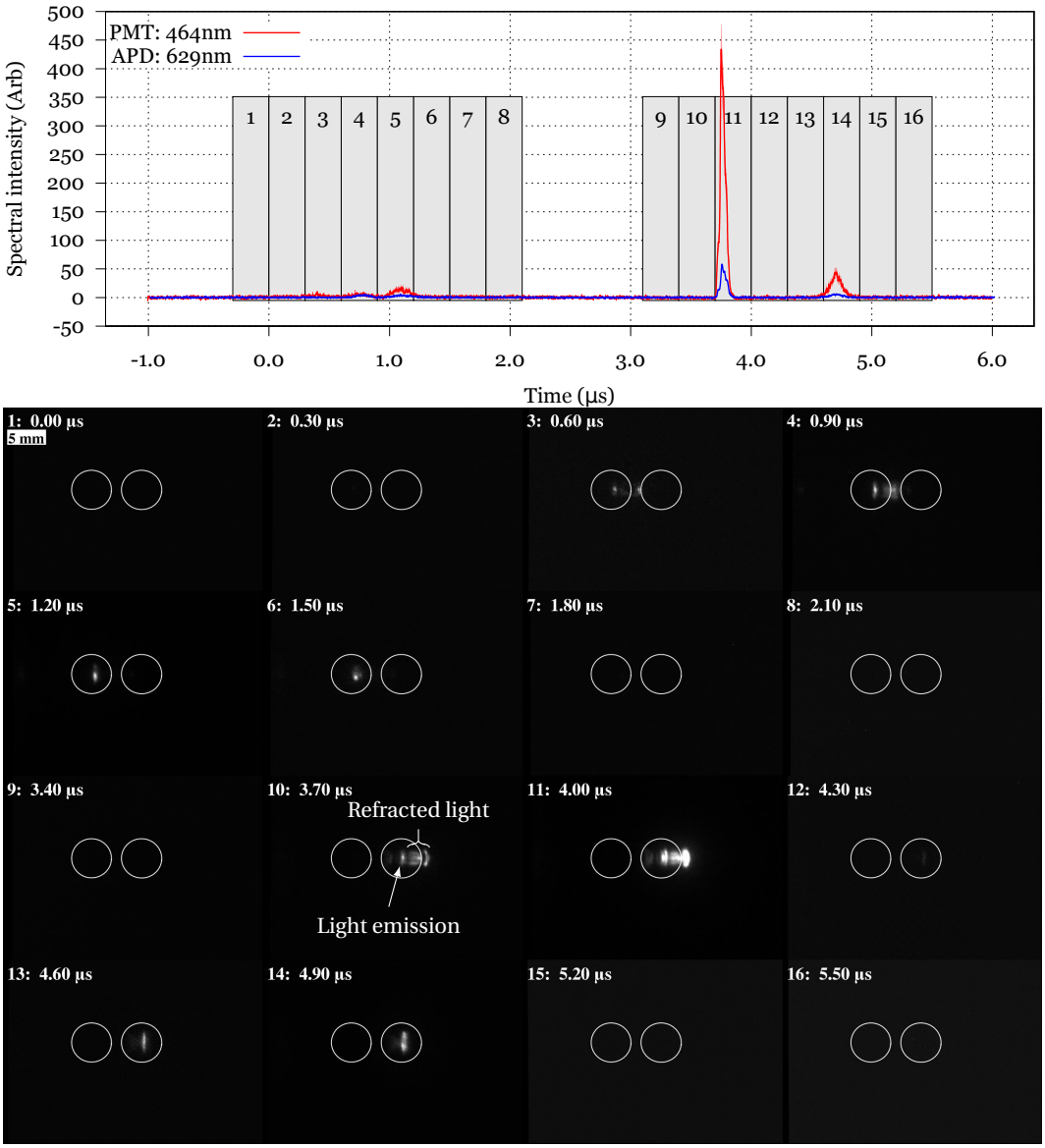

Figure 8.7: Light emission from the collapse of a two-cavity array, $S = 0.5R_i$. Side view, projectile velocity 390 ± 4 ms^{-1}. No external illumination in SimX images, plot shows the PMT and APD trace as recorded for the shot, with frame timings marked as in figure 7.4. PMT and APD traces adjusted for filter transmission, but uncalibrated.

of the third peak from the single cavity case.

As the second cavity water hammer shock propagates past the first cavity remains, the formation of additional shock waves is clearly visible (frame 16, figure 8.5). This suggests that recollapse of the first cavity remains, as discussed in section 4.3 is occurring, although these events do not correlate with significant bursts of light in the PMT traces.

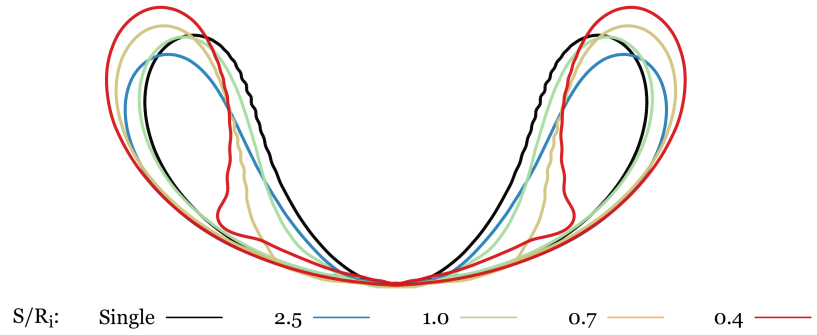

Figure 8.8: Effect of separation distance on the shape of the main transverse jet, at the point of impact in the second cavity in a two-cavity array. Lines show the outline of the second cavity for different initial separation distances, as predicted by simulations matched to experimental results.

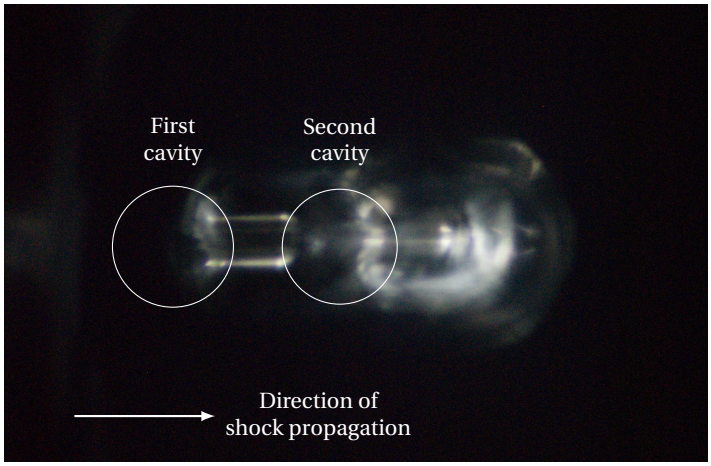

Figure 8.9: Long exposure image of the light emission from a two-cavity array, $S = 0.5R_i$. Taken with the SLR camera, side view.

An alternate view of the light emission from the collapse at $S = 0.5R_i$ is given by figure 8.9, which shows the light emission as recorded by the SLR camera. As described in section 5.5.3, with this camera a single long-exposure photograph is taken of the light emission produced by the collapse of the cavities. In the figure, the approximate size and position of the cavities prior to collapse, as taken from images of the cavities prior to the shot, has been indicated with two white circles. As can be seen the light emission is divided into two groups, as expected from the SimX images. The light emission from the second cavity group is brighter, but is also spread out over a wide area; this is likely due to the refraction of the light by the incident shock, although the movement of the cavity

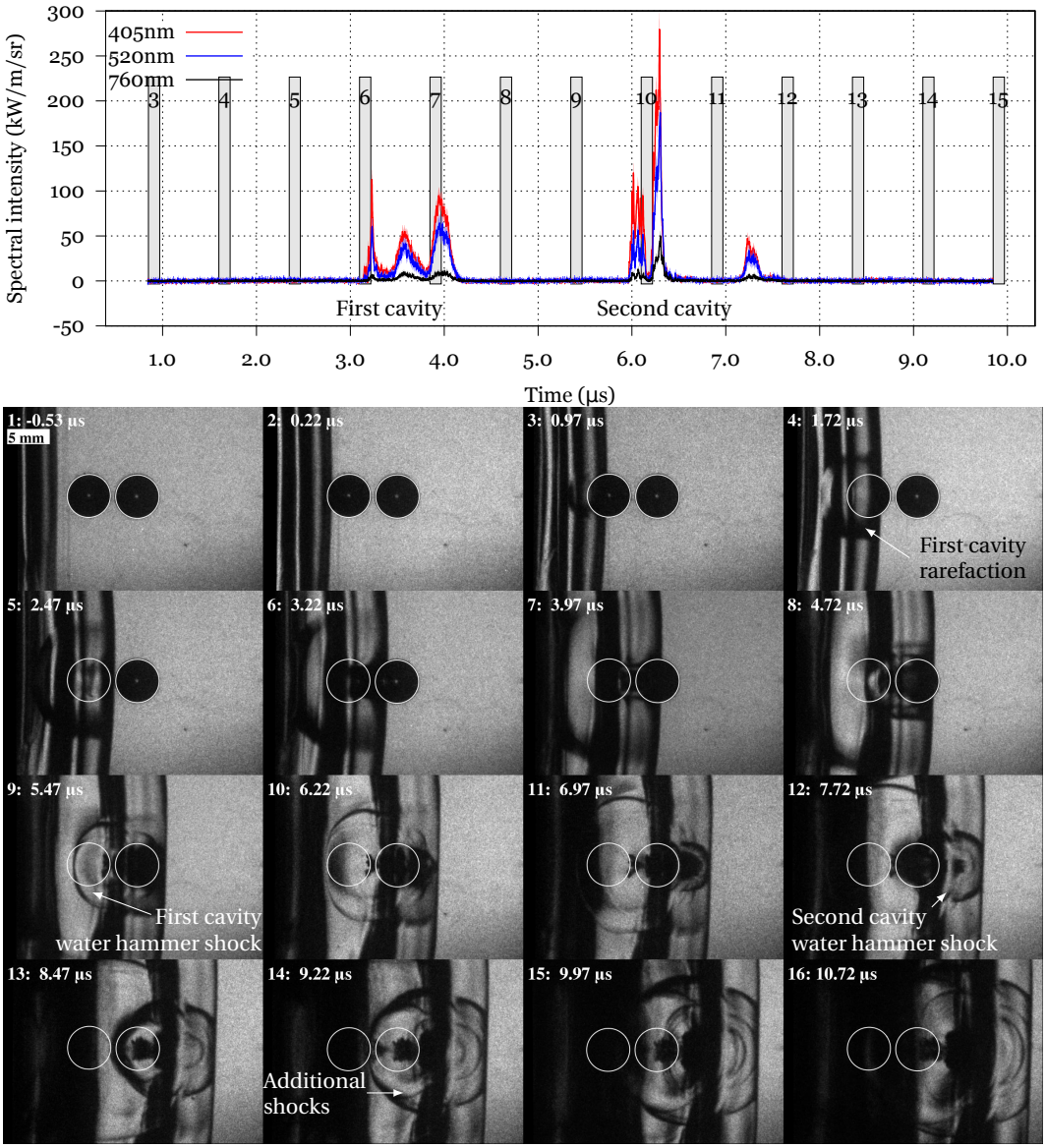

Figure 8.10: PMT traces and SimX images of a two-cavity array, $S = 0.2R_i$. Side view, incident shock pressure 680 ± 40 MPa, projectile velocity 393 ± 7 ms^{-1}. Images and plots as in figure 7.4.

after jet impact may also contribute.

Figure 8.10 shows the collapse of a two-cavity array at the closest separation distance of $S = 0.2R_i$. At this very close separation distance, there is substantial interaction between the cavities. As the second cavity collapses, the continued movement of the first cavity brings it into close contact with the second cavity. Although the view is obscured by a black band in the images at this point in time, looking at frames 10 and 11 in particular

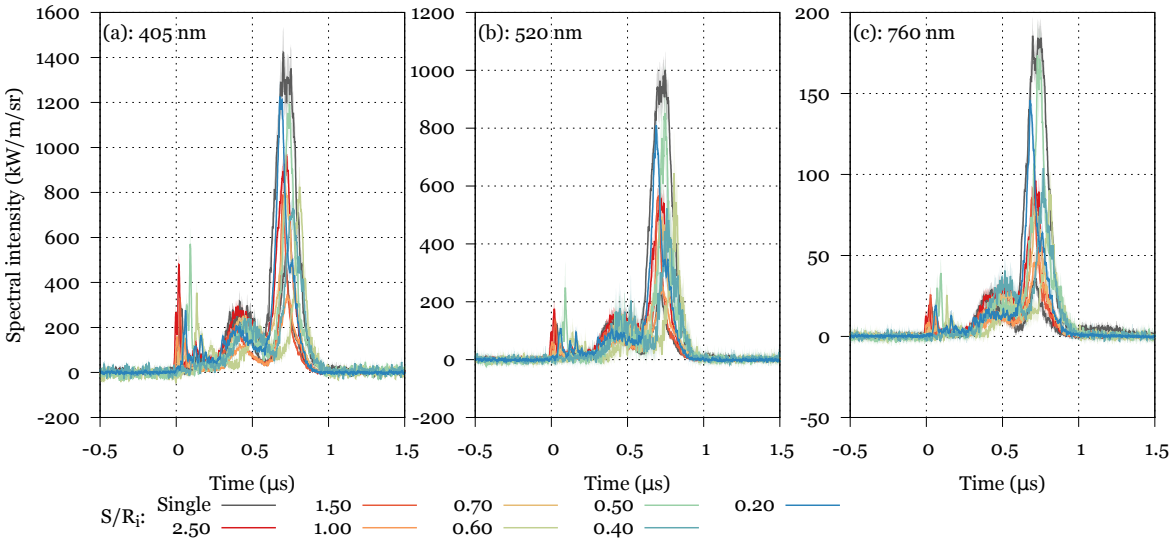

Figure 8.11: Effect of separation distance on first cavity spectral intensities in a two-cavity array. Incident shock pressure 830 ± 40 MPa.

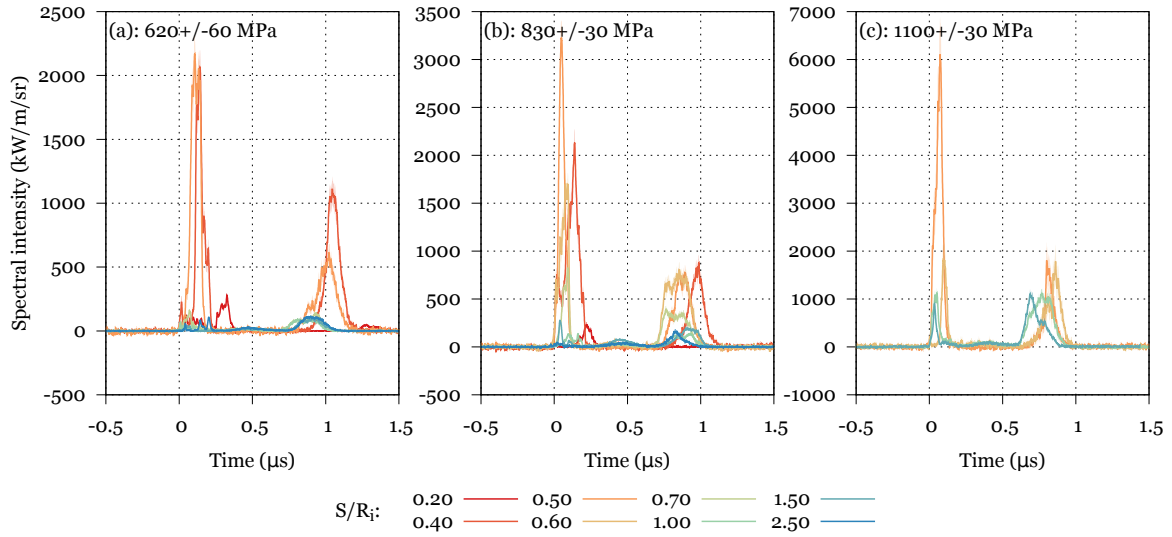

Figure 8.12: Effect of separation distance on PMT spectral intensities for the second cavity in a two-cavity array, at an incident shock pressures of 600, 800 and 1100 MPa. Wavelength 405 nm.

the two cavities can be seen to be almost touching. This affects the structure of the light emission produced, with PMT spectral intensities reduced back to single cavity levels in the second cavity. As an additional point of note, at this separation distance the band of gel between the cavities is very thin, and it is possible that the integrity of the cavity becomes compromised.

The effect of separation distance on the intensity of the light emission seen from the first and second cavity is further illustrated in figures 8.11 and 8.12 respectively. Figure 8.11 is effectively a repeat of figure 7.8 (b), with lines now coloured by the separation distance between the cavities. As can be seen, although there is some scatter in the relative amplitudes of the different peaks, at all separation distances and at all wavelengths the structure of the light emission follows the same pattern as for the single cavity case. By comparison, for the second cavity significant differences are seen at all shock pressures studied. As was shown in figure 8.5, first and third peak spectral intensities are seen to increase substantially as the separation distance is reduced. At 600 MPa, the intensity of the first peak of the light emission is found to increase by approximately a factor of 20 over the range of separation distances studied, while at 1.1 GPa this ratio is reduced to approximately a factor of 5. As exemplified by figure 8.10, this increase in peak spectral intensity is not found to continue at very small separation distances, with peak spectral intensities significantly reduced at the closest separation distance of $S = 0.2R_{\mathrm{i}}$. Comparing the structure of the light emission at the different separation distances, the timing of the light emission peaks would suggest that the phenomena leading to the formation of the different peaks is the same at all separation distances, with the timings of the first and third peaks staying reasonably consistent.

8.2.3 Comparison with simulation

Figure 8.13 compares the results of figure 8.5 to a matching simulation. As in section 7.3.3, the matching simulation was created using the methods outlined in section 5.8, using the front tracking code detailed in chapter 3. To allow comparison to the spherical cavities in the experimental results, simulations are modelled using axisymmetric coordinates. Comparing the results, shock waves and rarefactions in the bulk flow are very well matched. In particular, the recollapse of the first cavity remains by the second cavity wa-

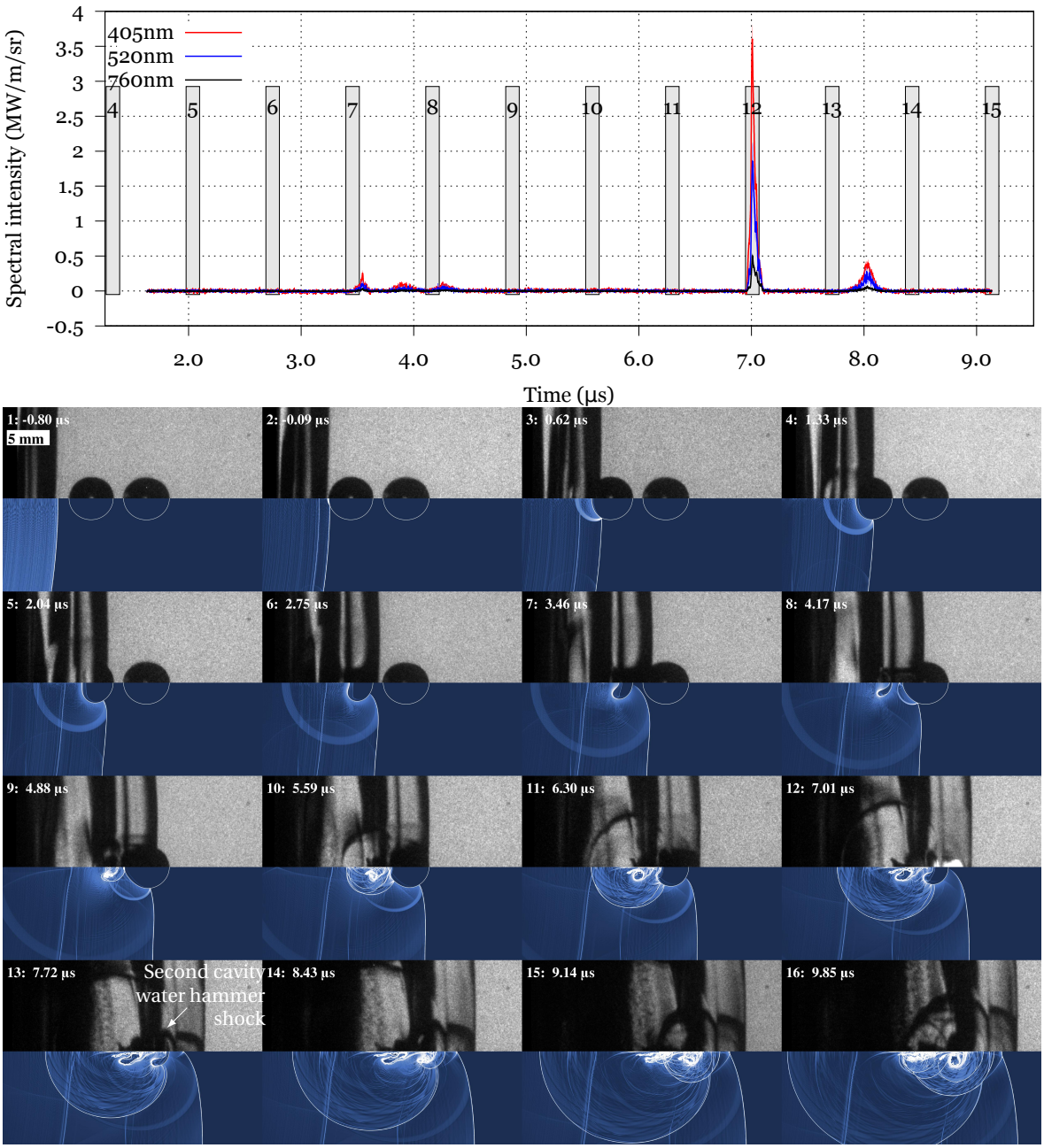

Figure 8.13: Comparison between simulated and experimental results for the two-cavity array of figure 8.5. $S = 0.5R_i$, incident shock pressure 470 ± 40 MPa, projectile velocity 385 ± 7 ms^{-1}.

ter hammer shock, for example in frame 16, is captured extremely well, with the complex superposition of multiple shock waves well replicated in the simulated results. Looking at frame 13, jet strike in the second cavity can clearly be seen to be late in the simulated result, with the experimental water hammer shock clearly visible prior to the simulated

jet strike. Comparing the simulated time of jet strike to the experimental jet strike time inferred from the time of first light emission, the first cavity is predicted to collapse 0.8 μs later in the simulation than in the experiment, a difference in collapse time of 21%. The second cavity is also predicted to collapse 0.8 μs later in the simulation. This difference can also be seen in figure 7.10, in the column marked as shot 440.

Looking at the simulated images of figure 8.13, a number of features not visible in the experimental images can be seen. As the incident shock propagates towards the second cavity, the shielding provided by the first cavity is clearly visible (frame 7). As a result, the shock does not strike the cavity on the axis of symmetry, but from the side. The collapse of the second cavity is thus driven primarily by the water hammer shock from the collapse of the first cavity, which can be seen striking the cavity from frame 9 onwards. This leads to the formation of a much wider jet in the second cavity, as was discussed in chapter 4 (frame 13). Additionally, the shielding effect of the first cavity means that the incident shock does not strike the second cavity until some time after the leading edge of the shock has passed the front of the cavity. Due to the curvature of the incident shock, neither the impact of the incident shock or water hammer shock on the second cavity are discernible from the SimX images. As a result, it is not possible to say exactly when a shock wave first strikes the second cavity, and thus cavity collapse times cannot be calculated. As an alternative metric for comparison, figure 8.14 shows the time difference between the first impact of the incident shock on the *first* cavity, and the time of jet strike in each cavity. In the case of the experimental results, this is assumed to be the time of the first peak of the light emission. As in figure 7.11, displayed pressures are the pressure on impact on the first cavity in the array, which, as explained in section 7.3.3, is not always exactly the same for an experimental result and its matched simulation. The left hand side graphs show the values as measured from the experimental results, while the right side shows the corresponding simulated results. The top figures show the results for the first cav-

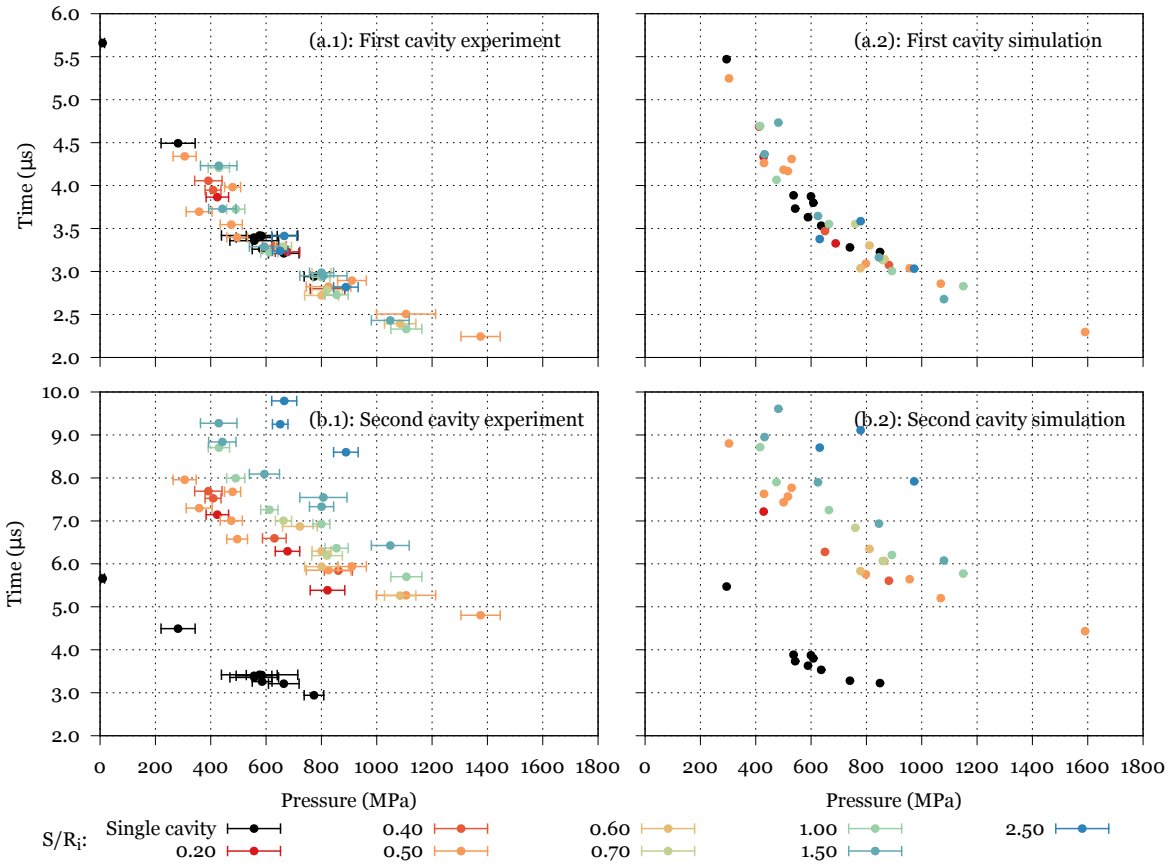

Figure 8.14: Time between initial contact of the shock on the first cavity and jet strike in each cavity, for different incident shock pressures for a two-cavity array. Single cavity results also shown for reference. Experimental results are shown on the left, simulations on the right. Experimental jet strike times inferred from the time of first light emission from each cavity.

ity, while the bottom figures show the results for the second. As can be seen, while there is some discrepancy in absolute values between the simulated and experimental result sets, the same general trends are returned. As was seen in figure 7.11, first cavity jet strike times are consistently slower in the simulated results, a result possibly attributable to the equation of state used to model the hydrogel. The accuracy of the fit of the simulations to the first cavity results improves as shock speed is increased, and first cavity jet strike times follow the same trend as the single cavity results for all separation distances studied, progressively reducing as the shock speed is increased. Mean percentage differences between simulated and experimental jet strike times are 12%, with a standard deviation of 8%.

In the second cavity, as would be expected the time to jet impact is seen to increase with separation distance, with an increase in incident shock pressure leading to a reduction in the time to jet strike for all separation distances. This result is seen for both simulated and experimental results. The accuracy of the fit of the simulations to the experimental results does not change consistently with shock pressure, with the mean percentage difference being 5% with a standard deviation of 4%.

If simulations can be matched accurately to experimental results, the much greater level of detail available can give insights into the possible shape and structure of the cavity over the course of the light-emitting period. Figure 8.15 compares a PMT spectral intensity trace to numerical schlieren images for the corresponding simulation, for a case in which the simulated and experimental cavity collapse timings are closely matched. For reference, the shot chosen can also be seen in figure 7.10, marked as shot number 497, and it is the collapse of the first cavity that is compared. As can be seen, if the first light emitting peak corresponds to jet strike, then the shock waves propagating in the torus reach the top of the cavity (approx. frame 11) shortly before the final peak (frame 15). This result is consistent with the result of section 7.3.5, where it was suggested that this event did not correlate with the third peak, but occurred just before it. The period of time between the first peak and this point thus corresponds to the time during which the shock waves and sheet jetting propagate across the torus. This result agrees well with experimental images, for example figure 7.6, in which the light emission was seen to start at the centre of the cavity and propagate outwards into an expanding torus during this period. This may therefore suggest that the final peak is in fact caused by the cooling, expanding toroidal remains of the cavity. This may suggest why the spectrum of the light emission during this time is relatively cool (see for example figure 7.14).

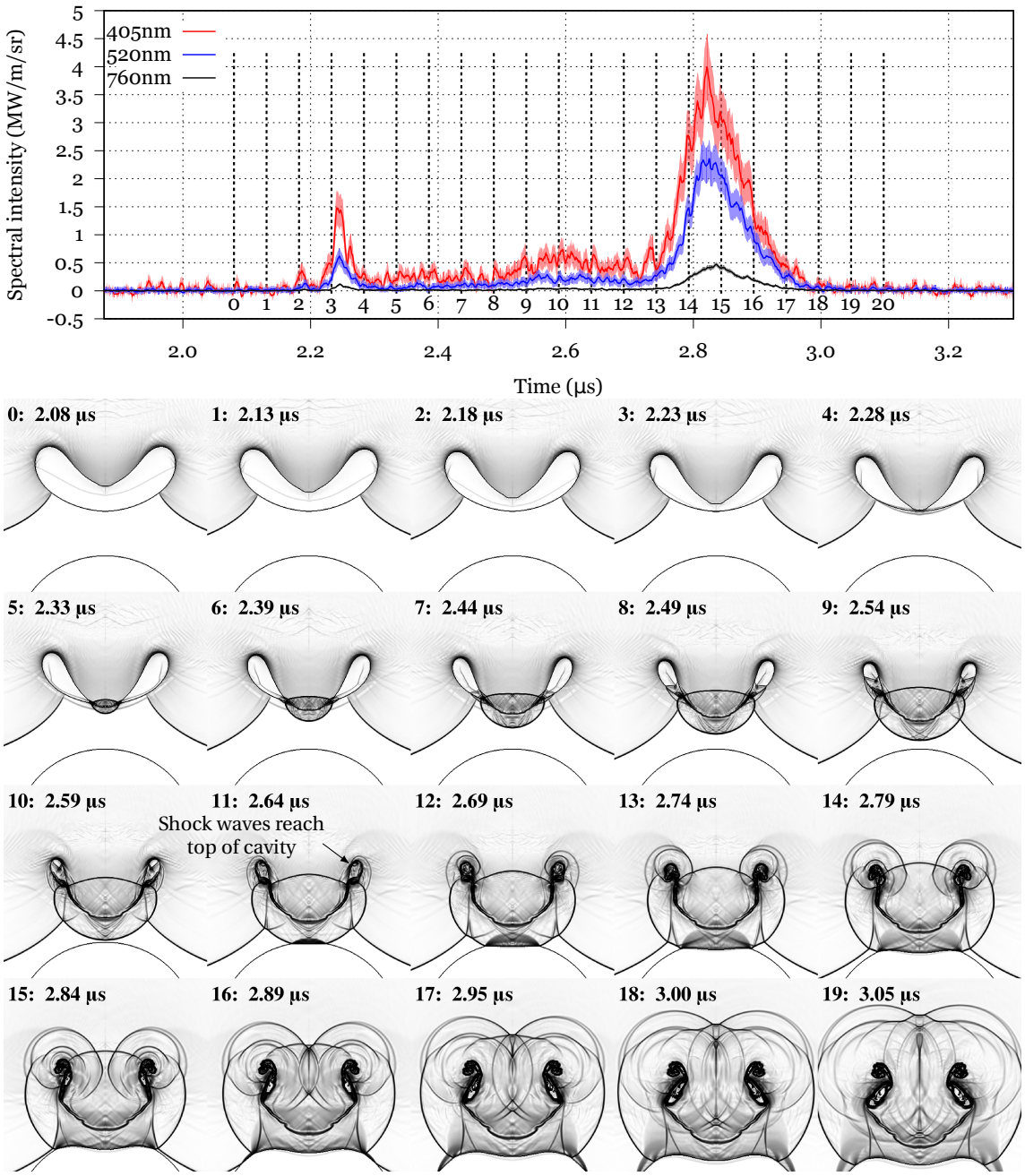

Figure 8.15: Comparison between the PMT traces and the matching simulation over the period of light emission from the collapse of the first cavity of a two-cavity array at an incident shock pressure of 1.38 ± 0.07 GPa. Experimental result from shot 497 in figure 7.10. Vertical lines on the PMT trace shown the timings of the simulation images.

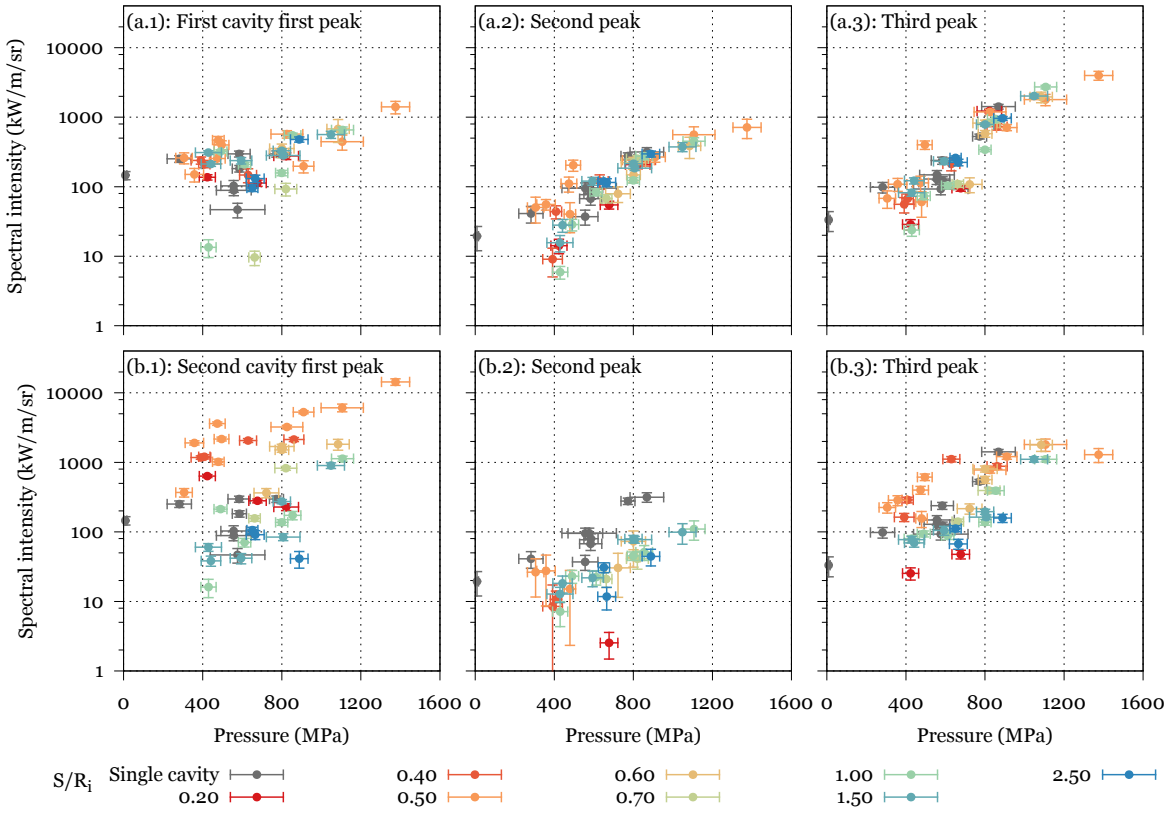

Figure 8.16: Effect of incident shock pressure on measured peak PMT spectral intensities for a two-cavity array. Single cavity results also shown for reference. Wavelength 405 nm.

8.2.4 Effect of shock strength

The effect of incident shock pressure on PMT spectral intensities at 405 nm for the three different peaks observed is shown in figure 8.16. Within the figure, the top row shows the peak spectral intensities for the first cavity in the arrangement, while the bottom row shows the peak spectral intensities for the second cavity. The three columns show how the peak spectral intensity varies for each of the different peaks. As was shown in section 7.3.4 and again in section 8.2.2, PMT spectral intensities from the collapse of the first cavity in the arrangement follow the same trends as was seen for the single cavity case. This result appears to hold equally true for all three peaks, and for all arrangements. Above approximately 600 MPa the light emission is dominated by the third peak, with peak spectral intensities significantly increasing with increased shock pressure above this value. Below

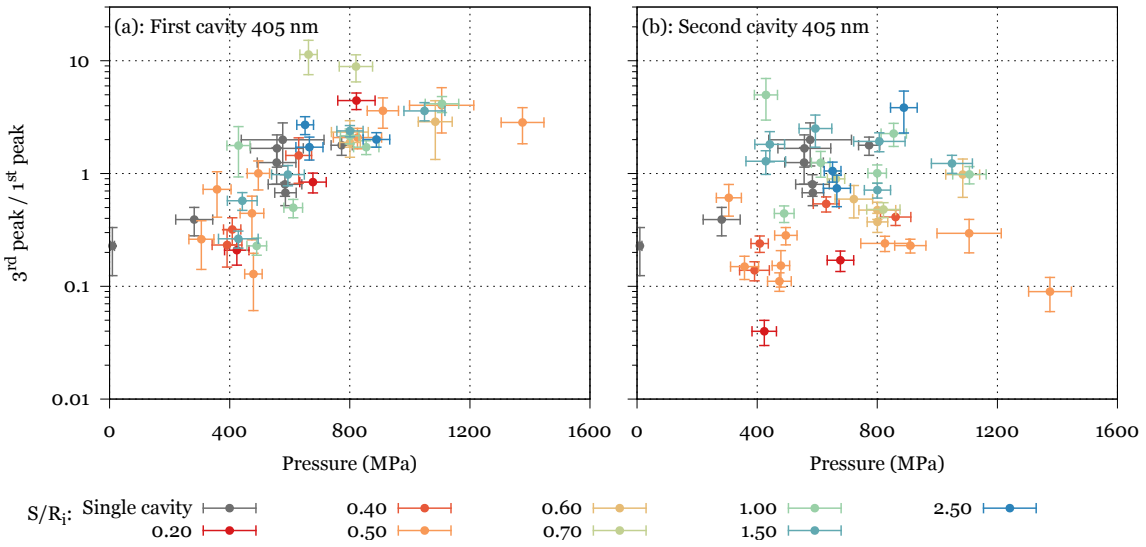

Figure 8.17: Ratio between the third and first peak PMT spectral intensities, for the first and second cavity in a two-cavity array at different separation distances. Single cavity results also shown for reference. Wavelength 405 nm.

600 MPa, the first peak is the major source of light emission from the collapse, and peak spectral intensities do not change substantially with shock pressure.

By contrast, substantial differences in the peak spectral intensity of the light emission from the second cavity are observed for different separation distances. As was seen in section 8.2.2, a narrow band of extremely high spectral intensities are observed for separation distances of approximately $0.4 \leq S/R_i \leq 0.6$, with order of magnitude increases seen. These separation distances correspond to the arrangements where the second cavity PMT traces consist of only two peaks, as in figure 8.5. The amplification seen with these arrangements over the equivalent single cavity case appears to reduce at higher shock pressures. It is plausible that this is because temperatures in the single cavity case increase at a faster rate with increased incident shock pressure. For $S/R_i > 0.6$, peak spectral intensities can be seen to consistently drop below the level seen for the single cavity result, as was seen in figures 8.2 and 8.4. As discussed in section 8.2.1, this is likely due to the shielding of the second cavity by the first from the incident shock, in addition to the reduction in incident shock and water hammer shock pressures as these shocks propa-

gate to these larger distances.

The effect of the incident shock pressure on the relative magnitude of the peaks can be seen more clearly in figure 8.17, which shows the ratio between the third and first peak spectral intensities for different separation distances at different incident shock pressures. For the first cavity, as was previously shown in section 7.3.4 the third peak progressively becomes the highest intensity source of light emission as the pressure is increased for all separation distances. For the second cavity, the first peak is seen to be the highest intensity source of light emission for all separation distances below approximately $S = R_{\mathrm{i}}$. For arrangements above this value, the third peak is consistently more intense than the first. This is primarily due to a reduction in the spectral intensity of the first peak, relative to the single cavity case (see figure 8.16 (b.1)). This may suggest that the compression of gas underneath the tip of the jet is less intense at these separation distances. The emitting area may also be smaller in these cases, although this is not predicted numerically (see for example figure 8.8).

As in section 8.2.3, matched simulations can offer insights into the cause of the variation in detected light emission with increased incident shock pressure. One useful metric for comparison is the average state of the gas during jet strike. As used by Tully *et al.*,[195,221] this metric is found to be more robust than the peak overall conditions during collapse (as adopted in chapter 4) as a metric for comparing results. Figure 8.18 illustrates how the metric works. At the point of jet strike (labelled as 'initial jet strike' in the figure), the main transverse jet does not immediately contact the leeward cavity wall, but rather compresses a thin section of gas between itself and the wall to high temperatures and densities. Contact of the main transverse jet on the wall occurs a short time later, at a position off the central axis of the cavity (marked as 'off axis jet strike'). The jet strike conditions are calculated as the time averaged value between these two times; this value for this example is marked with a red dotted line in figure 8.18.

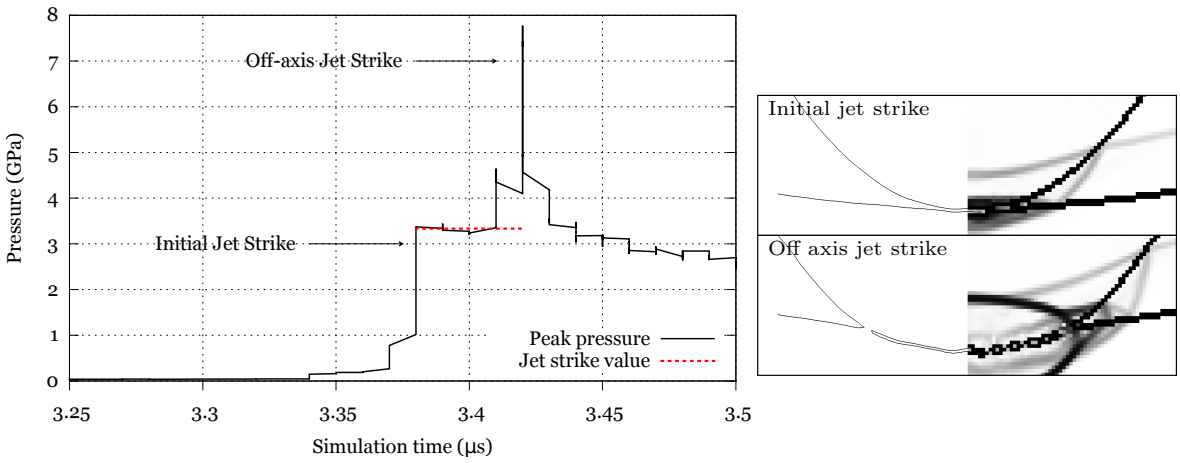

Figure 8.18: Method used to calculate jet strike conditions in simulated cavity collapse. The jet strike condition is found as the average value between the time of initial jet strike, and the time of off-axis jet strike.

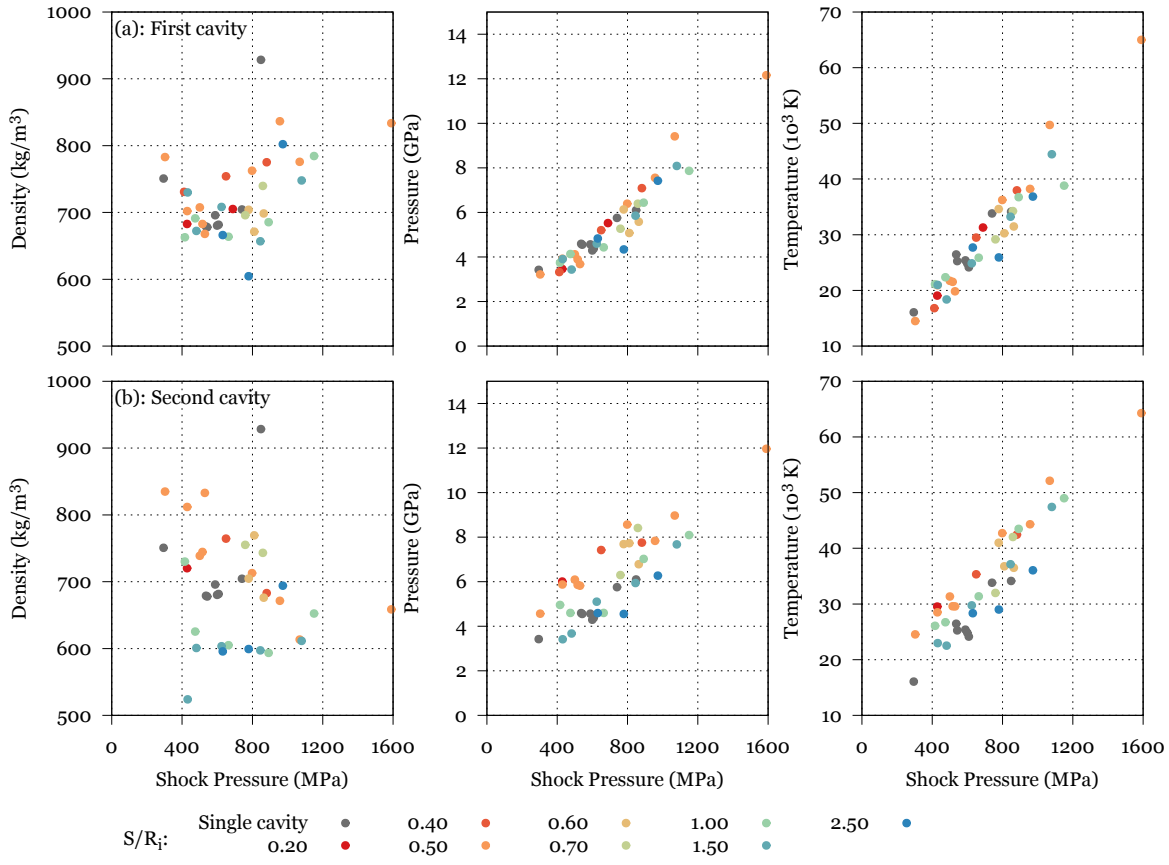

Figure 8.19: Effect of incident shock pressure on simulated jet strike conditions in the gas, for the first and second cavity in a two-cavity array. Single cavity results also shown for reference. Values calculated using the method described in figure 8.18. Air modelled as an ideal gas.

The variation in jet strike conditions in the gas with incident shock pressure from the simulated collapse of a two-cavity array are shown in figure 8.19. In the figure, the top row shows the calculated conditions in the first cavity, while the second row shows the conditions in the second cavity. The columns show the calculated jet strike densities, pressures and temperatures in each case. As the air in the cavities was modelled as an ideal gas, although trends will be modelled with reasonable accuracy, absolute values are likely to be overestimates, due to the omission of important loss mechanisms such as the ionisation of the gas (see section 3.3.1). Looking at the results, it can be seen that while jet-strike density trends are unclear, jet strike pressures and temperatures are predicted to strictly increase with incident shock pressure in both cavities. Echoing the trend seen in the experimental peak spectral intensity results, first cavity jet strike pressures and temperatures are predicted to follow the same trend as for the single cavity case at all separation distances, shown in grey in the plot. In the case of the second cavity, some delineation is seen between different separation distances. Separation distances of $S/R_\mathrm{i} < 0.7$ are predicted to reach slightly higher pressures on jet strike than the single cavity case, with pressures approximately 30% higher at 800 MPa. The delineation is also seen in both density and temperature results, although the difference is smaller (approx. 10%) in the case of the temperatures. It is likely that this intensification of jet strike conditions at shorter separation distances is principally caused by the increase in jet speed. As discussed in section 4.3.2 for the the cylindrical cavity case, the collapse of the second cavity is driven principally by the first cavity water hammer shock; as this wave attenuates as it spreads, the pressure on impact is highest at the shortest separation distances.

While the delineation observed in figure 8.19 replicates to some extent the variation in jet strike conditions seen in the experimental results (compare to figure 8.16 (a.1) and (b.1)), the spread in the second cavity data is not much larger than that seen for the first cavity in the arrangement, and is not sufficient to explain the large differences in spec-

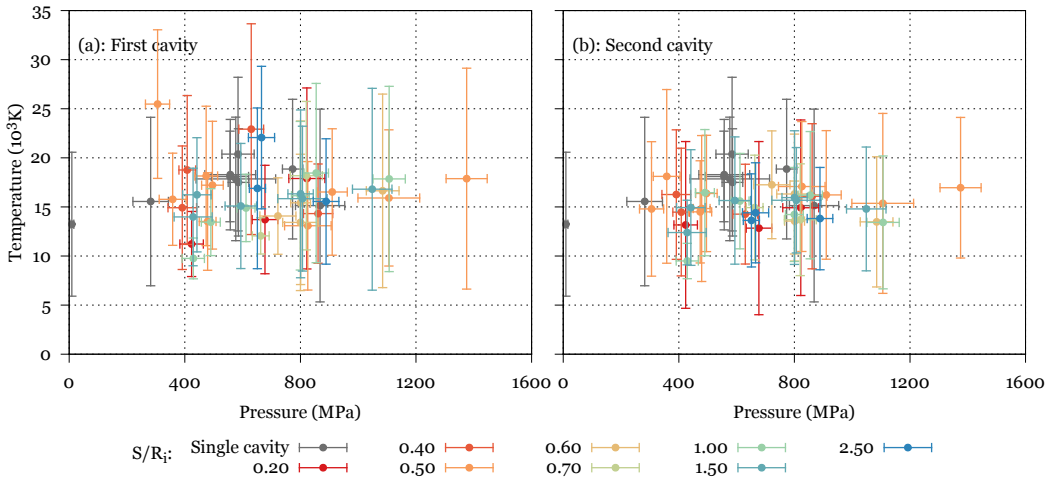

Figure 8.20: Variation in mean temperature of collapse with incident shock pressure for the first and second cavity in a two-cavity array, inferred from PMT traces using a fit to a black-body curve. Single cavity results also shown for reference. Error bars show the standard deviation in the fitted temperature over the collapse of the respective cavity for each shot.

tral intensities seen in the experimental results for different separation distances. However, it is possible that with the increase in jet area seen at short separation distances the combination of these two factors is enough to account for the difference in PMT spectral intensities seen in the experimental results.

8.2.5 Temperatures

The variation in mean temperature of collapse with incident shock pressure for both the first and second cavity is shown in figure 8.20. For each data point, the mean is calculated as the mean temperature over the periods in which light emission was detected from the particular cavity. The respective error bars show the standard deviation in the fitted temperature over the collapse of the cavity. Values are obtained by the fitting of black-body curves to the PMT spectral intensity data, as described in section 7.3.5. As shown, mean collapse temperatures as inferred using this method are not found to increase with incident shock pressure, and no difference is seen across different separation distances. Mean temperatures for the collapse of the first cavity are $16,000 \pm 3,000$ K, while those for the

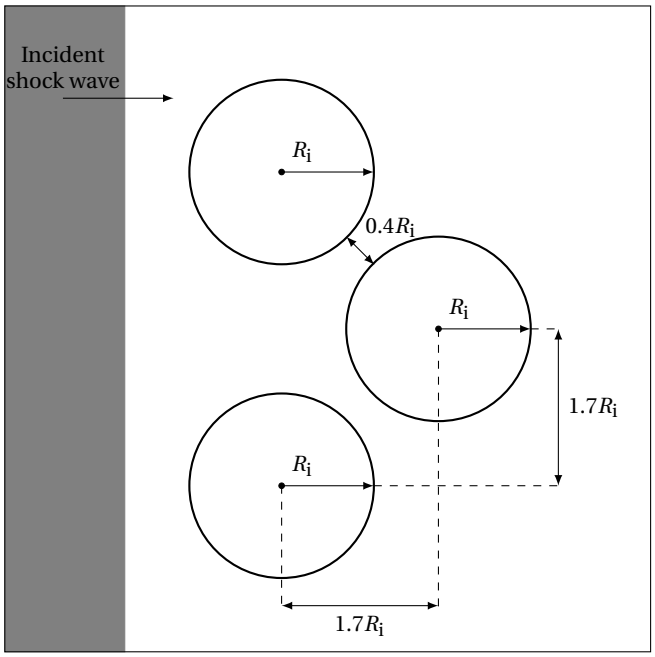

Figure 8.21: Diagram of the three-cavity arrangement. Three cavities of initial radius $R_i = 2.5\,\text{mm}$ are placed in a triangular arrangement, with two cavities placed ahead of a third relative to the incident shock.

second are $15,000 \pm 2,000$ K. The difference in these values is inconsequential compared to the standard deviation for a particular shot. Whilst it is possible that this is a physical result, a more likely explanation is that the limit at which the method as employed can discern different temperatures has been reached; for this result to be true, the surface area of the emitting region would have to vary in size by two orders of magnitude over the shots presented, to compensate for variations in emitting spectral intensity. It is thus difficult to make any further conclusions based on these results beyond that the mean temperature of the collapse is likely to be consistently at or above approximately 16,000 K.

8.3 THREE CAVITIES

Building on the two cavity results of section 8.2, figure 8.21 shows a diagram of a more complex arrangement. Three cavities are placed in a triangular array, with two cavities placed ahead of the third relative to the incident shock. As in previous results shown,

the initial cavity radius in all cases is 2.5 mm. Due to the three dimensional nature of this arrangement, it is not possible to model with spherical cavities with the front tracking software used in this study. Only experimental results are therefore presented in this section.

8.3.1 Analysis of the three-cavity array

Figures 8.22 and 8.23 show the collapse of the array of figure 8.21 from the side and rear. The incident shock pressure for figure 8.22 was calculated as 640 ± 40 MPa at the point of impact on the first cavities. Looking at frames 3 to 5 of figure 8.22, on impact of the incident shock on the first row of cavities, rarefaction waves can be seen to form over both cavities, which expand and overlap on the axis of symmetry. This process is also just visible in frames 1 to 4 of the rear view images of figure 8.23, as a set of progressively overlapping white circular regions centered on the front two cavities. Following this initial impact, the first two cavities collapse and emit light, just visible in frame 5 of figure 8.23 as two toroidal rings of light emission. By frame 6, the light emission is only visible at the outer edge of one of the cavities, perhaps suggesting that in this particular example the outer portion of the cavities collapsed more slowly than the inner.

The collapse of the first two cavities also leads to the formation of two water hammer shocks, visible from frame 8 onwards in figure 8.22 and frame 7 onwards in figure 8.23. As these shock waves expand, they overlap on the axis of symmetry at the position of the second cavity. This overlap is clearly visible from frame 9 in figures 8.22 and 8.23. These overlapping shock waves simultaneously collapse the third cavity. This can be seen in frame 10 and 11 of figure 8.23 to lead to the formation of a line of light emission from the third cavity, perpendicular to the plane of the array. This may suggest that the cavity is collapsing in a very different way to the single or two cavity cases, with the overlapping water hammer shocks driving a three-dimensional jet that is long in one dimension and

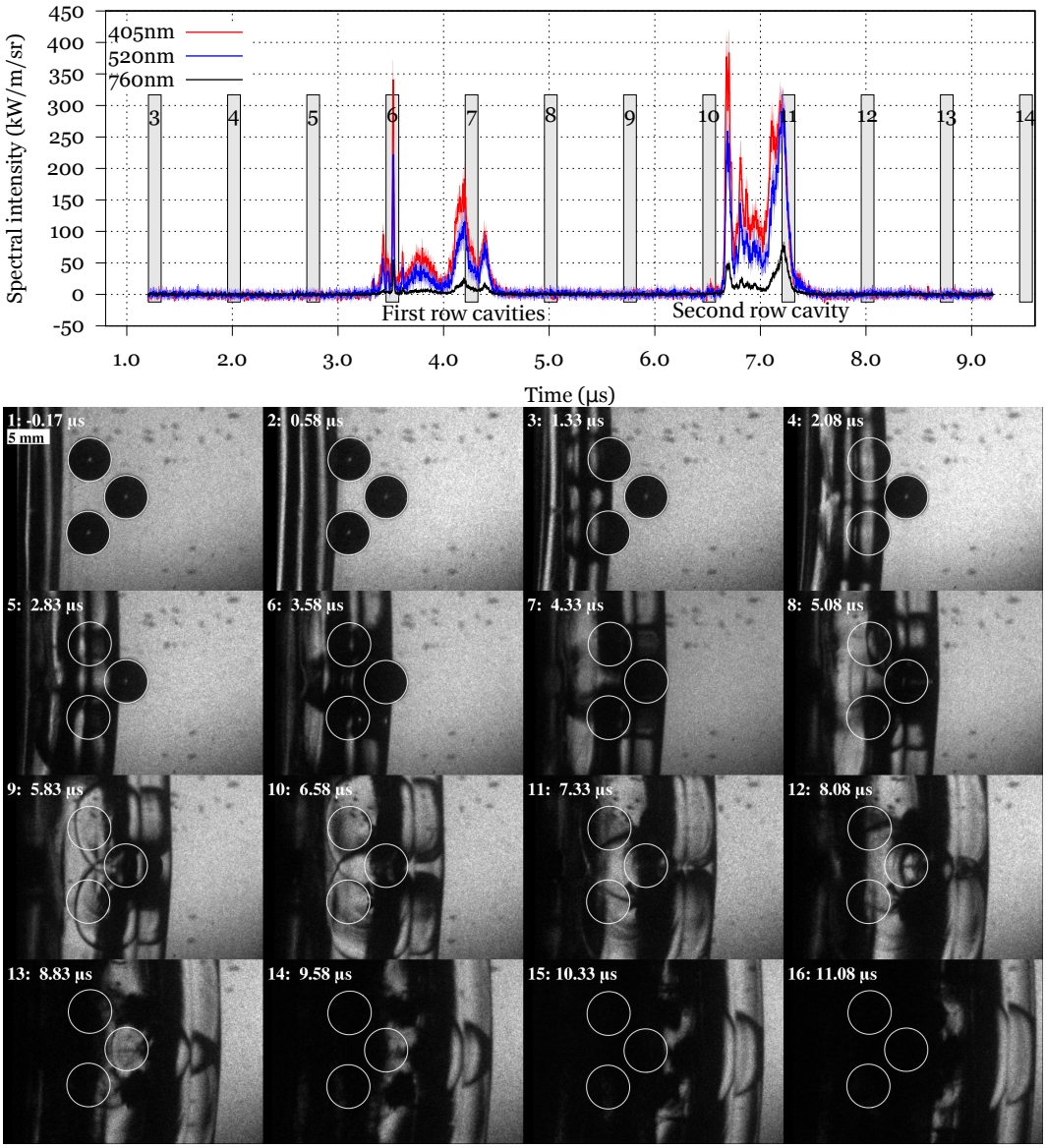

Figure 8.22: PMT traces and SimX images of the collapse of the three-cavity array of figure 8.21. Side view, incident shock pressure 640 ± 40 MPa, projectile velocity 390 ms^{-1}. Images and plots as in figure 7.4.

thin in the other. The light emission in frame 11 completely saturates the SimX image, making any conclusions about the source of the emission difficult. The corresponding PMT trace is complex, and consists of multiple small peaks. This may suggest that this frame contains the combined light emission from several individual light emitting events. Of additional note, the spectral intensity of the final peak of light emission from the collapse of the second row cavity is seen to be of comparative magnitude at 520 nm and

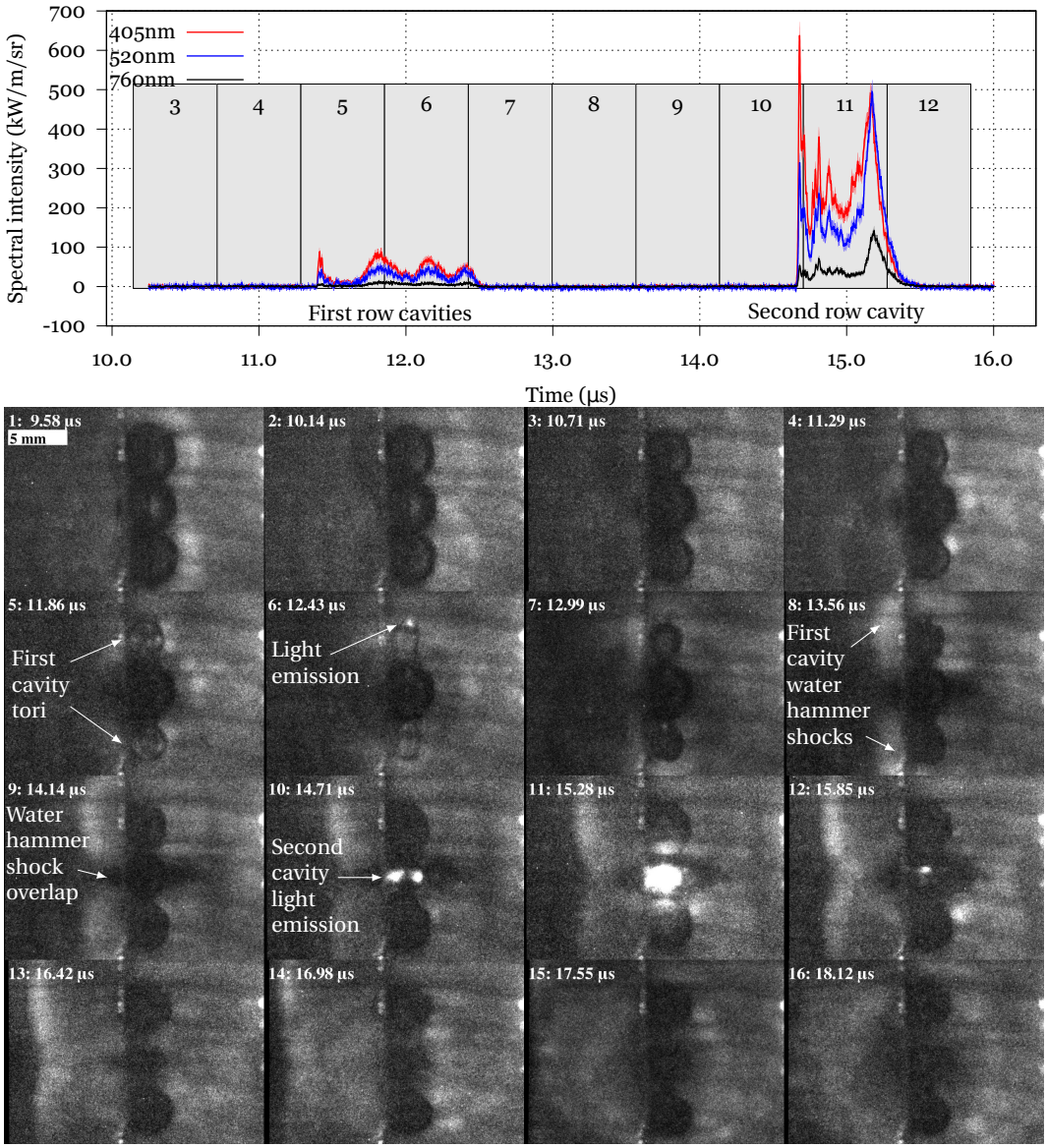

Figure 8.23: PMT traces and SimX images of the collapse of the three-cavity array of figure 8.21. Rear view, projectile velocity $390 \pm 7\ \mathrm{ms}^{-1}$. Images and plots as in figure 7.5.

405 nm in both the side and rear view results. This may suggest that the temperatures reached at this point in the collapse process are reduced relative to at other points. The best fitting black-body curves at this stage of the collapse correspond to a temperature of approximately 9,000 K.

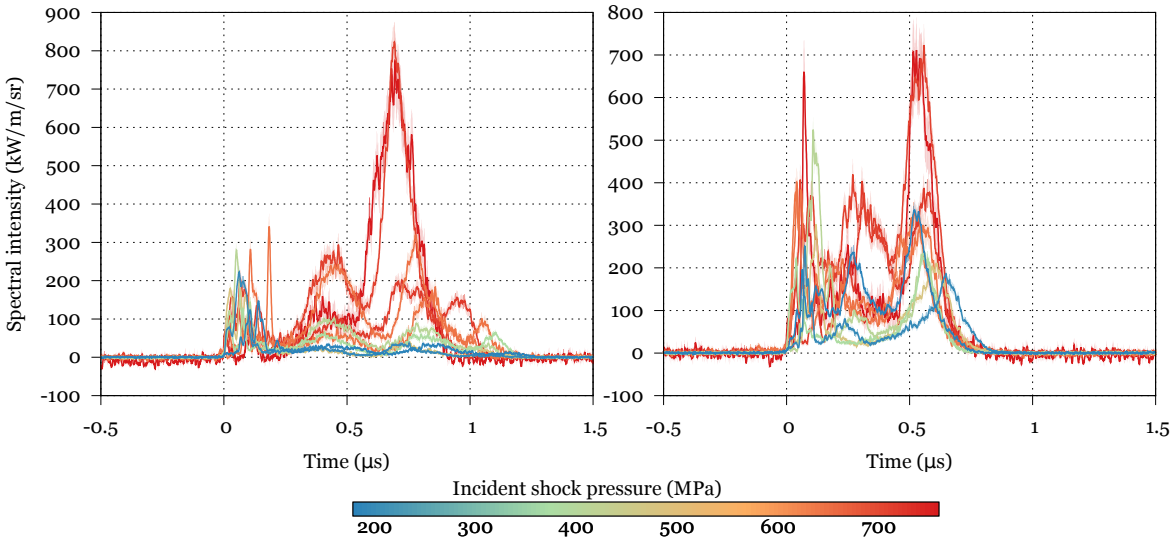

Figure 8.24: Effect of incident shock pressure on the structure of light emission from the collapse of a three-cavity array. Wavelength 405 nm. (a) Light emission from the first row of cavities, (b) the second row cavity.

8.3.2 Effect of shock strength

The effect of incident shock pressure on the structure and amplitude of the light emission is shown in figure 8.24, which shows the PMT traces as recorded for all three-cavity shots, coloured by the pressure of the incident shock for each case. The traces have been aligned based on the time of first light emission, to aid comparison between traces. As can be seen, the light emission from this arrangement is less repeatable than that seen for a single or two-cavity array. For the light emission from the first cavities, as two cavities are collapsing simultaneously the PMT traces for many shots consist of more than three peaks, where the cavities have not collapsed at exactly the same time. This complicates analysis of the light emission, as it is not possible to tell which peak corresponds to which cavity. As pressure is increased PMT spectral intensities consistently increase, with the highest intensity peak shifting from the first to the final peak as was seen for the single cavity case.

For the second row cavity, the light emission is again less repeatable than seen for

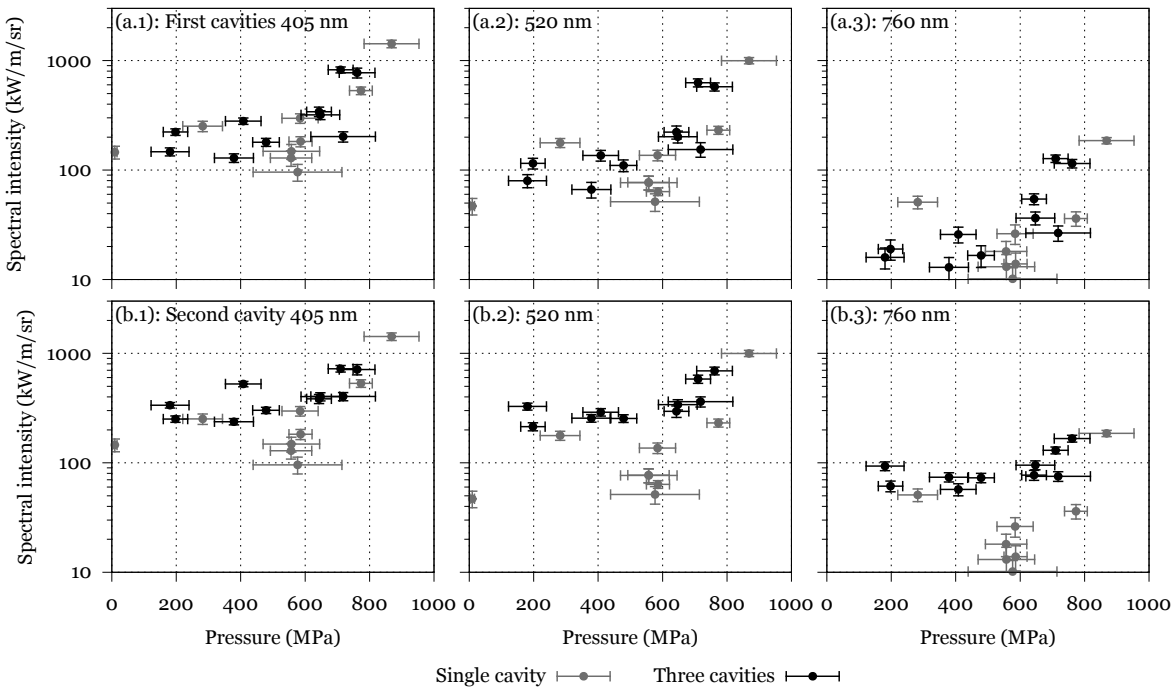

Figure 8.25: Variation in recorded peak PMT spectral intensity with incident shock pressure for a three-cavity array.

single and two cavity arrangements. As pressure is increased, the length of the light pulse does not change substantially (the standard deviation is approximately 6%) and no clear trend is seen in the ratio of the individual peaks, although the peak intensities do increase. Based on equivalent cylindrical-cavity simulations, the collapse of this cavity is highly complex and three dimensional, possibly involving a combination of multiple jets; small changes in the timings of the collapse of the first two cavities can in this case thus lead to quite different collapse dynamics in this cavity. This may be the cause of the variability seen in the detected light emission.

The effect of incident shock pressure on the peak overall PMT spectral intensity is shown in figure 8.25. Much as in the single cavity case, significant increases in peak spectral intensity with shock pressure are not observed below approximately 700 MPa, for either row of cavities. Beyond this point, there is some suggestion that peak spectral intensities begin to increase, but there are insufficient data points to fully assess the trend.

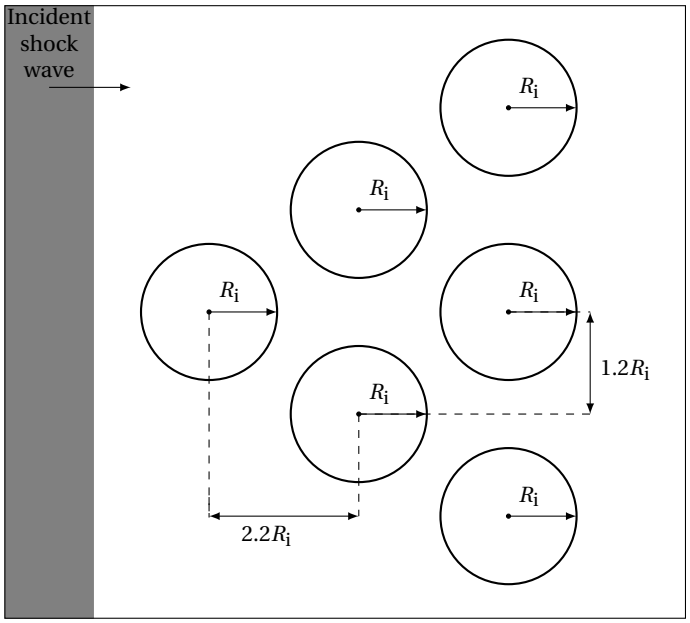

Figure 8.26: Diagram of the six-cavity arrangement.

Compared to the single cavity results, peak spectral intensities from the collapse of the first row of cavities appear to follow approximately the same trend. Light emission from the cavity in the second row appears more consistent below 700 MPa, with peak spectral intensities consistently exceeding the first cavities result and the single cavity result. This is primarily due to the higher final peak spectral intensities seen for this cavity at these pressures; this may suggest that the remains of the cavity after the initial jet strike are large but cool, given the spectra of the light emission at this time as discussed in section 8.3.1. As pressure is increased beyond 700 MPa, peak spectral intensities do not increase at the same rate as the single cavity case, and the values reached become comparative.

8.4 Six cavities

As a final multiple cavity arrangement, figure 8.27 shows the collapse of a triangular array of six cavities, a diagram of which is given in figure 8.26. The initial radius for all cavities was 2.5 mm. Although in this shot spherical cavities were used instead of cylinders,

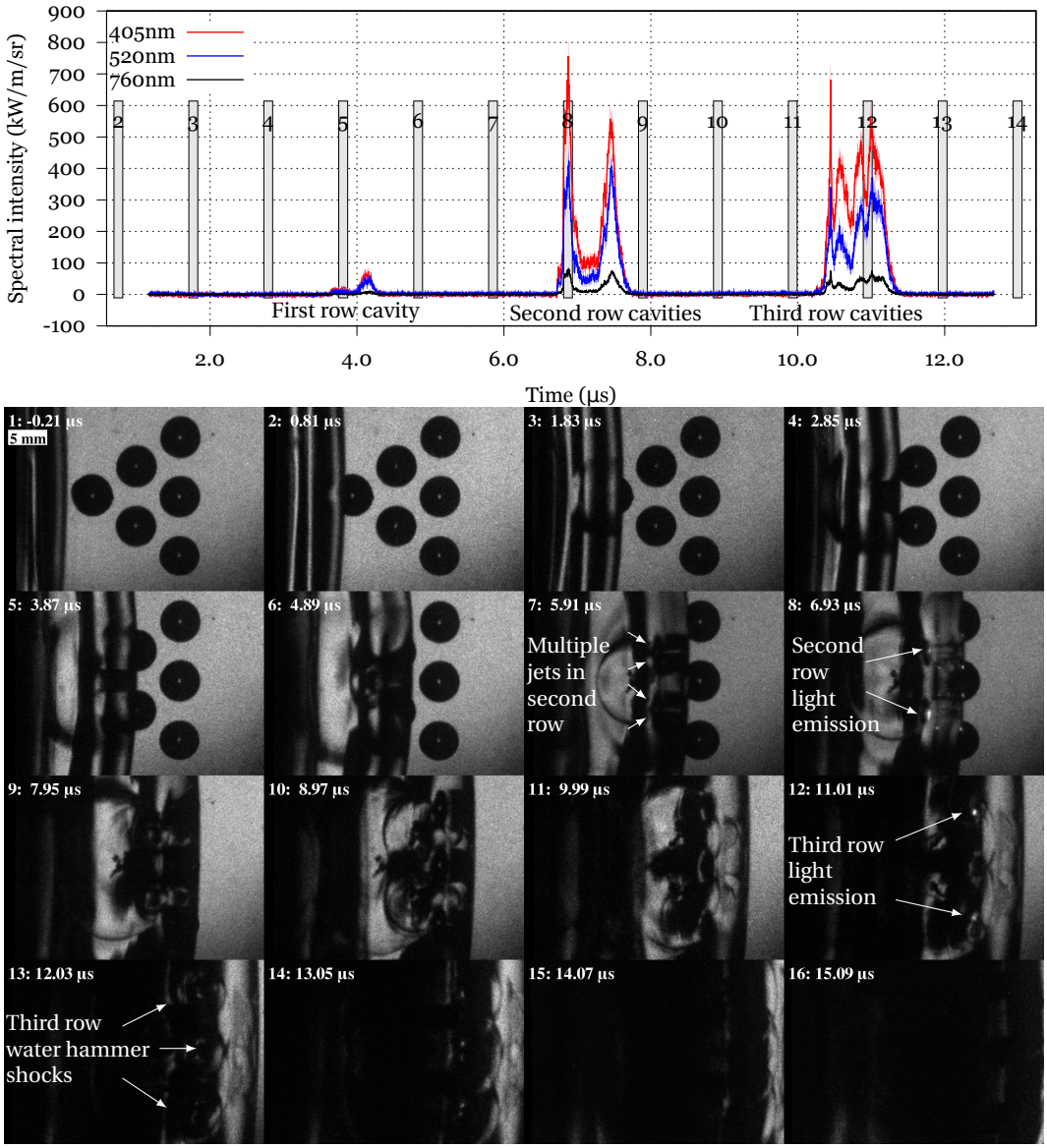

Figure 8.27: PMT traces and SimX images of the collapse of the six-cavity array of figure 8.26. Side view, incident shock pressure 590 ± 50 MPa, projectile velocity 394 ± 17 ms^{-1}. Images and plots as in figure 7.4.

notable comparisons can be made between this result and figure 4.3, which compares a front-tracking simulation to the six cavity results of Dear and Field.[4] In that result, the lead cavity was found to partially protect the second level of cavities, causing them to collapse with jets pointing in toward the centre of the array. Once the first cavity collapsed, the water hammer shock formed struck the second row of cavities from the inside, creating a second set of jets in the two cavities. Although much of the collapse is obscured by

the curvature of the incident shock and the black rarefaction band, some indication of a similar process occurring can be seen in frame 7, where the second row of cavities have adopted an almost triangular shape, suggesting that they may be collapsing with a jet from both the outside and inside. The shape and structure of the inside jets is consistent with the structure of the first cavity water hammer shock, which is visible in the frame. Light emission is clearly visible in frame 8 of the SimX images at the base of the two cavities, with the timings of the frame corresponding to the largest light emission peak seen in the collapse. The light emission can also be seen reflecting off the other cavities in the frame.

Following jet strike in the second row of cavities, water hammer shocks propagate from the cavities from frame 9 onwards. Although the images are almost completely opaque by frame 13, light emission from the collapse of the outer cavities in the third row is visible in frame 12, while water hammer shocks from the collapse of the third row can just be seen from frame 13.

Looking at the PMT traces of figure 8.27, the traces are temporally divided into three distinct groups, corresponding to the three rows of the array. The peak spectral intensity of the light emission from the collapse of the first cavity is approximately 40% reduced relative to the single cavity case of figure 7.4, with only two peaks present. When the incident shock strikes the second row of cavities, rarefaction waves are formed, which propagate outwards and strike the first cavity. It may be that in this arrangement at this shock pressure these rarefactions strike the first cavity prior to first cavity jet strike, quenching the collapse process and reducing the intensity of the light emission produced. Peak spectral intensities from the collapse of the second and third row of cavities exceed the peak single cavity result by approximately a factor of 4. At least some of this amplification is likely to be caused by the superposition of the light from multiple cavities.

8.5 DISCUSSION

Comparing across all multiple cavity arrangements studied, the results suggest that it is possible to intensify shock-driven cavity collapse using multiple cavities. This intensification is restricted to particular cases, and is highly dependent on the exact geometry of the arrangement. For the two cavity case, evidence of the intensification of the collapse process was seen for separation distances of $0.4 \leq S/R_{\mathrm{i}} \leq 0.6$, although the large increase in peak emitted spectral intensities observed at these separation distances is likely to be mainly due to an increase in the width of the main transverse jet. This intensification was found to hold across all incident shock pressures studied, but with the amplification in peak spectral intensities reduced at higher shock pressures. In the case of larger separation distances, the evidence suggests that the intensity of the collapse process is in fact reduced relative to the single cavity case, a result that was also seen for the three cavity array. An insufficient number of shots were conducted using the six cavity array to make an assessment of the levels of amplification achieved, although in the case of the single shot presented peak PMT spectral intensities were approximately twice those seen in the equivalent single cavity case.



CHAPTER 9

CONCLUSIONS

A numerical and experimental study has been conducted into the collapse of gas cavities in a higher density medium by incident shock waves. A front tracking method was employed to study the collapse of multiple cavity arrays numerically, revealing that intensification of the process can be achieved through the harnessing of inter-cavity effects in particular circumstances. Experimentally, a light-gas gun was utilised to create strong shock waves in hydrogel blocks, into which cavities were cast. With this setup, single and multiple cavity arrangements were studied, revealing that the cavities collapse to emit light, which increases in intensity as the incident shock pressure is increased. The dynamics of the collapse, and the subsequent light emission, change significantly when multiple cavity arrangements are employed.

9.1 EXECUTIVE SUMMARY

Building on the work of Hawker *et al.*[1], this study sought to answer two intertwined questions. The first of these was whether multiple cavity arrangements could be utilised to further intensify the conditions achieved in the collapse of a single cavity by an incident shock wave. The answering of this question initially involved the utilisation of the same numerical tools as used by Hawker *et al.*[1], but also formed a major part of the second branch of this study, namely the experimental study of shock driven cavity collapse. The primary goal of the experimental study was the assessment as to whether the conditions

predicted numerically were born out in reality.

The initial numerical study of multi-cavity collapse in this work (chapter 4) was conducted using the high resolution front tracking approach outlined in chapter 3. Cavities were modelled in 2D and axisymmetric geometries, with the gaseous contests of the cavities modelled as air using an ideal gas equation of state (EOS). The fluid in which the cavities were placed was modelled as water using a stiffened polytropic EOS. This work was tested for grid independence, and initially validated against the experimental results of Dear *et al.*[4]. Numerous arrangements were studied, all at an initial driving pressure of 1 GPa with an initial cavity radius of 0.5 mm. In the study of the collapse of two cylindrical cavities, one placed behind the other, it was shown that the fundamental dynamics of the collapse are the same for both cavities. The first cavity was seen to collapse in the same way as a single cavity, while the collapse of the second was heavily affected by the separation distance between the cavities. As the collapse of the second cavity was primarily driven by the shocks produced by the collapse of the first, the intensity of the collapse was seen to increase as the separation distance was reduced. Comparing axisymmetric and 2D simulations of the problem, it was revealed that whilst the collapse of both cavities is approximately 20 % faster in the axisymmetric case, due to the increased level of focussing, the general features of the collapse are qualitatively very similar.

Following on from the study of two cavities of equal size, the effect of the relative size of the cavities was explored. With the reduction of the size of the second cavity relative to the first, it was found that higher pressures were produced in the collapse of the second cavity. When the ratio in cavity sizes was reversed, entrainment of the first cavity into the jet of the second was observed under particular conditions.

In the final section of chapter 4 a more complex arrangement was studied, consisting of three cylindrical cavities in a triangular array, the middle cavity being much smaller than the outer cavities. It was demonstrated that through this arrangement very high lev-

els of energy focussing could be achieved, as the small central cavity was initially protected from the incident shock wave, before being struck almost simultaneously by a number of much stronger shock waves, leading to rapid and violent collapse. By this method an increase in pressure amplification of over five times relative to the single cavity case was demonstrated, an amplification of almost forty fold compared to the input pressure.

The experimental aspect of this project, described in detail in chapter 5, utilised a single stage light-gas gun to produce high pressure shock waves in hydrogel blocks. This work built upon previous experimental studies of the problem conducted at Cambridge University,[4,5] with a number of improvements. Spherical, rather than cylindrical cavities were placed on the centre-line of hydrogel blocks, significantly reducing boundaries effects on the process. The approximate radius of the cavities used was 2.5 mm. In addition to high-speed optical imagery, quantitative measurements of the light emission produced were conducted using an array of calibrated photomultiplier tubes (PMTs), sensitive to different wavelengths. Analysis of the shock waves produced using this arrangement (chapter 6), showed that this setup was capable of producing shock waves in the gel block at pressures of between 200 and 1300 MPa. The pressures behind the shock front were shown to be sustained for long periods of time, with the pressures at a point in the gel measured at approximately 80% of the peak value 4 μs after the shock front had passed.

Using this experimental arrangement, the collapse of both single and multiple cavity arrangements was studied in detail (chapters 7 and 8 respectively). In the case of the collapse of single cavities, cavities were found to collapse in quantitatively the same way as expected from numerical results. Although the formation of a high-speed jet could not be seen in any cavity due to the distortive effect of its curved walls, numerous features consistent with jet formation were clearly observed, for example the formation of a water hammer shock on jet impact. Based on indirect measurements, the mean percentage dif-

ference in jet strike timings between simulated and experimental results was found to be 13%, with the timing and structure of visible features also closely matched. Following jet impact the cavity was seen to form a torus - the axisymmetric equivalent of the 'lobe collapse' processes discussed in chapter 4. During this time light emission was also clearly observed from the cavity, starting initially as a single point at the point of jet impact, before propagating out into a torus of light emission. Analysis of PMT traces showed that the spectral intensity of this light emission could be split temporally into three separate peaks, the first of which corresponded to the impact of the high-speed jet, while the second and third corresponded to the collapse of the torus. Measurements of the intensity of this light emission at three different wavelengths suggested the light emission was broad band, with a peak in the ultra-violet part of the spectrum. Through the fitting of the PMT spectral intensities to black-body curves, a mean temperature for the collapse process of approximately 20,000 K was found. This temperature was deemed to be a lower-bound for the temperatures reached during collapse, due to the limitations of the method used to derive it. Comparing across different incident shock pressures, it was shown that the spectral intensity of the light emission continues to increase as the driving pressure is increased, over the range of pressures studied. Additionally, the relative importance of the different light emitting events changes. At low pressures, the first jet impact peak is the major source of light emission, but this is overtaken by the third peak as the pressure is increased.

An experimental study of multiple cavity arrangements is detailed in chapter 8. Arrangements studied include the collapse of a two cavity array, the second placed behind the first at different separation distances, as well as triangular arrays of three cavities and six cavities. In the case of the collapse of a two cavity array, as predicted numerically the collapse of both cavities was seen to follow the same process as the single cavity case. The first cavity in the array was indistinguishable from the single cavity result in all cases,

while the second was significantly affected by the separation distance between the cavities. Comparing to matched simulations, the mean percentage difference in jet strike timings was 12% for the first cavity, and 5% for the second. Analysis of the light emission produced showed that while at large separation distances the light from the second cavity is reduced in intensity relative to the single cavity case, at closer separation distances there exists a narrow range of distances at which a light emission event is seen, with spectral intensities over an order of magnitude higher than the maximum from the equivalent single cavity case. This light emission peak has been attributed to the time of jet strike in the cavity, and its intensity partially explained by the large increase in the width of the main transverse jet at these separation distances. This effect could not be fully quantified, as the light detection diagnostics utilised were not found to be sufficient to distinguish between variations in the light emitting area and temperature. Comparisons with simulated results suggested that both effects are likely to play a role. As in the single cavity case, the spectral intensity of the light emission was shown to increase progressively as the driving pressure was increased, for both cavities at all separation distances. The amplification in spectral intensity observed at particular separation distances was not consistent across incident shock pressures, with the peak light emission from the collapse of a single cavity approaching the peak second cavity result at higher shock pressures.

In the case of the collapse of the three cavity triangular array, it was shown that while light emission is also seen from this arrangement, the collapse occurs in a manifestly different way from the single cavity case. The collapse process was seen to be significantly more complex and less repeatable than the single and two cavity results. Analysis of the spectra of the light produced by the collapse of this arrangement suggested that peak temperatures reached were reduced relative to the single cavity case. Finally, in the collapse of an array of six cavities, some suggestion was seen that many of the complex inter-cavity effects observed in the collapse of an array of six cylindrical cavities in chapter 4 were also

present in the experimental results. Examples include the collapse of the second row of cavities, where multiple jets were seen to form in the cavities due to the combination of the incident shock and first cavity water hammer shock.

9.2 CONCLUSIONS

There are a number of conclusions which can be taken from this study. Firstly, it is clear that front-tracking, and more specifically the software tool *FronTier* is capable of modelling shock-driven cavity collapse. Even with simple equations of state, very good qualitative agreement has been shown between numerical and experimental results, with key processes such as the expansion of the water hammer shock formed by jet impact well replicated numerically. Additionally, using this numerical tool it has been shown that the amplification and superposition of shock waves seen in the collapse of multiple cavities is a powerful mechanism for intensifying the conditions reached in shock driven cavity collapse.

Experimentally, this study has substantiated the result of Dear, Bourne and Field[4,5] in demonstrating that the use of light-gas guns to collapse cavities cast in hydrogel blocks is an appropriate setup for the study of shock-driven cavity collapse. Strong shock waves are created in the hydrogel blocks, with pressures that reduce slowly behind the shock front, while the casting of cavities in the hydrogel allows accurate control over the size and placement of the cavities. Cavities in such a setup collapse as predicted numerically, and light is emitted from the cavities on collapse. This light has been shown to start at a single point, before propagating out into a torus; this is a result that agrees well with numerical predictions. Although the quantification of this light emission has not been comprehensive, these results have suggested that the light emission produced is broadband, with a spectrum that can be well approximated by Planck's law. This strongly indicates that temperatures of at least 10,000 K are reached in the current setup, with the fitting of

black-body curves to the data suggesting an approximate lower bound on temperature of 20,000 K.

Experimental results have shown that the light emission produced by cavity collapse may be substantially intensified through the use of multiple cavities. Similarly, it has been demonstrated that light emission from cavity collapse continues to intensify as the incident shock pressure is increased, for all cavities in all arrangements. While it is likely that these increases in intensity are at least partially due to increases in the temperatures and densities reached within the cavities, improved diagnostics will be required to verify this result. This is nonetheless a very encouraging outcome, and may offer fertile ground for further research into how shock-driven cavity collapse may be intensified.

9.3 SUGGESTIONS FOR FUTURE WORK

This work has looked at only a small cross-section of a highly complex and largely understudied problem, and much work could be done to further the understanding of the processes at work in shock-driven cavity collapse. In particular, there is substantial scope to expand the numerical study of multi-cavity arrangements, for example to include the effects of nearby walls or three-dimensional arrays of multiple cavities. The ability of the numerical tool used in this study to model three dimensional problems is very limited; the utilisation of a fully three-dimensional code would allow the modelling of a much wider set of problems, for example those presented in sections 8.3 and 8.4. This might offer new insights into ways in which multi-cavity effects can be utilised to intensify shock-driven cavity collapse. Additionally, the simple equations of state used in this study and the lack of radiation-transport modelling limits the accuracy of the solutions at key points in the collapse process, in particular at the point of jet strike and in lobe collapse. The implementation of an advanced equation of state for the gas and of radiation transport modelling could offer significant insights into the conditions reached within the cavities, and

allow accurate temperature predictions.

Experimentally, the use of more advanced diagnostic techniques would substantially increase understanding of the problem. In particular, the use of a streak-spectroscopy setup would enable a more accurate estimation of the temperatures and densities reached during cavity collapse. This would allow a more robust appraisal of the levels of amplification achievable with increases in shock strength and with multiple cavities. As an additional but perhaps less achievable point, it is possible that advanced imaging techniques could be used to image the inside of cavities. This would allow the direct observation of the fundamental processes that occur during shock-driven cavity collapse, such as the formation of the main transverse jet and the propagation of shock waves and the sheet-jetting in the toroidal cavity remains. With improved diagnostics, the expansion of this study to higher pressure incident shock regimes, such as those achievable with the use of two-stage gas guns would be the desirable next step. This would allow a more accurate assessment of the ultimate applicability of shock-driven cavity collapse in research requiring very high temperatures and densities, such as is the case in fusion research.

REFERENCES

[1] N. A. HAWKER & Y. VENTIKOS. Interaction of a strong shockwave with a gas bubble in a liquid medium: a numerical study. *Journal of Fluid Mechanics*, 701:59–97, 2012 .

[2] N. A. HAWKER. Computational Modelling of Intense Bubble Collapse. Ph.D. thesis, 2012 .

[3] G. J. BALL, B. P. HOWELL, T. G. LEIGHTON *et al.* Shock-induced collapse of a cylindrical air cavity in water: a Free-Lagrange simulation. *Shock Waves*, 10(4):265–276, 2000 .

[4] J. P. DEAR & J. E. FIELD. A study of the collapse of arrays of cavities. *Journal of Fluid Mechanics*, 190:409–425, 1988 .

[5] N. K. BOURNE & J. E. FIELD. Shock-induced collapse and luminescence by cavities. *Philosophical Transactions of the Royal Society A: Mathematical, Physical and Engineering Sciences*, 357(1751):295–311, 1999 .

[6] K. R. WENINGER, C. G. CAMARA & S. J. PUTTERMAN. Energy Focusing in a Converging Fluid Flow: Implications for Sonoluminescence. *Physical Review Letters*, 83(10):2081–2084, 1999 .

[7] J. P. DEAR, J. E. FIELD & A. J. WALTON. Gas compression and jet formation in cavities collapsed by a shock wave. *Nature*, 332(6164):505–508, 1988 .

[8] A. CHAKRAVARTY, T. GEORGHIOU, T. E. PHILLIPSON *et al.* Stable sonoluminescence within a water hammer tube. *Physical Review E*, 69(6):1–8, 2004 .

[9] D. F. GAITAN, L. A. CRUM, C. C. CHURCH *et al.* Sonoluminescence and bubble dynamics for a single, stable, cavitation bubble. *The Journal of the Acoustical Society of America*, 91(6):3166–3183, 1992 .

[10] H. FRENZEL & H. SCHULTES. Lumineszenz im ultraschall-beschickten Wasser. *Zeitschrift für Physikalische Chemie*, 27B:421–424, 1934 .

[11] P. JARMAN. Sonoluminescence: a discussion. *Journal of the Acoustical Society of America*, 32(11):1459–1462, 1960 .

[12] C. SEHGAL, R. G. SUTHERLAND & R. E. VERRALL. Optical spectra of sonoluminescence from transient and stable cavitation in water saturated with various gases. *The Journal of Physical Chemistry*, 84(4):388–395, 1980 .

[13] I. HANSSON, V. KEDRINSKII & K. A. MOÌŸRCH. On the dynamics of cavity clusters. *Journal of Physics D: Applied Physics*, 15:1725–1734, 1982 .

[14] E. B. FLINT & K. S. SUSLICK. Sonoluminescence from alkali-metal salt solutions. *The Journal of Physical Chemistry*, 95(3):1484–1488, 1991 .

[15] L. A. CRUM & G. T. REYNOLDS. Sonoluminescence produced by "stable" cavitation. *Journal of the Acoustical Society of America*, 78(1):137–139, 1985 .

[16] D. F. GAITAN, A. A. ATCHLEY, S. D. LEWIA *et al.* Spectra of single-bubble sonoluminescence in water and glycerin-water mixtures. *Physical review. E, Statistical physics, plasmas, fluids, and related interdisciplinary topics*, 54(1):525–528, 1996 .

[17] L. RAYLEIGH. On the pressure developed in a liquid during the collapse of a spherical cavity. *Philosophical Magazine*, 34:94–98, 1917 .

[18] M. S. PLESSET & A. PROSPERETTI. Bubble dynamics and cavitation. *Annual Review of Fluid Mechanics*, 9:145–185, 1977 .

[19] B. GOMPF, R. GÜNTHER, G. NICK *et al.* Resolving sonoluminescence pulse width with time-correlated single photon counting. *Physical Review Letters*, 79(7):1405–1408, 1997 .

[20] R. A. HILLER, S. J. PUTTERMAN & K. R. WENINGER. Time-resolved spectra of sonoluminescence. *Physical Review Letters*, 80(5):1090–1093, 1998 .

[21] R. PECHA, B. GOMPF, G. NICK *et al.* Resolving the sonoluminescence pulse shape with a streak camera. *Physical Review Letters*, 81(3):717–720, 1998 .

[22] B. P. BARBER & S. J. PUTTERMAN. Observation of synchronous picosecond sonoluminescence. *Nature*, 352:318–320, 1991 .

[23] B. P. BARBER, R. A. HILLER, K. ARISAKA *et al.* Resolving the picosecond characteristics of synchronous sonoluminescence. *Journal of the Acoustical Society of America*, 91(5):3061–3063, 1992 .

[24] R. A. HILLER, S. J. PUTTERMAN & B. P. BARBER. Spectrum of synchronous picosecond sonoluminescence. *Physical review letters*, 69(8):1182–1184, 1992 .

[25] C. C. WU & P. H. ROBERTS. Shock-wave propagation in a sonoluminescing gas bubble. *Physical review letters*, 70(22):3424–3427, 1993 .

[26] W. C. MOSS, D. B. CLARKE, J. W. WHITE *et al.* Hydrodynamic simulations of bubble collapse and picosecond sonoluminescence. *Physics of Fluids*, 6(9):2979–2985, 1994 .

[27] R. LÖFSTEDT, B. P. BARBER & S. J. PUTTERMAN. Toward a hydrodynamic theory of sonoluminescence. *Physics of Fluids A: Fluid Dynamics*, 5(11):2911, 1993 .

[28] K. R. WENINGER, B. P. BARBER & S. J. PUTTERMAN. Pulsed mie scattering measurements of the collapse of a sonoluminescing bubble. *Physical Review Letters*, 78(9):1799–1802, 1997 .

[29] B. P. BARBER & S. J. PUTTERMAN. Light scattering measurements of the repetitive supersonic implosion of a sonoluminescing bubble. *Physical Review Letters*, 69(26):3839–3842, 1992 .

[30] B. P. BARBER, R. A. HILLER, R. LÖFSTEDT *et al.* Defining the unknowns of sonoluminescence. *Physics Reports*, 281:65–143, 1997 .

[31] K. R. WENINGER, R. A. HILLER, B. P. BARBER *et al.* Sonoluminescence from single bubbles in nonaqueous liquids: new parameter space for sonochemistry. *The Journal of Physical Chemistry*, 99(39):14195–14197, 1995 .

[32] G. E. VAZQUEZ & S. J. PUTTERMAN. Temperature and pressure dependence of sonoluminescence. *Physical review letters*, 85(14):3037–40, 2000 .

[33] W. LAUTERBORN. Numerical investigation of nonlinear oscillations of gas bubbles in liquids. *Journal of the Acoustical Society of America*, 59(2):283–293, 1976 .

[34] W. LAUTERBORN & T. KURZ. Physics of bubble oscillations. *Reports on Progress in Physics*, 73(10):1–88, 2010 .

[35] R. G. HOLT, D. F. GAITAN, A. A. ATCHLEY *et al.* Chaotic Sonoluminescence. *Physical Review Letters*, 72(9):1376–1379, 1994 .

[36] M. P. BRENNER, S. HILGENFELDT & D. LOHSE. Single bubble sonoluminescence. *Reviews of Modern Physics*, 74(April):425–484, 2002 .

[37] S. HILGENFELDT, D. LOHSE & M. P. BRENNER. Phase diagrams for sonoluminescing bubbles. *Physics of Fluids*, 8(11):2808, 1996 .

[38] M. P. BRENNER, D. LOHSE & T. F. DUPONT. Bubble shape oscillations and the onset of sonoluminescence. *Physical Review Letters*, 75(5):954–957, 1995 .

[39] T. J. MATULA & L. A. CRUM. Evidence for Gas Exchange in Single-Bubble Sonoluminescence. *Physical Review Letters*, 80(4):865–868, 1998 .

[40] D. LOHSE, M. P. BRENNER, T. F. DUPONT *et al.* Sonoluminescing air bubbles rectify argon. *Physical Review Letters*, 78(7):1359–1362, 1997 .

[41] D. LOHSE & S. HILGENFELDT. Inert gas accumulation in sonoluminescing bubbles. *The Journal of Chemical Physics*, 107(17):6986, 1997 .

[42] R. G. HOLT & D. F. GAITAN. Observation of stability boundaries in the parameter space of single bubble sonoluminescence. *Physical Review Letters*, 77(18):3791–3794, 1996 .

[43] J. A. KETTERLING & R. E. APFEL. Experimental Validation of the Dissociation Hypothesis for Single Bubble Sonoluminescence. *Physical Review Letters*, 81(22):4991–4994, 1998 .

[44] J. A. KETTERLING & R. E. APFEL. Extensive experimental mapping of sonoluminescence parameter space. *Physical review. E, Statistical physics, plasmas, fluids, and related interdisciplinary topics*, 61(4 Pt A):3832–3837, 2000 .

[45] B. D. STOREY & A. J. SZERI. Water vapour, sonoluminescence and sonochemistry. *Proceedings of the Royal Society A: Mathematical, Physical and Engineering Sciences*, 456(1999):1685–1709, 2000 .

[46] M. ASHOKKUMAR, L. A. CRUM, C. A. FRENSLEY *et al.* Effect of solutes on single-bubble sonoluminescence in water. *Journal of Physical Chemistry A*, 104:8462–8465, 2000 .

[47] Y. T. DIDENKO, W. B. MCNAMARA III & K. S. SUSLICK. Molecular emission from single-bubble sonoluminescence. *Nature*, 407:877–879, 2000 .

[48] D. J. FLANNIGAN & K. S. SUSLICK. Plasma formation and temperature measurement during single-bubble cavitation. *Nature*, 434(March):52–55, 2005 .

[49] D. J. FLANNIGAN & K. S. SUSLICK. Inertially confined plasma in an imploding bubble. *Nature Physics*, 6(8):598–601, 2010 .

[50] S. D. HOPKINS, S. J. PUTTERMAN, B. A. KAPPUS *et al.* Dynamics of a Sonoluminescing Bubble in Sulfuric Acid. *Physical Review Letters*, 95(25):2–5, 2005 .

[51] V. Q. VUONG & A. J. SZERI. Sonoluminescence and diffusive transport. *Physics of Fluids*, 8(9):2354–2364, 1996 .

[52] V. Q. VUONG, A. J. SZERI & D. A. YOUNG. Shock formation within sonoluminescence bubbles. *Physics of Fluids*, 11(1):10–17, 1999 .

[53] C. EBERLEIN. Sonoluminescence as quantum vacuum radiation. *Physical review letters*, 76(20):3842–3845, 1996 .

[54] S. HILGENFELDT, S. GROSSMANN & D. LOHSE. A simple explanation of light emission in sonoluminescence. *Nature*, 398:402–405, 1999 .

[55] S. HILGENFELDT, S. GROSSMANN & D. LOHSE. Sonoluminescence light emission. *Physics of Fluids*, 11(6):1318–1330, 1999 .

[56] K. S. SUSLICK & D. J. FLANNIGAN. Inside a collapsing bubble: sonoluminescence and the conditions during cavitation. *Annual Review of Physical Chemistry*, 59:659–683, 2008 .

[57] W. C. MOSS, D. B. CLARKE & D. A. YOUNG. Calculated pulse widths and spectra of a single sonoluminescing bubble. *Science*, 276(5317):1398–1401, 1997 .

[58] G. E. VAZQUEZ, C. G. CAMARA, S. J. PUTTERMAN *et al.* Sonoluminescence: nature's smallest blackbody. *Optics Letters*, 26(9):575, 2001 .

[59] C. G. CAMARA, S. J. PUTTERMAN & E. KIRILOV. Sonoluminescence from a Single Bubble Driven at 1 Megahertz. *Physical Review Letters*, 92(12):1–4, 2004 .

[60] J. HOLZFUSS, M. RÜGGEBERG & A. BILLO. Shock wave emissions of a sonoluminescing bubble. *Physical Review Letters*, 81(24):5434–5437, 1998 .

[61] Z. Q. WANG, R. PECHA, B. GOMPF *et al.* Single bubble sonoluminescence: Investigations of the emitted pressure wave with a fiber optic probe hydrophone. *Physical Review E*, 59(2):1777–1780, 1999 .

[62] R. PECHA & B. GOMPF. Microimplosions: cavitation collapse and shock wave emission on a nanosecond time scale. *Physical review letters*, 84(6):1328–30, 2000 .

[63] R. H. MELLEN. An experimental study of the collapse of a spherical cavity in water. *The Journal of the Acoustical Society of America*, 28(3):447–454, 1956 .

[64] B. P. BARBER, C. C. WU, R. LÖFSTEDT *et al.* Sensitivity of sonoluminescence to experimental parameters. *Physical Review Letters*, 72(9):1380–1383, 1994 .

[65] W. C. MOSS, D. B. CLARKE, J. W. WHITE *et al.* Sonoluminescence and the prospects for table-top micro-thermonuclear fusion. *Physics Letters*, 211(February):69–74, 1996 .

[66] R. P. TALEYARKHAN, C. D. WEST, J. S. CHO *et al.* Evidence for nuclear emissions during acoustic cavitation. *Science (New York, N.Y.)*, 295(5561):1868–73, 2002 .

[67] A. GALONSKY. Tabletop fusion revisited. *Science*, 297:1645, 2002 .

[68] S. J. PUTTERMAN, L. A. CRUM & K. S. SUSLICK. Comments on "Evidence for Nuclear Emissions During Acoustic Cavitation"; by Taleyarkhan et al..,Science 295, 1868, March 8, 2002. *ArXiv e-prints*, 2002 .

[69] D. SHAPIRA & M. SALTMARSH. Nuclear Fusion in Collapsing Bubbles-Is It There? An Attempt to Repeat the Observation of Nuclear Emissions from Sonoluminescence. *Physical Review Letters*, 89(10):2–5, 2002 .

[70] C. G. CAMARA, S. D. HOPKINS, K. S. SUSLICK *et al.* Upper Bound for Neutron Emission from Sonoluminescing Bubbles in Deuterated Acetone. *Physical Review Letters*, 98(6):4–7, 2007 .

[71] L. TSOUKALAS, F. CLIKEMAN, M. BERTODANO *et al.* Tritium measurements in neutron-induced cavitation of deuterated acetone. *Nuclear Technology*, 155:248–251, 2006 .

[72] R. P. TALEYARKHAN, J. S. CHO, C. D. WEST *et al.* Additional evidence of nuclear emissions during acoustic cavitation. *Physical Review E*, 69(3):1–11, 2004 .

[73] R. P. TALEYARKHAN, C. D. WEST, R. T. LAHEY JR *et al.* Nuclear emissions during self-nucleated acoustic cavitation. *Physical Review Letters*, 96(3):1–4, 2006 .

[74] Y. XU & A. BUTT. Confirmatory experiments for nuclear emissions during acoustic cavitation. *Nuclear Engineering and Design*, 235(10-12):1317–1324, 2005 .

[75] E. R. FORRINGER, D. ROBBINS & J. MARTIN. Confirmation of neutron production during self-neucleated acoustic cavitation. In Proceedings of the American Nuclear Society International Conference (2006).

[76] R. I. NIGMATULIN, I. S. AKHATOV, A. S. TOPOLNIKOV *et al.* Theory of supercompression of vapor bubbles and nanoscale thermonuclear fusion. *Physics of Fluids*, 17(10):107106, 2005 .

[77] B. NARANJO. Comment on "Nuclear Emissions During Self-Nucleated Acoustic Cavitation". *Physical Review Letters*, 97(14):149403, 2006 .

[78] PURDUE UNIVERSITY INVESTIGATION COMMITTEE. Report of the investigation committee in the matter of Dr. Rusi P. Taleyarkhan, 2008 .

[79] D. F. GAITAN, R. A. TESSIEN, R. A. HILLER *et al.* Transient cavitation in high-quality-factor resonators at high static pressures. *The Journal of the Acoustical Society of America*, 127(6):3456–65, 2010 .

[80] P. A. ANDERSON, A. SAMPATHKUMAR, T. W. MURRAY *et al.* Optical nucleation of bubble clouds in a high pressure spherical resonator. *The Journal of the Acoustical Society of America*, 130(5):3389–95, 2011 .

[81] K. S. SUSLICK, Y. T. DIDENKO, M. M. FANG *et al.* Acoustic cavitation and its chemical consequences. *Philosophical Transactions of the Royal Society A: Mathematical, Physical and Engineering Sciences*, 357(1751):335–353, 1999 .

[82] K. S. SUSLICK & G. J. PRICE. Applications of ultrasound To materials chemistry. *Annual Review of Materials Science*, 29(1):295–326, 1999 .

[83] K. S. SUSLICK, S. J. DOKTYCZ & E. B. FLINT. On the origin of sonoluminescence and sonochemistry. *Ultrasonics*, 28(5):280–290, 1990 .

[84] K. S. SUSLICK, S.-B. CHOE, A. A. CICHOWLAS *et al.* Sonochemical synthesis of amorphous iron. *Nature*, 353:414–416, 1991 .

[85] T. PROZOROV, B. MCCARTY, Z. CAI *et al.* Effects of high-intensity ultrasound on Bi2Sr2CaCu2O8+x superconductor. *Applied Physics Letters*, 85(16):3513, 2004 .

[86] Y. G. ADEWUYI. Sonochemistry in environmental remediation. 1. Combinative and hybrid sonophotochemical oxidation processes for the treatment of pollutants in water. *Environmental Science and Technology*, 39(10):3409–3420, 2005 .

[87] D. G. SHCHUKIN & H. MÖHWALD. Sonochemical nanosynthesis at the engineered interface of a cavitation microbubble. *Physical chemistry chemical physics : PCCP*, 8(30):3496–506, 2006 .

[88] V. MANCIER, A.-L. DALTIN & D. LECLERCQ. Synthesis and characterization of copper oxide (I) nanoparticles produced by pulsed sonoelectrochemistry. *Ultrasonics sonochemistry*, 15(3):157–63, 2008 .

[89] M. A. KELKAR, P. R. GOGATE & A. B. PANDIT. Intensification of esterification of acids for synthesis of biodiesel using acoustic and hydrodynamic cavitation. *Ultrasonics sonochemistry*, 15(3):188–94, 2008 .

[90] M. VERSLUIS, B. SCHMITZ, A. VON DER HEYDT *et al.* How Snapping Shrimp Snap: Through Cavitating Bubbles. *Science*, 289(5487):2114–2117, 2000 .

[91] D. LOHSE, B. SCHMITZ & M. VERSLUIS. Snapping shrimp make flashing bubbles. *Nature*, 413(6855):477–8, 2001 .

[92] W. W. L. AU & K. BANKS. The acoustics of the snapping shrimp Synalpheus parneomeris in Kaneohe Bay. *Journal of the Acoustical Society of America*, 103(1):41–47, 1997 .

[93] O. LINDAU & W. LAUTERBORN. Cinematographic observation of the collapse and rebound of a laser-produced cavitation bubble near a wall. *Journal of Fluid Mechanics*, 479(2003):327–348, 2003 .

[94] M. KORNFELD & L. SUVOROV. On the destructive action of cavitation. *Journal of Applied Physics*, 15(6):495–506, 1944 .

[95] S. S. COOK. Erosion by water-hammer. *Proceedings of the Royal Society A: Mathematical, Physical and Engineering Sciences*, 119(783):481–488, 1928 .

[96] T. B. BENJAMIN & A. T. ELLIS. The collapse of cavitation bubbles and the pressures thereby produced against solid boundaries. *Philosophical Transactions of the Royal Society A: Mathematical, Physical and Engineering Sciences*, 260(1110):221–240, 1966 .

[97] M. S. PLESSET & R. B. CHAPMAN. Collapse of an initially spherical vapour cavity in the neighbourhood of a solid boundary. *Journal of Fluid Mechanics*, 47:283–290, 1971 .

[98] W. LAUTERBORN & H. BOLLE. Experimental investigations of cavitation-bubble collapse in the neighbourhood of a solid boundary. *Journal of Fluid Mechanics*, 72(2):391–399, 1975 .

[99] W. LAUTERBORN. Cavitation bubble dynamics - new tools for an intricate problem. *Applied Scientific Research*, 38:165–178, 1982 .

[100] A. VOGEL, W. LAUTERBORN & R. TIMM. Optical and acoustic investigations of the dynamics of laser-produced cavitation bubbles near a solid boundary. *Journal of Fluid Mechanics*, 206:299–338, 1989 .

[101] A. PHILIPP & W. LAUTERBORN. Cavitation erosion by single laser-produced bubbles. *Journal of Fluid Mechanics*, 361:75–116, 1998 .

[102] Y. TOMITA & A. SHIMA. Mechanisms of impulsive pressure generation and damage pit formation by bubble collapse. *Journal of Fluid Mechanics*, 169:535–564, 1986 .

[103] A. PHILIPP & W. LAUTERBORN. Damage of solid surfaces by single laser-produced cavitation bubbles. *Acustica*, 83:223–227, 1997 .

[104] A. VOGEL & W. LAUTERBORN. Acoustic transient generation by laser-produced cavitation bubbles near solid boundaries. *Journal of the Acoustical Society of America*, 84(2):719–731, 1988 .

[105] J. R. BLAKE, Y. TOMITA & R. P. TONG. The art , craft and science of modelling jet impact in a collapsing cavitation bubble. *Applied Scientific Research*, 58:77–90, 1998 .

[106] R. P. TONG, W. P. SCHIFFERS, S. J. SHAW *et al.* The role of 'splashing' in the collapse of a laser-generated cavity near a rigid boundary. *Journal of Fluid Mechanics*, 380:339–361, 1999 .

[107] F. P. BOWDEN & O. A. GURTON. Birth and growth of explosion in liquids and solids initiated by impact and friction. *Proceedings of the Royal Society A: Mathematical, Physical and Engineering Sciences*, 198(1054):350–372, 1949 .

[108] C. L. MADER. Initiation of detonation by the interaction of shocks with density discontinuities. *Physics of Fluids*, 8(10):1811–1816, 1965 .

[109] F. P. BOWDEN & M. P. MCONIE. Formation of Cavities and Microjets in Liquids and Their Role in Initiation and Growth of Explosion. *Proceedings of the Royal Society A: Mathematical, Physical and Engineering Sciences*, 298:38–50, 1967 .

[110] G. D. COLEY & J. E. FIELD. The role of cavities in the initiation and growth of explosion in liquids. *Proceedings of the Royal Society of London. Series A*, 335(1600):67–86, 1973 .

[111] M. M. CHAUDHRI & J. E. FIELD. The role of rapidly compressed gas pockets in the initiation of condensed explosives. *Proceedings of the Royal Society A: Mathematical, Physical and Engineering Sciences*, 340(1620):113–128, 1974 .

[112] N. K. BOURNE & J. E. FIELD. Bubble Collapse and the Initiation of Explosion. *Proceedings of the Royal Society A: Mathematical, Physical and Engineering Sciences*, 435(1894):423–435, 1991 .

[113] N. K. BOURNE & J. E. FIELD. Explosive ignition by the collapse of cavities. *Proceedings of the Royal Society A: Mathematical, Physical and Engineering Sciences*, 455(1987):2411–2426, 1999 .

[114] N. K. BOURNE & A. M. MILNE. On cavity collapse and subsequent ignition. In Proceedings of the 12th Internation Detonation Symposium Arlington, VA, pp. 1–9 (2002).

[115] A. J. COLEMAN, J. E. SAUNDERS, L. A. CRUM *et al.* Acoustic cavitation generated by an extracorporeal shockwave lithotripter. *Ultrasound in Medicine and Biology*, 13(2):69–76, 1987 .

[116] M. LOKHANDWALLA & B. STURTEVANT. Fracture mechanics model of stone comminution in ESWL and implications for tissue damage. *Physics in Medicine and Biology*, 45(7):1923–40, 2000 .

[117] A. J. COLEMAN & J. E. SAUNDERS. A review of the physical properties and biological effects of the high amplitude acoustic fields used in extracorporeal lithotripsy. *Ultrasonics*, 31(2):75–89, 1993 .

[118] S. ZHU, F. H. COCKS, G. M. PREMINGER *et al.* The role of stress waves and cavitation in stone comminution in shock wave lithotripsy. *Ultrasound in Medicine and Biology*, 28(5):661–671, 2002 .

[119] J. E. FIELD. The physics of liquid impact, shock wave interactions with cavities, and the implications to to shock wave lithotripsy. *Physics in Medicine and Biology*, 36(11):1475–1484, 1991 .

[120] M. DELIUS & W. BRENDEL. A mechanism of gallstone destruction by extracorporeal shock waves. *Naturwissenschaften*, 201:200–201, 1988 .

[121] R. O. CLEVELAND, O. A. SAPOZHNIKOV, M. R. BAILEY *et al.* A dual passive cavitation detector for localized detection of lithotripsy-induced cavitation in vitro. *The Journal of the Acoustical Society of America*, 107(3):1745–58, 2000 .

[122] C. C. CHURCH. A theoretical study of cavitation generated by an extracorporeal shock wave lithotripter. *The Journal of the Acoustical Society of America*, 86(1):215–227, 1989 .

[123] E. KLASEBOER, S. W. FONG, C. K. TURANGAN *et al.* Interaction of lithotripter shockwaves with single inertial cavitation bubbles. *Journal of Fluid Mechanics*, 593:33–56, 2007 .

[124] A. R. JAMALUDDIN, G. J. BALL, C. K. TURANGAN *et al.* The collapse of single bubbles and approximation of the far-field acoustic emissions for cavitation induced by shock wave lithotripsy. *Journal of Fluid Mechanics*, 677:305–341, 2011 .

[125] F. R. GILMORE. The growth or collapse of a spherical bubble in a viscous compressible liquid. *California Institute of Technology*, (Rep. No. 26-4):1–40, 1952 .

[126] A. PHILIPP, M. DELIUS, C. SCHEFFCZYK *et al.* Interaction of lithotripter-generated shock waves with air bubbles. *Journal of the Acoustical Society of America*, 93(5):2496–2509, 1993 .

[127] A. J. COLEMAN, M. WHITLOCK, T. G. LEIGHTON *et al.* The spatial distribution of cavitation induced acoustic emission, sonoluminescence and cell lysis in the field of a shock wave lithotripter. *Physics in medicine and biology*, 38(11):1545–60, 1993 .

[128] A. J. COLEMAN, M. J. CHOI & J. E. SAUNDERS. Detection of acoustic emission from cavitation in tissue during clinical extracorporeal lithotripsy. *Ultrasound in Medicine and Biology*, 22(8):1079–1087, 1996 .

[129] P. ZHONG, I. CIOANTA, F. H. COCKS *et al.* Inertial cavitation and associated acoustic emission produced during electrohydraulic shock wave lithotripsy. *The Journal of the Acoustical Society of America*, 101(5 Pt 1):2940–50, 1997 .

[130] A. J. COLEMAN, M. J. CHOI, J. E. SAUNDERS *et al.* Acoustic emission and sonoluminescence due to cavitation at the beam focus of an electrhydraulic shock wave lithotripter. *Ultrasound in Medicine and Biology*, 18(3):267–281, 1992 .

[131] T. KODAMA & Y. TOMITA. Cavitation bubble behavior and bubble-shock wave interaction near a gelatin surface as a study of in vivo bubble dynamics. *Applied Physics B: Lasers and Optics*, 70:139–149, 2000 .

[132] Y. A. PISHCHALNIKOV, O. A. SAPOZHNIKOV, M. R. BAILEY *et al.* Cavitation bubble cluster activity in the breakage of kidney stones by lithotripter shockwaves. *Journal of endourology*, 17(7):435–446, 2003 .

[133] M. F. HAMILTON, Y. A. ILINSKII, G. D. MEEGAN *et al.* Interaction of bubbles in a cluster near a rigid surface. *Acoustics Research Letters Online*, 6(3):207–213, 2005 .

[134] E. A. ZABOLOTSKAYA, Y. A. ILINSKII, G. D. MEEGAN *et al.* Bubble interactions in clouds produced during shock wave lithotripsy. *IEEE Ultrasonics Symposium, 2004*, 2(c):890–893, 2004 .

[135] M. DELIUS & S. GAMBIHLER. Sonographic imaging of extracorporeal shock wave effects in the liver and gallbladder of dogs. *Digestion*, 52:55–60, 1992 .

[136] J. E. LINGEMAN, J. A. MCATEER, E. GNESSIN *et al.* Shock wave lithotripsy: advances in technology and technique. *Nature Reviews Urology*, 6(12):660–670, 2009 .

[137] P. ZHONG, I. CIOANTA, S. ZHU *et al.* Effects of tissue constraint on shock wave-induced bubble expansion in vivo. *The Journal of the Acoustical Society of America*, 104(5):3126–9, 1998 .

[138] P. ZHONG, Y. ZHOU & S. ZHU. Dynamics of bubble oscillation in constrained media and mechanisms of vessel rupture in SWL. *Ultrasound in Medicine and Biology*, 27(1):119–134, 2001 .

[139] H. CHEN, A. A. BRAYMAN, M. R. BAILEY *et al.* Blood vessel rupture by cavitation. *Urological Research*, 38:321–326, 2010 .

[140] H. CHEN, W. KREIDER, A. A. BRAYMAN *et al.* Blood vessel deformations on microsecond time scales by ultrasonic cavitation. *Physical Review Letters*, 106:034301, 2011 .

[141] E. JOHNSEN & T. COLONIUS. Shock-induced collapse of a gas bubble in shockwave lithotripsy. *The Journal of the Acoustical Society of America*, 124(4):2011–2020, 2008 .

[142] E. JOHNSEN & T. COLONIUS. Numerical simulations of non-spherical bubble collapse. *Journal of Fluid Mechanics*, 629:231–262, 2009 .

[143] J. B. KELLER & M. MIKSIS. Bubble oscillations of large amplitude. *Journal of the Acoustical Society of America*, 68(2):628–633, 1980 .

[144] J. I. KATZ. Jets from collapsing bubbles. *Proceedings of the Royal Society A: Mathematical, Physical and Engineering Sciences*, 455(1981):323–328, 1999 .

[145] A. PROSPERETTI. A new mechanism for sonoluminescence. *Journal of the Acoustical Society of America*, 101(4):2003–2007, 1997 .

[146] Z. DING & S. M. GRACEWSKI. The behaviour of a gas cavity impacted by a weak or strong shock wave. *Journal of Fluid Mechanics*, 309(1996):183–209, 1996 .

[147] C. W. HIRT, A. A. AMSDEN & J. L. COOK. An arbitrary Lagrangian-Eulerian computing method for all flow speeds. *Journal of Computational Physics*, 14:227–253, 1974 .

[148] C. K. TURANGAN, A. R. JAMALUDDIN, G. J. BALL *et al.* Free-Lagrange simulations of the expansion and jetting collapse of air bubbles in water. *Journal of Fluid Mechanics*, 598:1–25, 2008 .

[149] A. R. JAMALUDDIN. Free-Lagrange simulations of shock-bubble interaction in extracorporeal shock wave lithotripsy. Ph.D. thesis, 2005 .

[150] T. G. LEIGHTON, C. K. TURANGAN, A. R. JAMALUDDIN *et al.* Prediction of far-field acoustic emissions from cavitation clouds during shock wave lithotripsy for development of a clinical device. *Proceedings of the Royal Society A: Mathematical, Physical and Engineering Sciences*, 469:1–21, 2013 .

[151] E. JOHNSEN & T. COLONIUS. Implementation of WENO schemes in compressible multicomponent flow problems. *Journal of Computational Physics*, 219(2):715–732, 2006 .

[152] C.-H. CHANG & M.-S. LIOU. A robust and accurate approach to computing compressible multiphase flow: Stratified flow model and AUSM+-up scheme. *Journal of Computational Physics*, 225(1):840–873, 2007 .

[153] M. SUSSMAN, P. SMEREKA & S. OSHER. A level set approach for computing solutions to incompressible two-phase flow. *Journal of Computational Physics*, 114:146–159, 1994 .

[154] R. P. FEDKIW, T. ASLAM, B. MERRIMAN *et al.* A non-oscillatory eulerian approach to interfaces in multimaterial flows (the ghost fluid method). *Journal of Computational Physics*, 152:457–492, 1999 .

[155] X. Y. HU & B. C. KHOO. An interface interaction method for compressible multifluids. *Journal of Computational Physics*, 198(1):35–64, 2004 .

[156] R. R. NOURGALIEV, S. Y. SUSHCHIKH, T. N. DINH *et al.* Shock wave refraction patterns at interfaces. *International Journal of Multiphase Flow*, 31(9):969–995, 2005 .

[157] R. R. NOURGALIEV, T. N. DINH & T. G. THEOFANOUS. Adaptive characteristics-based matching for compressible multifluid dynamics. *Journal of Computational Physics*, 213(2):500–529, 2006 .

[158] R. R. NOURGALIEV & T. G. THEOFANOUS. High-fidelity interface tracking in compressible flows: Unlimited anchored adaptive level set. *Journal of Computational Physics*, 224(2):836–866, 2007 .

[159] J. W. GROVE & R. MENIKOFF. Anomalous reflection of a shock wave at a fluid interface. *Journal of Fluid Mechanics*, 219:313–336, 1990 .

[160] G. TRYGGVASON, B. BUNNER, A. ESMAEELI *et al.* A Front-Tracking Method for the Computations of Multiphase Flow. *Journal of Computational Physics*, 169:708–759, 2001 .

[161] H. GRANDJEAN, N. JACQUES & S. ZALESKI. Shock propagation in liquids containing bubbly clusters: a continuum approach. *Journal of Fluid Mechanics*, 701:304–332, 2012 .

[162] R. K. S. HANKIN. The Euler Equations for Multiphase Compressible Flow in Conservation Form. *Journal of Computational Physics*, 172(2):808–826, 2001 .

[163] X. Y. HU, B. C. KHOO, N. A. ADAMS *et al.* A conservative interface method for compressible flows. *Journal of Computational Physics*, 219(2):553–578, 2006 .

[164] S. Y. SUSHCHIKH & R. R. NOURGALIEV. Shock waves and flow patterns in a shock-induced bubble collapse. In 43rd AIAA Aerospace Sciences Meeting and Exhibit, Reno, NV (2005).

[165] E. LAUER, X. Y. HU, S. HICKEL *et al.* Numerical investigation of collapsing cavity arrays. *Physics of Fluids*, 24(5):052104, 2012 .

[166] A. B. SWANTEK & J. M. AUSTIN. Collapse of void arrays under stress wave loading. *Journal of Fluid Mechanics*, 649(April 2010):399–427, 2010 .

[167] N. K. BOURNE & J. E. FIELD. Shock-induced collapse of single cavities in liquids. *Journal of Fluid Mechanics*, 244:225–240, 1992 .

[168] N. K. BOURNE & J. E. FIELD. Cavity collapse in a liquid with solid particles. *Journal of Fluid Mechanics*, 259:149–165, 1994 .

[169] Y. TOMITA, A. SHIMA & T. OHNO. Collapse of multiple gas bubbles by a shock wave and induced impulsive pressure. *Journal of Applied Physics*, 56(1):125, 1984 .

[170] P. TESTUD-GIOVANNESCHI, A. P. ALLONCLE & D. DUFRESNE. Collective effects of cavitation: Experimental study of bubble-bubble and bubble-shock wave interactions. *Journal of Applied Physics*, 67(8):3560–3564, 1990 .

[171] Y. TOMITA & A. SHIMA. High-Speed Photographic Observations of Laser-Induced Cavitation Bubbles in Water. *Acustica*, 71:161–171, 1990 .

[172] S. W. FONG, D. ADHIKARI, E. KLASEBOER *et al.* Interactions of multiple spark-generated bubbles with phase differences. *Experiments in Fluids*, 46(4):705–724, 2009 .

[173] J. F. HAAS & B. STURTEVANT. Interaction of weak shock waves with cylindrical and spherical gas inhomogeneities. *Journal of Fluid Mechanics*, 181:41–76, 1987 .

[174] J. GLIMM, E. ISAACSON, D. MARCHESIN *et al.* Front tracking for hyperbolic systems. *Advances in Applied Mathematics*, 2:91–119, 1981 .

[175] J. GLIMM & O. A. MCBRYAN. A computational model for interfaces. *Advances in Applied Mathematics*, 6:422–435, 1985 .

[176] J. GLIMM, M. J. GRAHAM, J. W. GROVE *et al.* Front tracking in two and three dimensions. *Computers & Mathematics with Applications*, 35(7):1–11, 1998 .

[177] J. GLIMM, J. W. GROVE, X. L. LI *et al.* Three-Dimensional Front Tracking. *SIAM Journal on Scientific Computing*, 19(3):703–727, 1998 .

[178] J. GLIMM, J. W. GROVE & Y. ZHANG. Interface tracking for axisymmetric flows. *SIAM Journal on Scientific Computing*, 24(1):208–236, 2002 .

[179] http://frontier.ams.sunysb.edu/download/download.php.

[180] J. GLIMM, J. W. GROVE, X. L. LI *et al.* Simple front tracking. *Contemporary Mathematics*, 238(2):133–149, 1999 .

[181] E. F. TORO. Riemann solvers and numerical methods for fluids dynamics: a practical introduction (2009), 3rd edition.

[182] M. FOURIER. Théorie analytique de la chaleur (1822).

[183] X. JIAO & H. ZHA. Consistent Computation of First- and Second-Order Differential Quantities for Surface Meshes. In Proceedings of the 2008 ACM Symposium on Solid and Physical Modeling, pp. 159–170 (2008).

[184] R. COURANT, K. FRIEDRICHS & H. LEWY. On the partial difference equations of mathematical physics. *IBM Journal of Research and Development*, 11(2):215–234, 1967 .

[185] J. DU, B. FIX, J. GLIMM *et al.* A simple package for front tracking. *Journal of Computational Physics*, 213(2):613–628, 2006 .

[186] W. J. RIDER & D. B. KOTHE. Reconstructing Volume Tracking. *Journal of Computational Physics*, 141:112–152, 1998 .

[187] I.-L. CHERN, J. GLIMM, O. A. MCBRYAN *et al.* Front tracking for gas dynamics. *Journal of Computational Physics*, 62:83–110, 1986 .

[188] B. VAN LEER. Towards the ultimate conservative difference scheme. V. A second-order sequel to Godunov's method. *Journal of Computational Physics*, 32:101–136, 1979 .

[189] J. GLIMM, J. W. GROVE, B. LINDQUIST *et al.* The bifurcation of tracked scalar waves. *SIAM Journal on Scientific and Statistical Computing*, 9(1):61–79, 1988 .

[190] J. GLIMM, J. W. GROVE, X. L. LI *et al.* Robust Computational Algorithms for Dynamic Interface Tracking in Three Dimensions. *SIAM Journal on Scientific Computing*, 21(6):2240–2256, 2000 .

[191] P. COLELLA. A direct eulerian muscl scheme for gas dynamics. *SIAM Journal on Scientific Computing*, 6(1):104–117, 1985 .

[192] S. K. GODUNOV. A difference method for numerical calculation of discontinuous solutions of the equations of hydrodynamics. *Mathmaticheskii Sbornik*, 47(89):271–306, 1959 .

[193] G. STRANG. Accurate partial difference methods II. Non-linear problems. *Numerische Mathematik*, 6:37–46, 1964 .

[194] G. STRANG. On the construction and comparison of difference schemes. *SIAM Journal on Numerical Analysis*, 5(3):506–517, 1968 .

[195] B. TULLY, N. A. HAWKER, M. R. BETNEY *et al.* Simulation of warm dense matter in intense bubble collapse. In Proceedings of Meetings on Acoustics, Montreal (Acoustical Society of America), volume 19, pp. 1–9 (2013).

[196] K. K. HALLER, Y. VENTIKOS, D. POULIKAKOS *et al.* Computational study of high-speed liquid droplet impact. *Journal of Applied Physics*, 92(5):2821, 2002 .

[197] J. H. DYMOND & R. MALHOTRA. The Tait equation: 100 years on. *International Journal of Thermophysics*, 9(6):941–951, 1988 .

[198] R. MENIKOFF & B. J. PLOHR. The Riemann problem for fluid flow of real materials. *Reviews of Modern Physics*, 61(1):75–130, 1989 .

[199] K. NAGAYAMA, Y. MORI, K. SHIMADA *et al.* Shock Hugoniot compression curve for water up to 1 GPa by using a compressed gas gun. *Journal of Applied Physics*, 91(1):476, 2002 .

[200] W. WAGNER & A. PRUSS. The IAPWS Formulation 1995 for the Thermodynamic Properties of Ordinary Water Substance for General and Scientific Use. *Journal of Physical and Chemical Reference Data*, 31(2):387–535, 2002 .

[201] S. P. MARSH. LASL shock Hugoniot data. Technical report, 1980 .

[202] B. TULLY & P. A. ANDERSON. Private communication, 2014 .

[203] H. CHILDS, E. BRUGGER, B. WHITLOCK *et al.* VisIt: An end-user tool for visualizing and analyzing very large data. In High Performance Visualization–Enabling Extreme-Scale Scientific Insight, pp. 357–372 (2012).

[204] M. R. BETNEY, N. A. HAWKER, B. TULLY *et al.* Computational modelling of the interaction of shock waves with multiple gas bubbles in a liquid. *Physics of Fluids*, 27(3):036101, 2015 .

[205] Y. VENTIKOS, N. A. HAWKER & M. R. BETNEY. Multicavity array for intensified collapse, 2012 .

[206] J. D. INGLE & S. R. CROUCH. Spectrochemical Analysis (1988).

[207] S. VAN DER WALT, J. L. SCHÖNBERGER, J. NUNEZ-IGLESIAS *et al.* Scikit-image: image processing in Python. *PeerJ*, 2:e453, 2014 .

[208] J. CANNY. A Computational approach to edge detection. *IEEE Transactions on Pattern Analysis and Machine Intelligence*, PAMI-8(6):679–698, 1986 .

[209] ISO 9288: Thermal insulation - heat transfer by radiation - physical quantities and definitions. Technical report, 1989 .

[210] A. SAVITZKY & M. J. E. GOLAY. Smoothing and Differentiation of Data by Simplified Least Squares Procedures. *Analytical Chemistry*, 36(8):1627–1639, 1964 .

[211] HAMAMATSU. Photomultiplier tubes: basics and applications (third edition) (2007).

[212] HAMAMATSU. Private communication. Technical report, 2014 .

[213] J. E. PARSONS, C. A. CAIN & J. B. FOWLKES. Cost-effective assembly of a basic fiber-optic hydrophone for measurement of high-amplitude therapeutic ultrasound fields. *The Journal of the Acoustical Society of America*, 119(3):1432, 2006 .

[214] J. H. GLADSTONE & T. P. DALE. Researches on the refraction, dispersion, and sensitiveness of liquids. *Philosophical Transactions of the Royal Society of London*, 153(January):317–343, 1863 .

[215] H. S. YADAV, D. S. MURTY, S. N. VERMA *et al.* Measurement of refractive index of water under high dynamic pressures. *Journal of Applied Physics*, 44(5):2197, 1973 .

[216] L. DAVISON & R. A. GRAHAM. Shock compression of solids. *Physics Reports*, 55(4):255–379, 1979 .

[217] R. P. DRAKE. High-energy-density physics (2006).

[218] G. W. COLLINS, P. M. CELLIERS, L. B. DA SILVA *et al.* Temperature measurements of shock compressed liquid deuterium up to 230 GPa. *Physical review letters*, 87(16):165504, 2001 .

[219] J. E. BAILEY, M. D. KNUDSON, A. L. CARLSON *et al.* Time-resolved optical spectroscopy measurements of shocked liquid deuterium. *Physical Review B - Condensed Matter and Materials Physics*, 78(14):144107, 2008 .

[220] Y. B. ZEL'DOVICH & Y. P. RAIZER. Physics of shock waves and high-temperature hydrodynamic phenomena (1966), dover edition.

[221] B. TULLY, N. A. HAWKER & Y. VENTIKOS. Modeling asymmetric cavity collapse with plasma equations of state (in review). *Physical Review E*, pp. 1–16, 2015 .

[222] S. ATZENI & J. MEYER-TER-VEHN. The physics of inertial fusion, (Oxford University Press2004).

[223] D. R. CHURCHILL, B. H. ARMSTRONG, R. R. JOHNSTON *et al.* Absorption coefficients of heated air: A tabulation to 24000 K. *Journal of Quantitative Spectroscopy and Radiative Transfer*, 6:371–442, 1966 .

[224] B. H. ARMSTRONG, J. SOKOLOFF, R. W. NICHOLLS *et al.* Radiative properties of high temperature air. *Journal of Quantitative Spectroscopy and Radiative Transfer*, 1:143–162, 1961 .

[225] L. M. BIBERMAN & I. T. YAKUBOV. State of gas behind front of a strong shockwave. Technical report, 1966 .

[226] L. M. BIBERMAN, S. Y. BRONIN & M. V. BRYKIN. Moving of a blunt body through the dense atmosphere under conditions of severe aerodynamic heating and ablation. *Acta Astronautica*, 7(1):53–65, 1980 .

[227] C. O. LAUX. Optical diagnostics and radiative emission of air plasmas. Ph.D. thesis, 1993 .

[228] J. C. KECK, J. C. CAMM, B. KIVEL *et al.* Radiation from hot air part 2. Shock tube study of absolute intensities. *Annals of Physics*, 7:1–38, 1959 .

[229] R. E. MEYEROTT, J. SOKOLOFF & R. W. NICHOLLS. Absorption coefficients of air. Technical report, 1960 .

[230] F. R. GILMORE. Equilibrium composition and thermodynamic properties of air to 24,000 K. Technical report, 1955 .

[231] J. HILSENRATH & M. KLIEN. Tables of thermodynamic properties of air in chemical equilibrium including second virial corrections from 1500 K To 15,000 K. Technical report, 1965 .

[232] S. CHAUVEAU, M.-Y. PERRIN, P. RIVIÈRE *et al.* Contributions of diatomic molecular electronic systems to heated air radiation. *Journal of Quantitative Spectroscopy and Radiative Transfer*, 72(4):503–530, 2002 .

[233] S. CHAUVEAU, C. DERON, M.-Y. PERRIN *et al.* Radiative transfer in LTE air plasmas for temperatures up to 15,000 K. *Journal of Quantitative Spectroscopy and Radiative Transfer*, 77(2):113–130, 2003 .

[234] B. PEYROU, L. CHEMARTIN, P. LALANDE *et al.* Radiative properties and radiative transfer in high pressure thermal air plasmas. *Journal of Physics D: Applied Physics*, 45:455203, 2012 .

[235] C. O. LAUX, T. G. SPENCE, C. H. KRUGER *et al.* Optical diagnostics of atmospheric pressure air plasmas. *Plasma Sources Science and Technology*, 12(2):125–138, 2003 .

[236] J. J. MACFARLANE, I. E. GOLOVKIN, P. R. WOODRUFF *et al.* Simulation of the ionization dynamics of aluminum irradiated by intense short-pulse lasers. In Proceedings of Inertial Fusion and Science Applications (American Nuclear Society, La Grange Park, IL), pp. 1–4 (2003).

[237] J. J. MACFARLANE, I. E. GOLOVKIN, P. WANG *et al.* SPECT3D - A multi-dimensional collisional-radiative code for generating diagnostic signatures based on hydrodynamics and PIC simulation output. *High Energy Density Physics*, 3:181–190, 2007 .

[238] J. J. MACFARLANE, I. E. GOLOVKIN & P. R. WOODRUFF. HELIOS-CR - A 1-D radiation-magnetohydrodynamics code with inline atomic kinetics modeling. *Journal of Quantitative Spectroscopy and Radiative Transfer*, 99:381–397, 2006 .

[239] P. WANG. Computation and application of atomic data for computation and application of atomic data for inertial confinement fusion plasmas: PhD thesis. Ph.D. thesis, 1991 .

[240] P. WANG, J. J. MACFARLANE & G. A. MOSES. Relativistic-configuration-interaction calculations of K alpha satellite properties for aluminium plasmas created by intense proton beams. *Physical Review E*, 48(5):3934–3942, 1993 .

[241] H. R. GRIEM. Semiempirical formulas for the electron-impact widths and shifts of isolated ion lines in plasmas. *Physical Review*, 165(1):258–266, 1968 .

[242] D. G. HUMMER & D. MIHALAS. The equation of state for stellar envelopes. I - an occupation probability formalism for the truncation of internal partition functions. *The Astrophysical Journal*, 331:794–814, 1988 .



APPENDIX A

EXPERIMENTAL INFORMATION

This appendix presents additional information with regard to the circuits used in the experimental sections of this thesis.

A.1 CONTACT TRIGGER

This section provides additional information on the circuit used in the contact trigger, described in section 5.3. A diagram of the triggering circuit is shown in figure A.1. This utilises a 555 timer, set up to operate in monostable mode. In this mode of operation the timer will produce a single positive pulse of length t_p at the output (3), when the triggering input (2) falls below $\frac{1}{3}(5) \approx 1.7$ V. The width of the pulse is set by the size of the resistor-capacitor combination ($t_p = RC\ln(3)$). In this case a 1 kΩ resistor and a 0.47 µF capacitor are used to give a pulse length of 516 µs. A Schmitt-trigger buffer chip between the contact strips and the 555 timer chip performs switch debouncing and isolation. This circuit simply performs the operation $V = A$, but with some hysteresis. At the contact strips, one strip is connected to ground, whilst the other is connected to the base of a voltage divider

via a pull-up resistor. When the contact strips are not connected, the voltage at A is held at 5 V. When the contact strips are connected, the signal at A is pulled to ground, triggering the timer circuit.

A.2 PHOTO-MULTIPLIER TUBE CIRCUITS

The triggering circuit used for the PMTs is shown in figure A.2. As with the contact trigger circuit, this utilises a 555 timer in monostable mode. The monostable 555 timer circuit requires the triggering input pulse at (2) to be a step from HIGH to LOW, and to be of a shorter duration than the required output pulse. As the output from the contact trigger circuit is a long, positive TTL pulse, a number of additions must be made to the circuit. To invert the signal, a 7404 Hex inverter chip is used. The resistor-capacitor-diode setup between the inverter chip and the 555 timer then reduces the length of the input pulse of the 555 timer. This setup holds the voltage at (2) high under normal operation. However, when the voltage at (6) falls from HIGH to LOW, a short negative-going spike is produced at (2), which is sufficient to trigger the 555 timer. The size of the capacitor determines the time constant of the spike, and thus by making the size of the capacitor small, the length of the input pulse of the 555 timer can be reduced to less than the length of the required output pulse. The diode is used to suppress the positive spike produced when the signal at (6) rises from LOW to HIGH. In order to reduce the effects of ground noise, 10 µF and 10 nF capacitors combinations are used to buffer the circuit.

In addition to the gating circuit, the PMTs module have an inbuilt error detection system. This system pulls the V_{error} output to ground should excessive light be incident on the photocathode. To facilitate detection of errors in the operation of the PMTs, a 555 timer circuit set up in a bistable configuration is used to illuminate an LED. This circuit simply acts as a flip-flop, powering the LED when the input signal V_{error} is pulled to ground, and requiring a manual reset.

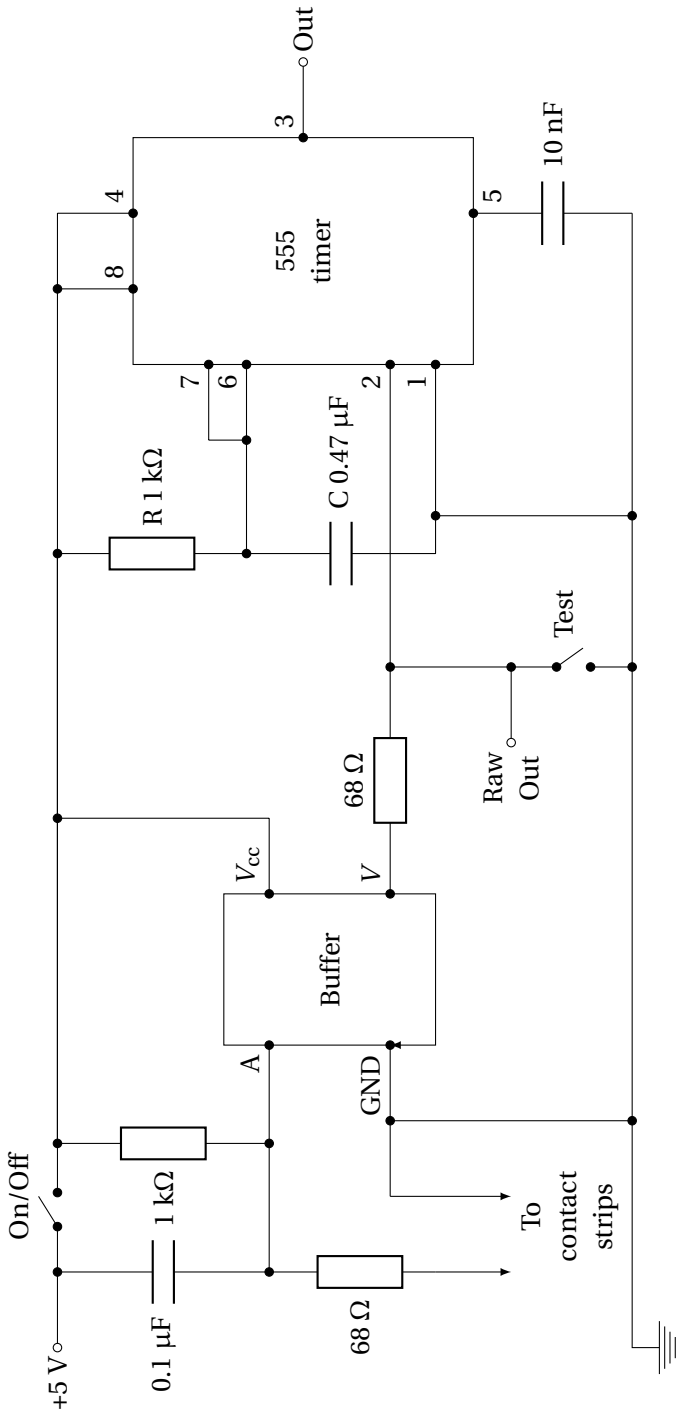

Figure A.1: Contact trigger: triggering circuit

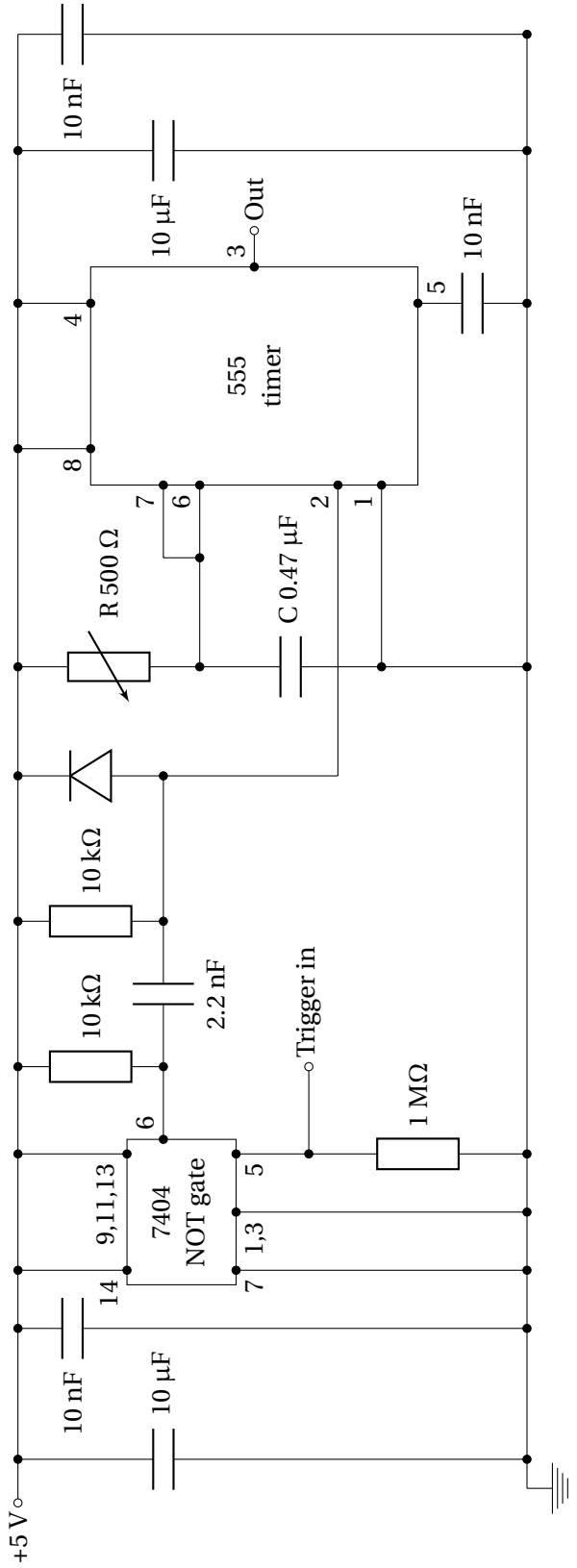

Figure A.2: Gating circuit for the PMTs

APPENDIX B

RADIATION FROM HOT AIR

This appendix details research conducted into the spectra of hot air plasmas. An outline of the fundamental light emitting processes at work in any plasma is given, which is then specialised to the case of air plasmas. The software tool PRISMSPECT is outlined and validated against other published results. This tool is then used to calculate spectra from air plasmas over a range of temperatures and densities. The black-body limit for different temperatures, densities and thicknesses is finally presented.

The spectra of light emission from an emitting entity is strongly related to the temperatures and densities reached. As such, these parameters can in some cases be inferred from the spectrum, provided the physical processes that lead to the formation of that spectrum are known. This can be a complicated process. Air, which forms the contents of the cavities within this work, is a complex mix of a number of gases, all of which will emit light with a particular spectrum when at a particular temperature and density. In this appendix, the processes that lead to this light emission are briefly outlined. Predicted spectra are then presented, and the limit at which an emitting body of air may be treated as a black body inferred.

B.1 RADIATION TRANSPORT AND PROCESSES

Radiation and radiative effects present an extremely complex problem, involving a large number of different processes. As such, only a very brief overview of the subject is presented here. For further information, the reader is referred to the many comprehensive texts on the subject, for example[217,220,222].

B.1.1 The radiative transfer equation

The passage of radiation through a medium in the direction $\mathbf{\Omega}$ is defined by the radiative transfer equation[222]

$$\frac{\lambda^2}{c^2}\frac{\partial L_\lambda}{\partial t} + \mathbf{\Omega}\cdot\nabla L_\lambda \frac{\lambda^2}{c} = \eta_\lambda\left(1+\frac{\lambda^5}{2hc^2}L_\lambda\right) - \mu_\lambda L_\lambda \frac{\lambda^2}{c}. \tag{B.1}$$

where L_λ is the spectral radiance per unit wavelength (units W/m^2/m/sr), c is the speed of light, ρ is the density, h is the Planck constant, and λ is the wavelength. The value η_λ is the coefficient of spontaneous spectral emission per unit mass, and μ_λ the coefficient of spectral absorption; the source terms on the right of this equation thus capture the emission and absorption processes at work. The bracket term $\left(1+\frac{\lambda^5}{2hc^2}L_\lambda\right)$ accounts for stimulated emission.

Under local thermal equilibrium (LTE), collisional equilibrium is achieved between the plasma constituents, with the particle energy spectra following a Boltzmann distribution. A *local* temperature T can therefore be defined for a particular point in space. Under this assumption, μ_λ and η_λ are material properties, dependent on the temperature and density of the material. Under complete thermal equilibrium, the spectral radiance of the emission will follow a black-body trend ($L_\lambda = L_{\lambda,\mathrm{BB}}$), and all the time and spatial varying terms reduce to zero. The relationship between the emission and absorption coefficients

is then

$$\frac{\eta_\lambda}{\mu_\lambda} = \frac{\lambda^2}{c} \frac{L_{\lambda,\mathrm{BB}}}{1 + \frac{\lambda^5}{2hc^2} L_{\lambda,\mathrm{BB}}} \tag{B.2}$$

where $L_{\lambda,\mathrm{BB}}$ is given by Planck's law (equation 7.2). Substituting in equation 7.2, equation B.2 then becomes

$$\frac{\eta_\lambda}{\mu_\lambda} = \frac{2hc}{\lambda^3} e^{-\frac{hc}{k_B \lambda T}} \tag{B.3}$$

which is Kirchhoff's law. As this is independent of L_λ, this relationship holds generally under LTE conditions, where $L_\lambda \neq L_{\lambda,\mathrm{BB}}$[222]. Substituting equation B.3 into equation B.1, in one dimension equation B.1 may be written as

$$\frac{\delta L_\lambda}{\delta x} = \mu_\lambda^{'} \left(L_{\lambda,\mathrm{BB}} - L_\lambda \right) \tag{B.4}$$

where the reduced absorption coefficient μ'_λ is given by

$$\mu_\lambda^{'} = \mu_\lambda \left(1 - e^{-hc/k_\mathrm{B} \lambda T} \right), \tag{B.5}$$

and is adjusted for re-emission. At a distance x, the solution to equation B.4 is then:

$$L_\lambda = L_{\lambda,\mathrm{BB}} \left(1 - e^{-\mu_\lambda^{'} x} \right). \tag{B.6}$$

This equation gives a comparatively simple way to calculate the spectrum of an emitting source of known composition, temperature and density. It should be noted that this equation is only valid under LTE conditions, where electron and ion temperatures are equal, and vary slowly with distance in relation to the mean free path $l_\lambda = 1/\mu_\lambda$. This is not a valid assumption under all circumstances. Due to the difference in mass between electrons and ions, energy transfer between the two is relatively slow, and an appreciable relaxation time exists before the electron and ion temperatures reach a single value. Zel'dovich *et al.*[220] estimate this time to be

$$\tau_{ei} = \frac{252 A T_e^{3/2}}{N Z^2 \ln \Lambda} \text{ seconds} \tag{B.7}$$

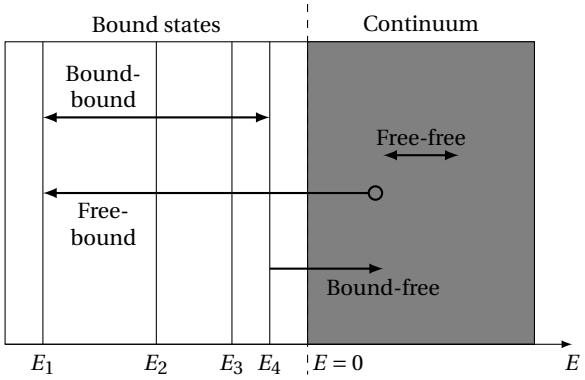

Figure B.1: Energy level diagram of radiative processes, showing the possible transitions.

where A is the atomic weight of the atoms, T_e is the electron temperature in Kelvin, N is the ion number density, Z is ionisation level and Λ is approximately given by

$$\Lambda = \frac{3\,(kT)^{3/2}}{2(4\pi)^{1/2}Z^3e^3N^{1/2}}. \tag{B.8}$$

This is a small number in relation to this experiment (for example, for a number density of $N = 10^{18}$ cm^{-3}, $T_e = 20,000$ K, $Z = 1$ and $A = 16$, $\tau_{ei} \approx 2.8 \times 10^{-9}$ seconds).

B.1.2 Radiative processes

All radiation processes are fundamentally driven by the movement of electrons within the medium, and the interaction of these electrons with the various species present.* Electrons may either be bound to a particular atom, with one of a specific set of possible discrete negative energy states, or are free in the continuum with an energy that can assume any positive value. The movement between these states dictates the spectra of radiation produced. Radiative processes may be broken down into three distinct groups: bound-bound, bound-free and free-free transitions (see figure B.1). Bound-bound transitions correspond to the movement of electrons between different discrete energy states in atoms or molecules. Photons may either be absorbed, raising an electron

*Molecular transitions may involve transitions between rotational and vibrational states only, however photons emitted or absorbed during these processes have very low energy (lying in the infra-red part of the spectrum), and are of negligible importance above a few thousand degrees [220]

to a higher energy state, or emitted, dropping the electron to a lower state. As energy states within atoms have specific values, photons may only be emitted or absorbed if they have the exact energy required to move an electron from one state to another. This thus leads to the formation of spectral lines. Within molecular transitions, molecules may also undergo rotational and vibrational transitions, leading to bands of large numbers of spectral lines.

Within bound-free transitions, electrons receive sufficient energy from the absorption of a photon that they are removed entirely from the particle and become free. As the electron can assume any energy value in the free state, this process leads to continuous spectra. The reverse of this process is free-bound transitions, whereby electrons are captured by particles, leading to the emission of photons. This process also leads to continuous spectra.

Free-free transitions, generally called *bremsstrahlung*, occur when electrons pass close to particles, but are not absorbed. The electron is either slowed down, leading to the formation of a photon, or is accelerated (reverse bremsstrahlung), leading to the absorption of a photon. Free-free transitions also lead to continuous spectra.[220]

The relative importance of these processes is greatly dependent on the particular conditions present within the plasma. At low temperatures, gases generally consist of molecules, and molecular transitions are thus the dominant process. As the temperature is increased, these molecules gradually become dissociated, and atomic spectral lines become more significant. At higher temperatures still, gases become progressively more ionised, and continuous processes such as bound-free transitions dominate.

B.2 RADIATION FROM AIR LITERATURE REVIEW

No attempt is made to control the gaseous contents of the cavities in this work, and cavities thus contain a mixture of air and water vapour, at approximately ambient conditions. This complicates the analysis of spectra, as air consists of a mixture of a number of different gases, although the ubiquity of air has meant the subject has been comprehensively studied. In particular, the region of temperatures between $\sim 10,000 - 20,000$ K and densities of $10^{-7}\rho_0$ to $10\rho_0$ has seen the greatest interest due to its applicability to radiative heating of high velocity missiles or rockets on re-entry[223–226], as well as plasma torches[227]. Air plasmas in the region of higher densities (up to solid density) at these temperatures have not been well researched to the author's knowledge; these studies are typically conducted with pure gas.

Significant work was done on the properties of air plasmas in the 1950s and 1960s, for research into nuclear detonations and re-entry bodies. Shock tube experiments were conducted by numerous authors, in particular at the AVCO research laboratory in the United States[228]. These results were coupled with a significant theoretical effort[224], and used to produce extensive tables of absorption coefficients[223,229] as well as chemical composition and transport properties[230,231]. More recent work has utilised improved computational ability as well as collated studies of line transitions to produce very detailed spectra at low densities over a wide temperature range. This work has primarily been conducted as a diagnostic tool for plasma torches.[227,232–235].

According to Zel'dovich and Raizer[220], at temperatures below approximately 15,000 K almost all processes outlined in section B.1.2 play some role, with the relative contribution heavily dependent on the frequency of the light, as well as the temperature and density. They outline the continuous and quasi-continuous processes involved at these conditions as: molecular transitions in N_2, O_2, N_2^+, NO and NO_2; photoelectric absorption

by O_2, N_2, NO, O, N and O^-; and free-free transitions in the field of O^+, N^+, NO^+, O_2^+, N_2^+, as well as a small contribution from neutral atoms and molecules. Above 15,000 K, molecules are almost completely dissociated into atoms, and a significant proportion of species are ionised. Under these conditions, the continuous spectrum is dominated by photoelectric absorption and bremsstrahlung.

B.3 PRISMSPECT

Calculations of absorption coefficients in this work are conducted using the collisional-radiative code PrismSPECT[236]. This commercial code was developed by Prism Computation Sciences Inc.(www.prism-cs.com), and uses the same physics engine as the more comprehensive code SPECT3D, also developed by the same authors. PrismSPECT calculates a spectrum given a temperature, density, depth and ambient composition, and does not take into account the complex three-dimensional effects accounted for in SPECT3D. The methods used in this code have been outlined extensively elsewhere[236–238], and thus only a brief summary will be given here.

B.3.1 Methods

Atomic level calculations in this work are accounted for using detailed configuration accounting, whereby atomic level populations are computed based on a list of relative number densities of atomic elements. Molecules and molecular effects are not included in the model. Local thermal equilibrium (LTE) is assumed, and populations are computed using the Saha equation[220] with Boltzmann statistics. Frequency dependent emission and absorption coefficients are calculated by summing over all contributions from bound-bound, bound-free and free-free transitions. Energy levels, photoionisation cross sections, oscillator strengths, autoionisation rates and electron collision cross sections are calculated using the ATBASE suite of codes[239,240].

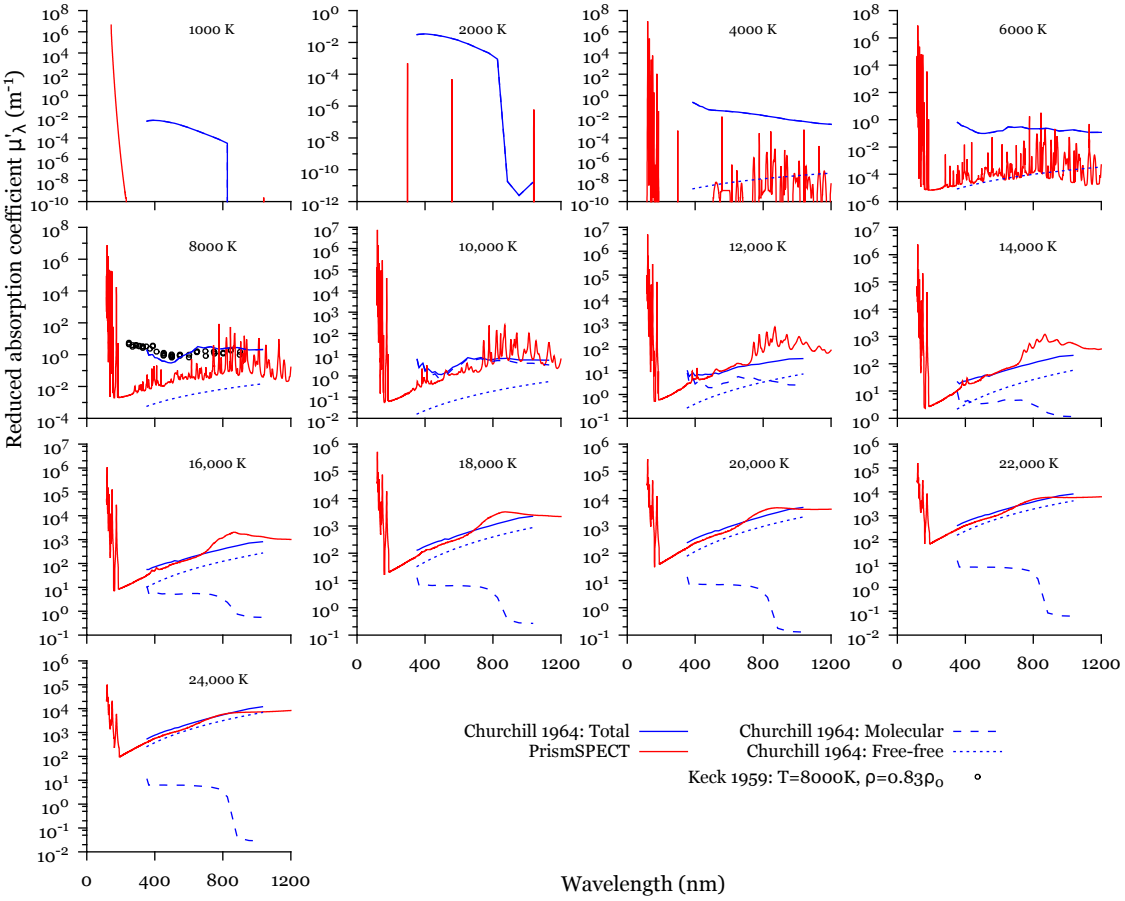

Figure B.2: Reduced absorption coefficients of an air plasma at a number of different temperatures at a density of 1.293 kg/m^3, calculated by Churchill *et al.*[223] and replicated in PrismSPECT. Also shown are the experimental results of Keck *et al.*[228].

Line profiles for bound-bound transitions are modelled using a Voigt profile, and include natural, Doppler and Stark broadening effects[237]. Bound-bound Stark widths are computed using a semi-empirical model[241], and continuum lowering effects are modelled using an occupation probability model[242]. This produces a continuous reduction in the effective statistical weights of energy levels with increasing density, meaning that high-n states cannot be populated at very high densities.[236].

Element	Atomic number	Fraction
N	7	78.44
O	8	21.07
Ar	18	0.47

Table B.1: Initialised atomic relative number densities for PrismSPECT simulations of air. Numbers taken from Gilmore[230]

B.3.2 Validity for modelling radiation from air

To assess the applicability of PrismSPECT for the analysis of air plasmas, comparison is made here between results calculated using the code, and those produced by other authors. Specifically, results are compared to the work of Churchill *et al.*[223] and Peyrou *et al.*[234]. The results of Peyrou are very detailed, incorporating all the processes as listed in section B.2 with the exception of NO_2 molecular transitions. The model was extended up to 35,000 K with the inclusion of N^{2+} and O^{2+} based processes. Atomic line transitions are taken from the NIST database. The older results of Churchill *et al.* do not include atomic line transitions, limiting their usefulness at higher temperatures. However, molecular transitions and continuous processes are included, and results are presented over a wide range of temperatures and densities. All presented result sets are modelled as zero-width.

Figures B.2 and B.3 compare reduced absorption coefficients calculated by Churchill *et al.*[223] to results at the same conditions modelled using PrismSPECT. The initialised atomic relative number densities in the PrismSPECT simulation are given in table B.1. As might be expected, the omission of molecular transitions in the PrismSPECT model greatly reduces the accuracy of the calculated result at low temperatures. However, as the relative contribution of the molecular transitions reduces (calculated by Churchill and shown in the figures by the blue dashed lines), the match between the two result sets improves significantly. The quality of the match improves with increased temperature,

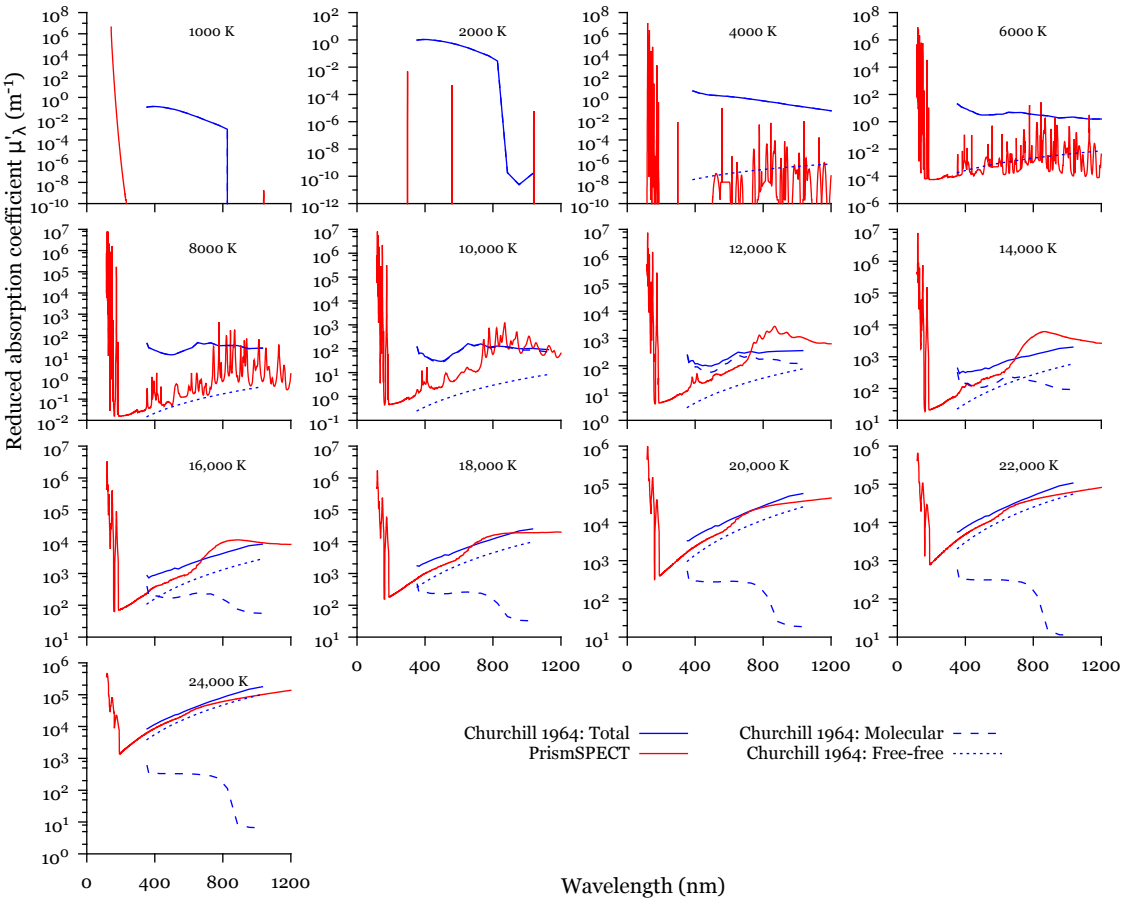

Figure B.3: Reduced absorption coefficients of an air plasma at a number of different temperatures at a density of 12.93 kg/m^3, calculated by Churchill *et al.*[223] and replicated in PrismSPECT.

but reduces slightly with increased density. Due to the omission of atomic line transitions in the Churchill result it is not possible to say which of the two models captures the correct result more accurately under these conditions.

Further comparison is given in figure B.4, which compares the results of Peyrou *et al.*[234] to equivalent PrismSPECT simulations at a pressure of 200 bar, and temperatures of 5,000 K and 25,000 K. These conditions correspond to densities of approximately 6.3 kg/m^3 and 0.4 kg/m^3 respectively, based on the results of Gilmore[230]. These results again show that the lack of molecular transitions in the PrismSPECT model leads to an inaccurate result at low temperatures. However, in this case the high temperature results are very closely matched.

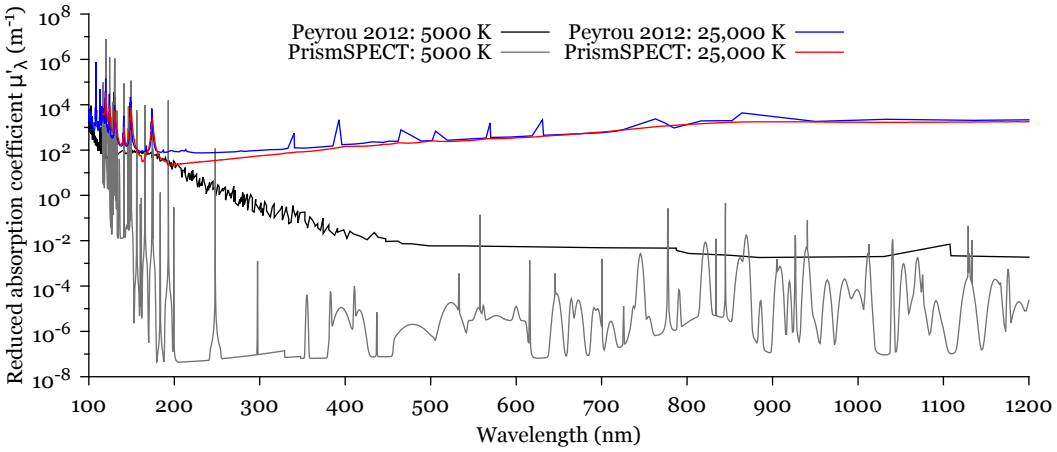

Figure B.4: Reduced absorption coefficients, calculated by *Peyrou* et al.[234] and replicated in PrismSPECT. At a pressure of 100 bar, results at a temperature of 5,000 K and 25,000 K are shown.

These comparisons suggest that PrismSPECT is an appropriate tool to use for the modelling of air plasmas at temperatures above at least 10,000 K, and is not valid below this threshold. Due to a lack of available data for comparison, it is not known whether results calculated at higher densities than presented here are adequately captured by the model.

B.4 Calculated spectra and the validity of a black-body approach

Figures B.5 and B.6 show the predicted variation in the spectral radiance of emitted radiation with wavelength, over a range of temperatures and densities, based on the result of Churchill *et al.*[223] and PrismSPECT respectively. The sample thickness at which the results were calculated is 1 mm. The Churchill based results are likely to be more accurate up to a temperature of approximately 10,000 K, with the PrismSPECT results more representative beyond this point. These results suggest that at lower densities of between 1 and 10 kg/m^3 atomic and molecular line emission is the dominant source of emission, up to temperatures of approximately 15,000 K. These lines smooth out into a black-body

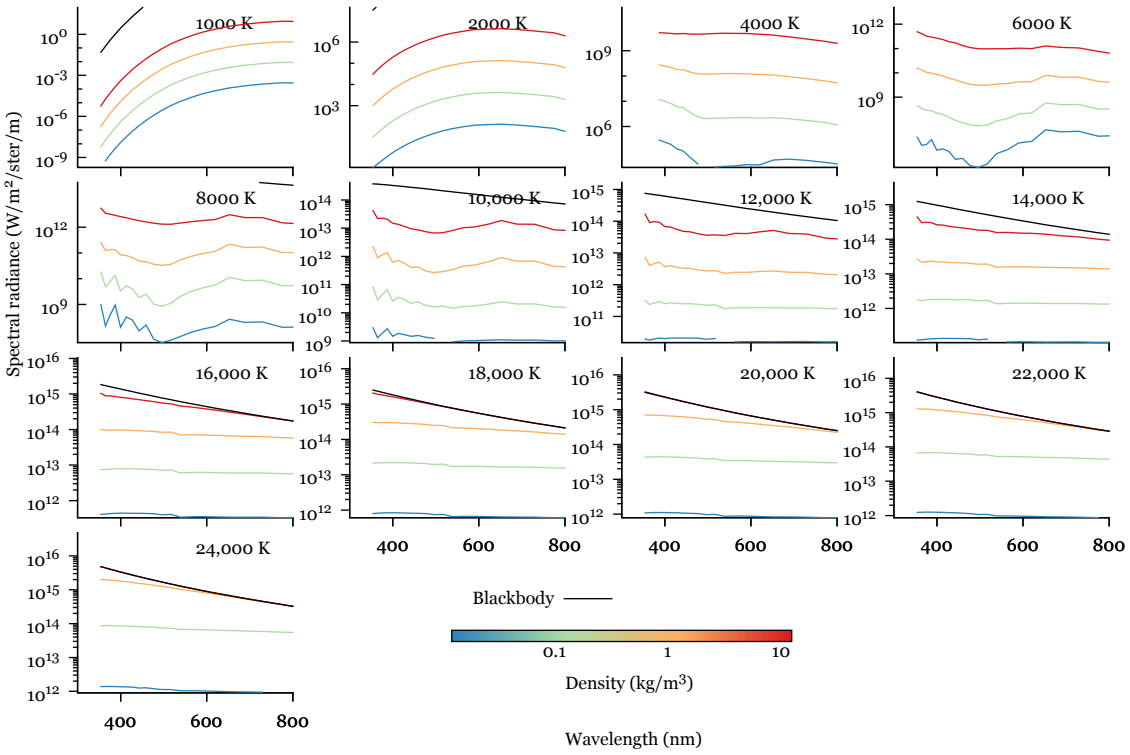

Figure B.5: Spectral radiance of emitted radiation from an air plasma for a range of temperatures and densities, calculated from the data of Churchill *et al.*[223]. Thickness 1 mm.

form at very high densities. Beyond this temperature, although some peaks are visible at low density all lines gradually approach the black-body curve, such that beyond approximately 40,000 K a black-body spectrum is expected at all modelled densities.

Further insight into the regions of the temperature-density space in which a black-body approximation is valid is given by figure B.7. Within the figure, each shaded region shows the portion of the temperature-density space in which the spectrum is predicted to be that of a black-body, for a particular thickness. The result is calculated from the PrismSPECT results. A spectrum is deemed to be a black body when the emissivity ($\epsilon_\lambda = \left(L_\lambda / L_{\lambda,\mathrm{BB}}\right)$) averaged over all wavelengths between 400 and 800 nm has a value of 0.95 or greater. As can be seen, these results suggest that very large depths are required to achieve a spectrum which approximates a black body below 10,000 K, at any density. This limit may reduce slightly due to the poor accuracy of the results below this threshold.

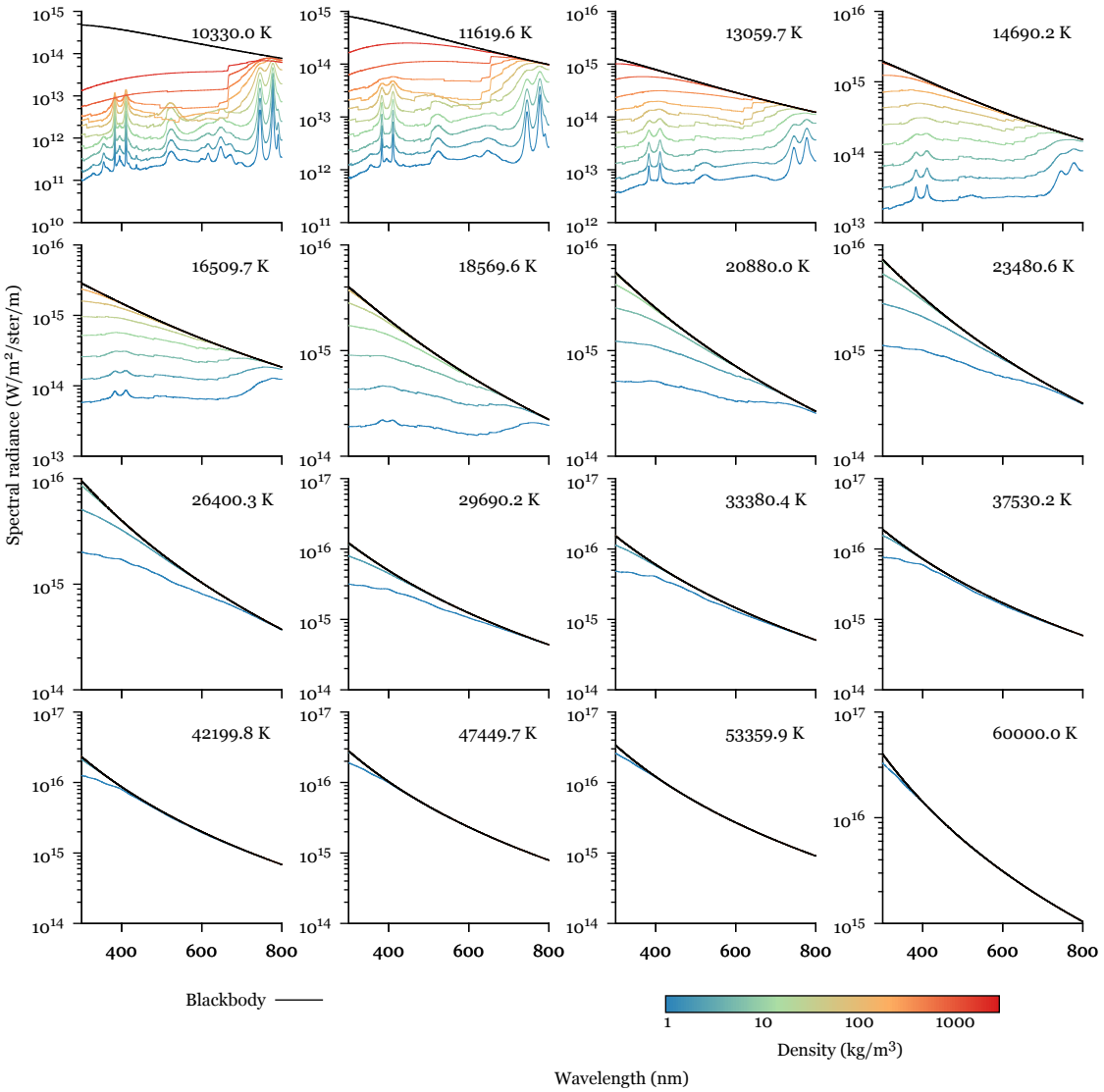

Figure B.6: Spectral radiance of emitted radiation from an air plasma, calculated using PrismSPECT. Thickness 1 mm.

At the depths seen in the experiment (of order 1 mm), the assumption of a black body can be seen to be neither applicable for all temperatures considered in this study, or an unreasonable assumption under all cases.

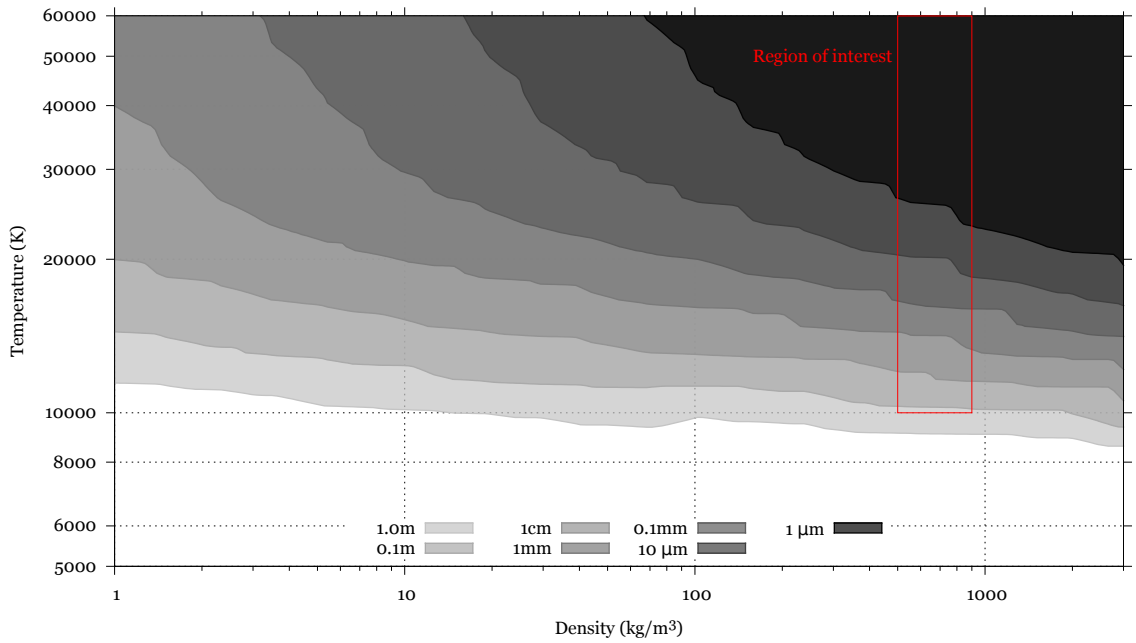

Figure B.7: Limits of the validity of a black-body approximation for a number of different sample thicknesses, calculated using PrismSPECT. Shaded regions show where the spectrum is predicted to be a black body. Red box shows the approximate region of interest, inferred from figure 8.19.